DOCTORAL DISSERTATION

eman ta zabal zazu

Universidad
del País Vasco

Euskal Herriko
Unibertsitatea

NAZIOARTEKO
BIKAINTASUN
CAMPUSA
CAMPUS DE
EXCELENCIA
INTERNACIONAL

Theoretical Design of CO Poisoning Resistant Pt Catalysts through Ge Alloying

ANDONI UGARTEMENDIA BIURRUN

Supervised by Elisa Jimenez Izal and Jose M. Mercero Larraza

Polimero eta Material Aurreratuak: Fisika, Kimika eta Teknologia saila

Euskal Herriko Unibertsitatea/Universidad del País Vasco (EHU/UPV)

January 2024

Theoretical Design of CO Poisoning Resistant Pt Catalysts through Ge Alloying

Dissertation presented in

Submitted in fulfillment of the requirements of the

DOCTORAL PROGRAMME IN THEORETICAL CHEMISTRY AND COMPUTATIONAL MODELING

Presented by

ANDONI UGARTEMENDIA BIURRUN

Supervised by

ELISA JIMENEZ IZAL

and

JOSE M. MERCERO LARRAZA

Tutorized by

XABIER LOPEZ PESTAÑA

In Donostia, January 2024

Nere amonei

Statement of Originality

Hereby I declare, that this dissertation is my original authorial work, which I have worked out by my own. All sources, references and literature used or excerpted during elaboration of this work are properly cited and listed in complete reference to the due source.

Andoni Ugartemendia Biurrun

Donostia, January 2024

Contents

Acknowledgements

Thalassa! *Thalassa*! Azkenean ikusten dut *oînops póntos*! Urte guzti hauetan igarotago gorabehera guztiez gain. Konfinamendu bat eta guzti! Zoritxarrez, honek ere esan nahi du periodo honen bukaera iritsi dela. Mingotsa egiten zait hitz hauek idaztea jakinda bukaera gerturatzen ari dela. Ez nuen imaginatzen hain laister bukatuko zenik, baina jada 6 urte igaro dira taldean sartu nintzenetik! Beti ikusten nuen nere burua masterreko ikasle bezala! Atzera begira, seguraski 6 urte hauek bizitzako baliotsuenak izan dira. Ezin dut esan abentura handiak bizi izan ditudala, baina agian oker egiten dugu uneoro abentura handi baten zain egoten gure ingurua ahaztuz. Tolkienen esanetan, "*If more of us valued food and cheer and song above hoarded gold, it would be a merrier world*". Hala ere, esan dezaket pertsona bezala gehien hazi naizen momentua izan dela, eta ziur nago oraindik bide luzea geratzen zaidala.

Momentu oso politak bizi ditut urte hauetan zuei esker. Beraz, eskerrak eman nahiko nizkieke urte hauetan ezagutu ditudan pertsona guztiei. *Merci*! Zaila da joan eta etorri diren pertsona guztiei behar bezala eskertzea, dexente izan baitira; hortaz, barkamena eskatzen dizuet aldez aurretik zerbait pasatzen bazait.

Lehenik, kimika teorikako taldea orokorrean eskertu nahiko nuke doktoretza egiteko aukera emateagatik. Hasieratik oso integratua sentitu naiz, taldearen parte garrantzitsu bat banintz bezala. Gehien apreziatzen dudana da taldean ez dagoela barrerarik senior eta hasi berrien artean; denok elkar errespetazen dugu eta kafea hartzeko garaian denok maila berean gaude. Izan ere, errespetuan eta pertsonetan zentratuta eraikitako taldea baita. Gainera, azpimarratu behar dut taldean sentitu

dudan babesa. Eskerrak eman nahiko nuke hasieratik nigan erakutsitako konfiantza handiagatik.

Bestetik, talde hau aukeratzeko arrazoietako bat da kuantikak ere kimikan bere papera duela erakusteagatik, eta oso garrantzitsua gainera. Badago kimika probetetatik haratago. Nire interesa kuantikan Stephen Hawking-en "*Denboraren Historia Laburra*" irakurri nuenean hasi zen, 17 urte nintuela, beste asko bezala. Orduan erabiki nuen zientzialaria izan nahi nuela. Hurrengo urte osoa zalantzan pasa nuen fisika edo kimika ikasi. Garai hortan, mundu mikroskopikoa interesatzen zitzaidan gehien eta beraz, kimika aukeratu nuen. Gradua hasi nintzenean enteratu nintzen kimika kuantikoa delakoa existitzen dela eta segituan jakin nuen honetara dedikatu nahi nuela. Graduko lehenengo bi urteak desiratzen pasa nuen Kifis II asignatura emateko eta kuantikan sakontzeko. Hemen datozte eskertu nahi ditudan hurrengo bi pertsonak.

Txoni eta Xabi eskertu behar ditut hain dozente honak izateagatik. Askorentzat "beldurgarria" izan daitekeen asignatura bat zuek modu oso entretenigarrian ematen zenuten. Hein batean, zuei eskertu behar dizuet kimika kuantikoari buruz trans-mititutako jakinmina. Izan ere, hauxe da ikasleok talde hau aukeratzen dugun arrazoietako bat.

Honen harira, ezinbestekoa iruditzen zait aipatzea Leonard Susskind-en "*The Theoretical Minimum*" eta Feynman-en ikastaroek paper garrantzitsua jokatu dutela nere kuantikako ikaskuntza prozesuan.

Berriro ere Txonirengana bueltatzen naiz, bera nere TFG-ko zuzendaria izan baitzen. Oraindik gogoan dut nola joan nintzen Txoniren bulegora eta lotsatuta komentatu nion TFG-a kimika teorikoari buruz egin nahi nuela. Zuk inongo trabarik gabe baiezkoa eman zenidan. Hementxe hasi zen dena. Gero, lehenengo kalkuluak eta erroreak etorri ziren Gaussianen. Nola ixten zen Moldeneko leihoa! Eta ni hainbeste akronimoen artean galduta, baina zuk beti explikazio argiak emateko gai zinen. Faltarik gabe ere eskertu behar dizut burokraziarekin emandako laguntzaga guztiagatik. Zenbat zalantza argitu dizkidazun!

Eta nola ahaztu zuetaz ekipo! Mila esker elkar konpartitu ditugun kafe guztiengatik! Zuek bidaia honetak akonpainatu didazue. David eta Oksana izan ziren lehenak. Elkarrekin joan ginen Madrid, Vigo eta Zaragozara masterrean. Eta horrez

bestie, how can I forget you. You have been probably one of the most important friends I have made during my PhD. It is very unfortunate that we stayed together so little time; by the time you came I was already leaving. Special thanks also to my roommates Milod, Stan and the rest. Thank you Milod for showing me persian music.

I would like to express my gratitude to Jaakko for giving me the opportunity to do a research stay in his group in Trondheim. I gained a lot of insight into catalysis and learned many computational techniques despite the little time I spent there. I really enjoyed the weekly meetings with Sander and you. I feel it has been a very rewarding experience. Thank you for making my stay so warm and comforting. In addition, despite not meeting him in person, I would also like to thank Marko who has been constantly helping me with the microkinetic simulations.

Por otro lado, expresar mi admiración a todos los participantes de LatinXChem por su tremendo entusiasmo para la ciencia. Aunque solo haya podido participar en dos ediciones lo pasé gratamente compartiendo ciencia con nuestros compañeros al otro lado del Atlántico.

Elisa eta Txema, zuei eskerrak ematea ez litzateke nahikoa izango, zuzendari baino gehiago izan baitzarete. Hitz egokiak bilatu ezinean, bihotzetik bakarrik ahal dizuet hitz egin. Batez ere, nigan edukitako konbikzioa eskertu behar dizuet. Hasieratik nigan apostatu zenuten eta egunero borrokatu duzute ni aurrera jarraitu ahal izateko. Nire etorkizun akademikoan apostatu duzute, zuenaren aurretik jarriz. Honengatik, zorretan nago zuekin. Beti baloratu dut eman didazuten tratua. Batetik, oso babestua sentituta naiz zuekin. Arazo bat banu, banekien zuek nere atzean egongo zinatela laguntzeko. Beti kontatu ahal izan dut zuekin, berdin dio zenbat lan zenuten. Hau eskertzekoa da jakinda mundu akademikoa oso berekoia izan daitekeela batzuetan. Bestetik, beti tratatu didazute igual bat bezala, superiodidade tantarik gabe; gure artean ez da barrerarik egon. Edozein bilera egiten genuela, nire hiritziak eta iradokizunak zuenak bezain beste balio zuten. Honekin lotuta, askatasun handia eman didazute gauza berriak exploratzeko. Nire ideiak garatzen utzi didazute. Oso proiektu polita eraiki dugu elkarrekin. Oraindik interes handia jarraitzen dut edukitzen PtGe klusterretan; kariño handia hartu diet:) Tesi hau bukatu eta gero, sentsazioa dut oraindik gauza asko geratzen

direla kluster hauek ulertzeko. PtGe klusterrei oraindik bizitza asko geratzen zaie! Esan beharra dut asko miresten dudala zuen lan egiteko modua. Nigatik hoberena ateretzan jakin izan duzute, nigan sinisten erakutsi didazute. Zuek oso barneratuta duzute pertsonak garela azken finean. Zuek zinaten lehenak esaten deskantso bat behar nuela! Ni askotan detaileetan galtzeko joera neukan. Elisa zuk beti ekartzen zenidan bueltan eta bide zuzena erakusten zenidan. Beti zenituen argi helburu nagusiak. Tradizioarekin jarraituz, mila esker Txema ordenagailuekin hainbeste laguntzeagatik! Behin baino gehiagotan salbatu didazu bizitza. Duo bikaina egiten duzute Txema eta Elisa! Baita lekzio bat baino gehiago erakutsi didazute, bai esparru akademikoan bai pertsonalean. Nahiz eta ez iruditu, bizitza pertsonalean pisu asko eduki duzute. Bizitza pertsonala akademikoarekin gestionatzen erakutsi didazute. Aholku asko jaso ditut urte hauetan oso baliogarriak izango direnak etorkizunean. Asko ikasi dut zuengandik, benetan. Txema eta Elisa tesian zehar asko hazi izan banaiz zientzialari eta pertsona bezala, hau zuei esker izan da. Hala ere, badakit oraindik oso bide luzea geratzen zaidala, baina zuek lehenengo harria jartzen lagundu didazue. Ohore bat izan da zuek zuzendari bezala edukitzea; ez zuzendari eta zuzendariorde bezala, baizik eta zuzendari eta zuzendari bezala. Txema Elisa bezain zuzendari izan dut. Mila esker nigatik egindako guztiagatik! Tesi hau aurrera atera bada, zuen laguntzari esker izan da bakarrik. By the way, sentitzen dut azkeneko hilabeteak korrika eta presaka ibili izana, susto bat baino gehiago izan baitugu.

El grupo del Germanio no se podría entender sin tí Abel. Gracias por enseñarme a interpretar los mecanismos de reacción, calcular EDAs y por hacer figuras tán chulas! Ves cosas en los diagramas de reacción que nadie más es capaz de ver. También gracias por darme la oportunidad de participar en el congreso del fósforo. Fue una experiencia muy enriquecedora aprender sobre un tema tan diferente al mío, y la cena en la sidrería estuvo genial! En lo más personal, has sido una compañero genial. Ha sido un placer trabajar contigo!

Aran eskertu nahiko nuke berarekin lan egiteko aukera emateagatik. Oso gustoko izan dut zurekin lan egiten eta izugarri ikasi dut grafenoaren munduari buruz. Eskertu behar dut ere nigan erakutsitako konfiantza eta bihotz ona.

Jarraian errusiar, persiar eta kaukasiar literatura eskertu nahiko nuke bere

osotasunean bizitza sakonago ulertuarazi didalako. Georgia eta Armenia arakatu gabeko bi diamante dira. Zientza ez da nahikoa gure mundua ulertzeko. Zientzian soilik zentratzea errealitatearen argazki bat bezala ikustea da, errealitate bera bizi beharrean. Literaturak imaginatzeko gai ez garena erakusten digu. Gauza interesgarri asko daude zientziatik haratago!

Gracias a mis padres por todo. Siempre habeís creído en mí y habeís hecho todo lo posible para que cumpliese mis sueños. Siento que sin vuestra constante ayuda no hubiera podido llegar hasta aquí. habeís sido mis dos pilares en esta vida. Como en nuestra casa no se está en ningun lado. Hemos compartido mucho humor y cariño en los últimos años, sobretodo cuando cierta persona se pone a hablar de pájaros. Por tanto, os voy a echar mucho de menos el próximo año. Gracias también a mi hermano que a pesar de nuestras diferencias significativamente significativas llegamos a entendernos bien. Nere gainontzeko familiari ere eskerrak, lehengusuak eta osaba-izebak. Y cómo no, agaredecer a mis dos amonas, por mostrarme un amor infinito. Me acuerdo de cada cholocate caliente y paseo que hemos compartido. Os quiero muchísimo! Esta tesis va dedicada a vosotras.

Y te dejo a ti para el final carinyet por todo lo que supones. Gracias por aparecer en mi vida, de una manera tan casual diría. Todo empezó en el ESPA en Vigo ¡Quién hubiera dicho que iba a pasar algo así en un congreso de química teórica! Pero sí, el ESPA nunca defrauda. Todavía me acuerdo cómo me pediste que te hiciera una foto en el barco y desapareciste sin más. Cuando hablé por primera vez contigo sentí que había una conexión especial. Fuimos los únicos que entendimos la referencia a *Aelita*; esto ya fue el primer indicio. Jajaja. Nunca había sentido tanta confianza hacia una persona. En la cena de gala nos pasamos horas hablando y no se nos acababan los temas. Apenas nos hemos conocido, pero hemos hecho infinidad de cosas juntos en los últimos años. Estaba genial tomar un chocolate en Santa Catalina, pasear por el río Turia o por el centro, o relajarnos en la Ciudad de las Artes. Los días en Chulilla y Burdeos fueron muy especiales. Estoy deseando volver a la Peña Judía y que tu abuelo nos cuente sus historietas. Lo que más valoro es la confianza mutua que tenemos; podemos gastarnos cualquier tipo de bromas sin que pase nada. Todavía estoy convencido de que eran estrellas-aviones! Si estoy contigo estoy seguro de que nos pasará algo gracioso y con un francés de por medio.

Hemos llegado a entendernos a un nivel muy profundo. No te imaginas cuánto me has ayudado en los últimos años. Por lo tanto, te pido que tú tampoco eches la toalla porque esto no es más que el primer párrafo de la primera página. Eres mi luz en este viaje María, y espero nunca se apague. Ahora tendremos un lugar en la hoguera de los sueños.

"Reshaping life! People who can say that have never understood a thing about life—they have never felt its breath, its heartbeat—however much they have seen or done. They look on it as a lump of raw material that needs to be processed by them, to be ennobled by their touch. But life is never a material, a substance to be molded. If you want to know, life is the principle of self-renewal, it is constantly renewing and remaking and changing and transfiguring itself, it is infinitely beyond your or my obtuse theories about it."

— Boris Pasternak, *Doctor Zhivago*

List of Figures

List of Tables

List of Abbreviations

AdNDP Adaptive Natural Density Partitioning.

AFC alkaline fuel cell.

AFM atomic force microscopy.

AIMD *ab initio* molecular dynamics.

AOR ammonia oxidation reaction.

AOs atomic orbitals.

APW augmented plane wave.

BDF backward differentiation formula.

BEs binding energies.

BGs binding free energies.

BLDA bond length distribution algorithm.

BO Born-Oppenheimer.

BSSE basis set superposition error.

BvK-PBCs Born von-Karman periodic boundary conditions.

BZ Brillouin zone.

CC coupled cluster.

CDD charge density difference.

CFT crystal field theory.

CG conjugate gradient.

CHE computational hydrogen electrode.

CI configuration interaction.

CI-NEB climbing image nudged elastic band.

CO−PROX CO preferential oxidation.

CO$_2$RR CO$_2$ electrochemical reduction.

CSTR continuous stirred-tank reactor.

DFAs density functional approximations.

DFT density functional theory.

DOE Department of Energy.

DOS density of states.

DRC degree of rate control.

ECP effective core potential.

EMSI electronic metal-support interaction.

ER Eley−Rideal.

EXAFS extended X-ray absorption fine structure.

FECCs fully exposed cluster catalysts.

FFT fast fourier transform.

FS final state.

FTIR Fourier transform infrared.

FWHM full width at half-maximum.

GA genetic algorithm.

GDL gas diffusion layer.

GDP gross domestic product.

GEA gradient expansion approximation.

GGA generalized gradient approximation.

GM global minimum.

HAADF-STEM high-angle annular dark-field scanning transmission electron microscopy.

HEAs high entropy alloys.

HEG homogeneous electron gas.

HER hydrogen evolution reaction.

HF Hartree-Fock.

HOMO highest occupied molecular orbital.

HOR hydrogen oxidation reaction.

IM intermediate state.

IS initial state.

ISS ion scattering spectroscopy.

KIE kinetic isotope effect.

KMC kinetic Monte Carlo.

KS Kohn-Sham.

LCAO linear combination of atomic orbital.

LDA local density approximation.

LH Langmuir−Hinshelwood.

LL Levy-Lieb.

LMTO linear muffin-tin orbitals.

LSDA local spin density approximation.

LUMO lowest unoccupied molecular orbital.

MCFC molten carbonate fuel cell.

MCSCF multi-configurational self-consistent field.

MEA membrane-electrode assembly.

meta-GGA meta-generalized gradient approximation.

MF-MKM mean-field microkinetic modeling.

ML monolayers.

MOFs metal-organic frameworks.

MOs molecular orbitals.

MOT molecular orbital theory.

MPPT Møller-Plesset perturbation theory.

MSI metal-support interaction.

MvK Mars−Van Krevelen.

NBO natural bond orbital.

NCI non-covalent interactions.

NCPPs Norm-conserving pseudopotentials.

ND nanodiamond.

NMR nuclear magnetic resonance.

NPs nanoparticles.

NWs nanowires.

ODEs ordinary differential equations.

OER oxygen evolution reaction.

ORR oxygen reduction reaction.

PAFC phosphoric acid fuel cell.

PAW projected augmented wave.

PBE Perdew-Burke-Ernzerhof.

PDH propane dehydrogenation.

PDOS projected density of states.

PEM proton exchange membrane.

PEMFC proton exchange membrane fuel cell.

PES potential energy surface.

PGMs Platinum group metals.

PMNPs plasmonic metal nanoparticles.

PW-DFT plane wave-density functional theory.

RMM-DIIS residual minimization method by direct inversion in the iterative subspace.

SACs single atom catalysts.

SCF self-consistent field.

SHE standard hydrogen electrode.

SIE self-interaction error.

SMSI strong metal-support interaction.

SOC spin-orbit coupling.

SOFC solid oxide fuel cell.

STM scanning tunneling microscopy.

TDDFT time-dependent density functional theory.

TDSE time-dependent Schrödinger equation.

TISE time independent Schrödinger equation.

TM transition metal.

TMDs transition metal dichalcogenides.

TOF turnover frequency.

TPD temperature programmed desorption.

TS transition state.

TST transition state theory.

UHV ultrahigh vacuum.

USPPs Ultrasoft pseudopotentials.

VASP Vienna ab initio Simulation Package.

VBT valence bond theory.

vdW van der Waals.

VWN Vosko, Wilk and Nusair.

WGSR water−gas shift reaction.

WS Wigner-Seitz.

XANES X-ray absorption near-edge structure.

XPS X-ray photoelectron spectroscopy.

ZPE zero-point energy.

Publications

This thesis is based on the following publications:

- A. Ugartemendia, K. Peeters, P. Ferrari, A. de Cózar, J.M. Mercero, E. Janssens and E. Jimenez-Izal, "Doping Platinum with Germanium: An Effective Way to Mitigate the CO Poisoning", ChemPhysChem **22**, 1603-1610 (2021).

- A. Ugartemendia, A. de Cózar, J.M. Mercero, E. Jimenez-Izal, "Does the Composition in PtGe Clusters Play any Role in Fighting CO Poisoning?", J. Chem. Phys. **156**, 174301-174311 (2022).

- A. Ugartemendia, J.M. Mercero, A. de Cózar, M.M. Melander, J. Akola and E. Jimenez-Izal, "Deposited PtGe Clusters as Active and Durable Catalysts for CO Oxidation", ChemCatChem 2024, e202301137.

- A. Ugartemendia, A. de Cózar, J.M. Mercero, E. Jimenez-Izal, "Unraveling the Metal-Support Interaction for the Design of PtGe Clusters Deposited on Novel 2D Materials for PEMFC Technologies". In preparation.

Publications not included in this thesis:

- A. Ugartemendia, A. Garcia-Lekue, E. Jimenez-Izal, "Tailoring Magnetism in Silicon-Doped Zigzag Graphene Edges", Sci. Rep. **12**, 13032-13038 (2022).

- A. Ugartemendia, I. Casademont-Reig, L. Zhao, Z. Zhang, G. Frenking, J.M. Ugalde, A. Garcia-Lekue and E. Jimenez-Izal, "Deciphering the Chemical Bond of Trivalent Oxygen Atom in Oxygen Doped Graphene". Submitted.

- A. Ugartemendia, J.M. Mercero, E. Jimenez-Izal, A. de Cózar, "Doping Effects on Ethane/Ethylene Dehydrogenation Catalyzed by Pt_2X Nanoclusters". Submitted.

Abstract

The rapid growth of population over the last decades has supposed a vast increment in the consumption of fossil fuels to meet our energy demands. This overconsumption has accelerated the emission of greenhouse gases, acidification of oceans, deforestation and socio-economical differences. As a result, there is an urge to transition to a greener energy economy.

In this context, the proton exchange membrane fuel cell (PEMFC) has gained a lot of attention recently as a more sustainable energy source. This device generates electricity by oxydizing a H_2 fuel, being water the only byproduct. Nonetheless, several issues must be solved before such device can be commerzialized. First, the electrochemical reactions occurring inside the PEMFC are inefficient. This makes mandatory the use of very active catalysts. Up to date, Pt remains the state-of-the-art catalyst. Unfortunately, this precious metal is very scarce and expensive. Second, the H_2 manufactured by current industrial processes is contaminated with trace amounts of CO, a well-known catalyst poison. The Pt surface gets covered by a CO layer, hindering the reaction; over a few catalytic cycles the catalyst can be left completely useless. Hence, effective solutions are required to design cheaper catalysts resistant to CO poisoning.

In this thesis, our endeavor is to make a modest yet meaningful contribution to the ongoing trajectory in this particular direction. Our goal is to theoretically predict a modern and efficient catalyst. For this, a robust computational framework is employed which combines global minima search techniques, electronic structure calculations at the DFT level, chemical bond analysis tools and microkinetic simulations. Our approach for catalyst design is the use surface-mounted subnano

clusters. Clusters present several advantages compared with bigger nanoparticles. First, owing to their smaller size, they possess a huge amount of surface area and atomic efficiency, which may help reduce the cost. Second, they have many degrees of freedom to control the catalytic properties which are accessible in experiment.

This is precisely the philosophy we have used throughout this thesis. Starting from pure Pt clusters, we have gradually added different layers of complexity to the catalytic system with the idea of designing a highly optimized catalyst. We begin by doping free-standing Pt clusters with Ge. Ge has previously been reported to improve the catalytic performance of Pt, albeit its exact promotional effect has not been entirely elucidated yet. Inspired by this work, in this thesis we propose that Ge can be an effective promoter to increase the CO tolerance of Pt. For that matter, doping can be a very effective technique to enhance the catalytic properties and at the same time decrease the precious Pt loading. Our results confirm this hypothesis. The reason behind this behaviour has an electronic origin: the Pt−Ge polarized covalent bonds build a charge accumulation in Pt sites, which hinder the charge back-donation from Pt d atomic orbitals (AOs) to CO 2π*, weakening the Pt−C bond.

Next, higher Ge concentrations are explored to find the optimal PtGe composition. Surprisingly, a very high reduction in the Pt−CO bond strength is found for the equimolar compositions. Again, our results reveal that Ge alters the electronic structure of Pt. In greater detail, the formation of Pt−Ge polarized covalent bonds carries several advantageous consequences, namely thermodynamic, electrostatic and covalent stabilization. It is precisely at equimolar compositions that such stabilization is maximized as a result of a very favourable mixing between Pt and Ge. Additionaly, we show that high Ge contents do not hamper the catalytic activity for H_2 dissociation.

Afterwards, the bimetallic PtGe clusters are deposited on MgO(100) to perform more realistic calculations on the catalytic activity. CO oxidation is chosen as the test reaction and because it could be a way to get rid of the poisonous CO. The results found thereof indicate that PtGe acts as a bifunctional catalyst. The greater oxophilicity of Ge creates new active sites for O_2 adsorption, alleviating the competition between CO and O_2 for adsorption on Pt sites. Namely, the

nanoalloy displays dual adsorption properties. Even though eventually part of Ge gets oxidized, surprisingly, this does not have an adverse effect, but indeed acts as a secondary oxygen source, diminishing CO poisoning. Additionally, the part of Ge that remains alloyed to Pt induces electronic effects to Pt, decreasing the interaction with CO.

Finally, a pool of 2D materials are studied as supports for monometallic Pt and bimetallic PtGe clusters with the aim of finding favourable metal-support interaction effects. Strikingly, most of the 2D materials such as phosphorene, silicene and germanene increase substantially the cluster-support adsorption strength and total charge of Pt. Our results hint that germanene and SmSI may be able to induce strong-metal-support interactions (SMSI) and encapsulate the cluster. Generally, Ge alloying reduces the adsorption energy due to a repulsion between Ge and the support. As a result of this repulsion, the PtGe mixing is somewhat worsened in many of the supports. However, in the case of phosphorene, Ge acts as an anchoring element between Pt linear chains, impeding particle ripening. More importantly, it is found that the 2D support also helps reducing the affinity to CO and improving the HOR performance, which can be further enhanced by Ge alloying. Thus, support modification is proved to be a technique as effective as alloying to boost the catalytic performance of Pt.

We expect that this thesis may inspire further research on the promising catalytic properties of bimetallic PtGe clusters, which for many industrially relevant reactions remains yet unexplored.

Laburpena

Azken hamarkadetan emandako populazio hazkunde azeleratuak erregai fosilen kontsumo izugarria suposatu du gure energia beharrak asetzeko. Gehiegizko kontsumo hau berotegi-efektuko gasen emisioan, ozeanoen azidifikazioan, deforestazioan eta desberdintasun sozio-ekonomikoetan itzultzen da. Ondorioz, agerian geratzen da beste energia iturri berdeagoen beharra dagoela.

Testuinguru honetan, protoi trukaketa mintzeko erregai pilak (PEMFC, ingelesez) arreta berezia jaso du azkeneko urteetan energia iturri jasangarriago gisa. Aparatu honek elektrizitatea sortzen du H_2 erregaia oxidatuz, ura izanik sortzen den produktu bakarra. Dena den, teknologia berri hau komertzializatu aurretik hainbat arazo garrantzitsu konpondu behar dira. Lehenik, kontuan eduki behar da PEMFC-an ematen diren erreakzio elektrokimikoak inefizienteak direla. Honek katalizatzaile oso aktiboak erabiltzea behartzen du. Gaur egun, Pt jarraitzen du katalizatzaile aktiboenetakoa izaten. Zorritxarrez, Pt oso urria eta garestia da. Bigarrenik, ohiko prozesuen bidez produzitutako H_2-a normalean CO-arekin kontaminatuta egoten da, katalizatzaile pozoi ezaguna. Pt gainazala CO geruza batekin geratzen da estalita, bere ahalmen katalitikoa eragotziz. Hortaz, soluzio eraginkorrak behar dira katalizatzaile merkeak eta CO-arekiko erresistenteak garatzeko.

Tesi honetan, gure kontribuzio txikia ematen saiatu gara norabide honetan. Gure helburua katalizatzaile moderno eta eraginkor bat teorikoki aurresatea da. Honetarako, teknika konputazional aurreratuak erabili dira, hala nola, minimo globalen bilaketarako optimizadoreak, egitura elektronikoaren kalkuluak DFT mailan, lotura kimikoaren analisirako tresnak eta simulazio mikrozinetikoak. Gure pro-

posamena kluster subnanometrikoen erabilera da katalizatzaile gisa. klusterrak hainbat abantail aurkezten dituzte nanopartikulekin alderatuz. Lehenik, bereaien tamaina txikiagoaren ondorioz, gainazal azalera eta efizientzia atomiko oso handia dute, katalizatzailearen kostua murrizten lagundu dezakeena. Bigarrenik, askatasun gradu asko daukate beraien propietate katalitikoak kontrolatzeko, experimentalki eskuragarri direnak.

Hau da zehazki tesi honetan zehar jarraitu dugun pentsamoldea. Pt kluster puruak abiapuntu bezala hartuz, konplexutasun geruza desberdinak gehitu dizkiogu gradualki sistema katalitikoari, katalizatzaile oso optimizatu bat diseinatzeko asmoz. Pt kluster txikiak Ge-arekin dopatzen hasten gara gas fasean. Lehenago erdietsi da Ge-ak, Pt-ren ahalmen katalitikoa hobetzen duela, baina mekanismo zehatza ez da guztiz ezagutzen oraindik. Lan hauetan inspiratuta, tesi honetan proposatzen dugu Ge promotore eraginkorra izan daitekeela Pt-ren CO-rekiko tolerantzia handitzeko. Izan ere, dopaketa teknika onuragarria da aldi berean propietate katalitikoak hobetzekoa eta Pt edukia murrizteko. Gure emaitzek hipotesi hau konfirmatzen dute. Portaera honen arrazoia jatorri elektronikoa du: Pt−Ge lotura kobalente polarizatuek karga akumulazioa suspertzen dute Pt leku aktiboetan, Pt d orbital atomikoetatik CO 2π*-rako errotrodonazioa oztopatuz eta Pt−C lotura ahulduz.

Ondoren, Ge kontzentrazio altuagoak analizatu dira PtGe konposizio optimoa bilatzeko. Hemen, erredukzio oso handia aurkitu da Pt−CO adsortzio indarrean konposizio ekimolarrentzat. Berriro ere, Ge-ak Pt-ren egitura elektronikoa modifikatzen du. Pt−Ge lotura kobalente polarizatuen formazioak hainbat eragin onuragarri dakar, hala nola, estabilizazio termodinamikoa, elektrostatikoa eta kobalentea. Zehazki, konposizio ekimolarretan maximizatzen da estabilizazio hau Pt eta Ge-ren arteko nahasketa mesedegarriaren ondorioz. Gainera erakusten dugu Ge kantitate handiek ez dutela ahalmen katalitikoa deuseztatzen H_2 disoziaziorako.

Behin Ge-aren efektu onuragarria ulertuta, aktibitate katalitikoaren kalkulu errealistagoak burutu ditugu PtGe klusterrak MgO(100) gainazalean adsorbatuz. CO oxidazioa aukeratu da aktibitate katalitikoa testeatzeko. Aurkitutako emaitzek adierazten dute PtGe katalizatzaile bifuntzional bat bezala jokatzen duela. Ge-ak, bere oxofilizitate handia dela medio, leku aktibo berriak sortzen ditu O_2 adsortziorako, CO eta O_2-ren arteko konpetizioa arinduz Pt atomoetan adsorbatzeko.

xli

Hau da, nanoaleazioak adsortzio duala izeneko propietatea erakusten du. Prozesu honen ondorioz, Ge-aren zati bat oxidatu egiten da Pt-rekin aleatuta egon beharrean. Hala era, honek ez du efektu kaltegarririk eragiten, baizik eta guztiz kontrakoa: oxidatutako Ge-a oxigeno iturri sekundario bat bezala jarduten du Pt tokietan adsorbatutako CO-arekin erreakzionatzeko. Gainera, lehen bezala, aleatuta mantentzen den Ge-aren zatia Pt-ren egitura elektronikoa modifikatzen du, CO-rekiko interakzio indarra murriztuz. Honek guztiak CO pozoiketa inhibitzen du hein batean.

Bukatzeko, hainbat 2D material aztertu dira Pt eta PtGe klusterrentzako euskarri bezala, kluster eta euskarriaren arteko interakzio mesedegarriak bilatzeko asmoz. Ikusi da material gehinek, hala nola, fosforenoa, silizenoa eta germanenoa nabarmenki handitzen dutela Pt kluster puruen adsortzio indarra eta karga totala. Haratago, gure emaitzek berresten dute germanenoa eta SmSI klusterra enkapsulatzeko gai direla gainazaleko atomoak migratuz. Orokorrean, Ge aleazioak adsortzio indarra murrizten du Ge eta gainazalaren arteko errepultsioarengatik. Errepultsio honek gainera Pt eta Ge-aren arteko nahasketan eragin negatiboa izan dezake hainbat gainazaletan. Hala ere, aipatzekoa da fosforenoan Ge atomoek Pt kateak lotzeko gai direla, klusterraren apurketa galeraziz. Bestetik, 2D gainazalak rol aktibo bat jokatzen du klusterraren adsortzio propietateak aldatuz; hau da, 2D gainazalak Pt kluster puruen CO-rekiko afinitatea jaisten du eta HOR aktibitatea hobetzen du. Era berean, efektu hau gehiago areagotu daiteke Pt Ge-arekin aleatuz gero. Hortaz, honekin frogatu da gainazal modifikazioak aleazioa bezain eraginkorra izan daitekeela.

Espero dugu tesi honek etorkizunean ikerketa gehiago suspertu ahal izatea PtGe kluster bimetalikoen propietate katalitiko interesgarrien inguruan, eta baita ere bidea ireki ahal izatea beste erreakzio industrialetan erabiltzeko.

Chapter 1

General Introduction

> "LO, praise of the prowess of people-kings
> of spear-armed Danes, in days long sped,
> we have heard, and what honor the athelings won!
> Oft Scyld the Scefing from squadroned foes,
> from many a tribe, the mead-bench tore,
> awing the earls. Since erst he lay
> friendless, a foundling, fate repaid him:
> for he waxed under welkin, in wealth he throve,
> till before him the folk, both far and near,
> who house by the whale-path, heard his mandate,
> gave him gifts: a good king he!"
>
> — Unknown, *Beowulf: An Anglo-Saxon Epic Poem*

SINCE the cradle of humanity we have taken the next steps in human history conditioned by the external environmental conditions. These external conditions force us to adapt to them in order to survive. This does not only mean to use available items as they are, but to manipulate them and create beneficial assets. To put some examples, in early history we have the crafting of stone tools, cooking (thanks to the discovery of fire), migration, development of a social structure and thus that of language. Later on, agriculture helps develop a sedentary life and thus establish the first civilizations; for centuries agriculture becomes the main economic sector until the industrial revolution in the XVIII*th* century. It is in this time that society moves from work driven by manpower and animal power to steam power. In the second industrial revolution the impact is

multiplied tenfold with the use of petroleum as the main energy source and the resulting transition to a society driven by electric power.

This illustrates one common fact that have shared all civilizations: energy is required to sustain a civilization. Animals for ploughing, water for milling, steam for railways and nowadays fossil fuels, natural gas, wind *etc.* to produce electricity. Progress comes with an increased input of energy. Nonetheless, access to natural resources to obtain this energy does not necessarily have to increase in the same way. This becomes obvious in ancient civilizations like ancient Egypt where they entirely relied on the Nile river and a drought could bring a devastating famine. Despite all the technological advances since then, current society is facing the same exact problem.

1.1 Fossil Fuels

Modern economy is largely based on non-renewable energy sources like fossil fuels, and an exponentially growing population which feeds on finite resources becomes unsustainable in the long term. This has been evidenced in recent years as there has been a continuous overconsumption of energy due to the drastic increment of population in developing countries.[1, 2] The fossil fuel supplies are not enough to guarantee a high standard of life for all population; the better the quality of life, the greater the energy consumption. Apart from shortage, it is important to note that the reservoirs of fossil fuels are not homogeneously distributed and they are only found in certain countries. This makes some countries extremely dependent on oil-rich countries and causes major geopolitical conflicts.

More importantly, the impact of fossil fuels on the environment is huge. Ironically, the very same energy resources we use are the cause of the deterioration of the environment. The largest part of anthropogenic emissions of greenhouse gasses such as CO_2 and CH_4, comes from the combustion of fossil fuels, and together with deforestation are the main contributors to global warming. The resulting temperature rise is causing a rapid desertification, heat waves, melting of ice sheets and glaciers, rise of the sea level and acidification of oceans.[3–6] Moreover, extreme weather conditions like droughts and storms are becoming more and more frequent.

The consequences for our hunger of energy are the destruction of entire ecosystems. Several species have been forced to migrate or disappear and the diversity of plants and flowers has decayed significantly. Current society will not be exempt from the consequences either. It is predicted that climate change will bring shortage of water and deterioration of crops, and thus an aggravation of socio-economical differences between developed and under-developed countries, originating massive migrations. As a result, we find ourselves at a point of inflexion in which the necessity to find other renewable energy sources is extremely important.[7–12]

1.2 Fuel Cells

1.2.1 Historical Overview

Fuel cells are electrochemical devices that convert the chemical energy of a fuel directly into electricity. With no emission of pollutants and high efficiency, fuel cells are considered one of the most promising alternatives to produce, convert and store electricity. The invention of fuel cells can be traced back to the early 1800's. In 1839 Sir William Grove built the first prototype by using two Zn and Pt electrodes submerged in an acidic media and separated by a porous compartment. However, it was not until 1932 that the first fully operational cell was developed by Francis Bacon, the alkaline fuel cell (AFC). AFCs have been widely used to propel satellites in NASA space programs, including the Apollo missions. In 1966 General Motors designed the first automobile powered by a fuel cell. Since then extensive research has been done in this new emerging technology and has found many applications in transportation (electric car, *etc.*) and as power plants for buildings including hospitals.[13]

1.2.2 Principle of Operation

The basic building block of a fuel cell consists of a pair of electrodes, anode and cathode, separated by an electrolyte and connected with an external circuit.[14, 15] The assembly of these three components is usually referred to as the membrane-electrode assembly (MEA). Each electrode is composed of a catalyst layer and a gas diffusion layer (GDL). The GDL enables a uniform flow of the reactants to

the catalyst, as well as removal of heat. The oxidation of the fuel occurs at the anode (negative potential), while the reduction of the oxidant takes place at the cathode (positive potential). Oxygen is usually the choice of oxidant due to its high oxidizing ability and abundance. Ion transport is done through the electrolyte layer whereas an external circuit is used to conduct electrons to the cathode. The electrolyte is an insulator, thus it is mandatory the use of an external circuit in order to be able to complete the other half reaction and produce electricity.

As fuel cells do not make use of a combustion reaction to burn the fuel they are not limited by the Carnot cycle, and thus operate at higher thermodynamic efficiency. In addition, fuel cells need less energy transformation steps to produce electricity, since it is not necessary a mechanical transformation. Besides, despite the working principle being the same in both fuel cells and batteries, they present some differences. In a battery the reactants are the very same electrodes. Consequently, once the electrodes are consumed a recharging operation is required. In a fuel cell however, the reactants are gasses which are supplied continuously, and the catalyst act as promoters of the reaction without being consumed in principle. Therefore, it can produce electricity as long as reactants are supplied.

1.2.3 Classification of Fuel Cells

Fuel cells can be classified according to the electrolyte used. This can be subdivided further based on the operating temperature which depends to a certain extent on the electrolyte.[14–18] On the one hand, low-temperature fuel cells include the polymer electrolyte membrane fuel cell (PEMFC), alkaline fuel cell (AFC) and phosphoric acid fuel cell (PAFC). The temperature of operation falls below 250ºC. Moreover, they show fast start-up times and are therefore more attractive for transportation and other portable applications. On the other hand, the most studied high-temperature fuel cells are the molten carbonate fuel cell (MCFC) and solid oxide fuel cell (SOFC), and operate at $500-1000$ºC. Such high temperature permits the internal reforming of small hydrocarbons into H_2, eliminating the preprocessing step to obtain pure H_2. Indeed, even the electrochemical oxidation of CH_4 is possible in this kind of cell. Nevertheless, these hard conditions limit significantly the choice of materials for the design of the cell; and also they are responsible for prolonging the

start-up time, making them not suitable for automotive transportation. Regardless, they have found applications as stationary power plants.

PEMFCs can be subdivided depending on the fuel used. The most common fuels are H_2 (proton exchange membrane fuel cell, PEMFC) and methanol (direct methanol fuel cell, DMFC). The advantages of these fuel cells are their low operating temperature (80ºC), high power density and zero emission nature. In the following section the PEMFC is explained in more detail.

1.2.4 Proton Exchange Membrane Fuel Cell (PEMFC)

The essence of PEMFCs lies in the fact that the energy stored in the chemical bonding of H_2 can be converted to electricity by oxidizing H_2 to water.[19–22] H_2 has a very high energy density per mass and electrochemical activity, and is a zero carbon fuel. A schematic diagram of a PEMFC is depicted in Figure 1.1. As can be observed H_2 is oxidized at the anode while oxygen is reduced at the cathode. The only product is water, with no emission of pollutants, making this technology environmentally friendly.
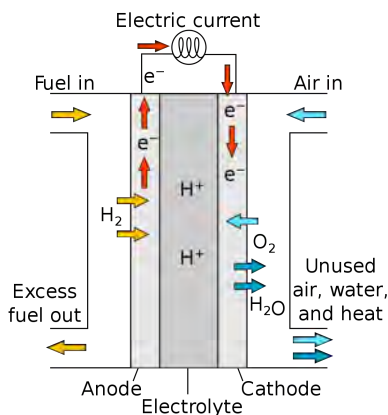
Figure 1.1: Schematic representation of a proton exchange membrane fuel cell (PEMFC).

The catalyst could be considered the heart and soul of the fuel cell. They provide active sites for the molecules and accelerate the reaction rates. Current catalysts are based on Pt nanoparticles (NPs) dispersed on a carbon support (carbon black, activated carbon).[23, 24] These catalysts show an excellent redox performance.

The redox half-reactions are the hydrogen oxidation reaction (HOR) and the oxygen reduction reaction (ORR). Both reactions have been extensively studied in the last decades.[25–28]

$$2\,H_2 \longrightarrow 4\,H^+ + 4\,e^- \qquad\qquad \text{HOR} \qquad (1.1)$$

$$O_2 + 4\,H^+ + 4\,e^- \longrightarrow 2\,H_2O \qquad\qquad \text{ORR} \qquad (1.2)$$

H_2 enters the catalyst layer in the anode through the GDL and dissociates into protons and electrons. Hydrogen dissociation can follow either an homolytic route (Tafel) or heterolytic route (Heyrovsky). Then the protons and electrons travel through the electrolyte membrane and electric circuit to the cathode, and react with O_2 to form water.

The maximum voltage attainable in a fuel cell largely depends on the potential difference between the cathode and anode. Nonetheless, owing to strongly adsorbed oxygenated species (*i.e.*, OOH*, OH*, O*), the ORR kinetics is 6 times slower than HOR in acidic media.[29, 30] Thus, in order to boost the sluggish ORR kinetics an extra applied voltage (kinetic overpotential , also known as kinetic loss) above the thermodynamic potential is required at the cathode, which causes a voltage drop of 70%. As a result, a very high Pt loading ($0.2 - 0.4$ mg$_{Pt}$ cm^{-2}) becomes mandatory at the cathode to reduce the overpotential and compensate the losses in the voltage.[31] PEMFC performance has also been extensively researched in alkaline media.[32–37] Unfortunately, the HOR activity is *ca.* two orders of magnitude lower than acid and consequently high Pt loadings are required as well.

Besides, Pt has a very low tolerance ($5-10$ ppm) for CO, a well known poison.[38–41] CO completely covers the catalytic surface, hindering the reaction and thus, causing a drop in the voltage. This makes mandatory an ultra pure H_2 feed as well as high Pt loadings. Pt is considered a precious metal due to its scarcity and huge technological and strategic importance. Therefore, as for now the PEMFC is not a competitive alternative for high scale commercialization. The U.S. Department of Energy (DOE) has established a target limit of less than 0.125 mg$_{Pt}$ cm^{-2} to make them commercially viable.[42] Current research in fuel cells is focused on developing new strategies to design active, stable and CO-poisoning resistant catalysts, while

simultaneously reducing the Pt loading, and thus the cost.[21] In this thesis we address this issue thoroughly.

Previously, it was mentioned that H_2 has a very high energy density per unit mass. However, it should be noted that per unit volume this energy density is extremely low compared with other liquid fuels like methanol. Hence, H_2 needs to be compressed or liquefied, which makes the management of this fuel dangerous and costly. The design of an infrastructure to store and distribute H_2 has become a serious challenge and topic of ongoing research.[43, 44]

It should be mentioned that although the PEMFC is a green technology *per se*, it truly depends on the source of H_2 used. Today approximately 95% percent of all H_2 is produced by steam reforming of natural gas.[45] This methods presents two major disadvantaged. First, the H_2 feedstock is unavoidably contaminated with CO which has a nocive effect on the catalyst (*vide supra*). Additional purification steps are needed, increasing the cost of the process. Second, the natural gas used in steam reforming comes from hydraulic fracturing, which is far from being regarded green. Accordingly, this supposes a great amount of CO_2 emissions to the atmosphere. Thus, it is essential to find other methods to synthesize H_2.[45, 46] In this regard, electrolysis of water ($2\,H_2O \longrightarrow 2\,H_2 + O_2$) seems a very promising route.[45–50] Despite being at an early stage significant progress has been made in recent years. Now, the efficiency of water electrolysis reaches about $70 - 80\%$ using proton exchange membrane (PEM) electrolyzers, and is expected to increase. It must also be said that the dissociation of water requires energy (1.23 eV), but this energy can be obtained from other renewable energy sources such as solar power.

These are but the first step towards the development of an energy industry driven by hydrogen, the so-called hydrogen economy.[50–54] Hydrogen production would be done via water electrolysis by means of photovoltaic energy. Afterwards, PEMFCs would use this hydrogen to produce electricity and the electricity would be supplied to power electric cars and buildings. As a final remark in this line, it should be pointed out that renewable energies have become an extremely profitable market for big energetic companies. The percentage of electricity produced by each method is finely balanced so as to obtain the greatest benefits. This underlines the fact that not only is the scientific and technological aspect important, but also the

economic and political side. There has to be political willingness to change the current energetic model so that the emerging technologies become beneficial for the whole society.

Summing up, PEMFCs are expected to play a key role in the future energy landscape and in the decarbonization of the current industry. And more importantly, the machinery that sets in motion all the gears so that this advancement becomes possible is known as heterogeneous catalysis.

1.3 Heterogeneous Catalysis

Heterogeneous catalysis has become one of the foundations of the current economy. It is used in sectors as diverse as the chemical, pharmaceutical, food and energy industry, medicine and pollution control. For instance, in the chemical industry it is involved in approximately 90% of the manufacturing processes, and contributes directly or indirectly to $\sim 35\%$ of the world's gross domestic product (GDP).[55] It is one the most important means to obtain high value-added chemicals at rates sufficient enough to satisfy the current demands. To name a few examples we have hydrogen which is obtained via steam reforming and the water$-$gas shift reaction (WGSR), or hydrocarbons produced via the Fischer$-$Tropsch process.

1.3.1 How a Catalyst Works

A catalyst is a substance that accelerates a chemical reaction without being consumed in the process. It must be kept in mind that a catalyst solely affects the reaction rates; the equilibrium composition of the reactants and products is still dictated by thermodynamics. That is, no more product than what is allowed by thermodynamics can be obtained, whatsoever the amount of catalyst used.

In heterogeneous catalysis solids are used to catalyze reactions of molecules in gas or solution. Figure 1.2 illustrates the difference in the reaction pathway between a catalyzed and uncatalyzed reaction. The catalytic reaction proceeds on the surface of the catalyst which has three major functions. First, it adsorbs the reactants from the fluid phase. Next, the adsorbates diffuse to the active sites and react with each other (cleavage and formation of chemical bonds) and finally, the products

are desorbed to the environment, leaving the clean surface (catalyst regeneration) for the next cycle. Hence, from this it can be inferred that the catalyst increases the reaction rate by providing an alternative pathway with lower energy barriers. Note however, that not only the reaction barriers are affected, but the catalyst can also be used to direct the reaction through a route with improved selectivity for the desired product.
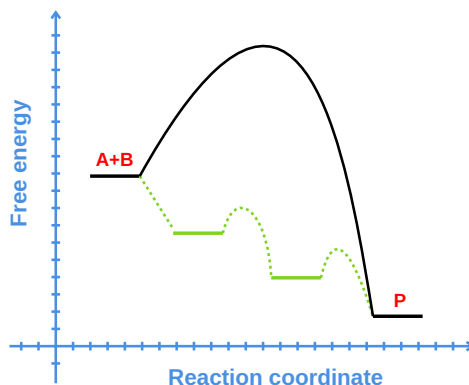
Figure 1.2: Schematic energy diagram of a chemical reaction $(A + B \longrightarrow P)$ with (green) and without (black) the assistance of a catalyst. The catalyst provides an alternative reaction pathway with lower energy barriers but the reaction energy remains unchanged.

Since heterogeneous catalysis is a surface process, catalysts are designed in such a way that the amount of exposed surface area is maximized. In industry, the most widely employed catalysts are precious metal NPs dispersed on porous (silica, alumina, *etc.*), mesoporous (aluminosilicates, *etc.*) and microporous (zeolites, aluminophosphates, *etc.*) supports.[56] The catalytic behaviour of the catalyst is mainly governed by the surface atoms. Therefore, understanding the interaction between the metallic surface and molecules is essential to design efficient and durable catalysts.

1.3.2 Chemisorption of Ligands

The d-band model of Nørskov and Hammer[57–59] is one of the simplest and most robust models to study the bonding of ligands with a transition metal (TM) surface. This model is particularly useful due to the fact that it correlates the electronic

structure of the TM with the binding strength of the ligand, and thus, allows us to predict trends in the catalytic activity in a simple way. As can be observed in Figure 1.3, chemisorption occurs through the interaction between the valence molecular orbitals (MOs) of the ligand and the sp and d-bands of the TM, in a two step process. The coupling between the sp-bands and the adsorbate localized MOs results in a shift and broadening of the adsorbate MOs. However, this interaction can be assumed constant for different TMs since they all have very broad (delocalized) and half-filled sp-bands. The main differences are associated with the d-band. In the second step, the broadened adsorbate MOs overlap with the narrow d-band giving rise to bonding and antibonding MOs.
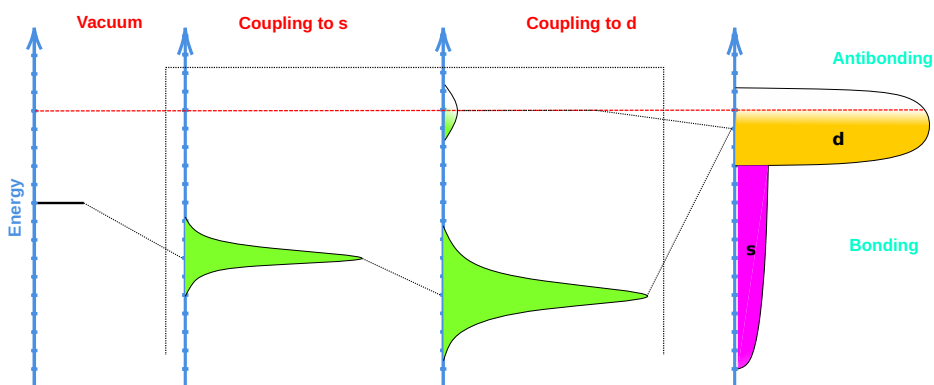
Figure 1.3: Schematic illustration of the d-band model showing the bond formation between the transition metal (TM) surface and ligand. The valence MO of the ligand is stabilized and broadened upon interaction with the TM sp-bands. Afterwards, coupling with the d-band causes a splitting into bonding and antibonding MOs. The binding strength is characterized by the filling of the antibonding MOs, which can be measured with the d-band center (ϵ_d).

From gas-phase chemistry we know that the bond strength will depend on the relative occupancy of bonding and antibonding MOs. A chemical bond is stronger when only the bonding MOs are filled, but as soon as electron density is transferred to the antibonding MOs, the bond is weakened. However, there are some slight differences in how the filling is done in surface chemistry. In gas-phase the filling of orbitals only depends on the total number of electrons, while in TM surfaces the

filling is given by the relative energy of the antibonding MOs to the Fermi level
(E_F). Here is where the essence of the d-band model lies. The antibonding MOs
are always higher in energy than the d-band and thus, any change in the d-band
will also result in a shift of the antibonding MOs in the same direction. With this,
the position of the d-band, more precisely the d-band center (ϵ_d), can be used as a
descriptor to measure the bond strength of adsorbates. If ϵ_d is shifted to higher
energies the antibonding MOs as well, and the bond becomes stronger. Whereas if
ϵ_d is stabilized to lower energies, the antibonding MOs are shifted below the Fermi
energy and the bond weakens.

1.3.3 Sabatier Principle

Efficient and cost-effective catalyst design is a problem of paramount difficulty
in heterogeneous catalysis. Thousands of different combinations of materials are
possible and this number keeps increasing as new synthesis routes are developed. In
order to sample this huge parameter space, descriptors are needed to systematically
rationalize the catalytic activity. The Sabatier principle goes one step further in this
direction. It states that for a given reaction, there is an optimal binding strength of
the reactants.[55, 60, 61] If the bond is too weak, the catalyst will not be able to
bind the reactants long enough so that they can react, whereas if it is too strong,
the products will not desorb from the surface, hindering the reaction. The Sabatier
principle can be quantified in terms of the so-called volcano plot, which shows a
volcano-type relationship between the reaction rate and binding strength, as shown
in Figure 1.4. The ideal catalyst should be located in the vertex of the volcano plot,
i.e., the Sabatier optimum. Thus by measuring the binding strength one can build
such relations and screen the materials with optimal performance from a pool of
possible candidates.

From here we arrive at the concept of the active site. It is known that not all the
atoms at the surface participate in the reaction;[62] the binding strength can vary
significantly from atom to atom depending on its environment. Hence, the atoms at
the edges or center of the crystal facets, or at the interface with the surface, or close
to defects such as vacancies, steps or kinks will present different catalytic activity.
There are different kinds of active sites, however, in the present thesis we only deal
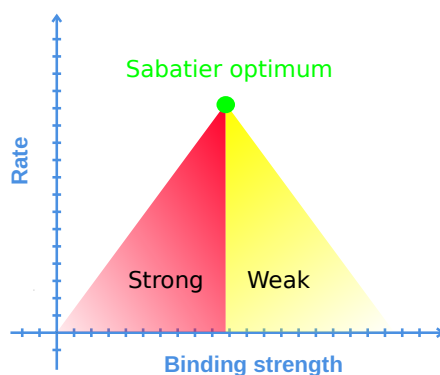
Figure 1.4: Schematic representation of the Sabatier principle. The optimal catalyst is the one lying on the vertex of the volcano plot (green dot).

with metal sites. An excellent review about this topic is given in Ref [63].

Ultimately, the goal of heterogeneous catalysis is to understand the processes involved in surface reactions, fundamentally. Only through a concise knowledge of the interplay between the ligands, catalyst NP, surface and environment, at the atomic level, can we develop catalysts with improved activity, stability and sustainability.

1.4 Nanoclusters

Heterogeneous catalysis, despite being a science that spans over 250 years, still remains one of the hot topics in current research and an incredible amount of research is being carried out. Undoubtedly, nanotechnology has had a tremendous impact on our lives and researchers in this field have known how to surf this tidal wave of new opportunities and exploit the new tools and understanding given by nanotechnology. Nanotechnology has opened a myriad of possibilities to design next generation atomically precise catalysts. One of the most promising candidates, and the central topic of this thesis, are subnanometric clusters.

1.4.1 Finite-Size Effects and Electronic Structure

Clusters are aggregates of atoms in the $0-2$ nm range (up to hundreds of atoms) and occupy the gap between discrete atoms and plasmonic metal nanoparticles

(PMNPs). Among clusters, the ones with size below 1 nm (< 20 atoms) are known as subnanometric clusters (hereon clusters). When the size of the cluster is reduced to this regime novel properties arise and deviate drastically from their analogous bulk counterpart.[64–75] What's more, the properties become size-dependent in a non-continuous way to the extent that the addition of a single atom can have a huge impact. There are two reasons for this behaviour. On the one hand, in this size regime the particle size becomes of the same order as the de Broglie wavelength of the electrons and quantum effects become predominant. The free electrons (the so-called electron sea) characteristic of bulk metals become confined in molecular dimensions. Due to this quantum confinement, a band gap is opened between HOMO and LUMO levels, and additionally, the valence and conduction bands split into discrete energy levels, resembling the electronic structure of molecules (see Figure 1.5). As a result, clusters show several peaks in the absorption spectrum differing from the usual plasmon band of spherical NPs. With this, clusters can be described as zero-dimensional quantum dots in which the discrete energy levels depend on the size of the particle.

On the other hand, due to their small size, clusters possess ultrahigh surface-to-volume ratio (so useful in catalysis!). Most of the atoms (or all) of the cluster are essentially part of the surface. Recall that surface atoms are energetically less favorable than bulk atoms since they present lower coordination numbers. Thus, in order to minimize the surface energy they will rearrange themselves into completely unexpected and unique structures. Adding or subtracting a single atom will have a drastic effect on the geometry and thus on the properties. We find ourselves in the regime where each atom counts.

As a result of finite-size effects and high surface-area, the physical and chemical properties such as photoluminescence, catalytic activity, chirality and magnetism become size dependent. In this regime, extrapolations from larger NPs are no longer valid. The size-dependence in most cases does not follow a scaling relationship; it is on the contrary, unexpected and unpredictable, inasmuch as the properties diverge completely from their bulk and NP counterparts.
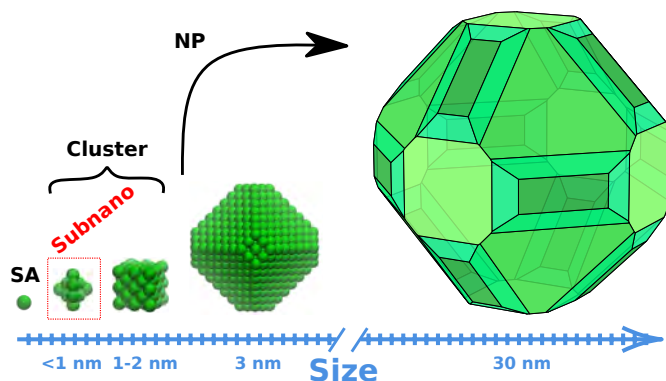
Figure 1.5: Schematic representation of geometric difference of materials with diverse sizes: single atom (SA), clusters and nanoparticles (NPs). Subnano clusters are higlighted from bigger clusters owing to their different properties. Two different NPs are shown to indicate the wide range in size that span NPs. Number of atoms: 10 in subnano cluster, 50 in cluster, ~ 1000 in 3 nm NP and $\sim 500,000$ in 30 nm NP.

1.4.2 Morphology

Clusters, unlike NPs, do not follow the Wulff theorem as they are not big enough to possess well defined crystal facets and planes. They are mainly composed of under-coordinated atoms and thus, will tend to adopt geometries in which the gain in stability is maximal. Nonetheless, the choice of geometry is not unique and for a given size clusters can display different configurations; that is, clusters have isomers.[64] Each isomer has a different relative stability and their thermal population depends on external conditions, such as temperature, pressure, pH and potential. As they have different geometries their electronic structure will differ and thus their properties. In this regard, gas-phase experiments facilitate the study of clusters under a controlled environment. Infrared spectroscopy is an excellent technique to characterize the vibrational modes and thus, elucidate the geometry of each isomer.[76, 77] Figure 1.6 shows the most relevant isomers for an hypothetical 5 atom cluster in gas-phase. As can be observed the most stable isomer (global minimum, GM) has a trigonal bipyramidal (D_{3h}) geometry. The following low-lying isomers also favour 3D structures against planar ones. It is interesting to note that small monometallic clusters usually present geometries with a high degree of symmetry.

As mentioned previously, the size of the cluster can have a big impact on the geometry. This is magnificently illustrated in Au clusters, which is perhaps the better studied case.[78, 79] In gas-phase Au_n ($n \leq 10$) show 2D planar structures. Then for Au_n ($n = 11 - 14$) there is a structural transition from planar to flat cage structure. Again, when $n \geq 15$ there is another transition to more compact near-spherical structures, which can be obtained by the continuous capping of an icosahedron. As the size increases the clusters begin to resemble the bulk-phase FCC structure. Pt[80] shows a similar 2D to 3D transition, while in Pd[81] 3D geometries are preferred throughout the same size range. Another example worth mentioning is Ge.[82] In this case, at $n \sim 13$ there is a structural transition from spherical to a prolate pattern with 1D growth sequence. This motif is composed of small units connected by a bulk fragment with the Ge diamond structure. This transformation has been attributed to a stability gain due to aromaticity.[83] At $n \sim 40$ clusters with a plate-like motif become more favorable, and then Ge adopts a spherical cage structure again.[84]
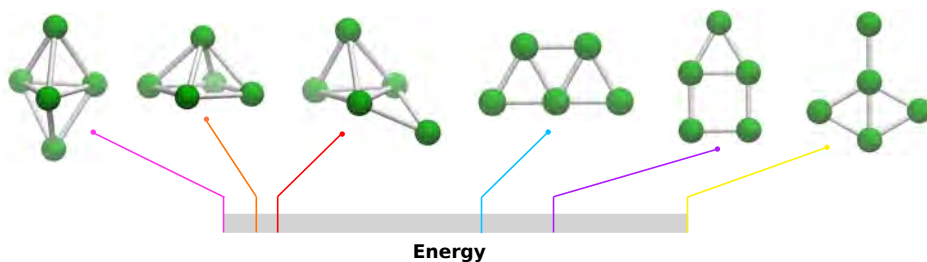
Figure 1.6: Schematic representation of the relative stability of the low-lying isomers for an hypothetical 5-atom cluster. The left-most structure corresponds to the global minimum (GM). Energy increases from left to right.

1.4.3 Metal-Support Interaction

NPs synthesized by microemulsion do not always satisfy the harsh conditions required for many industrial applications. Instead, they are typically deposited on a supporting matrix. In many cases, the support not only acts as an inert component, but can also affect the properties of the particle and unexpected phenomena might appear at the metal/support interface. This effect has been coined as metal-support

interaction (MSI) .[64, 85–88] In clusters the MSI is more pronounced as the number of atoms in contact with the surface increases. The support can induce different effects on the cluster, the extent of which will depend on the nature of both components. Note however, that in most cases all these effects are correlated and cannot be separated from one another.

- Thermal stability: The main role of the support is to offer anchoring sites for the clusters, as well as control their spatial dispersion on the surface. In many applications such as catalysis, elevated operating temperatures are used. Hence, supports with high adhesion energies are used to prevent the sintering of the particles. It is interesting to note that the adhesion energy is not only material specific, but also depends on the crystal orientation within the same support.

- Size and morphology: The support also has a big impact on the cluster size. Different supports will favour certain sizes over others, resulting in size distributions of different width and height. The shape of the cluster is dictated by the adhesion energy to the surface. This concept is illustrated in Figure 1.7a). If the interaction between the cluster and surface is weak, the cluster will undergo little distortion from the preferred geometry in gas-phase, and will show a spherical geometry. Nonetheless, as the interaction strength increases, the cluster will start wetting the surface and adopt a more faceted structure, until it becomes completely flat, in a raft-like fashion. For example, it has been observed that the different facets of α-Al$_2$O$_3$ favour different morphologies of Pt NPs.[85] Besides, when Pt$_4$ is adsorbed on MgO(100), the cluster retains the 3D geometry of gas-phase, but becomes planar after deposition on TiO$_2$(110).[89] Au$_m$Rh$_n$ ($4 \leq m + n \leq 6$) also undergoes structural transitions when adsorbed on MgO(100).[90] In both cases there is a competition between the stability gain by intracluster and intercluster bonding.

- Charge transfer: When a metallic cluster is deposited on a support, charge transfer phenomena can occur at the interface. The differences in the Fermi levels of both phases will give rise to a charge redistribution to equilibrate the

electron chemical potentials. The direction and amount of the charge transfer will depend on the nature of the cluster and substrate. Campbell termed this phenomenon electronic metal-support interaction (EMSI). In NPs this charge transfer is limited to a few atomic layers of the NP, while in clusters the effect is more prominent. The charge transfer can have a tremendous impact on the electronic structure of the cluster, and consequently on its properties. By adding or subtracting electrons we are shifting the HOMO and LUMO orbitals and thus modifying the accessibility to other oxidation states. This certainly will affect the redox properties of the cluster. In this line, charge transfer promotes the creation of active sites rich or deficient in electrons, thus changing the acid/base properties.

- Strain A lattice mismatch between the cluster and substrate can originate interfacial stress and induce changes in the morphology, resulting in a different electronic structure and properties. The stress-induced shape transformation becomes more enhanced as the size of the cluster decreases. Clean crystalline surfaces show greater strain than amorphous ones.

- Spillover of reactants: Spillover refers to the migration of an adsorbate molecule or atom from the substrate to cluster or *vice versa* (reverse spillover). This process greatly depends on the acidic properties of the substrate. H and O are the most well-known examples. It should be mentioned that spillover plays a crucial role in many surface reactions and is considered a key step in the storage of hydrogen.

- Strong metal-support interaction (SMSI): The support can also induce chemical changes in the cluster. The SMSI is a mass transport phenomenon where adatoms from the surface layer migrate to the cluster and encapsulate it with a thin layer, the extent of which depends on the surface energy and work function (see Figure 1.7b).[85, 87, 91] It usually occurs with oxides after reduction at high temperatures. Such an effect completely changes the chemisorption properties of the particle, not only of the sites in contact with the support, but of the whole structure. Apart from a geometric blocking, the oxide layer can also change the electronic structure of the atoms in contact

with it. Besides, adatoms can also detach from the cluster and sink into the crystal lattice of the support.

At this point a note should be made on the properties of metal oxides. Metal oxides are divided into two groups, *i.e*, irreducible and reducible oxides.[92, 93] Irreducible oxides have large band gaps and therefore very poor conductivity and tendency to be reduced. They are considered inert supports and their main role is to disperse the clusters. The MSI is limited only to the contact area. Al_2O_3, SiO_2 and MgO belong to this group of oxides. On the other hand, reducible oxides show high conductivity, access to multiple valence states and a high capacity to store and release oxygen. The support is no longer passive. It can provide active O atoms for reactions via a Mars$-$Van Krevelen (MvK) type mechanism or transfer the O atoms to the cluster via spillover mechanism. CeO_2 is one of the most studied oxide in this group. Here, part of the surface Ce^{4+} ions accept electrons from the cluster into the empty f orbitals and get reduced to Ce^{3+}. Other examples include TiO_2, SnO_2, ZrO_2, ZnO, FeO_x and V_2O_5.

1.4.4 Clusters in Catalysis

Catalysis is perhaps one of the fields that has benefited most from cluster science. Due to their unusual properties, clusters often have been shown to be superb catalysts for a wide range of reactions including CO oxidation, dehydrogenation of alkanes, epoxidation of alkenes, oxidation of alcohols, water$-$gas shift reaction (WGSR) and electrochemical reactions.[56, 64, 88, 94–104] The catalytic activity of a catalyst is connected to the density of active sites (or equivalently surface area). The active sites are low-coordinated atoms or groups of atoms located at the surface and display greater activity than the high-coordinated atoms typical of the bulk metal. In a big NP only the surface atoms are under-coordinated; that is, only a small fraction can adsorb and transform the reactants. In contrast, all atoms in the cluster are under-coordinated; not only the surface, but the core also participates in the reaction. There is a maximal utilization of atoms (atomic efficiency), optimizing the economic cost of the metal loading. Besides, in many cases clusters can activate the adsorbates more efficiently owing to their lower work function. This translates

A)   B)
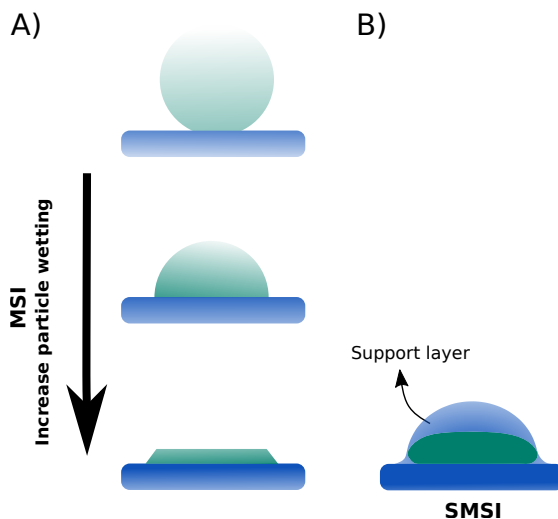
Figure 1.7: Schematic representation of A) metal-support interaction (MSI) and B)
          strong metal-support interaction SMSI effects. In A) the MSI increases
          downwards. If the MSI is weak the particle may retain a globular shape.
          However, as the MSI increases, the particle wets more the surface and
          becomes more planar. In B) surface atoms migrate to the particle and
          encapsulate the particle. The cluster and support are illustrated in
          green and blue, respectively.

into an easier electron transfer to the adsorbate empty antibonding orbitals which increases the internal bond length.

Cost-effective and scalable synthesis of monodispersed atomically precise supported clusters is one of the most ubiquitous goals in catalysis. Over the last decades several methods have been developed.[88, 92, 98] Herein, we focus on the two most important ones:

- Gas-phase deposition: A cluster ion source is generated in gas-phase via vaporization or sputtering of a rotating rod of the target metal. The newly formed ion source shows a wide distribution of sizes, making mandatory a size-selection step. Commonly employed techniques include time of flight, radiofrequency quadrupole and electrostatic quadrupole mass filters. Then, the size-selected clusters are soft-landed on a support in ultrahigh vacuum (UHV) conditions. This method allows to obtain perfect monodispersed catalysts with very high accuracy. The main disadvantages are however, the

efficiency of the soft-landing which reduces the catalyst loading and especially the large-scale utilization.

- Wet chemistry: Clusters are synthetized by mixing a metal precursor and the support powder in solution. Depending on the nature of the precursor we distinguish two main routes. In the direct method a polynuclear precursor is used; that is, a presynthesized organometallic metal cluster of the target size. Carbonyls, phosphines and thiolates are the most habitual ligands utilized to protect the clusters. After anchoring the clusters to the surface, the ligands are removed with thermal treatments such as reduction and calcination. Gates *et al.* successfully reported the synthesis of Os_3, Ru_3, Ir_4 and Rh_6 over MgO.[105] With this method perfect monodispersity can be achieved, but it requires the use of very stable clusters so as to avoid fragmentation and agglomeration during deposition. Thus it is only fitted for some particular metals and sizes. In addition, the thermal treatments may not be totally effective to remove all the ligands from the surface. However, this problem could be solved by using a dendrimer instead of a cluster organometallics.[106] The dendrimer core not only acts as an anchoring site, but also induces a nucleation process to build clusters of any given size. Even more, the dendrimer branches serve as natural barriers to prevent particle agglomeration. Impregnation is the second approach and the most widely extended one. In this case a mononuclear precursor in the form of an inorganic salt is employed. Some common examples include H_2PtCl_6, $Pt(acac)_2$, $Pd(acac)_2$, $PdCl_2$, $HAuCl_4$, $AgNO_3$, $RuCl_3$ and $GeCl_4$. For many reactions non-chlorinated sources are preferred to avoid poisoning. The experimental procedure is done in the following steps. First, the porous support is soaked in a solution of the precursor inorganic salt. Then, several subsequent purification steps are required to eliminate the inorganic anions, such as washing, centrifugation and drying; and finally, thermal treatments are used to agglomerate and redisperse the catalyst particles (catalyst activation). This is a very convenient and economic method to implement in large-scale manufacturing, but presents several issues with the degree of control over the polydispersity and cleanness

of the catalytic surface. It is not accurate enough to synthesize clusters of
very few atoms as the clusters tend to aggregate into bigger particles during
the thermal treatment. Thus, it is best suited for bigger clusters and NPs
($1 - 2$ nm) where there is not a need for such high precision in the dispersion.
Nonetheless, the use materials with molecular-size nanopores can help stabilize
clusters below 1 nm and prevent uncontrolled agglomeration.[92, 107]

1.5 Catalyst Deactivation

The operating reactor conditions can have a great impact on the performance of
the catalyst. The extreme conditions of temperature, pressure and pH inside the
reactor, as well as contaminants in the feed inevitably lead to the deactivation of
the catalyst. Catalyst deactivation can be defined as the loss of catalytic activity
and/or selectivity over time. Undoubtedly, it is a problem of the utmost importance
considering the fact that catalyst replacement costs losses of billions of dollars
in the industry annually.[108–110] The catalyst can be regenerated by thermal
treatments. Unfortunately, they are not effective after a few regeneration cycles and
are very costly since they may require the shutdown of the entire process. Moreover,
they often require the presence of chlorine which raises many environmental issues.
Precisely because of this, there is an urge to develop highly stable catalysts that can
retain their activity for long-term applications. The time scales of the deactivation
are ample, ranging from seconds to years depending on the process. For example,
in the catalytic cracking deactivation can occur in a matter of seconds, while in
catalytic reforming the catalyst can last up to a year. Deactivation can occur
through different mechanisms. Here we focus on what we believe are the most
crucial ones: sintering, coking and CO poisoning. The first mechanism is a physical
process whereas the other two are of chemical nature.

1.5.1 Sintering

Clusters are thermodynamically unstable. They possess a huge amount of surface
area and under-coordinated atoms which drastically increases the surface energy. As
a result, the clusters tend to agglomerate into bigger particles and adopt Wulff-like

structures to minimize the surface energy, *i.e.*, sintering. Logically, the tendency to sinter increases as the size decreases, ultra-small clusters being much more unstable than NPs. Sintering refers to the loss of catalytic surface owing to the crystallite growth of the active phase.[108–112] Larger particles are built at the expense of smaller ones. Sintering is a temperature dependent process; the higher the temperature, the higher the mobility of atoms and thus the propensity to sinter. This aggravates the issue since many reactions demand elevated temperatures. Sintering has a great detrimental impact on the catalytic activity and selectivity by reducing the surface area (density of active sites) and the density of under-coordinated atoms (since in a bigger particle the fraction of atoms in the facets is much higher than at the edges and corners). Besides, changes in size and morphology can also lead to a different electronic structure with less optimal adsorption/desorption energies and higher barriers.

Sintering can occur through two different mechanisms (see Figure 1.8a): Smoluchowski ripening (coalescence) and Ostwald ripening. In the Smoluchowski ripening two or more entire particles migrate through the surface in a Brownian motion, collide and merge with each other. In the Ostwald ripening on the other hand, single metal atoms leave one particle and diffuse across the surface or vapor-phase (if there is any volatile species present) to join another. In both cases bigger particles are favoured over smaller ones. Which one becomes the main mechanism strongly depends on the temperature and cluster size. Generally, Ostwald ripening will predominate at low temperature as less energy is needed to move a single atom than an entire particle. For smaller sizes Ostwald ripening is also more important. However, all this will be influenced by the nature of the cluster and support. When the internal cohesion energy of the cluster is stronger (strong metal-metal bonds) than the cluster adsorption energy, sintering will proceed via Smoluchowski ripening, whereas in the opposite case the preferred route will be Ostwald ripening.

1.5.2 Coking

Coking refers to the deposition of carbonaceous species on the catalyst surface under high temperature and an environment rich in hydrocarbons or CO, which results in the deactivation of the catalyst. Evidently, this issue takes an ubiquitous importance

in the petrochemical industry, as well as in CO abatement processes such as the three-way catalyst (catalytic converter). The mechanism of coke formation is very complex and typically involves the undesired continuous condensation (dehydrogenation) of hydrocarbons and subsequent polymerization. The reader can consult other sources for an in-depth review.[108] The chemical structure of the coke deposit depends on the temperature of operation, feed composition and catalyst materials. With this, the following species can be observed: atomic (carbidic) carbon, polynuclear aromatic compounds and at very high temperatures graphite. As depicted in Figure 1.8b, the coke usually deposits in the form of films which partially cover the catalytic surface or completely encapsulates the cluster blocking the adsorption of reactants. In the extreme case carbon filaments can be grown beneath the cluster detaching it from the support. The filaments cause a huge stress on the support which ends in its fracture. If left uncontrolled, the filaments will fill all the pores and break whole catalyst pellets.

1.5.3 CO Poisoning

Platinum group metals (PGMs) are very active catalysts employed in many important sectors of the chemical industry, ranging from petroleum processing to energy production and pollution control. Six very scarce transition metals of huge strategical importance make this group, *i.e.*, Pt, Pd, Ru, Rh, Os and Ir. Unfortunately, their high catalytic performance is accompanied by a high propensity to get poisoned by CO. CO poisoning is defined as the strong and irreversible chemisorption of CO onto the catalytic surface. Even at trace amounts CO might cover the surface, hindering any further reaction and thus abruptly diminishing the catalytic lifetime (see Figure 1.8c). This phenomenon is related to a low selectivity of PGMs towards CO, meaning that CO will adsorb more preferentially than the rest of the molecules in the feed. This type of deactivation can have the following effects on the catalyst: reduction of available active sites, blockage of surface diffusion of reactants and modification of catalytic activity and selectivity due to changes in the electronic structure induced by CO adsorption. Besides, CO poisoning can occur in different scenarios depending on whether it participates in the reaction (*e.g.*, CO oxidation in the three-way catalyst, WGSR, Fischer−Tropsch synthesis,...) or is found as

an impurity in the feed (*e.g.*, hydrogen production via steam reforming,...). An ultra-pure feed is a requisite for processes with risk of CO contamination. Apart from this, another preventive and very effective and economical measure is to make intrinsic alterations to the catalyst to reduce the affinity to CO (*vide infra*).

A) Sintering

Coalescence

Ostwald ripening

B) Coking

Carbon filament

Coke layer

C) CO poisoning

CO layer
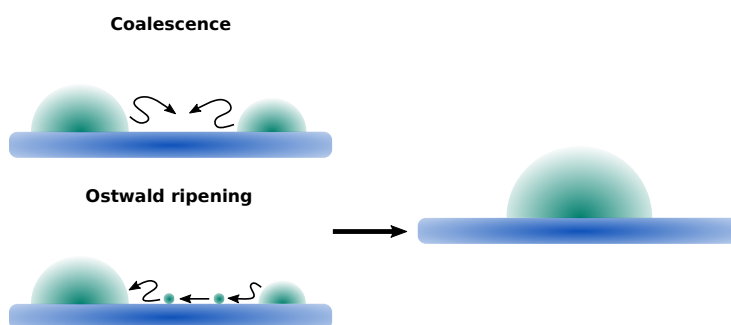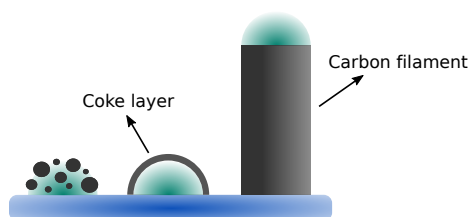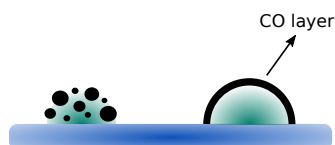
Figure 1.8: Schematic representation of the major types of catalyst deactivation: A) sintering, B) coking and C) CO poisoning. In A) the two principal sintering mechanisms are shown, *viz.*, coalescence and Ostwald ripening. In B) and C) different degrees of deactivation are shown. The cluster and support are illustrated in green and blue, respectively.

1.6 Structure-Activity Relationship as the Nexus Between Clusters and Catalysis

Hitherto, the design of industrial catalysts has generally relied on a trial-and-error approach. As can be understood, the parameter space sampled by such an approach cannot be very extended and inevitably excludes the optimal materials unless serendipity comes into play. Furthermore, catalysis is a science that involves processes with completely different time scales; starting from seconds/hours for mass transport and catalytic cycles at the reactor level to femtoseconds (fs) for bond breaking/formation. In addition, apart from optimal reactor design, an atomic level understanding of the catalyst surface is required in order to capture and rationalize the different processes occurring during the reaction. The catalytic performance of the catalyst is determined by the electronic structure via the well-known structure-activity relationship.[51, 94, 95, 104, 113–117] Structural reconstructions on the surface modify the electronic structure (energy of MOs, orbital symmetry and electron density), which in turn gives rise to alternative reaction pathways with different barriers (catalytic activity) which may favour one product over the other (selectivity). Nonetheless, it is far from trivial to understand *a priori* how this relationship is established. The difficulty resides in the delicate interplay between the electronic structure and geometrical features. In this regime where every atom counts, the structural properties of the cluster are constantly evolving in a dynamic way by external factors (pressure, temperature, pH, electrode potential, ligands) under operating conditions. All these factors act simultaneously making it difficult to discern the contribution of each. Understanding of the structure-activity relationship remains the main bottleneck in catalysis.

It should be mentioned that the dynamic nature of the catalyst has not gained enough relevance until recently, mainly due to experimental limitations to monitor catalyst evolution. The first catalyst characterizations were carried out *ex situ* in ultrahigh vacuum (UHV), neglecting the effect of the environment. However, since different conditions than the reaction conditions are used, these studies cannot derive a *bona fide* structure-activity relationship. Undoubtedly, this underlines the importance of studying the dynamics of catalytic reactions. Huge advancements

in the last few years have allowed the advent of experimental techniques that work *in situ* to reproduce the reaction conditions and *operando* to monitor the time evolution.[86, 98, 114, 115, 118–121] In this way, the time dependence of the catalytic properties can be probed with atomic level insight. Surface science characterization techniques can be adapted to function *in situ* and *operando*. Microscopic methods such as scanning tunneling microscopy (STM), atomic force microscopy (AFM) and aberration-corrected high-angle annular dark-field scanning transmission electron microscopy (HAADF-STEM) can be used to identify cluster size and distribution (agglomeration), morphology and chemical composition. Besides, UV-vis, Fourier transform infrared (FTIR), Raman, nuclear magnetic resonance (NMR), Mößbauer, ion scattering spectroscopy (ISS) and neutron diffraction can also be employed to probe the nature of active sites (*e.g.*, acidity *vs* basicity) and monitor the adsorption and rate of formation/consumption of molecules (binding strength, geometry and coverage). In this line, the temperature programmed desorption (TPD) is another widely extended and versatile spectrometric tool to study the adsorption strength of active sites and the kinetics of adsorbates. X-ray based spectroscopies like X-ray absorption near-edge structure (XANES), extended X-ray absorption fine structure (EXAFS) and X-ray photoelectron spectroscopy (XPS) provide local information about bond-lengths (intracluster and intercluster between cluster and support/adsorbates), coordination numbers, oxidation state and electronic structure of the active sites.

The core idea of atomic-precision catalyst design is based on the versatility to modify the catalytic properties through the structure-activity relationship. Clusters offer a plethora of different degrees of freedom that can be exploited to control the catalytic properties. At the subnano scale even a tiny alteration on the physical structure can cause a huge impact on the catalytic performance. It is precisely this ability to fine-tune their properties that clusters outperform NPs. The objective is to engineer the electronic structure (and thus the catalytic properties) of the cluster by changing the morphology and chemical composition. Several strategies have been devised towards this atomic level engineering which are discussed in the following subsections. See Figure 1.9 for a illustrative summary.

Figure 1.9: Schematic representation of the major strategies (outer circle) to engineer the catalytic properties (inner circle) of subnano clusters.

1.6.1 Size and Morphology

As many properties become size-dependent in the subnano regime, the most obvious degree of freedom is the cluster size. Cluster size offers control over the morphology and electronic structure which in turn control the catalytic properties.[64, 114, 115] Geometrical changes refer to modifications in the density of active sites or their spatial configuration making them more appropriate to activate the target reactants (*e.g.*, hollow sites, terrace sites, step sites, ensemble of planar atoms,...), while alterations in the electronic structure refer to the capacity of charge transfer and hybridization. Nonetheless, in the subnano scale the geometry and electronic structure are closely entangled since a restructuring of the cluster leads to a different electronic structure. Therefore, it is not trivial to ascribe the size effect solely to one or the other, but both act simultaneously.[122] Despite this intricacies, there are some studies which try to separate electronic effects on the adsorption properties from geometric ones.[123, 124] Moreover, geometric transformations cannot so easily be connected with size effects as there are many others factors affecting the cluster shape such as the support, ligands and temperature.

The size effects are material and reaction specific and the changes in the catalytic

properties are often unpredictable. Different structure-sensitivities can be observed: the properties can either monotonically increase or decrease with size, show a volcano-type relationship or remain constant.[125] Even more, the size-dependence can change at different size ranges, *e.g.*, volcano-shape at very small sizes and constant for the rest. In the following, several works studying size effects on a wide range of reactions are collected, which proves the advantage to manipulate the catalytic properties with size. It should be mentioned first that many works, especially older ones, deal with catalysts in the nanoscale regime (size > 2 nm). These results cannot be extrapolated to the subnano regime, so the size-depences found thereof may totally change.

There is a vast literature showing that clusters outperform their bulk or NP analogue. For example, in propane dehydrogenation (PDH) by Pt/Al_2O_3 catalyst[126] the turnover frequency (TOF) shows a decreasing tendency with size, while the propene selectivity and stability display an inverted volcano-shape, single atoms and ultra-small clusters having the best performance. Several studies link the size dependence directly to ensemble or geometric effects. One work which studies Pd catalysts on nanodiamond (ND) for H_2 production via dehydrogenation of nitrogen-containing organic molecules, observes that single atoms are inactive and underlines the importance of having atomic ensembles at the surface. A volcano trend is found with optimal size around $1-2$ nm.[127] In Pd/MgO(100) a critical ensemble of seven active sites is found for the acetylene cyclotrimerization, and clusters smaller or bigger than this threshold follow different mechanisms.[128] In a similar way, Molina *et al.* find a change of mechanism in propylene oxidation induced by morphological changes of the Ag/Al_2O_3 catalyst, and prove that the selectivity can be driven towards propylene oxide or acrolein with the cluster size.[129] Genest *et al.* also show a selectivity control of the 1-butene isomerization and hydrogenation reactions with the amount of surface Pd(111) paches in Pd NPs supported on Al_2O_3.[130] Besides, other studies connect the size effects to the electronic structure, as in the photocatalytic hydrogen evolution reaction (HER) , where the size dependence of H_2 production is correlated to the energy of the LUMO level of Pt/CdS nanorods;[131] or in the oxidation of CO by Pt/Al_2O_3, where it arises from the ratio between neutral and cationic Pt especies.[132] Other oxidation reactions worth mention-

ing that show a size dependent catalytic activity are the thiophenol oxidation by Au/MWCNT (functionalized multiwalled carbon nanotubes),[133] CO oxidation by Pd/TiO$_2$[134] and ethylene oxidation by Pt/carbon black.[135]

Size effects have also been widely investigated on electrocatalysis. Ultra-small clusters also display a higher catalytic performance than NPs in a wide range of electrochemical reactions, *e.g.*, ORR by Au/GC (glassy carbon),[136] oxygen evolution reaction (OER) by Co$_3$O$_4$/SiO$_2$[137] and ethanol electro-oxidation by Pt/ITO (indium tin oxide).[138] In contrast, a 2011 Nano Lett. article[139] hints a volcano relationship of the ORR activity in Pt/C, with 2.2 nm being the optimal size. Regardless, this study does not include clusters below 1 nm so the results cannot be extended to this regime. On top of an improved activity over NPs, Pt/ITO and Au/SiO$_2$ present a size dependent H$_2$O$_2$/H$_2$O and H$_2$/CO selectivity in ORR[140] and CO$_2$ electrochemical reduction (CO$_2$RR).[141] As discussed previously, in the subnano regime the addition or subtraction of a single atom can have a drastic impact on the catalytic performance of clusters, as evidenced in Cu/Al$_2$O$_3$ for methanol synthesis,[142] Pt/C for ORR[143] and Pd/ND for H$_2$O oxidation.[144] In the same line, sintering is also a size dependent phenomenon and Poths *et al.* have unraveled the existence of some highly stable "magic" sizes in Pt/Al$_2$O$_3$ with huge sintering resistance.[145]

Size and shape being strongly coupled in the subnano scale, NPs often turn out very convenient platforms to isolate shape effects due to their big size. For instance, Pt NPs with tetrahedral, cubic or near spherical shapes present different catalytic activities in the reaction between hexacyanoferrate (III) and thiosulfate.[146] A recent work by Cuenya and Luo reports that reshaping Rh NPs in a nanoflower-like structure increases significantly the catalytic performance in the electrochemical nitrate reduction.[147] A shape control of the selectivity has also been observed in the cis-trans isomerization of olefins[148] and methylcyclopentane (MCP) hydrogen-olysis.[149] The reader can consult references [114] and [115] for a more elaborate discussion.

1.6.2 Support

As explained before, the support exerts a huge impact on the cluster morphology and thus on the catalytic properties. The support not only serves as a dispersing matrix, but acts in synergy with the cluster to activate reactants and break and form bonds. Here, the *essence* lies in exploiting the MSI to control the catalytic properties of the cluster, an approach recently coined as interface engineering.[85–88, 92, 114, 115] The nature and degree of the MSI can be tuned by inducing chemical and physical modifications on either the support or cluster. In this subsection we deal with the former; that is, changes inherent to the support, while the latter is discussed in the other sections.

Evidently, the first thing to consider is the nature of the support. The impact of the MSI on the cluster will depend upon the structural and electronic features of the surface. A closed-packed planar surface, a surface with a high degree of roughness and hollow sites or an oxygen-rich surface will favour different cluster geometries. Apart from geometrical factors, the charge transfer (EMSI) is an important phenomenon that can be used to control the cluster shape, adsorption properties and reactivity of the active sites. For instance, γ-Mo_2N has been reported as a novel substrate which induces a sintering reversal effect of Ni NPs and an enhanced selectivity in CO_2 hydrogenation thanks to a strong MSI.[150] For a given support, exposing different lattice planes also affects the geometry as they have different packing structures and surface chemical composition. High Miller index Al_2O_3 surfaces have been shown to prevent the sintering of Pt NPs.[85] The high Miller index facets can be grown by capping the more stable low index facets.[115]

More importantly, the metal/support interface often gives rise to intriguing properties. The cluster and support may act in synergy to create new active sites with alternative reaction pathways at the metal/support interface. Hence, the objective is to design the catalyst in such a way that it maximizes the interface perimeter. Such phenomenon has been observed in Ag supported on $LaNiO_3$ perovskite where the interface offers a more reactive pathway enhancing the OER activity.[151] W carbide (WC) also turns out an advantageous support over carbon for the ammonia oxidation reaction (AOR) because of interface effects with Pt clusters.[152] In this regard, reducible oxides are excellent candidates to tailor

the interface.[93, 153] Here, the surface atoms are no longer spectators but can participate in the reaction via a MvK mechanism as an oxygen reservoir and as a source of Lewis acid/basis sites due to their multiple oxidation states. For instance, S. Kattel *et al.* compare the catalytic performance of ZrO_2 and TiO_2 supported Cu catalysts in the CO_2 hydrogenation.[154] Their findings reveal that the reduced Zr^{3+} sites at the interface bind more strongly than TiO_2 the intermediates facilitating the reaction. Extending their study, these same authors prove that the selectivity in this reaction can be controlled by the reducibility of the support.[155] Reducible oxides are also advantageous owing to their spillover properties. In the ammonia synthesis catalyzed by Ru/La_2O_3 the surface La−H act as an H reservoir and offer an alternative pathway through a MvK mechanism with a huge boost in activity.[156] La−H species can be regenerated by the continuous heterolytic dissociation of H_2 followed by the reverse spillover to the surface. It has been found that in Pt/CeO_2 the support preferentially absorbs CO by a reverse spillover mechanism, preventing the CO poisoning of Pt catalysts.[157]

Besides, the support can be nanostructured by inducing physical and chemical changes. In the same way as the cluster morphology can alter the catalytic properties, the support morphology can also induce structural and electronic changes on the cluster. By modifying the morphology one can gain control over the percentage of the exposed facets as well as the lattice strain. This is clearly illustrated in the CO preferential oxidation (CO−PROX) by Pt/CeO_2.[158] Herein, Pt clusters are deposited on CeO_2 nanocrystals of different shapes, *i.e.*, rods, cubes and polyhedra. The different nanostructures present different reducibilities and Pt^0/Pt^{2+} ratio, CeO_2 rods being the best candidates. Furthermore, surface modification can also be used to increase the sintering resistance. Two main strategies can be taken which differ whether they are of chemical or physical nature.[111, 112] The first relies on increasing the bond strength between the cluster and support. Defects such as steps and kinks serve as nucleation sites and hinder the diffusion of clusters, so that a completely clean surface may not always be the best option. Vacancies and heteroatom doping are also very attractive options to anchor particles as they offer a high degree of control over the defect concentration. Apart from increasing the stability, the defects introduce charge imbalances and can alter the morphology and

electronic structure of the cluster via EMSI, and in turn their catalytic properties.[86] It is well known that the adsorption properties of Au can be tuned by introducing oxygen vacancies in MgO.[159] In addition, a study by X. Liu *et al.* shows that doping the support with Cu in Pt/CeO_2 increases the CO oxidation activity.[160] The formation of $Cu-O-Ce$ sites at the interface offers a new pathway with lower CO adsorption strength, preventing CO poisoning. It is interesting to note that doping allows to control the reducibility of oxide supports.[153] The second route consists in the physical confinement of clusters in nanoporous materials like zeolites and metal-organic frameworks (MOFs).[88, 92, 161] Here, there is a physical barrier which keeps the clusters inside the pores and tunnels. Likewise, the nanopores can be doped to further increase the catalytic performance.[162]

Functionalization of the support has gained considerable attention in recent years. Decorating the support with functional groups can alter its electronic structure and hence can be used to enhance the MSI. This approach could be used to increase the Brønsted acidity/basicity of the surface atoms. An interesting case worth mentioning is the work by J. Lee *et al.*, where they prove that the SMSI in Pt/TiO_2 can be controlled by incorporating sulfur species.[163] As a final remark, it is important to mention that advancements in material science have led to the rise of a huge variety of 2D materials with exotic properties beyond metal oxides. Some examples include graphene and derivatives, hexagonal-boron nitride, phosphorene, TM dichalcogenides, carbides, nitrides and phosphides. These materials are expected to play a key role on the development of novel catalyst with ultra-low PGM loading (and even PGM free).[164, 165]

1.6.3 Fluxionality and Ensemble Representation

As has been mentioned previously, clusters have structural isomers. Clusters present a very complex potential energy surface (PES) full of many low-lying minima. Hence, at temperatures relevant in catalytic processes, the GM has enough thermal energy to climb the energy barriers and populate other low-energy metastable minima with potentially different properties. As a note of caution the reader should not take a static vision of this picture where we have separate isomers isolated from each other. The most surprising fact is that in the case of having a flat PES the isomers can

interconvert into each other during the timescale of the reaction, that is, undergo isomerization. This is known as fluxionality and is perhaps the most interesting, unique and poorly understood property of clusters.[94, 166–168] Under reaction conditions the support is decorated with a variety of different coexisting isomers, each of which is catalyzing the reaction at a different rate, directing the reaction through different pathways and continuously isomerizing into each other, provided the isomerization barriers are small.

The thermally accessible isomers form a statistical ensemble the size of which depends on external conditions (temperature, pressure, potential, *etc.*) and the nature of the catalyst. Assuming thermal equilibration the relative populations are given by a Boltzmann distribution. The ensemble evolves dynamically and the catalytic properties are altered accordingly. Often, there is a "mismatch" between thermodynamics and kinetics in the sense that the most stable isomer might not be the most active one. In other words, the thermodynamics and kinetics of the reaction might be controlled by different isomers. Indeed, catalysis is often driven by the less populated low-lying isomers. In spite of their smaller probability weight, their high activity compensates significantly for the time required for the GM to overcome the reaction barriers. For the case of having a more inert GM, the cluster will show low rates during the time it is in the GM, but once it starts visiting the more active isomers there will be a boost in the number of catalytic cycles. Therefore, focusing solely on thermodynamic properties can lead to quite misleading conclusions. Current research in catalysis urges to go beyond the single cluster catalyst concept and adapt an ensemble representation. Herein, the key question is how to control the size of the ensemble and kinetically stabilize only the most active meta-stable isomers, irrespective of their initial relative stability.

It is known that the PES depends on the structural properties of the system, so by modifying the structure of the catalyst we can in principle reshape the PES and thus control the ensemble size. Finally, by invoking the structure-activity relationship a link can be established between fluxionality and activity. Fluxionality is another lever to control the catalytic properties. This control, despite being beyond the current capabilities, can be achieved by making use of the degrees of freedom discussed in the other sections; *i.e.*, size, support, doping and adsorption of ligands.[169–

175] A striking example of size-effects is the case of ethylene dehydrogenation on Pt/Al_2O_3 studied by Alexandrova and co-workers.[176] According to experiment, Pt_7 is much more active than Pt_8 even though theory predicts a similar 3D structure for the GM. However, when taking an ensemble approach, the authors find that in Pt_8 only the inactive GM is thermally accessible, while Pt_7 has a broader ensemble with more active 2D isomers. Another study points to the possibility of controlling the selectivity in the oxidative dehydrogenation of cyclohexane by means of fluxionality.[177] Besides, the support can also be engineered to adjust the relative intra and intercluster strength and make more rigid and less fluxional clusters. The effect of adsorbates and dopants is postponed to later sections. Hereby, it is evident that fluxionality is a very intriguing property that should be fully exploited in current research. Notwithstanding, there is still lacking fundamental knowledge on its precise role on catalysis. Fluxionality is very reaction-specific and thus, cannot be known *a priori* which is the ideal ensemble size.

1.6.4 Doping and Alloying

Manipulation of chemical composition is perhaps the oldest and most well-known technique in material science. Metal alloys entailed a huge leap forward in the development of former civilizations as they offered a means to improve the properties of native elements and use them in applications previously not feasible. Often mixing two different elements can enhance certain properties or even display properties not present in the pure materials as a result of synergistic effects. Alloying offers a huge diversity of possible compositions which can be adjusted to meet the required properties. Importantly, it can help reduce the PGM loading while at the same time improving the catalytic performance. Hence, the question should be why not take advantage of the great tunability of alloying to design more reaction-specific and economic nanocatalysts.[178–181]

As a remark, here we distinguish doping as the addition (or substitution) of a foreign atom or impurity in small quantities into the parent cluster and alloying as the mixing between two or more elements without requiring the prior existence of a parent cluster. Bimetallic and trimetallic clusters are usually called nanoalloys and hereafter this term will be employed when referring to them. Alloying shows

very strong synergy in the nanometer scale. The mutual interaction between different neighbouring atoms may give rise to unexpected structures and properties completely different from the ancillary metals; that is, an active nanoalloy may be obtained from two inactive monometallic clusters. Apart from composition, it is also important to consider the mixing pattern (atomic ordering) of the nanoalloy since this will have a direct impact on their catalytic properties. The mixing patterns can be classified as follows:

- Core-shell segregation.

- Segregation into separate sub-clusters with varying size of the interface.

- Intermixed segregation. Here they can be further classified depending on whether the mixing is ordered or random.

- Multishell segregation.

It must be mentioned that it is not easy to know *a priori* the mixing pattern between the two metals as it depends on several factors which act simultaneously. However, some general lines can be drawn to help making a more judicious choice of metals in nanoalloy design:

- Relative homo and heteronuclear bond strengths.

- Surface energy of bulk elements.

- Atomic radius.

- Charge transfer. The direction and amount will depend on the electronegativity difference between both elements.

- Binding strength to the support and adsorbates. For example, if one of the metals binds more strongly to the support than to the other metal, the atoms of this metal will try to maximize the number of bonds with the surface and the nanoalloy will segregate into two sub-clusters instead of mixing together.

Linking the effect of alloying to the catalytic performance is not a trivial task. One of the major drawbacks in nanoalloy design is the fact that it is not known *a priori*

how the alloying affects the catalytic behaviour (structure-activity relationship), and hence it is extremely difficult to optimize the nanoalloy to maximize the catalytic performance. Moreover, this effect is also reaction-specific, so it is difficult to derive some general trends. Broadly speaking, the role of alloying can be divided into three different groups, *i.e.*, geometric, electronic and multifunctional effects.[182] The first two occur when an active metal is mixed with an inactive metal that does not take part in the reaction, while in the third both elements in the alloy have specific functions in the reaction. In the subnano regime, this differentiation gets blurred and is not so easy to solely ascribe the improvement in the catalytic behaviour to one or the other, as alloying usually reshapes the cluster and geometrical changes are followed by changes in the electronic structure. In reality, all effects are often strongly convoluted and act simultaneously.[183]

Geometric effects appear in nanoalloys made of an active and inert metal. They refer to changes in the adsorption properties and reactivity due to alterations in the geometry of the active sites introduced by the inactive metal.

- Ensemble effects: Certain molecules require multidentate adsorption (multiple active sites, *i.e.*, atomic ensemble) for activation, *e.g.*, ethylidyne on hollow sites and $C-C$ cracking on Pt_4 sites. Ensemble effects occur when the inactive metal atoms replace part of the atoms in the ensemble, rendering it inactive. The effect of the inactive element is purely geometrical, it acts as a diluting component separating the active atoms and reducing the concentration of active ensemble sites. As can be observed, this phenomenon can be used to inhibit undesired side reactions and enhance the selectivity.

- Steric effects: Alloying an active metal with an inactive metal of larger atomic radius can give rise to steric phenomena. If the concentration of the inactive metal is considerable, it can hinder the adsorption and consequent activation, as well as the diffusion of the reactants and intermediates.

Electronic effects appear in nanoalloys made of an active and inert metal. They

refer to changes in the adsorption properties and reactivity due to alterations in the electronic structure of the active sites.

- Ligand effects The formation of bimetallic bonds upon alloying can bring changes in the electronic structure and in turn alter the catalytic behaviour. These bimetallic bonds result from the d-d or sp-d hybridization (covalent bonds) depending on whether the inactive component is a d-block or p-block element. Orbital hybridization changes the d-band structure (energy of MOs and their electron density) and thus the reactivity. In case of the two elements having different electronegativity, it can give rise to charge transfer phenomena and form polarized bonds, together with nucleophilic and electrophilic sites.

- Strain effects Tensile and compressive strain can alter the d-band structure of the active metal and consequently have an impact on the catalytic performance. Such strain arises as a result of a lattice mismatch between two metallic phases formed upon alloying; that is, the metal-metal bond lengths are modified to adapt to these lattice differences. This effect is not very frequent in the subnano regime; it becomes more important in NPs and specially in core-shell nanoalloys.

Multifunctional effects appear in nanoalloys in which both components play an active role either together or separated. Alloying can bring the formation of new active ensemble sites composed of both elements not present in the pure clusters. Besides, each element in the alloy can display different adsorption properties for the same molecules (dual adsorption). In this regard, alloying PGMs with oxophilic metals (*e.g.*, Co, Mn, Cr, Fe, Re, Mo, Sn, Ge ...) is a very appealing approach to avoid poisoning and coking. Oxophilicity is the tendency to form metal-oxygen bonds. Pt-based catalysts show a high affinity to dehydrogenate oxygenated species like phenols, which are well-known coke precursors. Thus, by introducing a more oxophilic promoter the phenol groups will bind to it, hindering coke formation and leaving the Pt sites free to catalyze the target reaction. As can be observed, multifunctional effects cannot be entirely separated from ensemble and ligand effects as they usually

bring with them such effects.

One may think that in order to observe a meaningful effect a moderate alloy concentration is mandatory. Surprisingly, in some cases single atom doping is enough to alter significantly the catalytic properties, such as adsorption strength,[184] coking,[185] activity[186] and selectivity[187] of even clusters of considerable size. Moving to alloys, Cu has been found to be an excellent promoter to increase the catalytic activity and selectivity of Pt-based clusters in the acetylene semihydrogenation.[188] Such effect is mainly attributed to ligand effects. It is interesting to note that in the hydrodeoxygenation of amides, $RuMo/SiO_2$ acts as a bifunctional catalyst offering alternative low-coordinated $Mo^{5+}O_x$ sites to activate more easily the C= O bond.[189] Herein, a volcano-shape dependence of the catalytic activity with Mo content is also found. Sintering can also have a strong dependence with the alloying concentration. For instance, in $PtPd/TiO_2(110)$ a 1:1 ratio presents the greatest resistance owing to a maximization of entropic and electrostatic stabilization.[190]

Nanoalloys have also been extensively studied in electrochemistry, in particular the ORR reaction. It has been shown that alloying Pt with other PGMs like Ru, Rh and Ir, as well as 3d TMs like Co, Ni, Fe and Cu greatly improves the Pt ORR activity and stability. The reader is referred somewhere else for a more in-depth discussion.[28, 38, 191–197] Just to give an account of some recent works, PtZn and PtZnCu nanoalloys have been reported to show superior ORR activity to Pt due to positive strain effects.[198, 199] In this line, S. Gong and co-workers find that epitaxially grown PtCuNi nanorods (shape + composition effect) present excellent ORR activity, which the authors attribute to both strain and ligand effects.[200] It has been shown that in PtAu nanoalloys the ORR activity and resistance to Pt dissolution (stability) follow opposite trends with Au concentration, 10 at% Au being the optimal composition.[201] Bifunctional nanoalloys have also been synthetized for ORR, as is the case of PtPr. Here two phenomena occur which boost the ORR activity: first, Pr_6O_{11} species are formed which transfer electrons to Pt yielding an optimum electronic state; and second, new bifunctional PtPr sites are formed, which thanks to the great oxophilicity of Pr facilitate the adsorption and dissociation of O_2.[202] S. Wang *et al.* provide another example of a bifunctional catalyst for the

electrochemical WGSR. Alloying ultrasmall Pt clusters with CuO_2 on Fe_2O_3 creates new Pt$-$O$-$Cu sites with a more moderate OH* activation. Simultaneously, these sites also show lower CO binding strength which translates into a high reactivity in the CO electro-oxidation (CO removal from H_2 feedstock).[203]

1.6.5 Ligand Coverage

"Real world" catalysts cannot be considered as isolated systems from the environment. Under reaction conditions, the catalyst is embedded into a fluid matrix, leading to the formation of either a metal-gas or metal-liquid interface, depending on whether the reactants and products are in gas-phase or solution. Catalysis being a surface process, this metal-fluid interface will undoubtedly affect the reaction dynamics of the surface. The interactions with the molecular species in the fluid results in their effective chemisorption on the surface; or in other words, instead of a clean surface, the actual catalyst is covered with a variety of different species (*i.e.*, reactants, intermediates, products,...) in different concentrations. The adsorbed ligands are far from being passive agents, but can in fact induce structural rearrangements on the cluster and modify the catalytic properties.[204, 205] High coverages can entirely distort the cluster framework and hence alter the geometry of the active sites.[206] Apart from geometrical changes, exposure to strong oxidizing/reducing or acidic/basic environments can also induce charge transfer phenomena and change the acid/base and redox properties of the cluster. Moreover, the accumulation of polar adsorbates can induce dipole moments on the surface and change the adsorption/desorption affinities towards ligands with different polarities, as well as affect their diffusion along the surface. This underlines the importance of considering the catalysts made of three different phases, *viz.*, the cluster, surface, and environment.

Ligand adsorption (also ligation, ligand capping) can also be done in a control manner. In the field of colloidal clusters[65, 67, 70, 207] ligand capping is employed on a routine basis to stabilize the particles and protect them from agglomeration as the support is absent. Thiol protected Au and Ag clusters are perhaps the most widely studied cases. Colloidal clusters are usually synthesized in solution and consist of a metallic core protected by a dense shell of stabilizing ligands, usually with significant bulkiness. These systems are in stark contrast with supported

clusters in that the metallic surface is no longer exposed to the reactants; for this reason supported clusters are also called fully exposed cluster catalysts (FECCs). Another issue with colloidal clusters is that the ligands tend to detach from the core at temperatures relevant in catalysis and the stability gets compromised.

Notwithstanding, despite these drawbacks, the knowledge acquired in colloidal clusters can be transferred to supported clusters since ligation offers a huge opportunity to functionalize the catalysts with predefined properties.[204] Recently, carbon-supported Pt_6 clusters have been capped with triphenylphosphine (PPh_3) with atomic-precision.[208] Herein, the authors find that PPh_3 boosts the HOR performance and CO-tolerance by means of ligand (electronic) effects. Despite being studied in extended surfaces, it is also worth mentioning the work by Escudero-Escribano *et al.* in ligand-modified Pt electrodes, where she studies the poisoning-inhibition ability of surface coverage. For example, in one of her works,[209] cyanide (CN) decoration is found to remove the free sites for the adsorption of spectator species like sulphates and phosphates by atomic ensemble effects, and consequently the ORR is channeled effectively without ramifications. Ensemble effects caused by formate coverage also play a crucial role to prevent CO poisoning in the CO_2RR.[210] Likewise, a more recent work suggests that a Cu covered Pt(111) surface can help mitigate phosphate poisoning thanks to ligand effects introduced by Cu.[211] Besides, Roldan Cuenya *et al.* have developed a very promising technique to activate Cu catalysts for CO_2RR by low-pressure plasma pretreatments.[212, 213] This novel approach allows to tune the oxygen coverage of the catalytic surface and thus the degree of Cu oxidation, which turn out to be key components to achieve a high CO_2RR performance. Intriguingly, recently it has been shown that the adsorbate coverage can be used to control the cluster fluxionality and reshape the ensemble size.[214, 215] Even more, a controlled self-poisoning by coke can collapse the entire ensemble of Pt_4Ge into a single active isomer.[216, 217] In addition to this effect, coke deposition is self-limiting, so that once Pt_4GeC_2 is formed, an equilibrium state is reached that prevents further coking. In this isomer the partial coke deposition and the dopant act in synergy to induce electronic effects on Pt, enhancing the selectivity and stability. These findings refute the notion that poisoning is always detrimental to the catalyst and establish firm ground to reconsider the role of

poisoning in catalysis.

1.7 Overview of Ge as a Promoter for Pt Catalysts

For many decades, metalloids like boron (B) and tin (Sn) have been used in a routine basis to enhance the performance of Pt catalysts in various industrial processes. Nevertheless, germanium (Ge) has not raise as much interest as its cousins and studies about its potential catalytic role remain very scarce. Early studies of PtGe bimetallic NPs can be traced back to the beginning of the 2000s.[218–221] Then, an improved selectivity and resistance to coking and sulphur poisoning was found over pure Pt for naphtha reforming. It was argued that the role of Ge is twofold, depending on its oxidation state, which can be in turn controlled by the metal loading and temperature. On the one hand, part of Ge is reduced to metallic Ge^0, alloying with Pt. Ge^0 sites are catalytically inactive and only dilute Pt atoms destroying Pt ensemble sites. On the other hand, part of Ge is left in the oxidized form GeO_x, which alters the acid strength of the Al_2O_3 support and increases the electrophilicity of Pt by electronic effects. However, these works were not devoid of controversy as the preparation method had a great impact and a clear consensus was not reached on the exact role of Ge. Besides, the findings for big NPs may not be transferable to the subnanometer regime as the scaling laws break in this regime, and Ge may behave completely differently.

Moreover, an enhanced activity has also been observed in the CO electro-oxidation.[222, 223] Crabb *et al.* suggested that the promotional effect might be related to the presence of GeO_x.[222] However, metallic Ge is also known to reduce CO chemisorption of extended Pt(111) surface by electronic effects without the assistance of GeO_x.[224] Thus, it is not clear yet how Ge assists the Pt catalyst. Similarly, PtGe also exhibits remarkable HER and DMFCs performance.[225, 226] The enhancement comes from the interaction between Ge and oxigenated functional groups in the HNO_3-functionalized carbon support. As of late, there has been extensive investigation in alkane dehydrogenation reactions as Ge has been shown to have superior selectivity and resistance to coking and sintering.[216, 227–232] The promotional effect is ascribed to geometric and/or electronic effects.

1.8 Scope and Structure of This Work

In the quest to achieve next-generation active, durable, economic and green catalysts, clusters appear very promising candidates. First, their maximal atomic efficiency helps optimize the PGM loading; and second, their great tunability makes them very attractive to engineer the catalytic properties with atomic precision. It is often the case that the catalytic properties like activity, selectivity and stability show opposite trends in the parameter space. This indicates that a juxtaposition has to be found by a most adequate selection of cluster size, composition, support, *etc.* that maximizes all catalytic properties simultaneously. That is to say, catalyst design involves the optimization of a multidimensional parameter space of extreme complexity. Unfortunately, our ability to engineer with such a degree of accuracy remains at an early stage. Nevertheless, in recent years there has been a huge advancement in surface science techniques that has allowed the construction of very sophisticated catalysts with different levels of engineering. On top of this, theory has not lagged behind either; nowadays it has become a routine work to simulate extended systems with hundreds of atoms; and more importantly, the predicting power of theoretical modeling has increased to the point where theory can take a leading role and guide the experiment. Computational research has proven to be a very efficient approach to sample and limit the ample choice of material design, significantly reducing the experimental workload.

The main goal of the present thesis is the design of novel catalysts with enhanced resistance to CO poisoning. Our approach consists on alloying Pt clusters with Ge, a novel promoter that has been gaining relevance over the last years. More specifically, the core idea of this thesis lies in understanding and rationalizing by means of a combination of state-of-the-art computational methodologies how Ge alloying can hinder CO poisoning on Pt clusters under different catalytic environments. Our intention is to first gain a thorough knowledge of the Ge alloying effects so that then, these effects can be boosted further by incorporating other degrees of freedom like size, shape, support and adsorbate coverage to develop a highly engineered PtGe bimetallic catalyst for target reactions.

The choice of Ge as a promoter is not trivial; it stems from previously reported results in which a positive effect of Ge is hinted at for several key reactions, as well

as a need to address current open questions in the field of catalysis regarding for example the precise role of the alloy concentration and support. The literature review of section 1.7 shows that Ge is a very versatile promoter, but at the same time its promoting effects are hardly understood, preventing its full exploitation. This lack of knowledge is further increased at the subnano scale. Consequently, as a continuation of previous research, herein we intend to explore further the possible applications of PtGe nanoalloys in the current context of a necessary transition towards a greener catalysis.

   The results reported herein are presented in order of increasing complexity of the system. First, gas-phase (vacuum) studies are introduced so that the size, shape and composition effects can be correctly determined in an isolated controlled system. Then, the support is added to comprehend how the nature of the support affects the previously characterized degrees of freedom; and finally, the adsorbate coverage is considered to simulate a catalyst in more realistic conditions. By building upon previously laid fundations, this bottom-up approach guarantees that the specific objectives are smoothly fulfilled without losing focus of the main goal. The specific goals of this thesis are classified as follows:

Chapter 2 presents the general theoretical background and concepts. A very broad overview of the theoretical methods and computational tools used to achieve the specific objectives is provided.

In **Chapter 3** the ability of Ge doping to reduce CO poisoning is assessed. For this, we investigate Ge single atom doping on small-size Pt clusters in gas-phase. The main advantage of gas-phase studies is that they offer a simplified picture where it is easier to understand the role of the dopant on the interaction with CO, as the support and environment are absent. The rich conformational space of clusters makes mandatory the use of GM search algorithms to locate the energetically most relevant isomers. Bearing this in mind, the first step in our workflow always involves a GM search. Subsequently, the electronic structure is thoroughly characterized by advanced computational tools in order to discern the role of Ge on the Pt−CO bond. These results are additionally confirmed experimentally by mass spectrometry experiments.

In **Chapter 4**, based on the favourable results of the previous chapter, we carry out a systematic study of the size and composition effects on CO poisoning of PtGe clusters in gas-phase. All possible PtGe compositions are tested for clusters smaller than 10 atoms. A GM search is done followed by an analysis of the electronic structure. Besides, the catalytic activity on the H_2 dissociation is also tested to verify that Ge alloying does not have a detrimental effect. In this chapter crucial information is obtained about the energetic, structural and electronic properties of PtGe nanoalloys on which the following chapters are based.

In **Chapter 5** the catalytic activity of PtGe nanoalloys supported on MgO(100) is evaluated. For this goal, CO oxidation is chosen as a test reaction for the following reasons: it is one of the most simple reactions, but simultaneously is present as an intermediate step in many important reactions such as the WGSR, and Pt is known to suffer a strong CO poisoning that can hinder this reaction. The main task is to understand the role of Ge concentration on the catalytic performance, linking the electronic structure directly to the catalytic activity. The reaction pathways are characterized by atomistic simulations, in combination with microkinetic modeling to quantify CO poisoning in terms of macroscopic parameters such as reaction rates and surface coverages.

Chapter 6 is devoted to the study of 2D materials as novel supports with antisintering properties for PEMFCs. More concretely, the deposition of pure Pt and PtGe clusters is explored over a variety of cutting-edge 2D supports such as defective graphene, phosphorene, silicene, germanene, molybdenum disulphide (MoS_2) and samarium sulfoiodide (SmSI). The main objective is to estimate the impact of the MSI of each support on the cluster's sintering tendency, as well as on the HOR activity, and try to establish a direct structure-activity relationship. Namely, the MSI is tested as a lever to control the catalytic properties.

Last but not least, the main results and conclusions achieved in this thesis are summarized in **Chapter 7**. An outlook into possible lines of studies for future work in the short term, as well as the long term is also proposed.

Chapter 2

Theory and Methods

"Just as in a clock, the result of the complicated motion of innumerable wheels and pulleys is merely a slow and regular movement of the hands which show the time, so the result of all the complicated human activities of 160,000 Russians and French—all their passions, desires, remorse, humiliations, sufferings, outbursts of pride, fear, and enthusiasm—was only the loss of the battle of Austerlitz, the so-called battle of the three Emperors—that is to say, a slow movement of the hand on the dial of human history."

— Leo Tolstoy, *War and Peace*

2.1 Foundations of Quantum Chemistry

BY the end of the XIX*th* century the ground of the known physics became firmly established under the pillars of the classical laws of mechanics and electromagnetism. Most of the physical laws had already been discovered and virtually all phenomena of relevance at that time could be understood. Only few exceptions remained to which classical physics failed to find an explanation, but it was generally believed that they would be solved upon further refinement of the theory. However, the rise of further discrepancies started casting doubts about the completeness of classical physics. It became apparent that beneath lay a structural problem that required the reformulation of current physics. Unbeknownst to scientists, these failures served as a seed that would grow into a golden age of scientific productions where new ideas were constantly interchanged

that swept the former notions, to finally ripen in the development of a nascent field, *i.e.*, quantum mechanics.

The origins of quantum mechanics can be traced back to Planck's study of the emission spectrum of heated bodies.[233] He suggested that a black body can only emit light in certain amounts of energy quanta $h\nu$, where ν is the frequency and h Planck's constant; that is, energy is quantized. In 1905, Einstein extended this idea to explain the photoelectric effect,[234] emission of electrons from a metal by interaction with light, by postulating the particle-wave dual behaviour of light. Light itself is quantized in indivisible particle-like entities called photons, not the energy of the radiating atoms in the black body.

Besides, cathode rays experiments revealed that atoms are composed of positively charged heavy particles and negatively charged electrons. Rutherford proposed in 1911 an atomic model[235] in which electrons orbit around a positively charged nucleus at any arbitrary distance. However, as it is known from classical electrodynamics, an accelerating charged particle is continually emitting radiation, which means that the electrons are losing energy and will end up spiraling towards the nucleus. According to Rutherfords's model atoms should not exist! This problem was partly circumvented by Bohr in 1913.[236–238] In his new model of the hydrogen atom the orbits of the electrons are quantized in the so-called atomic energy levels. Transitions from one energy level to another can only occur by absorbing or emitting a photon whose energy corresponds to the energy difference between the two orbits. The discrete nature of the atomic emission spectra was naturally incorporated into the model. Nonetheless, it failed to correctly describe the electron motion since a classical motion was assumed. Several years later, de Broglie corrected the Bohr model by extending the wave-particle duality of Einstein to matter.[239] Now, electrons behave like stationary waves around the nucleus where only orbits with circumference equal to an integer number of the electron's wavelength are permitted. Now, what was left was the mathematical formulation of the quantum theory.

In 1925 Heisenberg, Born and Jordan developed the matricial formulation in order to explain the discrete energy transitions in the Bohr model.[240–242] Physical observables were represented by matrices and the set of possible values in a measurement were given by their eigenvalues. The non-commutativity of matrices also led

naturally to Heisenberg's uncertainty principle.[243] Simultaneously, following de Broglie's particle-wave duality, Schrödinger presented the wave mechanics formalism in 1926.[244–246] A quantum system was associated with a wavefunction whose time evolution is given by a differential equation, *i.e.*, the Schrödinger equation. Born gave a probabilistic interpretation[247] to the wavefunction which later evolved into the Copenhagen interpretation. Dirac reconciled the two approaches in 1930 by introducing the bra-ket notation and the concept of Hilbert spaces.[248] But the complete rigorous mathematical framework came by the hands of Neumann who reformulated quantum mechanics in terms of linear operators acting on Hilbert spaces in his 1932 classic *"Mathematische Grundlagen der Quantenmechanik"*.[249]

Until the beginning of the XX*th* century physics and chemistry remained two fields of science separated by clear boundaries and with little overlap. Although it was long since chemistry adopted the scientific method, they both differed significantly in their epistemology. This could be perhaps attributed to the generalized indifference on the utility of mathematics in chemistry. The reader should be cautious not to fall in a temporal bias by assuming that the connection between mathematics and natural sciences can be so easily established. In physics, it had already become routine work to describe complex real systems with simplified models, in which deep physical laws could be obtained using fairly simple mathematics, like the harmonic oscillator and point particle approximations. The structure of physics is more hierarchized; often, the simpler laws are a limit case of the more complex ones. This makes it easier to apply mathematical reasoning and build new hypotheses upon former ones. Hence, it followed naturally to reformulate physics in the language of mathematics and adopt a more rational (*a priori*) view.

In contrast, the systems of interest in chemistry show a much higher level of complexity. A fundamental understanding becomes more difficult as the complexity increases and a mathematical approach becomes more dubious and less practical. The macroscopic properties are a consequence of the interactions among microscopic particles. Thus, understanding of the macroscopic properties demands knowledge of the microscopic world. Since the necessary mathematical framework for such a task was not yet constructed, chemistry acquired a more pragmatic epistemology, leaving the question of the existence of atoms to ontology. Chemistry relied heavily

on empirical evidence and was regarded mainly as a descriptive science.[250] A mathematical description was lacking that could allow derive fundamental physical laws from empirical observations and gain predictive power.

Now it seems the right moment to introduce Wigner's reflections about mathematics and the laws of nature collected in his celebrated article by the title *"The Unreasonable Effectiveness of Mathematics in the Natural Sciences".*[251] The author remarks that there is a striking coincidence in the accuracy of mathematics as the language of nature. Mathematics puts in evidence that often the patterns of nature repeat themselves; many theories share the same mathematical structure, which points to the existence of some underlying universal principle. Some examples are Newton's law of gravitation and Coulomb's law of electrostatics. In addition, an abstract mathematical theory can make its way into natural sciences and find applications in totally unexpected places. It is often the case that the mathematical framework is developed first and then an application is found. Thus happened with quantum mechanics. Its first applications to atomic and molecular systems proved extremely accurate and the new theory presented itself as a unifying theory that could explain quantitatively all chemical phenomena, signaling the beginning of quantum chemistry. Undoubtedly, quantum chemistry made reconsider a mathematical reformulation of chemistry and brought profound epistemological changes to its foundations.

The direct application of the Schrödigner equation to chemical systems required the development of novel approximate methods. The first successful approach was made in 1927 by Heitler and London[252–258] with their valence bond theory (VBT) to solve the hydrogen molecule, which was based on the ideas introduced by Lewis.[259] In 1928, Hylleraas applied perturbation theory to solve the two-electron helium problem.[260] During these years, Hund[261–263] and Mulliken[264–267] presented an alternative approach to the VBT, the molecular orbital theory (MOT), which made use of the linear combination of atomic orbital (LCAO) method. In the following years the MOT was formalized and made more rigorous by Hartree,[268, 269] Fock,[270, 271] Roothaan,[272] Hall[273] and Löwdin,[274] and condensed into the so-called Hartree-Fock (HF) method. The HF method would later become the basis for a plethora of more accurate methods to solve multi-electronic problems.

If quantum chemistry ever reached the ears of chemists, it was thanks to the classic textbook of Pauling *"The Nature of the Chemical Bond and the Structure of Molecules and Crystals: An Introduction to Modern Structural Chemistry"* published in 1939,[275] which translated the mathematical formalism of quantum chemistry into a language more familiar to chemists. Here he introduced the concepts of resonance, orbital hybridization and electronegativity, which served as a basis for our current understanding of chemistry.

2.2 The Schrödinger Equation in Molecular Systems

The nature of the evolution of a quantum system depends on whether a measurement has been involved or not. The act of measurement is a probabilistic and non-unitary change which results from the interaction with an external classical apparatus. In the absence of a measurement however, an isolated quantum system evolves according to the time-dependent Schrödinger equation (TDSE) which is deterministic and unitary. The TDSE is a linear differential equation of first order in time and second order in space. In the most general form, the TDSE for a non-relativistic single particle is given by the following expression:

$$ih\frac{\partial}{\partial t}\Psi(\mathbf{r},t) = \hat{\mathcal{H}}\Psi(\mathbf{r},t) = \left[-\frac{h^2}{2m}\nabla^2 + \hat{V}(\mathbf{r},t)\right]\Psi(\mathbf{r},t) \qquad (2.1)$$

where $\hat{\mathcal{H}}$ denotes the Hamiltonian operator, $\Psi(\mathbf{r},t)$ the wavefunction, $\hat{V}(\mathbf{r},t)$ the potential energy operator, m the mass of the particle, i the imaginary unit and $\hbar$ the reduced Planck constant, respectively. The Hamiltonian is the sum of the kinetic and potential energy operators. All the possible interactions and their symmetries, either internal among the different particles or with external sources, are inserted into $\hat{V}(\mathbf{r},t)$. One of the differences with the classical equations of motion is that instead of the evolution of the particle position, the TSDE describes the evolution of an object called the wavefunction, Ψ. The probability of a particle being at a certain point in space is given by probability density

$$\rho(\mathbf{r},t) = \Psi(\mathbf{r},t)^*\Psi(\mathbf{r},t) = |\Psi(\mathbf{r},t)|^2 \qquad (2.2)$$

(* denotes complex conjugate) which is a locally conserved quantity, that is, it

satisfies the continuity equation

$$\frac{\partial}{\partial t}\rho(\mathbf{r},t) + \nabla \cdot j(\mathbf{r},t) = 0 \tag{2.3}$$

where $j(\mathbf{r},t)$ is the probability current (flux)

$$j(\mathbf{r},t) = \frac{h^2}{2im}\left[\Psi^*(\nabla\Psi) - \Psi(\nabla\Psi^*)\right]. \tag{2.4}$$

In principle, if we stick to the Copenhagen interpretation and set aside the possibility of hidden variables, all the information of the system is stored in the wavefunction. Here we do not attempt to start a discussion about what is and what is not the wavefunction. However, one cannot help but become disturbed that, due to the wavefunction collapse, this interpretation poses some serious concerns about the ontical meaning of the information stored in the wavefunction by itself prior to a measurement, and about whether an ontological relationship of any kind can be established between the wavefunction and the observer, besides the epistemic knowledge the observer gains through a measurement; it may lead us too quickly to a muddy metaphysical ground. For the sake of convenience, following the philosophy of quantum chemistry, we adopt a more instrumentalist view and explain the recipes to solve the multi-electronic problem.

The resolution of the Schrödinger equation for molecular systems, either in gas or condensed phase, amounts to the study of the interactions among a collection of nuclei and electrons. In chemistry, we are often interested in equilibrium properties in the absence of any external perturbation such as bond lengths, angles, dipole moments and polarizabilities. In these cases, one can ignore the time dependence and the TDSE simplifies to the time independent Schrödinger equation (TISE)

$$\hat{\mathcal{H}}\Psi_{tot}(\{\mathbf{r}_i\},\{\mathbf{R}_\alpha\}) = E_{tot}\Psi_{tot}(\{\mathbf{r}_i\},\{\mathbf{R}_\alpha\}) \tag{2.5}$$

where $\hat{\mathcal{H}}$ is the molecular Hamiltonian, Ψ_{tot} the many-body molecular wavefunction and E_{tot} the total energy. $\mathbf{R}_\alpha$ and $\mathbf{r}_i$ are the set of nuclear and electronic spatial coordinates. The solutions of the TISE are called stationary states because they do not change over time, up to a phase factor $\exp(-iEt/\hbar)$. As can be observed, Equation (2.5) has the form of a generalized eigenvalue problem. The energy observable is substituted with an hermitian operator, the Hamiltonian, that acts on

a stationary state (or energy eigenstates) to give its energy, which is an eigenvalue of the Hamiltonian.

The molecular Hamiltonian contains the kinetic energy of the nuclei and electrons and the coulombic interactions among them. For a system with M nuclei and N electrons it is defined in atomic units by

$$
\begin{aligned}
\hat{\mathcal{H}} &= \hat{T}_N + \hat{T}_e + \hat{V}_{NN} + \hat{V}_{ee} + \hat{V}_{eN} \\
&= -\frac{1}{2}\sum_{\alpha}\frac{1}{M_\alpha}\nabla_\alpha^2 - \frac{1}{2}\sum_i \nabla_i^2 + \sum_{\alpha>\beta}\frac{Z_\alpha Z_\beta}{|\mathbf{R}_\alpha - \mathbf{R}_\beta|} + \\
&\quad + \sum_{i>j}\frac{1}{|\mathbf{r}_i - \mathbf{r}_j|} - \sum_\alpha \sum_i \frac{Z_\alpha}{|\mathbf{r}_i - \mathbf{R}_\alpha|}
\end{aligned}
\tag{2.6}
$$

where $\hat{T}_N$ and $\hat{T}_e$ are the nuclear and electronic kinetic energy, and $\hat{V}_{NN}$ the nucleus-nucleus, $\hat{V}_{ee}$ electron-electron and $\hat{V}_{eN}$ electron-nucleus interactions. M_α and Z_α are the mass and atomic number of nucleus α, $|\mathbf{R}_\alpha - \mathbf{R}_\beta|$, $|\mathbf{r}_i - \mathbf{r}_j|$ and $|\mathbf{r}_i - \mathbf{R}_\alpha|$ are the euclidean distances between nuclei α and β, electrons i and j, and nucleus α and electron i, respectively.

In quantum chemistry we are usually interested in obtaining the total energy of the system. Thus the electronic structure problem reduces to the diagonalization of the molecular Hamiltonian.[276] Unfortunately, this is a formidable task even for the smallest molecules. The many-body nature of the problem makes its resolution intractable. Only a very few cases like the H_2^+ molecule have an exact solution. The use of approximate methods becomes mandatory.

2.3 Born-Oppenheimer Approximation

The Born-Oppenheimer (BO) approximation [277] lies at the core of quantum chemistry. It stems from the difference in mass between the nuclei and electrons. Since nuclei are much heavier than electrons, on the time-scale of electron motion the nuclei can be regarded as stationary objects, fixed at certain positions in space. The electrons can be considered to move in the potential created by the electrons and the fixed nuclei. Due to the difference in the time-scale of both motions, the BO approximation decouples the molecular TISE into a couple of equations: the electronic equation for the electron motion and nuclear equation for the nuclear

motion.

For the electron motion, the nuclear kinetic term $(\hat{T}_N)$ is neglected and the nucleus-nucleus repulsion $(\hat{V}_{NN})$ is taken for constant, as the nuclei are assumed to be fixed. With this, the electronic equation reduces to the following expression:

$$\hat{\mathcal{H}}_e \Psi_e(\{\mathbf{r}_i\}; \{\mathbf{R}_\alpha\}) = E_e(\{\mathbf{R}_\alpha\}) \Psi_e(\{\mathbf{r}_i\}; \{\mathbf{R}_\alpha\})$$

$$(\hat{T}_e + \hat{V}_{ee} + \hat{V}_{eN}) \Psi_e(\{\mathbf{r}_i\}; \{\mathbf{R}_\alpha\}) = E_e(\{\mathbf{R}_\alpha\}) \Psi_e(\{\mathbf{r}_i\}; \{\mathbf{R}_\alpha\}). \qquad (2.7)$$

The electronic wavefunction Ψ_e depends explicitly on the electronic coordinates but parametrically on the nuclear coordinates, as does the electronic energy (E_e). This means that for each nuclear configuration different Ψ_e and E_e are obtained. Still, the nucleus-nucleus repulsion $(\hat{V}_{NN})$ has to be added to E_e to obtain the total energy at a fixed nuclear arrangement. This energy is known as the potential energy surface (PES), $U(\{\mathbf{R}_\alpha\})$.

Likewise, the same assumption made for the electron motion can be reformulated to write down the nuclear equation. As the electrons move much faster than the nuclei, it is a reasonable approximation to replace the position of the electrons by their average values. Electrons are assumed to respond instantaneously to any change of the nuclear configuration. Or stated in another way, the nuclear kinetic energy is much smaller than the energy gaps between adiabatic electronic states and so, the electrons remain in a given state as the nuclei move. Consequently, the nuclei move in the mean field generated by the electrons; that is, the nuclei move along the PES which is computed from the electronic equation. Inserting $U(\{\mathbf{R}_\alpha\})$ as the potential on the nuclear equation gives

$$\hat{\mathcal{H}}_N \Psi_N(\{\mathbf{R}_\alpha\}) = E_{tot}(\{\mathbf{R}_\alpha\}) \Psi_N(\{\mathbf{R}_\alpha\})$$

$$(\hat{T}_N + U(\{\mathbf{R}_\alpha\})) \Psi_N(\{\mathbf{R}_\alpha\}) = E_{tot}(\{\mathbf{R}_\alpha\}) \Psi_N(\{\mathbf{R}_\alpha\}). \qquad (2.8)$$

By solving equation (2.8), knowledge about the rotational, vibrational and translational motion of molecules can be obtained.

The concept of PES is of central importance in chemistry. The PES is a $3M$ dimensional surface with a very complex energy landscape that contains information about the stability and reactivity of molecules. Its topology describes the different

chemical species that can exist and their connectivity among them. The possible chemical structures are given by stationary points: local minima (no forces) represent stable structures like conformers and isomers, while first order saddle points (one imaginary frequency) represent transition states (TSs). A chemical reaction is nothing else than a trajectory along the PES that connects two local minima (initial and final states) and crosses an energy barrier through the TS. Since two points can in principle be connected by a countless number of paths, a chemical reaction can have different reaction mechanisms. To make an analogy, one can think of the PES as a landscape portrayed with valleys and mountains.

Regarding the validity of the BO approximation, it should be mentioned that it can only be trusted when the electronic energy levels are well separated between each other throughout the whole PES.[276] Nonetheless, it can occur that the ground state and a higher energy excited state come so close in some region of the PES that they cross each other, giving rise to a conical intersection. A well-known example is the Jahn-Teller distortion, where a geometrical distortion changes the stability of the electronic states.

In summary, the BO approximation decouples the electronic and nuclear dynamics and reduces the original electronic structure problem to a system of interacting electrons under the influence of an external potential due to the nuclei. Within this approximation, the problem reduces to finding the energy for a given atomic configuration. Unfortunately, even after separating the nuclear motion, the electronic Schrödinger equation cannot be solved exactly. The many-body interactions of the electrons are still being treated explicitly through the electron-electron potential ($\hat{V}_{ee}$). We are still facing a many-body problem, which requires further approximations.

The Hartree-Fock (HF) method is the simplest approach to solve the electronic equation. This method breaks down an equation of N interacting electrons into N independent one-electron equations, where each electron is feeling an average potential due the rest of the electrons. In addition, the electronic wavefunction is approximated as an antisymmetrized product of one-electron wavefunctions (orbitals), *i.e.*, a Slater determinant.[276] The permutation symmetry of the Slater determinants makes sure that the Pauli exclusion principle is met. Such symmetry

requirement give rise to the Fermi correlation, also known as exchange correlation. Fermi correlation refers to the fact that the motion of two electrons with parallel spin is not independent, it is correlated. Electrons with parallel spin cannot occupy simultaneously the same position in space; they tend to avoid each other and the probability of finding two electrons nearby decreases. Each electron is surrounded by a Fermi hole.

Nevertheless, the motion of electrons with opposite spin is left uncorrelated. This comes from the fact that in the HF approach the electrostatic repulsions between electrons ($\hat{V}_{ee}$) are not treated explicitly, but only as an average field. As a result, electrons move unaware of the position of the others, and the probability of finding two electrons close together is overestimated. This type of electron correlation is known as Coulomb correlation. It is a dynamical phenomenon that arises from the electron movement; electrons move trying to minimize the electronic repulsion. For this, a Coulomb hole (cusp) is introduced at $\mathbf{r}_{ij} = 0$ to describe the correct behaviour at close distances and avoid singularities in the electronic repulsion. Coulomb correlation happens for any pair of electrons regardless of spin; however, for parallel spin electrons the effect is less important since the Fermi correlation already keeps them apart, while for opposite spin electrons there is nothing that prevents them from getting too close. From this, it is evident that a single Slater determinant cannot capture Coulomb correlation and thus it is considered an uncorrelated wavefunction.

In order to address the deficiencies of the HF method regarding electron correlation, a great number of wavefunction (post-HF) methods have been developed, which over the years have molded the field of quantum chemistry. Among the most popular ones can be found the Møller-Plesset perturbation theory (MPPT) [278] (*e.g.*, MP2), configuration interaction (CI) [279–281], coupled cluster (CC) [282–286] and multi-configurational self-consistent field (MCSCF) methods.[287–294] It is beyond the scope of this thesis to give a full account of these methods, so the interested reader can consult the pertinent references. However, it should be mentioned, that although these methods are able to capture most of the correlation and provide very accurate energies, their computational cost is extremely expensive, and thus are only applicable for very small molecules. The size of the many-body wavefunction,

or paraphrasing the information stored therein, increases exponentially with the number of electrons to the point that it becomes a completely intractable object.

As a way to bypass the size-scaling problem of the many-body wavefunction in post-HF methods, alternative approaches have been devised that recover the correlation energy without the need of employing a wavefunction. density functional theory (DFT) is perhaps the most extended example. The art of DFT lies in that it reformulates an N-particle problem into a system of N non-interacting one-particle problems by substituting the $3N$-dimensional many-body wavefunction (omitting spin) with a single 3 dimensional scalar function, the electron density $\rho(\mathbf{r})$, from which in principle, all the information of the wavefunction can be obtained. In this way, DFT significantly reduces the computational cost and allows to solve the electronic equation for systems of hundreds of atoms including (to some extent) the many-body effects. Mainly, all the work presented in this thesis has been carried out within the DFT framework. In the following section we explain this method in greater detail.

2.4 Density Functional Theory

Density Functional Theory (DFT) is a ground state theory that presents as an alternative approach to wavefunction methods. The many-electron wavefunction contains much more information than what is necessary to obtain properties of interest such as energies, dipole moments and polarizabilities; there is an excess of information. Thus, it may seem a waste of resources to compute the wavefunction to calculate only such properties. This issue becomes more severe as the size of the system increases because the complexity of the wavefunction grows exponentially. DFT replaces the $3N$-dimensional wavefunction with a 3-dimensional scalar function, the ground state density $\rho_o(\mathbf{r})$. The fundamental tenet of DFT is that any property of the many-electron system can be obtained from the ground state density; *i.e.*, it is a functional of the ground state density. DFT has made the many-electron problem tractable for a vast majority of systems up to hundreds of atoms. Not only is it used to study molecules, but also extended systems like bulk or surfaces. DFT provided a means to make accurate predictions of condensed matter at the atomic

level. In short, it can be said that it has brought quantum chemistry to the realm of the doable. Currently, DFT has become the most popular choice as it offers similar computational cost to HF, but at the same time incorporates correlation effects, which if they are known, yields the exact energy.

2.4.1 The Hohenberg-Kohn Theorems

The origin of modern DFT dates back to the pioneering work of Hohenberg and Kohn in 1964.[295] Their approach was to reformulate DFT as an exact theory of many-body systems and provided the basic existence proofs that later became known as the Hohenberg-Kohn (HK) theorems. Before going in depth with the HK theorems, it is convenient to define the density. The ground state density expresses the single-particle probability density of the electronic ground state. Given a ground state wavefunction Ψ_0, which is a solution of the TISE, it is calculated as the expectation value of the electron density operator ($\hat{\rho}(\mathbf{r}) = \sum_{i=1}^{N} \delta(\mathbf{r} - \mathbf{r}_i)$)

$$\begin{aligned} \rho_0(\mathbf{r}) &= \langle \Psi_0 | \hat{\rho}(\mathbf{r}) | \Psi_0 \rangle \\ &= N \int d\mathbf{r}_2 \cdots \int d\mathbf{r}_N \, |\Psi_0(\mathbf{r}, \mathbf{r}_2, \ldots, r_N)|^2. \end{aligned} \quad (2.9)$$

From this definition, it follows that the next conditions are fulfilled:

$$N = \int d\mathbf{r} \, \rho_0(\mathbf{r}); \qquad \rho_0(\mathbf{r}) \geq 0. \quad (2.10)$$

Integrating the ground state density gives the total number of electrons.

With this, the KH theorems can be summarized as follows:

Theorem 2.4.1 (First HK Theorem). *For any system of N electrons interacting in an external potential $V_{ext}(\mathbf{r})$, the external potential $V_{ext}(\mathbf{r})$ is (to within a constant) uniquely determined by the ground state density $\rho_0(\mathbf{r})$. In other words, the external potential $V_{ext}(\mathbf{r})$ is a unique functional of the ground state density $\rho_0(\mathbf{r})$.*

This means that there is a one-to-one map between the ground state density and external potential. Moreover, one can go one step further and make the following statement. Since the external potential $V_{ext}(\mathbf{r})$ fixes the Hamiltonian $\hat{\mathcal{H}}$ (except for a constant energy shift), the Hamiltonian is also a functional of the ground state density $\rho_0(\mathbf{r})$. Via the Schrödinger equation it then follows that the wavefunctions

for all electronic states (ground and excited) are also unique functionals of the ground state density $\rho_0(\mathbf{r})$. Therefore, all properties of the system can be derived from the ground state density $\rho_0(\mathbf{r})$. To put it another way, knowing the ground state density $\rho_0(\mathbf{r})$ is equivalent to knowing the wavefunction for the ground state and all excited states as well.

Despite the appealing appearance of the theorem, actually not much progress has been made. According to the first theorem, we need the external potential to calculate the ground state density, so we are still left with the problem of solving the many-electron TISE. Even more, it does not give any recipe to know if a given density is the actual ground state density, and if so, how can be established a mapping between the ground state wavefunction and density. This mapping may be too complex to be of practical use.

Theorem 2.4.2 (Second HK Theorem). *For any external potential $V_{ext}(\mathbf{r})$ we can define a universal functional for the energy $E[\rho(\mathbf{r})]$ in terms of ground state density $\rho(\mathbf{r})$. The ground state energy E_0 is the minimum of this functional and the density that minimizes this functional is the exact ground state density $\rho_0(\mathbf{r})$.*

This theorem ensures the existence of a variational principle, and hence, provides a means to obtain the energy of the ground state from the ground state density. It is also the reason why DFT is a ground state theory. Once the ground state density is found, the ground state energy is uniquely determined. The energy functional can be written as

$$\begin{aligned} E_{HK}[\rho] &= \langle \Psi_0[\rho] | \hat{\mathcal{H}} | \Psi_0[\rho] \rangle \\ &= T[\rho] + E_{ext}[\rho] + E_{ee}[\rho] \\ &= T[\rho] + \int d\mathbf{r}\, V_{ext}(\mathbf{r})\rho(\mathbf{r}) + E_{ee}[\rho] \end{aligned} \tag{2.11}$$

where $T[\rho]$, $E_{ext}[\rho]$ and $E_{ee}[\rho]$ are the kinetic energy, external energy and electron-electron repulsion functionals. Note that for the molecular Hamiltonian, the external energy $E_{ext}[\rho]$ corresponds to the electron-nucleus attraction E_{eN}. All the internal energies, *i.e.*, kinetic energy and electron-electron repulsion, can be regrouped into the Hohenberg and Kohn functional (F_{HK})

$$F_{HK}[\rho] = T[\rho] + E_{ee}[\rho] \tag{2.12}$$

which is universal as it only depends on the density and not on the external potential.

The HK approach requires that the ground state density $\rho(\mathbf{r})$ be V-representable. An V-representable density is a density that is generated by some external potential $V_{ext}(\mathbf{r})$; that is, it is a density built from wavefunctions which are a solution of the Schrödinger equation. When applying the variational principle, functional derivatives of the type $\delta E_{HK}/\delta\rho(\mathbf{r})$ have to be done. The existence of such derivatives requires that $E[\rho]$ be defined on a sufficiently dense set of densities. So far, $E[\rho]$ has only been defined for the ground state density obtained from the Schrödinger equation. However, the issue is that we do not know how to find the corresponding external potential $V_{ext}(\mathbf{r})$, if it exists, for any other density. We do not know how to identify these densities. The domain of V-representable densities is still unknown. This is referred to as the V-representability problem.[296]

The V-representability problem is solved by the Levy-Lieb (LL) constrained search.[297–299] This approach relaxes the criteria for the admissible densities (it is no longer needed the V-representability) and provides a procedure to build the exact ground state density. Levy and Lieb proposed a two step procedure for the minimization of the energy given by

$$E_0[\rho] = \min_{\rho}\{F_{LL}[\rho] + \int d\mathbf{r}\ V_{ext}(\mathbf{r})\rho(\mathbf{r})\} \tag{2.13}$$

$$F_{LL}[\rho] = \min_{\Psi \to \rho(\mathbf{r})} \langle\Psi|\hat{T} + \hat{V}_{ee}|\Psi\rangle. \tag{2.14}$$

First, we search over the class of N-electron wavefunctions that have the same density (constrained minimization), and in a second step we search for the density that yields the lowest energy, $i.e.$, the ground state energy E_0. Note that all wavefunctions with the same density also have the same expectation value for the external potential $V_{ext}(\mathbf{r})$. Thus, it suffices to minimize the Levy-Lieb functional $F_{LL}[\rho]$ to yield a unique ground state energy. $F_{LL}[\rho]$ is universal as it does not depend on any external potential.

In addition, the LL approach makes another deviation from the HK theorems.

Instead of searching over the set of V-representable densities, which we do not know how to define it, the search is extended to the larger set of N-representable densities. The inner minimization (2.14) is restricted over all wavefunctions that lead to a particular density, but no conditions whatsoever are imposed on these wavefunction being solutions of the Schrödiger equation with a given external potential $V_{ext}(\mathbf{r})$. They can be any functions as long as they yield a density that integrates to the total number of electrons N, which is a condition imposed by the outer minimization (2.13). Such densities are known as N-representable densities and their exact definition is encompassed in equations (2.9) and (2.10) (substitute now ψ by any function ϕ). N-representability imposes much weaker conditions and more importantly, it is already know which conditions have to be fulfilled, *i.e*, precisely those given by eq. (2.9) and (2.10). Unfortunately, the LL procedure is not very practical for the following reasons. First, it involves a search over an infinite number of N-electron wavefunctions. Second, just as in the HK approach, we are still facing a many-body problem. The LL functional $F_{LL}[\rho]$ is defined in terms of N-electron wavefunctions, making it intractable.

Summing up, at this point we realize that the HK theorems are mere proofs of existence. No prescription is given about how to find the explicit form of the HK functional $F_{KH}[\rho]$ and solve the many-body problem. Precisely, the functional dependence of the kinetic energy $T[\rho]$ with the ground state density $\rho(\mathbf{r})$ is unknown. There is no known way to derive the kinetic energy from the ground state density $\rho(\mathbf{r})$. It has to be reformulated in terms of the N-electron wavefunctions. Nonetheless, expressing the kinetic energy with wavefunctions introduces discontinuities in the functional derivative of the energy functional $\delta E[\rho]/\delta\rho(\mathbf{r})$ at non-integer electron numbers; it varies in a non-analytic manner as a function of the number of electrons.[296] This issue was solved by Kohn and Sham. The key of their success was to replace the N-electron problem by an auxiliary non-interacting system where the kinetic energy can be evaluated in terms of one-electron orbitals. Were it not for the insight provided by Kohn and Sham, DFT would become a mere curiosity; it was thanks to them that DFT actually became a practical tool for rigorous calculations.

2.4.2 Kohn-Sham Equations

Kohn and Sham laid the basis for a methodology to evaluate the energy functional systematically and solve the electronic structure problem in their landmark work published in 1965.[300] Their approach consists on substituting the original N-electron problem with an auxiliary non-interacting system; that is, establishing a mapping between the N-electron system and an auxiliary independent-electron system. In order to make this connection the Kohn-Sham (KS) *ansatz* rests on two assumptions:

- The ground state density $\rho(\mathbf{r})$ of the original many-body system can be represented exactly by the ground state density of an auxiliary non-interacting system. Such densities are called non-interacting V-representable densities.

- The Hamiltonian of the auxiliary system is composed of the sum of the kinetic energy of the electrons and some effective potential $V_{\text{eff}}(\mathbf{r})$ which absorbs all the many-body effects. This effective potential $V_{\text{eff}}(\mathbf{r})$ is chosen in such a way that it yields the ground state density $\rho(\mathbf{r})$ of the original system.

The KS approach recasts the original problem of interacting electrons into a problem of non-interacting electrons with an interacting density. This leads to independent-particle equations which are much easier to solve. In this way, one can use single-particle (HF) machinery to compute all the problematic terms in the HK functional $E_{HK}[\rho]$. The kinetic energy and the density are readily determined in terms of a simple set of single-electron orbitals (spin orbitals considering spin).

The ground state wavefunction of the fictitious non-interacting system is given by a single Slater determinant

$$\Psi_{KS}(\mathbf{r}_1, \mathbf{r}_2, \ldots, \mathbf{r}_N) = \frac{1}{\sqrt{N!}} \begin{vmatrix} \psi_1(\mathbf{r}_1) & \psi_2(\mathbf{r}_1) & \ldots & \psi_N(\mathbf{r}_1) \\ \psi_1(\mathbf{r}_2) & \psi_2(\mathbf{r}_2) & \ldots & \psi_N(\mathbf{r}_2) \\ \vdots & \vdots & \ddots & \vdots \\ \psi_1(\mathbf{r}_N) & \psi_2(\mathbf{r}_N) & \ldots & \psi_N(\mathbf{r}_N) \end{vmatrix} \tag{2.15}$$

where ψ_i are one-electron orbitals, also known as Kohn-Sham (KS) orbitals. It is important to note that the ground state of the fictitious system Ψ_{KS} does not represent the exact ground state of the interacting system Ψ_0. The mapping only

establishes that the ground state densities of both systems are equal. The ground
state density reduces to a straightforward sum of the squares of the energetically
lowest N KS eigenstates

$$\rho(\mathbf{r}) = \sum_{i=1}^{N} |\psi_i(\mathbf{r})|^2. \tag{2.16}$$

Comparing Equation (2.16) with Equation (2.9), it can easily be realized to what
extent the calculation of the ground state density has been simplified. This density
is exact, and only one-electron orbitals are needed, completely avoiding the use of
the many-body wavefunction. The independent-particle kinetic energy T_s is directly
obtained by averaging over the KS orbitals,

$$T_s[\rho] = -\frac{1}{2} \sum_{i=1}^{N} \langle \psi_i | \nabla^2 | \psi_i \rangle. \tag{2.17}$$

Note that the kinetic energy is not an explicit functional of the density, it is
treated instead in terms of the KS orbitals. Another necessary ingredient is the
classical Coulomb self-interaction energy (Hartree energy) of the electron density

$$E_{\text{Hartree}}[\rho] = \frac{1}{2} \int d\mathbf{r} d\mathbf{r}' \frac{\rho(\mathbf{r})\rho(\mathbf{r}')}{|\mathbf{r} - \mathbf{r}'|} \tag{2.18}$$

which encapsulates the interaction of the density with itself.

The trick of the KS approach is to rewrite the HK functional $E_{HK}[\rho]$ by playing
with the addition and subtraction of the terms introduced for the auxiliary system
in the following way

$$E_{KS}[\rho] = E_{KS}[\rho] + T_s[\rho] - T_s[\rho] + E_{\text{Hartree}}[\rho] - E_{\text{Hartree}}[\rho]. \tag{2.19}$$

After some clever rearrangement we arrive at the well-known KS energy functional

$$E_{KS}[\rho] = T_s[\rho] + \int d\mathbf{r}\, V_{ext}(\mathbf{r})\rho(\mathbf{r}) + E_{\text{Hartree}}[\rho] + E_{xc}[\rho] \tag{2.20}$$

where $E_{xc}[\rho]$ is the exchange-correlation energy defined as

$$E_{xc}[\rho] = (T[\rho] - T_s[\rho]) + (E_{ee}[\rho] - E_{\text{Hartree}}[\rho]) \tag{2.21}$$

As can be observed, all the many-body effects are absorbed into this expression. It
contains the residual contributions of the kinetic and the non-classical electrostatic

interaction for approximating the fully-interacting many-body system as a system of independent-particles.

The decomposition of the KS functional $E_{KS}[\rho]$ (Equation (2.20)) isolates exactly those contributions to the ground state energy which can be treated rigorously, *i.e.*, the Hartree energy $E_{\text{Hartree}}[\rho]$, external energy $E_{ext}[\rho]$ and independent-particle kinetic energy $T_s[\rho]$. The functional dependence of the first two terms is known, and as the density is also known, their evaluation is straightforward. $T_s[\rho]$ can also be easily computed in terms of one-electron orbitals. Besides, $E_{\text{Hartree}}[\rho]$, $E_{ext}[\rho]$ and $E_{KS}[\rho]$ are universal functionals by virtue of the HK theorems. $T_s[\rho]$ is also universal because the HK theorems also hold for the fictitious system, although it depends on the density implicitly. Since all the terms in the right-hand side of Equation (2.21) are universal, it follows that the exchange correlation functional $E_{xc}[\rho]$ is also universal. Thus, the same $E_{xc}[\rho]$ can be applied for any system under an external potential $V_{ext}(\mathbf{r})$ governed by Coulomb interactions.

The variational minimization of the KS energy functional $E_{KS}[\rho]$ (Equation (2.20)) leads to a set of N single-particle Schrödinger-like equations for the auxiliary system, better known as the Kohn-Sham equations

$$(\hat{\mathcal{H}}_{KS} - \epsilon_i)\psi_i(\mathbf{r}) = 0 \tag{2.22}$$

where ϵ_i are the KS eigenvalues and HKS the KS Hamiltonian defined as

$$\hat{\mathcal{H}}_{KS} = -\frac{1}{2}\nabla^2 + V_{\text{eff}}(\mathbf{r}) \tag{2.23}$$

with the effective potential

$$\begin{aligned}
V_{\text{eff}}(\mathbf{r}) &= \frac{\delta E_{KS}[\rho]}{\delta\rho(\mathbf{r})} \\
&= V_{ext}(\mathbf{r}) + \frac{\delta E_{\text{Hartree}}[\rho]}{\delta\rho(\mathbf{r})} + \frac{\delta E_{xc}[\rho]}{\delta\rho(\mathbf{r})} \\
&= V_{ext}(\mathbf{r}) + V_{\text{Hartree}}(\mathbf{r}) + V_{xc}(\mathbf{r}).
\end{aligned} \tag{2.24}$$

Equation (2.24) reveals that the unknown effective potential $V_{\text{eff}}(\mathbf{r})$ is also a functional itself, which makes the KS equations (Equation (2.22)) non-linear. The KS equations are solved self-consistently in the spirit of the HF equations. One starts with an *ansatz* for the KS orbitals and builds the initial density (Equation (2.16)).

This density is then used to calculate the effective potential (Equation (2.24)) which in turn defines the KS Hamiltonian (Equation (2.23)). The KS equations (Equation (2.22)) are solved, obtaining a new set of KS orbitals which restarts the whole process. This process is repeated iteratively until convergence is achieved.

Unlike the HF approach, the KS equations are in principle exact. No approximation whatsoever has been made so far. So if the exchange-correlation functional $E_{xc}[\rho]$ is known, it would be possible to obtain the exact ground state energy for the interacting system. Unfortunately, no explicit analytic expression exists for this term except for the uniform electron gas; approximations have to be made.

It should be remarked that the KS orbitals and their associated energy eigenvalues have no physical significance as they belong to a fictitious reference system. The very reason of their existence is that they serve to compute the exact ground state density. There is only one exception: the energy of the highest lying occupied KS orbital (HOMO) of a N-electron system equals the negative of the ionization energy, $-I$:

$$\epsilon_N(N) = E(N) - E(N-1) = -I(N) \tag{2.25}$$

where $E(N)$ and $E(N-1)$ are the total ground state energies of N and $N-1$ electron systems, respectively.[301] Although again, such a statement only holds for the exact exchange-correlation functional $E_{xc}[\rho]$. The rest of the eigenvalues have no relation with the real system and thus, do not yield the correct excitation energies. At any rate, the best solution may be to take a pragmatic approach. Within the KS theory, they are legitimate tools from which valuable information about physical quantities can be extracted.

2.4.3 Approximations to Exchange-Correlation Energy

As stated previously, the exact form of the exchange-correlation functional $E_{xc}[\rho]$ is not known. Notwithstanding, the genius of the KS method is that by explicitly separating the independent-particle kinetic energy and the long-range Hartree terms, the remaining contribution from $E_{xc}[\rho]$ can be reasonably approximated as a local or semi-local functional[296, 301]

$$E_{xc}[\rho] = \int d\mathbf{r} \; \rho(\mathbf{r}) \; \epsilon_{xc}([\rho], \mathbf{r}) \tag{2.26}$$

where $\epsilon_{xc}([\rho], \mathbf{r})$ is the energy per electron that depends solely on the density $\rho(\mathbf{r})$ in some neighbourhood of $\mathbf{r}$. Expression (2.26) is the basis for all the approximations collectively known as the density functional approximations (DFAs). Hence, the art of DFT consists of developing accurate expressions for $E_{xc}[\rho]$ that can correctly capture all quantum effects. In this section, the most common DFAs are presented.

2.4.3.1 Local Density Approximation (LDA)

The local density approximation (LDA) is the simplest functional as well as the starting point for the more advanced functionals. Herein, the density of the real system is treated locally as that of an homogeneous electron gas (HEG), also known as the Jellium model. The HEG is a model of interacting electrons where the nuclei are assumed as a uniform positive charge background; hence, the density is constant. In the case of a slowly varying density the exchange-correlation energy can be simplified to

$$E_{xc}^{\text{LDA}}[\rho] = \int d\mathbf{r} \; \rho(\mathbf{r}) \; \epsilon_{xc}^{\text{Hom}}([\rho]) \tag{2.27}$$

where $\epsilon_{xc}^{\text{Hom}}([\rho])$ is the exchange-correlation energy density of the HEG with density $\rho(\mathbf{r})$. In general, E_{xc}^{LDA} can be decomposed into separate contributions accounting for exchange and correlation

$$E_{xc}^{\text{LDA}}[\rho] = E_x^{\text{LDA}}[\rho] + E_c^{\text{LDA}}[\rho]. \tag{2.28}$$

The most popular approach is probably the one presented by Vosko, Wilk and Nusair (VWN),[302] while the most recent and probably also most accurate one has been given by Perdew and Wang (PW92).[303] The LDA can also be generalized to open-shell systems under the local spin density approximation (LSDA) framework, where $\rho(\mathbf{r})$ is replaced by $\rho_\alpha(\mathbf{r})$ and $\rho_\beta(\mathbf{r})$ for electrons with different spins.

Accordingly, the LDA is considered a good approximation for solids close to a HEG like simple metals (*e.g.*, bulk sodium), whereas for inhomogeneous systems like molecules, where the density varies rapidly, its performance is considerably worse. This is related to the fact that the unphysical Hartree self-interaction is

not exactly canceled by the local approximation to the exchange energy $E_x^{\text{LDA}}[\rho]$; there remains a residual energy known as the self-interaction error (SIE). Despite these evident limitations, LDA provides surprisingly good results for equilibrium geometries, harmonic frequencies and dipole moments. However, LDA does not provide accurate enough energies and is considered inadequate for the proper description of molecules.

2.4.3.2 Generalized Gradient Approximation (GGA)

In order to account for the non-homogeneity of the real density, the first natural step is to expand the LDA functional as a Taylor series in powers of the density gradients, resulting in the gradient expansion approximation (GEA). Unfortunately, the GEA does not show any systematic improvement over the LDA, the reason being that the low-order expansion violates many important properties of LDA. This issue was circumvented by the development of the generalized gradient approximation (GGA) functionals. Instead of making an order-by-order expansion as in the GEA, each term in the series is constructed by an explicit mathematical expression, in such a way as to preserve as many properties as possible. As there is no unique prescription, a plethora of GGA functionals have been published over the years, both derived from first principles and parametrized with empirical data. Their general form is given by the following expression

$$E_{xc}^{\text{GGA}}[\rho] = \int d\mathbf{r}\ \rho(\mathbf{r})\ \epsilon_{xc}^{\text{GGA}}([\rho, \nabla\rho]). \tag{2.29}$$

The most important characteristic of GGA functionals is that they correct the overestimation in the LDA binding energies. Nonetheless, the bond lengths and vibrational modes are not considerably improved, and as with the LDA, the band gap of semiconductors is significantly underestimated. Chemical processes are governed by energy differences, not absolute energies. Although GGA functionals show accurate absolute energies, the SIE may become of similar magnitude than the energy difference, resulting in a big error percentage. As a result, GGA may not be precise enough to reach the so-called chemical accuracy ($1 kcal/mol$) in the calculation of ionization potentials, cohesive energies, reaction barriers, *etc.*. The improvement of GGA over LDA is not as significant for many cases. In any case,

GGA represents the minimum allowed accuracy for quantitative calculations. It can be said that it has become the *de facto* standard approximation in quantum chemistry.

2.4.3.3 Meta-Generalized Gradient Approximation (meta-GGA)

In addition to the density gradient, the meta-generalized gradient approximation (meta-GGA) incorporates the laplacian of the density and/or the KS kinetic energy density $\tau(\mathbf{r})$, *i.e.*, second order corrections.

$$E_{xc}^{\mathrm{mGGA}}[\rho] = \int d\mathbf{r} \, \rho(\mathbf{r}) \, \epsilon_{xc}^{\mathrm{mGGA}}([\rho, \nabla\rho, \nabla^2\rho, \tau]). \tag{2.30}$$

The SIE is partially corrected, but the price to pay is an increment in the computational cost; the numerical evaluation of the laplacians becomes much more demanding than the gradients.

2.4.3.4 Hybrid functionals

The previously discussed DFAs fail in the description of the exchange energy; they cannot completely cancel the SIE. Hybrid functionals arose as a response to address this issue. Becke's idea[304] was to mix the DFAs with a fraction of the non-local HF exchange, which is calculated exactly in the HF formalism. Such mixing is formally justified by an adiabatic connection[305] between the non-interacting (HF) system and the fully coupled system, approximated by a LDA or GGA functional. Generally, the constraints on the coupling strength can be relaxed, and the weights of the exact exchange and DFA exchange and correlation are controlled with a set of adjustable parameters obtained by fitting either *ab initio* or experimental thermochemical data. The expression for a 2-parameter hybrid functional reads as follows

$$E_{xc}^{\mathrm{Hyb}}[\rho] = c_0 E_x^{\mathrm{HF}}[\rho] + c_1 E_{xc}^{\mathrm{DFA}}[\rho] \tag{2.31}$$

where DFA denotes either a LDA or GGA functional. In principle, hybrid functionals can include contributions from different LDA and GGA functionals simultaneously. Nowadays, the most popular one is the B3LYP[302, 306–308] functional which contains 3 parameters:

$$E_{xc}^{\text{B3LYP}} = (1 - a_0)E_x^{\text{LDA}} + a_0 E_x^{\text{HF}} + a_x E_x^{\text{B88}} + a_c E_c^{\text{LYP}} + (1 - a_c)E_c^{\text{VWN}} \quad (2.32)$$

with $a_0 = 0.20$, $a_x = 0.72$ and $a_c = 0.81$. In general lines, as far as energetics is concerned, hybrid functionals outperform most of the LDA and GGA functionals. The accuracy of thermochemical properties and band gap calculation is also substantially improved. Besides, one can make further refinements to the hybrid functionals by adding meta-GGA functionals (meta-GGA hybrids) or non-local electron correlation from MP2 (double hybrids).

As a final remark, it should be borne in mind the fact that using an approximate $E_{xc}[\rho]$ means that we are considering an approximate Hamiltonian as well, which will yield approximate energies. This violates the variational theorem and energies below the exact energy can be obtained. Consequently, the evaluation of the performance of the different functionals becomes very arduous. Improving the quality of a functional does not necessarily mean that the energy is closer to the exact value. For some applications GGA functionals may perform better than Hybrids due to error cancellation effects. There exists no systematic way to improve the energy by applying more and more sophistication, so the results must be accepted as they stand. The only way to determine the usefulness of a functional is to benchmark its performance with respect to a suitable set of reference data. However, one may be tempted to sin from an excessive parameter fitting in the design of new functionals, as there is an uncountable amount of molecular data available. The data sets can be continually fed with new information about this and that type of molecule to extend *ad hoc* the range of performance of the functionals. A heavily parametrized method is devoid of any physical meaning. Unfortunately, such an approach departs from the spirit of *ab initio* methods.

2.5 Condensed Matter: Crystalline Solids

Atoms and molecules are hardly ever found isolated in nature; rather, they tend to group together and "condensed" into macroscopic entities, *i.e.*, condensed matter. Condensed matter is made of an Avogadro's number of atoms, which to practical purposes can be treated as infinite. The whole structure of the condensed matter is

held together by electrostatic interactions occurring among the electrons and nuclei. Their macroscopic properties are a consequence of these microscopic interactions, which often emerge in unexpected ways. There are a plethora of different condensed phases, but in this work we will only focus on crystalline solids. Crystalline solids, or simply crystals, form an ordered phase where ions are arranged in a periodic array repeated in space *ad infinitum*. They comprise the vast majority of solids, including metals. Their main characteristic is the possession of translational symmetry. However, this symmetry is not always in the eyes of the beholder. What the naked eye regards as a disordered material, may indeed hide in its interior a highly regular microscopic structure. A snowflake has no more symmetry than a piece of rusted iron.

2.5.1 Crystal Structure: Direct and Reciprocal Lattice

The crystal structure is completely specified by two components: the Bravais lattice and basis.[296, 309] The Bravais lattice is an infinite array of points which is generated by a set of discrete translation operations of the form (in three dimensions)

$$\mathbf{T}(\mathbf{n}) \equiv \mathbf{T}(n_1, n_2, n_3) = n_1 \mathbf{a}_1 + n_2 \mathbf{a}_2 + n_3 \mathbf{a}_3 \qquad (2.33)$$

where n_i are any integers and $\mathbf{a}_i$ are the primitive lattice vectors. All points in the Bravais lattice are equivalent as they are connected by translation vectors. This means that the Bravais lattice appears exactly the same in a given direction from all the lattice points. The basis describes the position and type of motif within the primitive cell (*vide infra*). This motif may consist of atoms, molecules or polymers. The basis is repeated along the Bravais lattice by the primitive vectors; that is, the periodic images of the basis are located at the lattice points of the Bravais lattice.

In three dimensions there are 14 different Bravais lattices. The Bravais lattices differ in their translational symmetry. However, when the basis is added, the crystal structure adopts a point group symmetry. The crystal structure is invariant to further nontranslational symmetry operations such as reflection, rotation, inversion, glide planes and screw axis. Combining the 14 Bravais lattices with the 32 point groups gives rise to 230 space groups, which are sufficient to classify all known crystal structures.

A unit cell is a volume of space that fills all space when translated through all vectors of the Bravais lattice. A primitive cell is a type of unit cell that has minimum volume. This condition is achieved if the unit cell has i) a single lattice point and ii) a single formula unit of the basis. With this definition, it is evident that the choice of primitive cell is not unique. As there is an infinite number of possible primitive vectors, so is the number of primitive cells. It is possible to construct infinitely many primitive cells of different shapes but all having the same minimal volume. Nonetheless, there is one choice which distinguishes among the rest: it is that of the Wigner-Seitz (WS) cell. The WS cell around a lattice point is defined as the locus of points that are closer to that lattice point than to any of the other lattice points. It is constructed in the following way: first, a given lattice point is connected to all nearby points. Then each line is bisected at the midpoint by a perpendicular plane. The smallest volume enclosed by these planes is the WS cell. This type of construction is more formally known as Voronoi tessellation. One of the main advantages is that there is a unique WS cell for a given Bravais lattice; it is independent of the choice of primitive vectors and contains the full symmetry of the Bravais lattice.

Since all the primitive cells have the same volume, including the WS cell, the easiest way to calculate the volume is to choose a primitive cell with the shape of a parallelepiped. It follows that the volume can easily be calculated by the determinant of the lattice vectors $\mathbf{a}$

$$\Omega_{\text{cell}} = \det(\mathbf{a}) = |\mathbf{a}_1 \cdot (\mathbf{a}_2 \times \mathbf{a}_3)| \tag{2.34}$$

and all the cyclic permutations of $\mathbf{a}_i$ vectors.

The reciprocal lattice is defined as the set of wavevectors $\mathbf{G}$ (units of length^{-1}) that yield plane waves with the periodicity of the Bravais lattice (hereafter direct lattice). Mathematically, this can be expressed with the relation

$$e^{i\mathbf{G} \cdot \mathbf{T}} = 1 \tag{2.35}$$

for all primitive vectors $\mathbf{T}$ of the direct lattice.

The reciprocal lattice can be spanned by linear combinations of primitive translation vectors $\mathbf{b}_i$, commonly known as reciprocal vectors:

$$\mathbf{G}(\mathbf{m}) \equiv \mathbf{G}(m_1, m_2, m_3) = m_1\mathbf{b}_1 + m_2\mathbf{b}_2 + m_3\mathbf{b}_3 \tag{2.36}$$

where m_i are any integers. Therefore, the reciprocal lattice is also a Bravais lattice. The exponential in Equation (2.35) equals unity if the lattice vectors $\mathbf{a}_i$ and reciprocal vectors $\mathbf{b}_i$ obey the relation

$$\mathbf{b}_i \cdot \mathbf{a}_j = 2\pi\delta_{ij} \tag{2.37}$$

where δ_{ij} is the kronecker delta. This result suggests that applying any translation $\mathbf{T}$ in the direct lattice to a plane wave with wavevector $\mathbf{G}$, only results in a phase-shift of a multiple of 2π. From here, it is apparent that the vectors $\mathbf{a}_i$ and $\mathbf{b}_i$ present a mutual reciprocal relationship. Precisely, the connection is done via a Fourier transform. Besides, it provides a recipe to compute the vectors $\mathbf{b}_i$ in terms of $\mathbf{a}_i$:

$$\mathbf{b}_1 = 2\pi\frac{\mathbf{a}_2 \times \mathbf{a}_3}{\Omega_{cell}}; \qquad \mathbf{b}_2 = 2\pi\frac{\mathbf{a}_3 \times \mathbf{a}_1}{\Omega_{cell}}; \qquad \mathbf{b}_3 = 2\pi\frac{\mathbf{a}_1 \times \mathbf{a}_2}{\Omega_{cell}}. \tag{2.38}$$

Equation (2.38) provides a physical interpretation of the reciprocal lattice. When moving from the direct to the reciprocal lattice, the spacing between the lattice points at a given direction becomes inversely proportional to that of the direct lattice along the same direction. One can go further and define the following correspondence between both lattices. For any family of planes in the direct lattice separated by a distance d, there is a primitive vector $\mathbf{G}$ in the reciprocal lattice normal to the planes and with magnitude $2\pi/d$.

Analogous to the direct lattice, the primitive cell in the reciprocal lattice is not uniquely determined. Hence, the most convenient choice of primitive cell will again be the WS cell. In this case it receives the special name of first Brillouin zone (BZ) . Since the reciprocal lattice is a Bravais lattice, any wavevector $\mathbf{q}$ outside the first BZ has to be equivalent to a wavevector $\mathbf{k}$ inside the first BZ via

$$\mathbf{q} = \mathbf{k} + \mathbf{G} \tag{2.39}$$

The volume of the BZ can be calculated by

$$\Omega_{\mathrm{BZ}} = \det(\mathbf{b}) = |\mathbf{b}_1 \cdot (\mathbf{b}_2 \times \mathbf{b}_3)| = \frac{(2\pi)^3}{\Omega_{\mathrm{cell}}} \tag{2.40}$$

Note that it is inversely proportional to the volume of the direct lattice. The

bigger the direct lattice, the smaller the reciprocal lattice and *vice versa.*

2.5.2 Bloch Theorem and Born von-Karman Periodic Boundary Conditions

The electronic problem in an extended system amounts to the resolution of the KS equations of a system of an infinite number of electrons and nuclei under an external periodic potential with the periodicity of the Bravais lattice. However, by taking advantage of this same periodicity, the infinite system can be simplified to the study of a finite number of particles in the primitive cell. This arises naturally due to the translational symmetry inherent to the crystal. This idea is embodied in the celebrated Bloch theorem,[310] which states that the eigenstates of the KS Hamiltonian under an external periodic potential can be written as

$$\psi_{i,\mathbf{k}}(\mathbf{r}) = e^{i\mathbf{k}\cdot\mathbf{r}} u_{i,\mathbf{k}}(\mathbf{r}) \tag{2.41}$$

where $u_{i,\mathbf{k}}(\mathbf{r}$ has the full translational symmetry of the Bravais lattice ($u_{i,\mathbf{k}}(\mathbf{r} + \mathbf{T}) = u_{i,\mathbf{k}}(\mathbf{r})$). i is the band index and $\mathbf{k}$ is the wavenumber index, typically known as crystal momentum, yet to be defined. Electron motion is not described by standing waves, but a periodic function modulated by a planewave; that is, electrons do have motion inside the crystal. Equation (2.41) automatically implies that

$$\psi_{i,\mathbf{k}}(\mathbf{r} + \mathbf{T}) = e^{i\mathbf{k}\cdot\mathbf{T}} \psi_{i,\mathbf{k}}(\mathbf{r}). \tag{2.42}$$

The Bloch wavefunctions have the same periodicity as the Bravais lattice up to an imaginary phase factor. Thus, the probability of finding an electron is the same at any equivalent position in the lattice. Similarly, by virtue of Equation (2.35), wavevectors $\mathbf{k}$ differing by a reciprocal vector $\mathbf{G}$ characterize the same Bloch state. In other words, the wavevector $\mathbf{k}$ is conserved modulo $\mathbf{G}$

$$\psi_{i,\mathbf{k}+\mathbf{G}}(\mathbf{r}) = \psi_{i,\mathbf{k}}(\mathbf{r}). \tag{2.43}$$

This is known as the conservation of crystal momentum and has a huge importance in the study of crystal excitations. Additionally, it tells us that the range of $\mathbf{k}$ can be restricted to the BZ. Nonetheless, the Bloch theorem does not give information

about the possible allowed values of **k** and their total number in the BZ. This becomes problematic as many properties require a summation over **k**. This is solved by imposing appropriate boundary conditions to the Bloch wavefunctions.

The Born von-Karman periodic boundary conditions (BvK-PBCs) are a type of cyclic boundary conditions of macroscopic periodicity. They rest on the assumption that if a very large but finite crystal is chosen, the properties of the crystal become independent of the choice of boundary conditions. It follows naturally from the Bloch theorem that the best choice is PBCs. Thus, the idea of the BvK-PBCs is to connect the primitive cells in opposite edges for all directions, so that the finite crystal resembles an infinite crystal. Mathematically, this reads as

$$\psi_{i,\mathbf{k}}(\mathbf{r} + N_1\mathbf{a}_1) = \psi_{i,\mathbf{k}}(\mathbf{r} + N_2\mathbf{a}_2) = \psi_{i,\mathbf{k}}(\mathbf{r} + N_3\mathbf{a}_3) = \psi_{i,\mathbf{k}}(\mathbf{r}) \qquad (2.44)$$

where N_i are the number of primitive cells in the direction of the lattice vectors $\mathbf{a}_i$, with the total number of primitive cells being ($N_{\text{cell}} = N_1 N_2 N_3$). The BvK-PBCs only hold in the limit $N_i \to \infty$, so one thinks of the N_i in terms of Avogadro's number. In this way, surface effects become negligible; the cells deep within the lattice do not "feel" the surface. Macroscopic crystals of different shape and size will yield the same bulk properties.

One comment should be stressed. The BvK-PBCs are applied to a macroscopic Bravais lattice and not a single primitive cell. In this last case BvK-PBC breaks as there is just a single cell. But recall that the Bloch wavefunctions not in the edges are connected by virtue of the Bloch theorem. The BvK-PBCs in turn, connect the cells in the edges, completing the cycle. Conceptually, it is the same as having a single primitive cell which is replicated infinitely in all directions. When one particle passes through one side of the cell, it reappears on the opposite side with equal velocity.

Applying the Bloch theorem to Equation (2.44) implies that

$$e^{iN_i\mathbf{k}\cdot\mathbf{a}_i} = e^{i2\pi N_i x_i} = 1, \qquad (2.45)$$

which only holds if $x_i = n_i/N_i$ where n_i is an integer. Then, the expression for the permitted values of **k** by the BvK-PBCs is given by

$$\mathbf{k} = \sum_{i=1}^{3} \frac{n_i}{N_i} \mathbf{b}_i. \tag{2.46}$$

This leads to two important results. First, the coefficients x_i of $\mathbf{k}$ are real. And second, the number of distinct values of $\mathbf{k}$ are N_{cell} because n_i can take only N_i inequivalent values; values greater than N_i differ by a multiple of 2π (Equation (2.35)). This indicates that there is exactly one value of $\mathbf{k}$ per primitive cell; the BZ contains as many $\mathbf{k}$ wavevectors as primitive cells in the whole crystal. Hence, in a finite crystal $\mathbf{k}$ is discrete. However, since the values of $\mathbf{k}$ are very densely packed, it can be approximated as continuous, which becomes exact in the limit $N_i \to \infty$. Such wavevectors are known as BvK wavevectors and are the only ones compatible with BvK-PBCs. This has tremendous consequences for the filling of the energy bands as explained below.

Diagonalization of the KS equations for a crystal yields the eigenvalues $\epsilon_{i,k}$, commonly known as energy bands. The set of all bands form the band structure of the crystal. For a given i, the eigenvalues are analytic functions of $\mathbf{k}$ inside the BZ, which form a band. This is in stark contrast with molecules, where the energy eigenvalues only depend on i. A molecule can be thought of as the limiting case where the BZ has zero volume. Alternatively, for each $\mathbf{k}$, there is a discrete set of eigenvalues labeled by i, which are separated by energy gaps where no eigenstate exists for some range of $\mathbf{k}$. Since bands are continuous and periodic, they will be bounded by an upper and lower bound. This difference is known as dispersion and determines the amount of overlap between two orbitals (*i.e.*, a chemical bond) in a similar way to the splitting of MOs in molecules. The more effective the overlap, the greater the dispersion. Localized states such as unpaired electrons show planar bands. The number of eigenstates in a band is given by N_{cell} due to the BvK-PBCs. Therefore, each band can accommodate $2N_{\text{cell}}$ electrons, where the factor two has come from spin-degeneracy. Suppose now that we are dealing with a primitive cell with n_e electrons. Then, the total number of electrons in the crystal will be $n_e N_{\text{cell}}$, which will occupy $n_e N_{\text{cell}}/2$ eigenstates. Consequently, we have that $n_e N_{\text{cell}}$ electrons will fill $n_e/2$ bands in the BZ.

In short, the Bloch theorem indicates that it is not necessary to determine the

wavefunctions in the whole crystal; it suffices to know the solution in the primitive cell, In this way, the problem has been transformed from treating an infinite number of electrons to only treating those within the primitive cell.

2.5.3 Density of States

A concept of fundamental importance in the analysis of chemical bonding and reactivity is the so-called density of states (DOS) . The DOS is a measure of the energy levels available to an electron (charge carrier).[309] It is defined as the number of states per unit volume in the energy interval from E to $E + dE$:

$$g(E) = \frac{\Omega_{\text{cell}}}{(2\pi)^3} \sum_i \int_{BZ} d\mathbf{k} \; \delta(\epsilon_{i,\mathbf{k}} - E) \qquad (2.47)$$

where δ is the Dirac delta function. Because of the Dirac delta function, the DOS is directly related to the dispersion of the bands. A high value of DOS at a given energy means that many states are available at that energy. Notice however, that these states, despite having the same energy, can belong to bands of different symmetries and thus, do not interact (hybridize).

The DOS only gives information about how the electronic states are distributed in energy, but does not say anything about their occupancies. This is done with the Fermi function. The Fermi function gives the probability that an available state will be occupied by an electron at temperature T. The average number of electrons in a given KS state at T is given by

$$f(\epsilon_{i,\mathbf{k}}) = \frac{1}{e^{(\epsilon_{i,\mathbf{k}} - E_F)/k_b T} + 1} \qquad (2.48)$$

where $\epsilon_{i,\mathbf{k}}$, is the energy of the KS state, k_B the Boltzmann constant and E_F the Fermi level. E_F is the energy at which the probability of having a state occupied by an electron is $1/2$. At $0K$ the electron occupation is given by the Heaviside function; all states below the E_F are occupied while all states above the E_F are empty. As the temperature increases, the distribution gets smeared and electrons start filling the states above E_F. In a metal E_F lies at the last occupied state, *i.e.*, HOMO, whereas in an insulator or semiconductor E_F is located inside the band gap.

The Fermi function can also be generalized for any arbitrary energy. In this way,

it can be used to compute the electron concentration by integrating over the energy,

$$N_{\text{occ}} = \int_{-\infty}^{E_F} dE \ f(E) \ g(E). \tag{2.49}$$

Figure 2.1 summarizes the differences among the different concepts described in this section. The DOS is related to the band structure by averaging the number of states over the BZ at a given energy. In turn, N_{occ} is connected to the DOS by averaging the number of electrons over all occupied states below E_F.
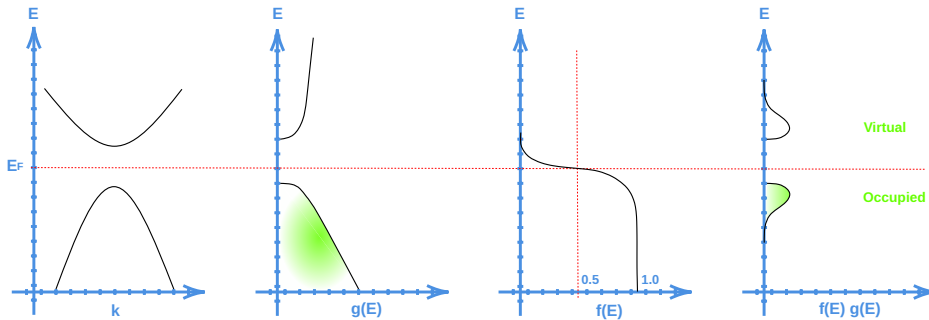
Figure 2.1: Schematic sketch of the band structure, density of states (DOS), Fermi function and electron concentration ($f(E) \ g(E)$) for a semiconductor with a band gap. E_F denotes the Fermi level.

It is important to stress the following point. Ground state calculations are usually done at $0K$. Here, the Fermi distribution equals the Heaviside function. Nevertheless, treating the electronic occupation with such a function results in convergence problems when performing integrals over the BZ. To avoid these issues, a fictitious temperature is introduced to broaden the Fermi distribution. As a consequence, fractional occupancies of KS states are obtained in a similar way to multideterminantal wavefunction methods. However, it should be kept in mind that this is just an artifact employed to solve a numerical issue particular to periodic systems; it has no physical meaning.

It is well-known that the slope of the DOS diverges at the critical points of the bands. This results in the appearance of kinks in the DOS known as van Hove singularities. The different types of van Hove singularities are listed in Figure 2.2. Identification of the van Hove singularities can help extract from the DOS valuable information about the electric properties. Namely, it can help classify materials as

conductors, semiconductors or insulators, as each possesses a different number and type of van Hove singularities. In our case of interest, *i.e.*, catalysis, it may aid to deconvolute the role of the support in the catalytic properties of the cluster via the MSI.
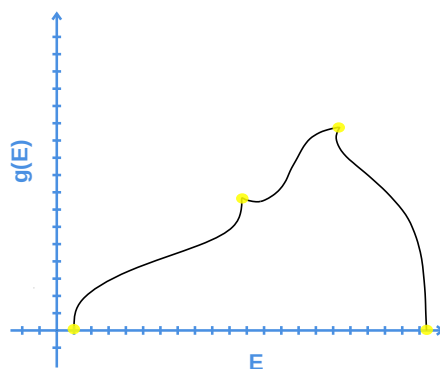
Figure 2.2: Types of van Hove singularities (highlighted with yellow circles) at band critical points.

We dedicate the next paragraphs to the discussion of the bonding analysis. Despite being written in a language perhaps not familiar to chemists, the DOS contains crucial information about the chemical bonding.[311] It is read similar to a MO diagram. The s and p bands tend to show a parabolic dispersion and are delocalized over the entire DOS; the d band in contrast, is no longer parabolic and is much more localized. The relative stability of the d orbitals will depend on their local coordination environment according to crystal field theory (CFT). The MOs of molecules appear as very sharp peaks, indicating no interaction, *i.e.*, they lack translational symmetry. However, as a result of an interaction with other fragments, their MOs shift to lower energies and are broadened over a wider range of energy, as new bonding and antibonding states are formed. This is usually referred to as orbital hybridization. One such relevant example is ligand chemisorption.

Ionic and covalent bonds show completely different features in the DOS. On the one hand, in an ionic bond, there is hardly any overlap visible between the interacting atoms. The orbitals corresponding to the electron acceptor appear below E_F with an increased density, while those of the electron donor appear above E_F

as unoccupied states. On the other hand, covalent bonds are characteristic of a strong overlap between the interacting orbitals. These orbitals are located at similar energies: the closer they are, the more effective is the overlap and the stronger is the bond. Regardless, chemical bonds do not always have such a definite nature, especially when dealing with the adsorption of a ligand to a TM. Often, they are a mixture between covalent and ionic, named polarized covalent bonds. This occurs when there is a significant difference in electronegativity between the interacting fragments.

Importantly, it should be remembered that loosely speaking, the DOS only contains information about the occupancy of the orbitals. Notwithstanding, it says nothing about their bonding or antibonding nature. It is often the case that due to charge transfer effects, antibonding orbitals become populated below E_F, while bonding orbitals become depopulated above E_F. Thus, one should have special care in assigning orbitals. Further studies become mandatory such as population analysis and MO fragment analysis.

2.5.4 Plane Waves Basis Set

As previously discussed, the KS equations (Equation (2.22)) are a set of coupled integro-differential equations. These types of problems are rather cumbersome to solve with numerical techniques. Considering the efficient algorithms for matrix algebra, the idea is to reformulate the KS equations in terms of matrices. In this regard, the Roothaan-Hall equations[272, 273] reconvert the integro-differential equations into a generalized eigenvalue problem by expanding the KS orbitals in terms of an appropriate basis set.

From the Bloch theorem, it follows that plane waves arise as a natural choice of basis set in extended systems. The periodic component $u_{i,\mathbf{k}}(\mathbf{r})$ in the Bloch wavefunction can then be expanded as a Fourier series[296]

$$u_{i,\mathbf{k}}(\mathbf{r}) = \frac{1}{\sqrt{\Omega_{\text{cell}}}} \sum_{\mathbf{G}} c_{i,\mathbf{k}+\mathbf{G}} e^{i\mathbf{G}\cdot\mathbf{r}} \tag{2.50}$$

where $c_{i,\mathbf{k}+\mathbf{G}}$ are the expansion coefficient of the Fourier components. Plugging this expression into Equation (2.41) gives the Bloch wavefunction in a plane wave basis

$$\psi_{i,\mathbf{k}}(\mathbf{r}) = \frac{1}{\sqrt{\Omega_{\text{cell}}}} \sum_{\mathbf{G}} c_{i,\mathbf{k}+\mathbf{G}} e^{i(\mathbf{k}+\mathbf{G})\cdot\mathbf{r}}. \tag{2.51}$$

Since the plane wave basis set is complete, the expansion is infinite. However, the high frequency Fourier components usually have a minor contribution, so the expansion can be effectively truncated. Only plane waves with kinetic energy lower than some cutoff energy are included:

$$\frac{1}{2}|\mathbf{k} + \mathbf{G}|^2 < E_{\text{cut}}; \tag{2.52}$$

or in other words, only the plane waves inside a sphere of radius $|\mathbf{k} + \mathbf{G}|$ are considered (the Fourier transform of a plane wave is a Dirac delta function). Notice that with this definition, not all $\mathbf{k}$ wavevectors are treated equally, *i.e.*, the number of plane waves differs for each $\mathbf{k}$.

Even after truncation, the size of the plane wave basis (N_{PW}) is still too large compared with localized basis functions. An electronic structure calculation of a supported catalyst may need the order of 10^5 plane waves. This leads to a matrix Hamiltonian of huge dimensions. There are too many matrix elements to be able to handle in an efficient manner; not to speak about a full diagonalization which becomes completely impractical. Strikingly, the solution is found on the huge size of the basis set itself. Since the number of plane waves (N_{PW}) exceeds considerably the number of eigenstates, most of the Hamiltonian matrix elements will contain unnecessary information; we do not need all the eigenvalues. Consequently, the Hamiltonian matrix can be made sparse and thus, make use of efficient algorithms developed for such matrices. Iterative methods undoubtedly stand out as the method of choice.[296] Here, the full Hamiltonian is never constructed, but divided into several Krylov subspaces containing each a different range of the full energy spectrum. Then, the full Hamiltonian diagonalization is recast as an iterated minimization procedure in each of these Krylov subspaces. Some examples include conjugate gradient (CG) method, Lanczos method, Davidson method and the residual minimization method by direct inversion in the iterative subspace (RMM-DIIS).

Plane waves present a considerable number of advantages:

- They are not biased by the nature of the problem. Due to their delocalized nature they are independent of the atomic positions. They represent all regions of space with equal accuracy, so they do not give rise to Pulay forces. Moreover, the basis set superposition error (BSSE) is also avoided.

- They form an orthonormal basis set. Therefore, the Hamiltonian matrix elements are easy to compute. Operators become diagonal in either real or reciprocal space. For instance, the kinetic energy is diagonal in reciprocal space, while the external potential is diagonal in real space.

- They allow to exploit the full machinery of fast fourier transform (FFT) techniques. Matrix multiplications and convolutions (*e.g.*, double sums over $\mathbf{k}$), which require N_{PW}^2 operations, become simple scalar products in the opposite space after taking only $N_{\mathrm{PW}} \log N_{\mathrm{PW}}$ operations. This difference in the computational cost becomes abysmal for very large N_{PW}. This indicates that we can switch from real to reciprocal space and *v.v.* at convenience via FFT and evaluate the operators in the space they are diagonal. This is the key idea to make the Hamiltonian matrix sparse and use iterative methods. The evaluation of the kinetic energy and potential is done separately. On the one hand, the kinetic energy is trivially evaluated in reciprocal space. On the other hand, the potential is calculated in real space since it is diagonal. Then, a FFT is applied to transform the potential to reciprocal space and both results are collected together. This approach reduces the computational cost from N_{PW}^3 of full diagonalization to N_{PW}^2.

- Highly optimized real-space multi-grid algorithms can be employed to evaluate potentials and the density.

- Calculation of forces and stress is straightforward. As plane waves are not atom-centered, the Hellmann-Feynman theorem can be applied directly to calculate forces.

- A single parameter, E_{cut}, controls the convergence of the energy with respect to the basis set. The energy can always be systematically improved by increasing

E_{cut}. This is in contrast with nonorthogonal basis sets where increasing the basis set size does not necessarily imply an improvement in the energy.

Unfortunately, plane waves also carry two main disadvantages:

- The basis set size scales with the simulation cell volume. The vacuum also has to be represented; it cannot be ignored. It is as expensive as atoms. This becomes more problematic in systems of low dimensionality such as surfaces and nanowires, where vacuum can amount to more than half of the cell.

- The core electrons are very tightly bound to the nucleus, showing very rapid oscillations. In order to capture such a behaviour a prohibitive cutoff energy is required, making it computationally very expensive. Regardless, this issue can be overcome with the use of pseudopotentials which tend to smooth these oscillations. Pseudopotentials are discussed in greater detail in the following subsection.

2.5.5 Pseudopotentials

Core states originate deep in the nucleus due to the strong confining nuclear potential. They are highly localized and have very sharp oscillations. Thus, they have no capacity to interact with other states and can be regarded as chemically inert to a great extent. Core electrons remain virtually unchanged irrespective of the chemical environment. Meanwhile, valence states show a different behaviour depending on the proximity to the nucleus: outside the core region, the valence wavefunction is delocalized over the entire crystal. Nonetheless, the valence wavefunction becomes oscillatory inside the core region so as to maintain orthogonality with the core wavefunctions of the same angular momentum. Precisely, the radial part of the valence wavefunction must have $n - l - 1$ nodes. Unfortunately, plane waves are a poor choice to represent these sharp features, as well as the diverging asymptotic behaviour of the nuclear potential at the origin. A vast amount of plane waves becomes mandatory. Nonetheless, the behaviour of the valence wavefunction in the core region is not very important to gain a correct description of the system. Chemistry originates from the interaction of valence electrons in the internuclear

regions. It is the valence electrons that are responsible for the chemical bonding. Motivated by these observations, pseudopotentials aim to replace the effect of the core electrons and the nuclear potential with an effective potential acting on the valence electrons.[296]

Pseudopotentials find their formal justification in two important results of scattering theory. First, different potentials can yield the same phase shift (*i.e.*, scattering) modulo $2\pi n$. And second, the properties of the wavefunction outside the scattering region are invariant to changes in the phase shift modulo $2\pi n$. The first observation suggests that it is possible to choose a more convenient potential with an easier representation in the scattering region, while the second does the same for the choice of scattering wavefunction. For example, a smooth and weak potential with no bound states and a nodeless scattering wavefunction could be chosen. The crystal structure can be viewed as a problem where valence electrons are scattered by the potential created by the nuclei and core electrons.

The pseudopotential approach is embodied in Figure 2.3. Herein, only the valence electrons are included explicitly. The core electrons are instead treated implicitly with an effective core potential (ECP) that approximates the joint influence of the core electrons and nucleus on the valence electrons near the core region, *i.e.*, the pseudopotential. The pseudopotential is characterized by a cutoff radius R_c. Inside R_c, it is a smoother version of the true potential that does not contain the singularity at the origin, whereas outside R_c, it matches exactly the true potential. In addition, the pseudopotential also gives rise to an effective atomic Schrödinger equation whose solutions are pseudowavefunctions. For $r < R_c$, the behaviour of the pseudowavefunctions differs from the true valence wavefunctions; they are smooth and lack the complicated nodes. Despite these differences, the pseudowavefunctions are designed to guarantee the same properties as the true valence wavefunctions for $r > R_c$.

Pseudopotentials are usually chosen to be semi-local. Namely, they are local in the radial variable but non-local in the angular momentum l. The pseudopotential acts differently on wavefunctions of different angular momentum l; that is, it depends on the angular momentum l. This is a direct consequence of the spherical symmetry of pseudopotentials.
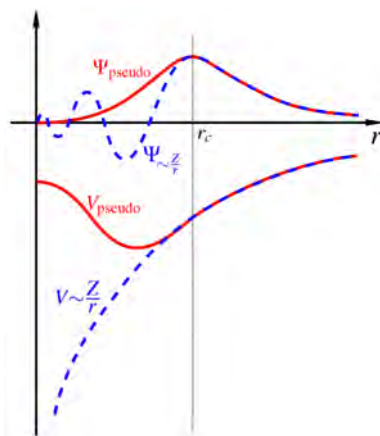
Figure 2.3: Comparison between the all-electron and pseudo potentials and wave-functions. The pseudopotential and pseudowavefunction coincide with the real values above a chosen core radius R_c, whereas below R_c the pseudized versions are nodeless and smooth.

Ab initio pseudopotentials are generated from all-electron atomic DFT calculations. The following prescription is followed:

1. A reference atomic configuration is chosen that can correctly represent that given atom in the real environment.

2. The all-electron radial Schrödinger equation is solved for the reference system to obtain the eigenvalues and eigenfunctions.

3. The pseudowavefunctions are constructed from the valence wavefunctions by imposing a set of constraints in both the core and outer region.

4. Knowing the eigenvalues and pseudowavefunctions, the screened pseudopotential is obtained by inverting the radial Schrödinger equation.

5. The screened potential is unscreened by subtracting the Hartree and exchange-correlation potentials calculated only for the pseudowavefunctions.

The choice of pseudopotential is not uniquely determined. However, two juxtaposed factors must always be considered when designing new pseudopotentials:

Transferability refers to the ability of the pseudopotential to reproduce the same atomic species in different chemical environments, *viz.*, molecule, cluster, solid,

etc.. Pseudopotentials are constructed for a specific atomic environment. However, a pseudopotential with good transferability properties should be as independent as possible from the choice of reference system and be able to capture the changes in the environment.

Hardness is related to the plane wave cutoff energy required to construct the pseudopotential. The smoother it is, the fewer plane waves it will need and the softer will be.

One way of improving transferability is to reduce R_c. Although the pseudowavefunction becomes closer to the real one in this way, it also becomes more oscillatory, resulting in a harder pseudopotential. The reduction of R_c is limited to the position of the outermost node of the real wavefunction due to the nodeless condition. On the contrary, if one tries to soften the pseudopotential by increasing R_c, transferability will be lost. Inevitably, one comes at the expense of the other; a balance has to be found.

In the following, we summarize the most relevant pseudopotentials employed in plane wave electronic structure calculations:

Norm-conserving pseudopotentials (NCPPs) were the first *ab initio* pseudopotentials to produce accurate results. Hamann, Schuluter and Chiang proposed a list of requirements for NCPPs:[312]

- All-electron and pseudo valence eigenvalues agree for the chosen reference system.

- The all-electron and pseudowavefunction must agree beyond R_c.

- The logarithmic derivatives of the all-electron and pseudowavefunctions agree at R_c.

- The first energy derivative of the logarithmic derivatives of the all-electron and pseudowavefunctions agrees for $r \geq R_c$. Outside R_c they must reproduce the same scattering properties as the true wavefunction.

- The integrated charge density of the all-electron and pseudowavefunction must agree inside R_c (norm-conservation).

The norm-conservation condition is imposed to improve the transferability. Nonetheless, it comes at the price of increasing the hardness of the NCPP. This specially becomes an issue for nodeless valence wavefunctions, where the pseudopotential approach is not able to smooth them inside R_c.

Ultrasoft pseudopotentials (USPPs) were devised to overcome the hardness of NCPPs. Vanderbilt[313] proposed that the norm-conservation condition is not a necessary condition to obtain good transferability, it can be relaxed. It suffices only to match the logarithmic derivatives of the all-electron and pseudowavefunction at the R_c. This allows to increase R_c and thus reduce the hardness.

Projector augmented wave (PAW) method developed by Blöchl,[314, 315] merges together the pseudopotential approach and real space partitioning methods such as the augmented plane wave (APW) method. The essence of this method lies in the fact that the all-electron wavefunction with all its oscillations can be mapped with a linear transformation onto auxiliary wavefunctions, which can be conveniently made as smooth as possible. For the transformation to be effective, the crystal structure is partitioned into augmented spheres containing the nuclei and interstitial regions with the linear muffin-tin orbitals (LMTO) method. In this way, the transformation will act differently on different parts of space. In the interstitial regions, the wavefunction is smooth, so it can be correctly represented with a Bloch pseudowavefunction. The transformation has no effect. However, inside the augmentation spheres, the wavefunction is projected onto a partial wave basis that captures the correct nodal behaviour. This has the advantage that the resulting wavefunction can be calculated independently in each region. Namely, in the interstitial region, a plane wave expansion is used together with FFT techniques and real grids, while in the augmented spheres, atom-centered radial grids are used without invoking any plane waves. The PAW method stands out for its accuracy and simplicity to calculate energies, densities and forces. Moreover, it can also be employed to obtain properties in which the core states play an active role, such as chemical shifts.

Pseudopotentials present another important advantage concerning the treatment of scalar relativistic effects. Scalar relativistic effects originate deep in the core, so the valence states have a minor role. This suggests that scalar relativistic corrections can be incorporated naturally into the pseudopotential without treating them explicitly in the Hamiltonian. That is, scalar relativistic effects can be accounted for within a non-relativistic KS framework without significant additional effort. Notwithstanding, for the heavier TM atoms spin-orbit coupling (SOC) also becomes important. In this case, it is no longer possible to consider its effect via a pseudopotential. The SOC must be included in the Hamiltonian, which transforms the KS equations into a complicated spinor representation.

2.5.6 van der Waals Dispersion Correction

Besides the usual $1/r$ short-range coulombic interactions defined in the molecular Hamiltonian (Equation (2.6)), molecules and condensed matter also feel long-range interactions known as van der Waals (vdW) forces.[316] They are non-covalent interactions (NCI) that occur typically (although not necessarily) between electrically neutral fragments. VdW forces are quantum mechanical phenomena in origin; they arise from non-local correlation effects, where fluctuations of the electron density at one point of space distort the density at another point. The fragments interact via the dipole moments or higher order multipoles, according to their point group symmetry. Depending on the nature of these dipole moments (hereafter I will simply refer them as dipoles), three types of vdW forces can be distinguished:

- Orientation (or Keesom) interaction: It consists of the interaction between a pair of polar molecules, *i.e.*, molecules with permanent dipoles. It can be attractive or repulsive depending on the relative orientation of the molecules.

- Induction (or Debye) interaction: This type of interaction occurs between a polar and nonpolar molecule. The dipole moment of the polar molecule distorts the electron density of the nonpolar molecule, inducing a dipole moment. It is always attractive. The strength of the induced dipole will be determined by the polarizability of the molecule.

- London (or vdW) dispersion interaction It is an attractive interaction that happens between nonpolar molecules. Random fluctuations in the electron density of one of the molecules alters its charge distribution, creating an instantaneous dipole. This dipole in turn, induces a dipole moment on the other molecule.

All vdW forces are anisotropic as they depend on the relative orientation of the fragments. In this work we only focus on the vdW dispersion interactions. The first two types of interactions are not always present because they require a permanent dipole moment, while vdW dispersion is universal: all molecules have polarizability.

Most DFAs fail to capture the correct $1/r^6$ (at first order) asymptotic behaviour of the vdW dispersion energy for large intermolecular distances, owing to their semilocal character. Several methods have been developed over the years. One of the most popular ones is Grimme's DFT-D3 approach.[317] It is a coarse-grained method where the dispersion interaction is treated semiclassically. The dispersion energy is built by an atomic pairwise (two-body terms) sum under C_n/r^n type potentials in the following way

$$E_{\text{disp}} = -\frac{1}{2} \sum_{i=1}^{N} \sum_{j=1}^{N} {\sum_{\mathbf{T}}}' \sum_{n=6,8,10,\cdots} \left[s_n \frac{C_n^{ij}}{r_{ij,\mathbf{T}}^n} f_{\text{damp.n}}(r_{ij,\mathbf{T}}) \right] \tag{2.53}$$

where the first two summations are over all N atoms in the unit cell, the third summation is over all translations of the lattice vectors $\mathbf{T} = (\mathbf{a}_1, \mathbf{a}_2, \mathbf{a}_3)$, and the fourth summation is over all orders considered in the multipole expansion of $1/r_{ij}$. Normally, the fourth summation is truncated at 8th order. The prime indicates that the $i = j$ term must be omitted for $\mathbf{T} = 0$ to avoid the unreal interaction of a particle with itself. C_n^{ij} denotes the nth order isotropic dispersion coefficient for the atom pair ij, $f_{\text{damp.n}}$ is the nth order damping function, s_n is a scaling factor, and r_{ij} is the interatomic distance between atoms i and j ($r_{ij} = |\mathbf{r}_i - \mathbf{r}_j|$), respectively. Note that E_{disp} is attractive for any distance r_{ij} and hence stabilizes the molecules. The damping functions are introduced in order to provide the correct asymptotic behaviour, *e.g.*, zero dispersion at short r_{ij}. The most common definition is

$$f_{\text{damp.n}}(r_{ij}) = \frac{1}{1 + 6 \left(\frac{r_{ij}}{s_{r,n} R_0^{ij}} \right)^{-\alpha_n}} \tag{2.54}$$

where $s_{r,n}$ is the nth order scaling factor of the cutoff radius R_0^{ij} ($R_0^{ij} = \sqrt{C_8^{ij}/C_6^{ij}}$), and α_n is the nth order steepness parameter. The empiricism is significantly reduced in the DFT-D3 approach. Only the s_n and $s_{n,r}$ scaling factors are obtained by an empirical fitting. The most relevant parameters like the dispersion coefficients are derived instead from advanced time-dependent density functional theory (TDDFT) techniques. One of the main drawbacks however, is that they are calculated for isolated atomic pairs and thus, do not reflect the real chemical environment.

Equation (2.53) presents an additional problem inherent to all extended systems with PBCs. Because dispersion is a long-range interaction, it cannot be directly evaluated as a sum in real space.[296] The infinite sum over all periodic cells is not well-defined; it is conditionally convergent as the result depends on the order of the summation. The Ewald summation method splits the sum into two contributions: a short-range and long-range term, each of which is now absolutely convergent. The former is computed in real space, whereas the latter in reciprocal space. Each term requires charge neutrality which is achieved with the help of a compensating uniform background.

Finally, the dispersion-corrected energy is given by

$$E_{\text{DFT-D3}} = E_{\text{KS-DFT}} + E_{\text{disp}} \tag{2.55}$$

where $E_{\text{KS-DFT}}$ is the self-consistent ground state energy as obtained within the KS framework.

The vdW dispersion corrections have been proved to play a crucial role in the correct description of the interaction between adsorbates and metals. Accurate binding energies and reaction barriers demand the use of such corrections. This is related to the fact that in catalysis the quantities of interest are energy differences and not total energies. The dispersion correction may become of the same magnitude as the difference between two competitive adsorption modes or reaction pathways, so that its omission may lead us to the wrong conclusions.

2.5.7 Modeling Surfaces With The Supercell Approach

Surface formation causes the symmetry breaking of the Bravais translation in the normal direction to the surface. The full periodicity is reduced to a periodic lattice in the plane. Catalysis concerns the study of the interaction between this semiperiodic surface and a nonperiodic element like a molecule or cluster. In this regard, the question arises naturally of how can be modelled these kinds of systems.

The supercell approach has become perhaps one of the most popular methods.[318] It consists of creating a unit cell made up of several primitive cells, large enough so that the nonperiodic defect can be correctly embedded in an artificially made infinite crystal. More specifically, when applied to surfaces a slab model is obtained. The crystal structure is cut in two surfaces and a region of vacuum is inserted in both sides. Notice that the periodicity in the perpendicular dimension does not disappear, so we will have an artificial construct of infinite copies of the slab in the z direction. The role of the vacuum buffer is precisely to separate both surfaces to avoid spurious interactions between periodic replicas.

The forced artificial periodicity can introduce finite-size effects. As a result, it becomes compulsory to perform convergence tests with respect to the supercell size. We distinguish three different regimes: first, as explained above, the size of the vacuum region has to be large enough to decouple periodic images. The size of this region will be limited by the extension of vdW interactions which decay much slower than the wavefunction. The rule of thumb is about $15-20$ Å. Second, interactions can also occur between the top and bottom surfaces in the opposite direction. Apart from this, there should be sufficient atomic layers to be able to represent the bulk. The intermediate layers should be unaffected by surface effects and yield the correct bulk properties. This can be controlled with the thickness of the slab. Convergence can be achieved by simply adding more layers to the slab. And third, lateral interactions can also occur between periodic images in the plane when studying the adsorption of molecules and clusters. This introduces an extra nonperiodicity which forces it to increase the size of the supercell in the plane. Typical distances are $8-10$ Å between periodic images.

The slab approach presents several additional problems. When a surface is cleavage, uncoordinated atoms are formed. In metals in principle, this is not an

issue since the charge in excess can be redistributed among the neighbouring atoms. Nonetheless, in semiconductors the electron remains localized in the atoms, forming a radical. This is usually called a dangling bond. The formation of dangling bonds usually results in a surface reconstruction of completely unexpected geometry and properties. For example, in Ge(100) surface dimer structures of different buckling angles are formed which can serve for sensing and catalytic applications. However, such surface reconstructions can also be avoided by passivating the dangling bonds with chemical agents, *e.g.*, hydrogen.

It is a requirement of PBCs that the supercell does not possess a net dipole moment. However, polar surfaces show a dipole moment in the normal direction to the surface, which does not have the periodicity of the lattice. So in order to compensate for this dipole moment a spurious electric field is formed in the vacuum region. This electric field, in turn, causes an artificial polarization in the slab, especially in the surface layers. Semiconductors in particular suffer from this problem while in metals it is generally marginal. Accurate calculations always require getting rid of this artificial polarization. One possible approach is to construct a symmetric slab. However, the main disadvantage is that the supercell becomes very large as the surface and adsorbates have to be reduplicated. A significant number of bulk layers must also be added to prevent interaction between both surfaces due to the long-range nature. This particularly becomes very demanding for cluster adsorption. Furthermore, it is not always easy to get a mirror surface depending on the stacking manner of the atomic layers. A better approach is to employ dipole corrections. The idea here is to introduce a discontinuity in the electrostatic potential to eliminate the spurious polarization. In this way, it is possible to reduce the thickness of the vacuum and slab.

To conclude this section, it is important to mention that the supercell approach can also be applied in systems with no inherent translational symmetry such as amorphous solids, liquids, polymer chains, DNA strands and NPs. The main reason in favour of supercells is the fact that very efficient algorithms based on FFT and real grids are available to study systems of hundreds of atoms with reasonable computational cost.

2.6 Microkinetic Modeling

A catalytic reaction is the results of a number of processes which differ by many orders of magnitude in their time scale. The fastest processes occur at the atomic scale with the bond breaking and formation of molecules, followed by molecular transport at the mesoscale, and ending with the macroscopic heat and mass transport at the reactor level. In each time scale, the behaviour of the system is governed by different equations. This means that there is not a single method that can capture the behaviour of all time scales. A multiscale approach is required which solves the problem layer by layer.

First-principles-based mean-field microkinetic modeling (MF-MKM) aims to bridge the gap between the atomic and macroscopic properties.[319–321] MF-MKM was first presented in the 1993 book "The Microkinetics of Heterogeneous Catalysis" by Dumesic and Rudd,[322] and was later extended by Stoltze and Nørskov in the 1980s-1990s.[323, 324] First, a reaction mechanism is developed which encompasses all elementary steps occurring during the catalytic process, including side reactions and surface diffusion. Second, the kinetic and thermodynamic properties of all elementary steps are estimated with electronic structure methods, usually DFT. This data is then fed to the microkinetic model as it is, without making any *a priori* assumption about the rate determining step; no bias is introduced towards any specific event. The MK model is parametrized by DFT data. Finally, a set of material balance equations is derived and solved within a reactor model.

The MK model is usually built in a mean-field approach. Local inhomogeneities in the topology are neglected and all surface species and active sites are assumed to be uniformly distributed at the atomic scale. There is no defined topology for the surface structure, so the spatial information about adsorbates and active sites is lost. The rate constants no longer depend on the microscopic distribution of adsorbates and catalyst sites, but on an average picture. Regardless, it is possible to define different types of active sites, although the workload doubles as different rate equations have to be defined for each type of active site. And more importantly, spatial interactions are still missing since one is still working on a mean field framework. Recently, lateral interactions have been introduced into the MF-MKM to account for surface coverage effects on reaction barriers and energies. However,

in order to fully resolve the spatial correlation other methods should be used, such as on-lattice kinetic Monte Carlo (KMC). Unfortunately, it is computationally more demanding than MF-MKM and becomes prohibitive for very long events.

2.6.1 Phenomenology of Chemical Reactions

The theory of chemical reactions is a theory of quantum scattering at the most fundamental level.[325] A chemical reaction is a reactive scattering which involves a change in the internal degrees of freedom besides the linear momenta. Symbolically, a bimolecular reaction can be defined by the following expression:

$$A + B[\mu, \upsilon, \Gamma] \longrightarrow C + D[\mu', \upsilon', \Gamma'] \tag{2.56}$$
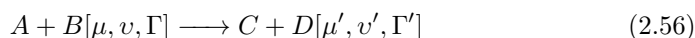
where A and B are the reactants and C and D are the products. μ, υ and Γ are the reduced mass, relative velocity and internal states. A central object in the scattering problem is the so-called scattering matrix. The scattering matrix is defined in terms of time propagator operators which connect the wavefunction before and after the collision. It contains all the information about the scattering process such as the cross sections and reaction rates. The scattering problem can be resolved within a path integral formalism. Unfortunately, such an approach is only affordable for very small-size molecules; for surface reactions it is beyond current capabilities. The price to pay is to ignore the quantum behaviour of the nuclear degrees of freedom as well as the time dependence of the electronic Schrödinger equation. Although naïve but necessary, these approximations are justified for the majority of cases since it is not always needed a complete knowledge of the trajectories along the PES. Reaction rates can be computed by accessing only a single special point in the PES, an activated complex known as transition state (TS), as explained below.

When moving to a macroscopic system, it becomes a paramount challenge to monitor the time evolution of every particle during the reaction. The number of possible states accessible to each particle is virtually infinite, so it would need infinite time to visit all possible states. Stately, statistical mechanics bridges the gap between the microscopic and macroscopic world. Under the umbrella of the ergodic hypothesis, it reformulates the time average into an average over an

ensemble. An ensemble consists of a large number of copies of the system that share the same macroscopic properties (macrostate), but differ in the internal structure; in each of them the states of the particles are rearranged in different ways (microstates). Different microstates can give rise to the same macrostate. Therefore, the macroscopic properties have to be averaged to include all possibilities. There is an incomplete knowledge of the systems from a microscopic point of view which results from treating a very large number of particles, but is of different kind than the uncertainty principle. Namely, the laws of reaction kinetics have an underlying statistical nature.[326]

2.6.2 Microscopic Reversibility, Detailed Balance and Elementary Reactions

Having adopted a statistical interpretation of the reaction kinetics, the macroscopic evolution of the system can be viewed as the result of a collection of elementary processes occurring between molecules such as collisions and reactions. In the absence of an external magnetic field, the equations of motion governing microscopic particles, the Schrödinger equation, is invariant under the time-reversal transformation. This leads to the principle of microscopic reversibility which states that in an equilibrium state the forward and reverse process occur at the same rate.[326]

Microscopic reversibility is related to mechanical properties such as cross sections. However, one may ask what consequences may this principle have at the macroscopic level, namely, in the thermodynamic properties. For this, let's first make a brief digression to explain some concepts of reaction kinetics. A chemical reaction can be decomposed into a set of elementary reactions, each of which is represented by a stoichiometric equation

$$R_i : \left\{ \sum_{\nu_{ij}<0} \nu_{ij} X_j \rightleftharpoons \sum_{\nu_{ij}>0} \nu_{ij} X_j \right\} \qquad (2.57)$$
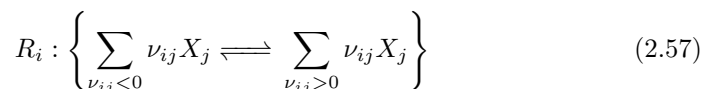
where X_j denotes a chemical species and ν_{ij} is its corresponding stoichiometric coefficient. $\nu_{ij} < 0$ indicates reactants while $\nu_{ij} > 0$ indicates products. The set of elementary reactions is known as the reaction mechanism. According to the mass action law, the reaction rate for each elementary reaction is given by

$$r_i = k_{f,i} \prod_{\nu_{ij}<0} [X_j]^{-\nu_{ij}} - k_{r,i} \prod_{\nu_{ij}>0} [X_j]^{\nu_{ij}} \tag{2.58}$$

where $k_{f,i}$ and $k_{r,i}$ are the forward and reverse rate constants of the ith elementary reaction. $[X_j]$ is the concentration of species X_j.

The significance of the microscopic reversibility at the macroscopic level is that at equilibrium the forward and reverse reactions are balanced. This is known as detailed balance or thermodynamic consistency and can be written in mathematical form as

$$\frac{k_{f,i}}{k_{r,i}} = K_{\text{eq},i} \tag{2.59}$$

where $K_{\text{eq},i}$ is the equilibrium constant of the ith elementary reaction. Namely, chemical equilibrium is rather a state of dynamic equilibrium. At the macroscopic level no apparent change is observable in the concentrations of the reactants and products. However, this is so because the forward reaction is compensated with the reverse reaction. At the molecular level, molecules continue in a dynamic state. It is important to mention that the equilibration process, despite being the result of a large number of reversible microscopic processes, is in general irreversible. And in general, most of the macroscopic phenomena are irreversible. That is, microscopic reversibility leads to macroscopic irreversibility. This asymmetry can be explained by Boltzmann's statistical interpretation of entropy: the system will evolve towards a state of maximal number of microstates (entropy). Entropy is a magnitude that arises only when a large number of degrees of freedom is present, being hence no preferred direction to evolve in molecular systems.

2.6.3 Equilibrium Constant Estimation

In microkinetic modeling, instead of using Equation (2.59), it is customary to calculate the equilibrium constants with the expression

$$K_{\text{eq},i} = e^{-\Delta G_i / k_B T} \tag{2.60}$$

where ΔG_i is the Gibbs free energy change of the ith elementary reaction. In this way, by using an independent source to calculate the equilibrium constants,

the reverse rate constants can be computed via Equation (2.59) and hence achieved detailed balance.

2.6.4 Rate Constant Estimation

Rate constants of elementary reactions are calculated on the basis of the existence of a reaction barrier. Non-activated processes (*e.g.*, adsorption, desorption) are usually barrierless and are described by collision theory. Meanwhile, activated processes (*e.g.*, surface reactions) require the crossing of a reaction barrier and are treated within the framework of transition state theory (TST) .

2.6.4.1 Collision Theory

Adsorption is viewed as the impact of a flux of gas-phase molecules with the surface. The adsorption rate constant is calculated with the Hertz-Knudsen equation[327]

$$k_{\text{ads}} = \frac{P_j A}{\sqrt{2\pi m_j k_B T}} S \qquad (2.61)$$

where P_j is the partial pressure of the adsorbate, m_j is the molecular weight of the adsorbate, k_B is Boltzmann's constant, T is the temperature and A is the area of the adsorption site (*e.g.*, atop, bridge, hollow). S is a sticking coefficient which controls the effectiveness of the adsorption: not all molecules that collide with the surface are adsorbed. This equation assumes the ideal gas law and rigid sphere approximation. Therefore, entropic effects due to a loss of rotational degrees of freedom are not included.

2.6.4.2 Transition State Theory

Developed by Eyring, Evans and Polanyi, transition state theory (TST) gives qualitative as well as quantitative understanding about chemical reactivity.[328, 329] TST explains that the reactants and products are connected by an activated complex in the PES, the transition state (TS). The TS is a first order saddle point in the PES, *i.e.*, a critical point where the Hessian has exactly one negative eigenvalue. The imaginary vibration mode corresponds precisely to the motion along the reaction coordinates. As the TS lies higher in energy than the reactants and products, an energy barrier has to be crossed.

TST is built upon the following postulates:[326]

- Molecules that have crossed the TS in the direction of the system cannot turn around (no-recrossing postulate).

- In the TS, motion along the reaction coordinate may be separated from the rest and treated classically.

- The reactants and TS are in quasi-equilibrium, irrespective of the existence of chemical equilibrium for the reaction. The reactants and TS follow a Maxwell-Boltzmann distribution.

By applying statistical thermodynamics we arrive at the main result of TST: the Eyring-Polanyi equation. The Eyring-Polanyi equation is used to calculate rate constants of elementary reactions and is expressed as

$$k_{f,i} = \frac{k_B T}{h} e^{-\Delta G_i^{\ddagger}/k_B T} \tag{2.62}$$

where $\Delta G_i^{\ddagger}$ is the activation (barrier) free energy of the ith elementary reaction (energy difference between TS and reactants), k_B is Boltzmann's constant, h is Planck's constant and T is the temperature. This equation suggests that it is not necessary to follow the entire reaction path in the PES; it suffices to characterize the TS to obtain the reaction rates.

One drawback of TST is that many quantum effects are neglected. Precisely, quantum tunneling becomes important when very light atoms are involved, such as in proton transfer. Instead of proceeding through the TS, the reactants may tunnel through the energy barrier to give the products. Such behaviour becomes reflected in the kinetic isotope effect (KIE) .

2.6.5 Model Development

Developing a model is not an easy task. One has to first assess what it is intended to represent with the model and to what accuracy. Understanding the range of applicability and limitations of the model is essential and natural; one cannot fall into the error of overcomplicating the model or using too many parameters. The workflow to construct a microkinetic model is summarized as follows:[321]

1. Design the reaction mechanism.

2. Perform DFT calculations to obtain kinetic and thermodynamic data of all the elementary steps.

3. Derive reaction rates for the elementary steps using the DFT data as external parameters.

4. Incorporate the reaction mechanism into a reactor model.

5. Solve the material balance equations with appropriate initial conditions.

6. Carry out the analysis of the results.

In the following subsections each of these steps is explained in greater detail.

2.6.5.1 Choosing The Reaction Mechanism

Generally, regardless of the complexity of the catalytic reaction, three different stages can be distinguished in a catalytic cycle, *viz.*, adsorption of reactants, chemical reaction and catalyst regeneration. More specifically, surface reactions are divided in the following types:

- Adsorption: Reaction between gas-phase species and active site. It can be molecular, dissociative and competitive.

- Langmuir−Hinshelwood (LH) reaction: Reaction between two adsorbed species.

- Eley−Rideal (ER) reaction: Reaction between adsorbed species and gas-phase species.

- Multisite reaction: Reaction between two adsorbed species on different types of active sites, *e.g.*, bimetallic alloy.

- Desorption: Release of an adsorbed species to the environment.

Designing the reaction network is of fundamental importance since the MF-MKM will only model what it has been coded to model. The reaction network should include all the elementary steps that play a significant role in the catalytic reaction.

That is, the selected elementary steps should correctly represent the catalytic reaction. The level of mechanistic detail depends on the scope of the model. In principle, one can include as many elementary steps as desired. This may improve the accuracy of the model, although it will come at the cost of becoming too complicated to extract any useful information. Usually, a balance is found following the principle of parsimony.

2.6.5.2 Reaction Rates and Time Evolution of Surface Coverages

Having defined the reaction network, the mass action law (Equation (2.58)) is applied to derive expressions for the reaction rates of the elementary steps of the form

$$r_i = k_{f,i} \prod_{\nu_{ij}<0} P_j^{-\nu_{ij}} \prod_{\nu_{ij}<0} \theta_j^{-\nu_{ij}} - k_{r,i} \prod_{\nu_{ij}>0} P_j^{\nu_{ij}} \prod_{\nu_{ij}>0} \theta_j^{\nu_{ij}} \tag{2.63}$$

where P_j is partial pressure of the gas species j and θ_j coverage of adsorbed species j. Different products are used for gas-phase and adsorbed species, although they may not necessarily be present. For instance, pressures will only appear in the adsorption (reactant) and desorption steps (product), as well as in the ER mechanism (reactant and product). In surface reactions the concentration of an adsorbate is represented with the coverage. The coverage measures the number of active sites a given adsorbate is occupying and has units of monolayers (ML). The forward rate constants are calculated with the Hertz-Knudsen equation (Equation (2.61)) or from the DFT energy barriers using the Eyring equation (Equation (2.62)). The reverse rate constants in turn, are obtained with Equation (2.59), which enforces thermodynamic consistency to the model.

The rate of change of the coverage of a given species will be determined by its rate of production and consumption:

$$\frac{d}{dt}\theta_j = \sum_i \nu_{ij} r_i. \tag{2.64}$$

The sum runs over all reactions in which species j appears, either as a reactant ($\nu_{ij} < 0$) or product ($\nu_{ij} > 0$). The coverages are constrained to the condition

$$\theta_* + \sum_j \theta_j = 1 \tag{2.65}$$

where θ_* is the concentration of free surface sites.

2.6.5.3 Continuous Stirred-Tank Reactor (CSTR) Design

One can directly solve Equations (2.64) to obtain the time evolution of the coverages. However, Equations (2.64) are still a very crude abstraction of the experimental setup and omit important information. In order to get a more realistic representation these rate expressions are introduced in a reactor model. A reactor model gives access to macroscopic parameters not present in atomistic simulations which can be used to make a direct comparison with experiment. These include design parameters such as reactor volume, residence time and operating conditions such as temperature, pressure and feed flux. The advantage of reactor models is that they allow to optimize these parameters with low computational cost and transfer them directly to experimental work.

The net change of the chemical species is evaluated in terms of material balances, *i.e.*, mass conservation. The material balance expressions depend on the type of reactor, but here we only focus on the continuous stirred-tank reactor (CSTR) , as this is the one employed in the current work. The corresponding material balance equation for a given species j amounts to

$$\frac{d}{dt}N_j = F_j^{\text{inlet}} - F_j^{\text{outlet}}(t) + \sum_{i=\text{generation}} n_{\text{sites}}r_i - \sum_{i=\text{consumption}} n_{\text{sites}}r_i \tag{2.66}$$

where N_j is the number of moles of species j in the reactor, F_j^{inlet} is the inlet molar flow (units $\text{mol}s^{-1}$) of species j, $F_j^{\text{outlet}}(t)$ is the outlet molar flow of species j and n_{sites} is the total number of active surface moles of the catalyst.

Equations (2.66) form a system of coupled ordinary differential equations (ODEs). To solve the ODE system appropriate initial conditions of feed composition and initial coverages are required. Once the initial conditions have been defined, Equations (2.66) are time-integrated to obtain the trajectories of the adsorbate coverages and partial pressures of gas species through time.

It is usually the case that rate constants of different elementary steps differ by

many orders of magnitude, making the ODE system stiff.[319] In stiff equations the solutions show a different behaviour at different time intervals. In the beginning, there is usually a regime of very rapid oscillations for a very short time interval, which is followed by a long regime of very slow oscillations. Most of the changes can occur at the first instants of the simulation. As a result, different time steps are needed at different times. The most common approach to solve stiff ODEs is the backward differentiation formula (BDF) method. However, if the ODE is very stiff, Radau method may be safer. Eventually, all solutions converge to a dynamic steady-state which differs from thermodynamic equilibrium. At steady-state, there is still an inlet and outlet of gas species which kicks the system out of equilibrium.

2.6.5.4 Analysis Techniques

MF-MKK produces a significant amount of data. Tools are needed to evaluate quantitatively the performance of a microkinetic simulations, in terms of high product formation and poisoning free. But not only that, tools can also be developed to deconvolute the mechanistic details of the simulation and discern the most important elementary steps that control the catalytic reaction. A wide variety of tools exist to extract chemically valuable information from the microkinetic data. Herein, we summarize the techniques employed in this work. The expressions given in this subsection are derived for the bimolecular reactions (A + B $\rightleftharpoons$ C; A + B $\rightleftharpoons$ D).

The coverage gives information about the species adsorbed to the surface at a given time. By monitoring changes in the coverages, it is possible to learn which elementary steps are participating with more weight and discard between competing reaction channels. Also, dominant adsorbate species can be identified (in connection to selectivity) and possible poisoning agents. A poisoning agent will present a constant coverage with time as the blocked active sites are not regenerated.

The conversion of reactant A gives a measurement of the amount of A that has been consumed in the course of the reaction. It is defined as

$$X_A(\%) = \frac{F_A^{\text{inlet}} - F_A^{\text{outlet}}}{F_A^{\text{inlet}}} \times 100 \tag{2.67}$$

where F_A^{inlet} and F_A^{outlet} are the inlet and outlet molar flow of A ($\text{mol} s^{-1}$).

Likewise, the conversion can be defined for a product. Here, one would be talking about production rather than consumption.

The selectivity is used to assess the viability of different competing reaction channels. It is defined as the production rate of the desired product (C) against the production rate of the undesired product (D):

$$S_C(\%) = \frac{F_C^{\text{outlet}} - F_C^{\text{inlet}}}{F_D^{\text{inlet}} - F_D^{\text{outlet}}} \times 100. \qquad (2.68)$$

The turnover frequency (TOF) gives an idea of the amount of desired product (C) that has been formed in the course of the reaction. It is a measure of the instantaneous efficiency of the catalyst. It is defined as the number of product moles formed per number of active sites moles per site and has units of s^{-1}:

$$\text{TOF}_C = \frac{F_C^{\text{outlet}}}{n_{\text{sites}}}. \qquad (2.69)$$

Combining all these techniques in unison can provide the researcher ample flexibility to investigate complex reaction networks by means of MF-MFM and fill the gaps left by atomistic simulations.

Chapter 3

Effect of Single-Ge-Atom Doping of Small-Size Pt Clusters on the CO Poisoning

"Deeds will not be less valiant because they are unpraised"
— J.R.R. Tolkien, *The Lord of the Rings*

This chapter discusses the promotional effect of Ge doping against CO poisoning on small-size Pt clusters in gas-phase. For this, a global minima search is carried out on $Pt_n(CO)^+$ and $GePt_{n-1}(CO)^+$ ($n = 5 - 9$) complexes, followed by a detailed structural and electronic analysis. The $Pt-C$ and $Pt-Ge$ chemical bonds are characterized by a series of different computational tools, revealing that Ge influences the electronic structure of Pt. Namely, Ge blocks the charge transfer in the back-donation step, weakening the CO binding strength.

3.1 Introduction

METAL NPs and clusters have attracted enormous attention in the last decades for their use as catalysts, due to their high activity and maximal atoms utilization. In NPs, a large fraction of the atoms are available as active sites.[94] Among them, Pt has been widely studied in a number of catalytic processes, such as the dehydrogenation of alkanes,[330, 331] WGSR, or the Fischer−Tropsch process.[55] To date, Pt nanoparticles dispersed on high specific surface area carbon materials are the best catalysts for FCs.[332–334] FCs are electrochemical edvices that convert directly chemical energy into electricity with high efficiency and low emission of pollutants.[17, 335] The PEMFC is identified as the ultimate power source for transport applications.[18, 336] At the cathode of the PEMFC, the catalytic reaction taking place is the oxygen reduction reaction ($O_2 + 4\,H^+ + 4\,e^- \longrightarrow 2\,H_2O$), while at the anode usually hydrogen or methanol is oxidized ($2\,H_2 \longrightarrow 4\,H^+ + 4\,e^-$ or $CH_3OH + H_2O \longrightarrow 6\,H^+ + 6\,e^- + CO_2$, respectively). Albeit PEMFCs are a promising alternative to the combustion of fossil fuels as a source of energy, some key problems must be overcome to achieve their widespread commercialization.[24] In this vein, one of the challenges arises from the high affinity of Pt towards CO, which eventually leads to the poisoning of the active sites and deactivation of the catalyst.[38–40] CO binds very strongly to the surface of the catalyst, blocking access of reactants and hindering further reactions.

Several methods have been developed to tackle CO poisoning on Pt. One possible way is to promote CO desorption by operating at elevated temperatures. However, high temperatures trigger the sintering of the Pt NPs and increase the energy requirements of the FCs.[337] Another option is to reduce the CO concentration using pressure swing adsorption,[338] methanation of CO,[339] and membrane separation.[340] Unfortunately, these methods are complicated, expensive, and not very efficient. Another route, which has become very popular in the last years, is alloying the catalyst with a second element. This strategy is very promising because it allows the Pt loading in FCs to be reduced. Over the years several dopants have been found to act as promoters on Pt, such as Sn, Ru, Ag, Nb, Mo, Co, Pd, Ni, or

Ir.[341–352] It is believed that the dopant not only induces a geometrical change but also affects the local electronic structure of the Pt active sites.[353] Besides this electronic effect, a bifunctional mechanism has been observed, where the adsorption of a second molecule, such as OH^-, on the dopants enhances the CO oxidation.[350] Quite often a suitable dopant is found by serendipity, and thus it is possible that other useful promoters exist.

In the present chapter, we make use density functional theory (DFT) calculations to test and understand the promotional effect of Ge on Pt for the mitigation of CO poisoning, a promoter which is still hardly understood. Pt_n^+ and $GePt_{n-1}^+$ ($n = 5-9$) clusters in gas-phase are chosen as the system models. Despite differing from real conditions of catalysts in industry, small gas-phase clusters are good model systems to study catalytic reactions due to the ability to control the catalytic properties by modifying the size, composition, and charge state of the system.[354–356] Although the support is absent in these studies, clusters are very useful and convenient owing to the local character of ligand adsorption.

3.2 Computational Methods

Two different methodologies were used to identify the most stable Pt_n^+, $GePt_{n-1}^+$, $Pt_n(CO)^+$, and $GePt_{n-1}(CO)^+$ ($n = 5-9$) structures. First, the PGOPT package,[357] interfaced with the Vienna ab initio Simulation Package (VASP) was used.[358–361] For each cluster between 300 and 800 initial structures were generated as a starting point for geometrical optimization using the bond length distribution algorithm (BLDA).[357] The Perdew-Burke-Ernzerhof (PBE) exchange-correlation functional[362, 363] was used within the projected augmented wave (PAW) method[315] to describe the ionic cores. The planewave kinetic energy cutoff was set to 450 eV, while the self-consistent field (SCF) convergence criterion was fixed at 10^{-6} eV. The unit cell was set to $15\mathring{A} \times 15\mathring{A} \times 25\mathring{A}$ to avoid spurious interactions between repeating images. The DFT-D3 scheme[317] was used to account for the dispersion interactions, thus better describing the interactions between the cluster and the CO/H_2 molecules. Second, we used the DoDo algorithm[364] as implemented in Turbomole 7.4.1.[365, 366] DoDo is a genetic algorithm (GA),

designed to search for the most stable structures of a given composition. In this case the hybrid TPSSh functional[367, 368] was used with the def2-TZVP basis set and the corresponding effective core pseudopotentials (ECP),[369, 370] as well as the DFT-D3 correction. These two different methodologies allow for a thorough exploration of the configurational space and subsequent search of the most stable clusters and cluster complexes. For example, it is known that pure and hybrid DFT functionals might yield different GM of metallic clusters.

The lowest-lying isomers (those within 0.5 eV) identified using both methodologies, were then reoptimized at the LC-ωPBEh/def2-TZVP level of theory[371, 372] with Gaussian 16.[373] LC-ωPBEh was chosen in order to treat long-range charge transfer effects due to the difference in electronegativity between Pt and the dopant. This DFT functional has been used previously with great success for investigating Ag, Au and Pd nanoclusters.[184, 374, 375] Vibrational frequencies were calculated to ensure that the structures were true minima on the PES and to calculate the zero-point energy (ZPE) corrections.

The global minima search of $Pt_n(H_2)^+$ and $GePt_{n-1}(H_2)^+$ ($n = 5 - 9$) clusters was performed using the first methodology explained above (PGOPT), due to the considerable amount of computational work, followed by the geometry reoptimization at the LC-ωPBEh/def2-TZVP level. Different electronic structure tools were used to characterize the bare and complexed clusters: projected density of states (PDOS) calculated with Multiwfn 3.8[376] and natural bond orbital (NBO) analysis.[377]

The binding free energies between the cluster and adsorbates (CO or H_2) were calculated from free energies at 300K as

$$BE[X] = E(\text{cluster-X}) - E(\text{cluster}) - E(\text{X}) \tag{3.1}$$

where $E(\text{cluster-X})$ is the free energy of the cluster with CO or H_2 adsorbed on it, $E(\text{cluster})$ is the free energy of the bare cluster and $E(\text{X})$ is the free energy of isolated CO or H_2.

3.3 Results and Discussion

3.3.1 Interaction Between CO and $(Ge)Pt_n^+$ Clusters

DFT calculations were performed on monometallic Pt_n^+ and Ge-doped $GePt_{n-1}^+$ $(n = 5 - 9)$ clusters, with and without adsorbed CO molecule. To identify the most stable structures, the PES of each structure was carefully scrutinized. A very complex PES was found, with many isomers in a small energy range, with different spin multiplicities (doublet, quadruplet, sextuplet, and even octuplet in the largest monometallic complexes). The $Pt_n(CO)^+$ and $GePt_{n-1}(CO)^+$ $(n = 5 - 9)$ putative global minima structures at the LC-ωPBEh/def2-TZVP level of theory are shown in Figure 3.1. The structures of the bare clusters, *i.e.*, CO dissociation products, are shown in Figure B.1 of Appendix B. All CO-complexes have 3D structures except $GePt_4(CO)^+$, where the dopant induces a change from a 3D to a quasi-planar geometry. For $n = 9$, doping does not have a great impact on the geometry of the cluster; the Ge atom substitutes a Pt atom causing little distortion. However, for the other sizes, the rearrangement upon doping is more significant. In all cases, CO prefers to adsorb in atop configuration with the C atom binding to Pt and forming a Pt$-$C$-$O angle of 180°. Note that, as found in previous studies,[228] Ge reduces the number of unpaired electrons in the small Pt clusters.
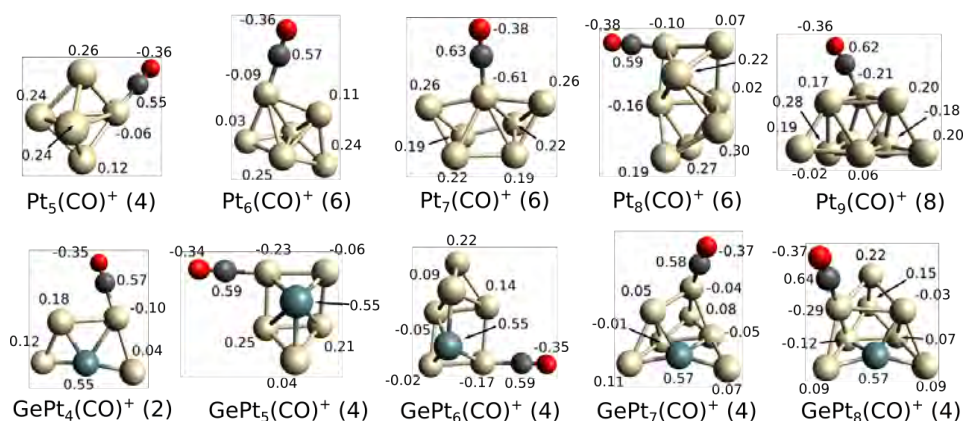
Figure 3.1: Global minimum (GM) structures of the $Pt_n(CO)^+$ and $GePt_{n-1}(CO)^+$ $(n = 5 - 9)$ complexes calculated at the LC-ωPBEh/def2-TZVP level. The multiplicity of each structure is given in parentheses. Natural charges are depicted on the atoms. Pt, Ge, C, and O are depicted in white, dark green, dark grey, and red, respectively.

In order to determine the effect of Ge on the interaction strength between Pt and CO, we computed the CO binding free energies. As shown in Figure 3.2(a), the CO binding free energies change discontinuously with the size of the cluster. When comparing clusters of equal size, it can be seen that the CO binding energies are reduced by up to ~ 0.5 eV upon Ge doping, demonstrating a clear weakening of the Pt$-$CO interaction. The weakening shows pronounced size effects; $Pt_6(CO)^+/GePt_5(CO)^+$ exhibits a small reduction of the binding energy, while for $Pt_9(CO)^+/GePt_8(CO)^+$ the reduction is the largest.
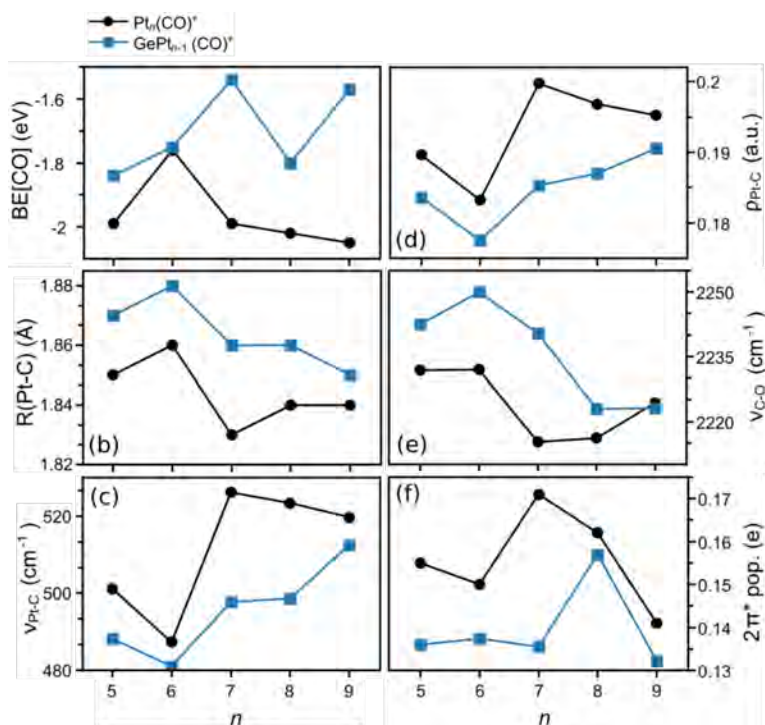
Figure 3.2: Structural and electronic properties of $Pt_n(CO)^+$ and $GePt_{n-1}(CO)^+$ ($n = 5 - 9$) complexes. (a) CO binding free energies, in eV. (b) Pt$-$C bond distance, R(Pt$-$C), in $\mathring{A}$. (c) Pt$-$C stretching frequency, ν_{Pt-C}, in cm^{-1}. (d) Charge density of Pt$-$C bond critical point, ρ_{Pt-C}, in a.u. (e) C$-$O stretching frequency ν_{C-O} in cm^{-1}. (f) $2\pi^*$ population of NBOs, in units of $|e|$.

Besides the CO binding free energies, we analyzed other properties of the adducts to gain deeper insight into the interaction strength between Pt and CO, $i.e.$, Pt$-$C bond length and stretching frequency, as well as the electron density at that bond

critical point. An overview of these properties is given in the different panels of Figure 3.2, as a function of cluster size. As it can be seen in Figures 3.2(b) and (c), the Pt−C bond lengths increase, and the Pt−C vibrational frequencies decrease upon Ge doping, evidencing the weakening of the bond. Similarly, the Pt−C bond critical points, ρ_{Pt-C}, are smaller in the doped compounds (Figure 3.2(d)), indicating again a weaker Pt−C bond strength when alloying Pt clusters with Ge. Thus all the studied electronic parameters point to the weakening of the Pt−CO interaction upon doping, suggesting that Ge could be a promising dopant to help mitigate the CO poisoning of Pt catalysts. This is also true for $GePt_5(CO)^+$; despite that its calculated CO binding energy is similar to that of the pure Pt_6^+ cluster, all other analyzed properties indicate a weakening of the bond in the presence of the Ge dopant.

The interaction between TMs, especially Pt, and CO has become a widely studied problem in surface science. Over the years, different models have been developed to explain CO adsorption. The Blyholder model is simple but effective and provides an illustrative picture of the Pt−CO interaction. This model only involves CO frontier molecular orbitals (MOs) and a donor-acceptor mechanism is used to explain the bonding, namely electron density donation from 5σ highest occupied molecular orbital (HOMO) of CO to Pt unoccupied d orbitals and electron density back-donation from Pt occupied d orbitals to CO $2\pi^*$ lowest unoccupied molecular orbital (LUMO).[353, 378, 379]

In order to understand the effect that Ge exerts on the electronic structure of Pt clusters, the NBO charges of $Pt_n(CO)^+$ and $GePt_{n-1}(CO)^+$ clusters were calculated. The values of these charges are shown in Figure 3.1, next to each atom in the cluster structures. The natural charges of the bare clusters are given in Figure B.1 of Appendix B. Pt atoms carry more negative charge in the Ge doped clusters than in the pure Pt clusters, indicating an overall charge transfer of *ca.* 0.55 |e| from Ge to Pt. CO has a slightly more positive charge after adsorption on the doped clusters.

Considering the natural charges, it could be concluded that Ge weakens the Pt−CO binding by reducing the CO → Pt σ-donation step in the Blyholder model, since the Pt atomic orbitals (AOs) have less capacity to take electrons in the presence
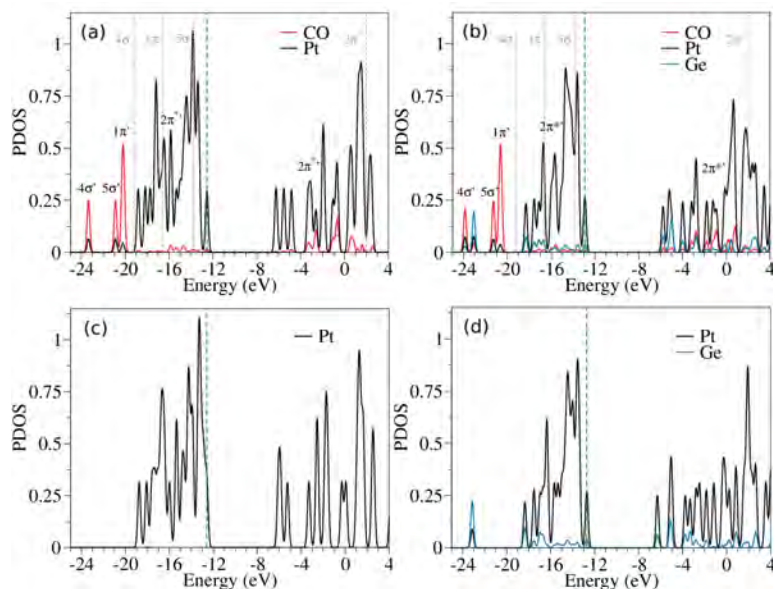
Figure 3.3: Projected density of states (PDOS) of the complex and bare cluster pair for $n = 5$. (a) $Pt_5(CO)^+$, (b) $GePt_4(CO)^+$, (c) Pt_5^+ and (d) $GePt_4^+$. Gaussian full width at half-maximum (FWHM): 0.3 eV. For the sake of clarity only the α electrons are shown. The green dashed vertical line indicates the position of the α HOMO orbital. The energy of the free CO MOs is given by the grey vertical dashed lines.

of Ge. However, a closer look at the electronic structure of the clusters indicates otherwise. First, using the Natural Bond Orbital (NBO) analysis, the population of CO $2\pi^*$ MOs was calculated, as shown in Figure 3.2(f). Overall, the population of $2\pi^*$ MO (related to the π-back-donation) is significantly less populated in the doped ones. Second, upon CO adsorption, the C−O stretching frequency is lowered (see Figure 3.2(e). Such redshift originates from the Pt $\rightarrow$ CO π-back-donation to the $2\pi^*$ MO, which results in a population of the CO antibonding MO, destabilizing the CO bond and lowering the C−O stretching frequency.[380] The effect of the redshift on the C−O frequency, however, is milder in the doped clusters, corresponding to a smaller π-back-donation. Third, the projected density of states (PDOS) of the $Pt_n(CO)^+$ and $GePt_{n-1}(CO)^+$ complexes were computed, projected into CO, and the AOs of Pt and Ge atoms. For the sake of brevity, the PDOS of Pt_5^+ and $GePt_4^+$ with and without CO are shown in Figure 3.3, and the PDOS of the other sizes are given in Figure B.2 and B.3 of Appendix B.

Comparing the PDOS of bare Pt_5^+ and $GePt_4^+$ clusters, the d band of Pt is narrowed in the latter. In this region, the AOs of Pt and Ge hybridize, forming covalent bonds between them, as opposed to a more metallic and delocalized bonding characteristic of pure metal clusters. Due to the electronegativity difference (Pt 2.28 *vs* Ge 2.01), such bonds are polarized, which explains the above-mentioned charge transfer from Ge to Pt. When CO is adsorbed, its 4σ, 5σ, and 1π MOs are stabilized due to the interaction with the cluster. The 5σ MO undergoes the greatest shift (located at *ca.* -21 eV), as a result of the hybridization with Pt's AOs. The 5σ orbital is located at similar energies in the CO complexes of monometallic and doped clusters. In fact, in this energy region, there is hardly any contribution from the dopant atom. Thus, Ge has no influence on the σ-donation step. Regarding the CO 2π* antibonding MO, it hybridizes with Pt AOs, resulting in levels with partially 2π* character below E_F, in the same energy range where the overlap between Pt and Ge AOs occurs (*ca.* from -19 to -12 eV). This result suggests that the availability of Pt AOs to interact with CO 2π* is compromised, due to the Pt−Ge bonds. Therefore, the presence of Ge weakens the Pt−CO interaction by hindering the Pt $\rightarrow$ CO π-back-donation. Doping Pt with Ge shows a promising way to mitigate the CO poisoning.

3.3.2 H$_2$ Dissociation on (Ge)Pt$_n^+$ Clusters

Finally, with the aim of verifying that the catalytic activity of Pt is not suppressed after doping it with Ge, we studied the H_2 adsorption on pure and doped clusters. The mechanism of the Hydrogen Oxidation Reaction (HOR) taking place at the anode of PEMFCs is beyond the scope of this work. Instead, we looked at the Tafel step needed to initiate this reaction, which is the rate determining step in Pt(111),[381] *i.e.*, $H_2 \longrightarrow 2\,H_{ads}$.

We found that in all of the clusters, H_2 prefers to adsorb on Pt where it is dissociated spontaneously. Thus, the doped clusters remain catalytically active towards the dissociation of H_2. The optimized geometries of $Pt_n(2H)^+$ and $GePt_{n-1}(2H)^+$ GM complexes are presented in Figure B.4 of the Appendix B. Furthermore, previous works demonstrated that for several Pt-based catalysts, HOR activity increases as the H binding energy decreases.[34, 382, 383] The computed binding energies,
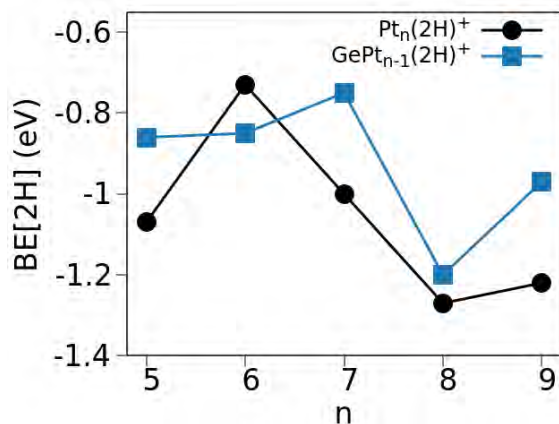
Figure 3.4: 2H binding free energies (BE[2H]), in eV, of $Pt_n(2H)^+$ and $GePt_{n-1}(2H)^+$ ($n = 5 - 9$) GM computed at the LC-ωPBEh/def2-TZVP level.

BE[2H] are shown in Figure 3.4. With the exception of $Pt_6(2H)^+/GePt_5(2H)^+$, the doped clusters exhibit slightly reduced binding energies. Therefore, the presence of Ge not only does not impede the H_2 dissociation, but facilitates the desorption of the product.

3.4 Conclusions

The vulnerability of Pt towards CO poisoning is a major drawback affecting the efficiency and the long-term performance of Fuel Cells' electrodes. In the present work, by a combination of DFT calculations, we show that alloying Pt with Ge leads to more stable catalysts with higher resistance to deactivation via CO poisoning. The configurational space is thoroughly explored using GM search techniques, to identify the most stable $Pt_n(CO)^+$ and $GePt_{n-1}(CO)^+$ ($n = 5 - 9$) complexes. A detailed analysis of their electronic structure reveals that the interaction between Pt and CO is weakened in the presence of Ge. It is found that the availability of Pt d orbitals is compromised due to the covalent interactions with Ge, and as a result, the Pt $\rightarrow$ CO 2π-back-donation step is hindered. Finally, H_2 is spontaneously dissociated when adsorbing on the clusters, suggesting that the catalytic activity of Pt is retained upon the inclusion of Ge. Ge can be a promising alloying agent to tune the selectivity of Pt and improve the CO poisoning resistance, and could

open the way to a novel family of hybrid catalysts in Fuel Cells. The effect might be dependent on the concentration of the dopant, and we plan to perform further studies in this direction.

Role of Composition of Small-Size PtGe Bimetallic Clusters on the CO Poisoning

"I am, a stride at a time. A very short space of time through very short times of space. Five, six: the nacheinander. Exactly: and that is the ineluctable modality of the audible. Open your eyes. No. Jesus! If I fell over a cliff that beetles o'er his base, fell through the nebeneinander ineluctably. I am getting on nicely in the dark. My ash sword hangs at my side. Tap with it: they do. My two feet in his boots are at the end of his legs, nebeneinander. Sounds solid: made by the mallet of Los Demiurgos. Am I walking into eternity along Sandymount strand?"

— James Joyce, *Ulysses*

In this chapter, a computational study of the interaction between small-size PtGe bimetallic clusters and CO is performed. The main objective is to understand the role of Ge concentration on the CO poisoning. For this, a global minima search is carried out on $\mathrm{Pt}_{n-m}\mathrm{Ge}_m(\mathrm{CO})$ ($3 \leq n \leq 10$, $0 \leq m \leq 9$) complexes, followed by a detailed analysis of the electronic structure. Ge concentration is found to

be a key parameter in catalyst design. The obtained results reveal a volcano-shape dependence of the CO binding energies with Ge concentration. Equimolar compositions are found to be the clusters with greatest resistance to CO. This can be explained in terms of an extra stabilization of the clusters given by the formation of the Pt−Ge polarized covalent bonds. Such stabilization has three sources: thermodynamic, electrostatic and covalent. Precisely, equimolar clusters show the greatest number of Pt−Ge bonds (mixing), maximizing the stabilization.

4.1 Introduction

THE rapid growth of population over the last decades has increased significantly the global energy demands. As for now, fossil fuels including coal and natural gas are the main sources of energy.[1] The limited supplies and environmental impact of such fuels have raised serious concerns in the current energy industry landscape. Consequently, there is an urge to develop a greener and more sustainable energy industry.[9, 11, 12, 384–386]

FCs have gained a growing interest as a possible alternative to overcome the current energy crisis.[14–16] FCs convert the chemical energy of a fuel directly into electricity with a high efficiency. Among FCs the PEMFC has gained a lot of attention in recent years.[20, 21, 23, 24] The half reactions taking place at the anode and cathode of PEMFC are the hydrogen oxidation reaction (HOR) and oxygen evolution reaction (ORR), respectively. The PEMFC is regarded as a clean energy source since only water is produced, and could help establish the so-called hydrogen economy.[50–54]

Carbon supported Pt-based catalysts are used in both electrodes due to their high activity for HOR and ORR.[29, 31] Note that Pt is a rare and expensive element, albeit PEMFCs rely on this metal. Thus, to make PEMFCs commercially viable, Pt loading should be reduced and its durability improved. In this vein, the use of small-size clusters as catalytic systems has attracted a lot of attention since they allow a maximal utilization of the atoms. Besides, decreasing the size of the nanoparticles to the subnanometer size regime can lead to remarkable catalytic properties.[94, 95]

Another major drawback of PEMFCs is the so-called CO poisoning of the catalyst. Indeed, the high activity of Pt is followed by a high affinity towards CO, which is found in the hydrogen feed stream produced from hydrocarbon reforming.[38–41] Even with a relatively small CO concentration (*i.e.*, $10-100$ ppm), the catalyst can undergo a severe poisoning. CO covers the active sites of the catalytic surface hindering the reaction and thus, diminishing the power density produced by the cell. Note that Pt nanoclusters are poisoned in a similar way to larger nanoparticles. Therefore, CO poisoning is one of the most important issues that must be solved in order to achieve a routine use of the PEMFCs.

A very promising route to tackle CO poisoning is the use of Pt bimetallic catalysts.[350] Alloying permits the use of more economical elements and thus decreases the cost of the FC. Different promoters have been proposed such as Ru,[343, 344] Sn,[344, 345] Mo,[346–348] Nb,[347] Co,[349, 387] Ni,[351] Ag[341] and Au,[342] as well as multimetallic alloys.[388] Promoters act either modifying the electronic structure of Pt (ligand effect) or the adsorption properties of the system (bifunctional effect).[350, 389]

In this chapter we perform first principles calculations to investigate the effect of Ge concentration on the CO-tolerance of Pt. Clusters of different size and composition are studied in gas-phase to determine the optimal dopant concentration that simultaneously reduces the poisoning and maintains the catalytic power of Pt nanocatalysts. As we will show, clusters with roughly the same amount of Pt and Ge exhibit an outstanding resistance against CO poisoning. The reason for such tolerance is traced down to electronic effects. Our results suggest that Ge could be a promising promoter to improve the durability of Pt catalysts, opening the way to novel alternatives for FCs.

4.2 Computational Methods

The calculations were performed with plane wave-density functional theory (PW-DFT) and PAW pseudopotentials,[315] as implemented in the Vienna ab initio simulation package (VASP).[358–361] The PBE[362, 363] version of the exchange-correlation functional was chosen. A $15\mathring{A} \times 15\mathring{A} \times 25\mathring{A}$ unit cell was used to avoid

spurious interactions between nearby images. The Brillouin zone was sampled at the Γ point. The plane wave cutoff energy was truncated at 450 eV and a convergence criteria of 10^{-6} eV and 10^{-5} eV/$\mathring{A}$ was employed for the electronic energy and the geometry relaxation, respectively. In addition, Gaussian smearing method was used to describe the electronic occupations with a sigma value of 0.1 eV. Grimme's semiempirical DFT-D3 scheme[317] of dispersion correction was adopted for a better description of the interactions between the cluster and adsorbate. The global minima structures of $Pt_{n-m}Ge_m(CO)$ ($3 \leq n \leq 10, 0 \leq m \leq 9$) and $Pt_{n-m}Ge_m(2H)$ ($n = 4, 6, 8, 10; 0 \leq m \leq 7$) complexes in gas-phase were obtained with the global optimization PGOPT package.[357] Within this toolkit, for each cluster between 300 and 800 initial structures were generated as a starting point for geometry optimization using the bond length distribution algorithm (BLDA). All the calculations are spin polarized to allow the structures to relax to the most stable spin state. Energy barriers for H_2 dissociation were computed with the climbing image nudged elastic band (CI-NEB) method.[390, 391] Convergence for the forces was set to 0.05 eV $\mathring{A}^{-1}$ and the saddle point nature of the transition state was verified with a vibrational analysis.

Several energetic descriptors were evaluated to study the effect of size and dopant concentration on the structural stability of the clusters. In gas phase, the intracluster binding energy per atom (E_b) is calculated as follows

$$E_b = \frac{1}{N}[E(Pt_nGe_m) - nE(Pt) - mE(Ge)], \qquad (4.1)$$

where $E(Pt_nGe_m)$, $E(Pt)$ and $E(Ge)$ are the total energies of the Pt_nGe_m cluster and an isolated Pt and Ge atom. $N = n + m$ is the total number of atoms. The mixing energy (Δ) is an indicator of the stability of the binary cluster with respect to its unitary counterparts:

$$\Delta = E(Pt_nGe_m) - n\frac{E(Pt_N)}{N} - m\frac{E(Ge_N)}{N}, \qquad (4.2)$$

where $E(Pt_N)$ and $E(Ge_N)$ are the total energies of the monometallic Pt_N and Ge_N with size $N = n + m$. The binding energy of CO and H_2 to the cluster was calculated as:

$$BE[X] = E(\mathrm{Pt}_{n_m}\mathrm{Ge}_m(X)) - E(\mathrm{Pt}_{n-m}\mathrm{Ge}_m) - E(X), \qquad (4.3)$$

where $E(Pt_{n-m}Ge_m(X))$ is the energy of the $\mathrm{Pt}_{n-m}\mathrm{Ge}_m$(X) complex with X, $E(Pt_{n-m}Ge_m)$ is the energy of the bare $\mathrm{Pt}_n\mathrm{Ge}_m$ cluster optimized from the complex geometry (dissociation product), and E(X) is the energy of the isolated X molecule (X = CO, H_2).

To study the chemical bonding in terms of n centers and 2e bonds (Lewis structure-like picture), the Adaptive Natural Density Partitioning (AdNDP) tool was used.[392] For this analysis, gas-phase clusters were re-optimized using Gaussian 16 program[373] with the PBE functional and def2-TZVP basis set.[369, 370]

4.3 Results and Discussion

4.3.1 $\mathrm{Pt}_{n-m}\mathrm{Ge}_m(\mathrm{CO})$ ($3 \leq n \leq 10$, $0 \leq m \leq 9$) Complexes

In order to study how the propensity of Pt catalysts for CO poisoning changes with Ge concentration, first a thorough analysis of the potential energy surface of pure and doped $\mathrm{Pt}_{n-m}\mathrm{Ge}_m(\mathrm{CO})$ ($3 \leq n \leq 10, 0 \leq m \leq 9$) complexes was performed. For the sake of clarity, during the discussion we will mostly focus on the smallest and the largest clusters, *i.e.*, 4 and 10 atom clusters with varying PtGe composition. We anticipate that equivalent conclusions can be drawn for clusters of other sizes. The optimized structures of $\mathrm{Pt}_{n-m}\mathrm{Ge}_m$ and $\mathrm{Pt}_{n-m}\mathrm{Ge}_m(\mathrm{CO})$ ($n = 4, 10; 0 \leq m \leq 9$) are shown in Figure 4.1, and the rest are given in Figures C.1 and C.2. CO always binds to Pt and the atop configuration is found to be the most stable adsorption mode, with a Pt−C−O angle of 180º. The only exceptions are $\mathrm{Pt}_7\mathrm{Ge}_2(\mathrm{CO})$ and $\mathrm{Pt}_7\mathrm{Ge}_3(\mathrm{CO})$ where CO binds to two Pt atoms in a bridge configuration. The smallest monometallic $\mathrm{Pt}_n(\mathrm{CO})$ complexes (n $\leq$ 6) tend to adopt planar structures, whereas Ge doping favors more globular geometries. Similar results were obtained for PtCo clusters.[393] Note that, as found in previous works,[228, 394, 395] Ge quenches the unpaired electrons of Pt (*e.g.*, 7 in $\mathrm{Pt}_{10}(\mathrm{CO})$ *vs* none in $\mathrm{Pt}_{10-m}\mathrm{Ge}_m(\mathrm{CO})$ when $m \geq 2$). Another important observation is that there is a very good mixing between Pt and Ge, similar to SiO_2 and $\mathrm{Al}_2\mathrm{O}_3$ supported PtS_n clusters.[394, 395] Rather than separating into two different phases, Pt and Ge tend to maximize the number

of heteronuclear bonds. This is in contrast to other alloys, such as, PtRu[396, 397] and PtRe[398] clusters, where Ru/Re atoms tend to separate from Pt. As found in Chapter 3, the desorption of CO does not alter the geometry of the nanoclusters significantly (Figure 4.1 a and c and Figure C.1), except in Pt_2Ge_2, where the cluster undergoes a transition from tetrahedral to planar geometry.
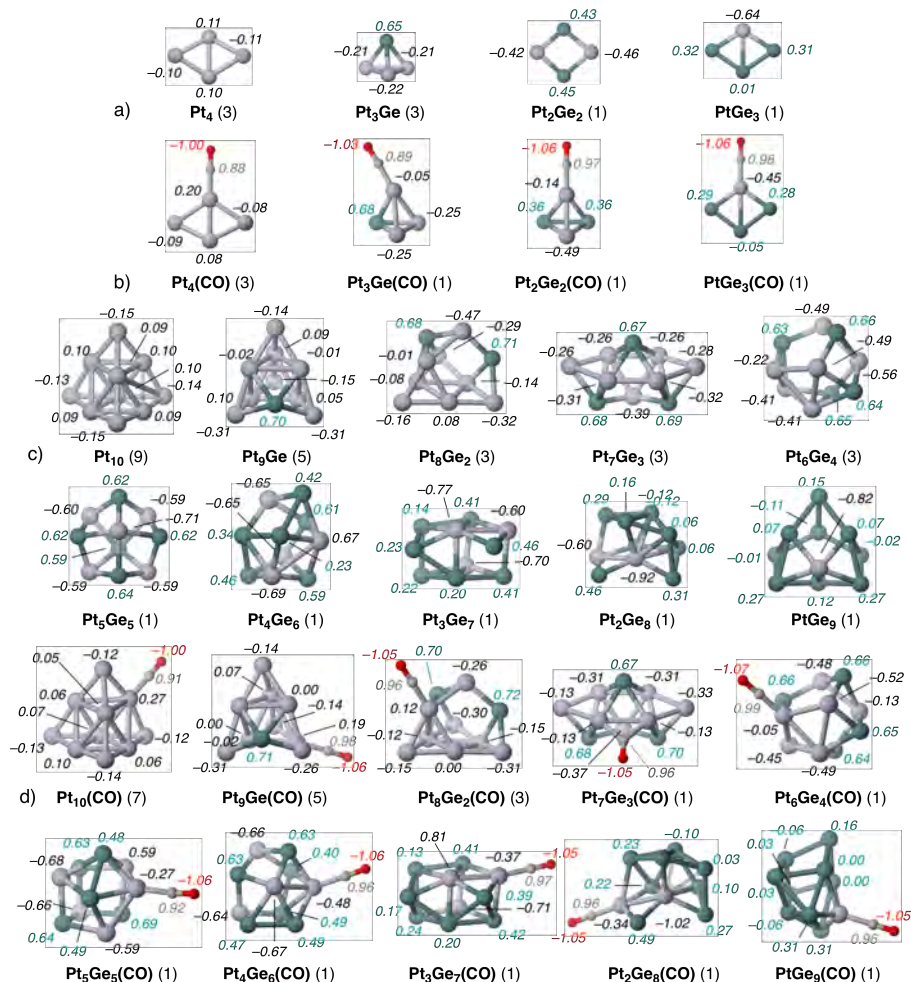
Figure 4.1: a) $Pt_{4-m}Ge_m$, b) $Pt_{4-m}Ge_m(CO)$ $(0 \leq m \leq 3)$, c) $Pt_{10-m}Ge_m$ and d) $Pt_{10-m}Ge_m(CO)$ $(0 \leq m \leq 9)$ geometries. The multiplicity $(2S+1)$ of each structure is given in parentheses. Bader charges are printed on the atoms in values of |e|. Pt, Ge, C, and O are depicted in grey, green, dark grey and red, respectively.

The probability of a catalyst to undergo CO poisoning will be dictated by the strength of the P−CO bond. Thus, to assess the tendency of the monometallic and alloyed catalysts to poison, the CO binding energies to the nanoclusters were computed. The results are summarized in Figure 4.2 and Table C.1. The substitution of a single Pt atom with Ge does not systematically decrease the CO bond strength. Instead, the BE[CO] starts decreasing mildly with increasing Ge content, until an abrupt drop occurs. As can be seen in Figure 4.2, for clusters with an even number of atoms the sudden drop of the BE[CO] occurs in the species that have the same amount of Pt and Ge. The reduction in the binding energy of CO in these equimolar clusters is enormous. For instance, for $n = 4$ the BE[CO] is reduced by *ca.* 1.7 eV. Because CO always bonds to Pt, it could be expected that increasing the Ge content would be beneficial to mitigate the CO poisoning. Nonetheless, our results clearly show that when Ge concentration exceeds that of Pt, the affinity to CO recovers moderately. The only exception is Pt_3Ge_5 that exhibits a slightly lower BE[CO] compared to Pt_4Ge_4 (-1.42 eV *vs* -1.64 eV). In the case of clusters with an odd number of atoms, there is no such a clear pattern on how the Pt−CO bond strength changes as a function of the composition. For the smallest clusters, Ge-rich compositions provide the weakest Pt−CO interaction. But as the clusters become larger, the lowest BE[CO] values are obtained with intermediate compositions, more similar to the behavior of the clusters with an even number of atom.

These results imply that the dopant concentration is a critical parameter to consider in the design of Pt-based catalysts. In PtGe alloys it is found that intermediate compositions exhibit the largest resistance towards CO poisoning. Such compositions minimize the interaction between Pt and CO, and will improve the durability of the catalyst. Lower and higher Ge concentrations will yield a weaker resistance against CO poisoning. Note that these compositions have the advantage of reducing the Pt loading while offering a large amount of active sites.

To understand the effect of Ge on the cluster−CO bonding, the Bader charges were computed, as shown in Figure 4.1 and Figures C.1 and C.2. In all cases charge is transferred from the dopant to Pt (electronegativity of Pt 2.28 *vs* Ge 2.01) and from the cluster to CO. A closer inspection of Figure C.1 suggests a limit to the amount of electron donation. At high Ge concentration there is a significant drop
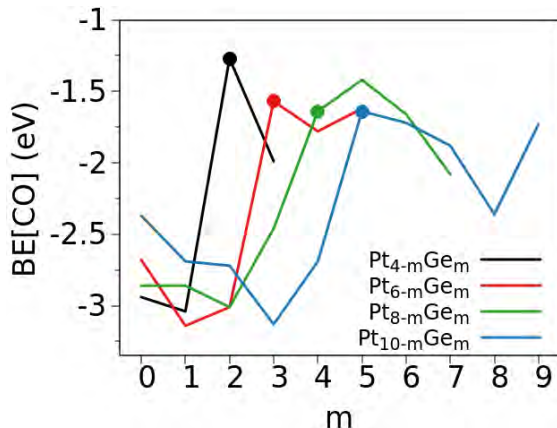
Figure 4.2: CO binding energies (eV) of $Pt_{n-m}Ge_m$ ($3 \leq n \leq 10$, $0 \leq m \leq 9$) clusters.

of charge in Ge atoms; *viz.*, ~ 0.6 |e| in Pt_5Ge_5 and ~ 0.1 |e| in $PtGe_9$. Although the charge on Pt can continue increasing slightly up to 0.8 |e| in the larger clusters.

The interaction between TMs and CO can be rationalized using the Blyholder model,[353, 378, 379] where the bonding is explained in terms of electron density donation from 5σ MO (HOMO) of CO to TM unoccupied d Atomic Orbitals, AOs, and electron density back-donation from TM occupied d AOs to CO $2\pi^*$ MOs (LUMO). Projected density of states (PDOS) were computed to understand the effect of the dopant on the donation and back-donation steps.

The PDOS of $Pt_{4-m}Ge_m(CO)$ ($0 \leq m \leq 3$) and $Pt_{10-m}Ge_m(CO)$ ($m = 0, 1, 5, 9$) are illustrated in Figure 4.3, while the rest are given in C.4. The total DOS after adsorption is projected onto the CO molecule (orange), sum of all Pt s atomic AOs (red), sum of all Pt p AOs (blue), sum of all Pt d AOs (black), and sum of all Ge atoms (green). After adsorption, the CO MOs are downshifted to lower energies relative to the gas phase values in all the clusters due to the interaction with Pt. On the one hand, CO $2\pi^*$ broadens and becomes populated below the E_F as a result of the hybridization with Pt d AOs, suggesting the weakening of the C−O. In the region where the back-donation occurs (from *ca.* -5 eV to E_F) an overlap between Pt and Ge AOs can be observed in all the PtGe clusters. These results suggest that the dopant influences the back-donation step by compromising the availability of Pt d AOs due to the formation of Pt−Ge bonds. This same phenomenon was observed

in Chapter 3. Note that in few cases a single Ge atom does not weaken the Pt−CO interaction (for example Pt_3Ge or Pt_7Ge) and the contribution of the dopant in the back-donation region is indeed minimal, as observed in the PDOS plots.

On the other hand, the 5σ MO of CO is stabilized as a result of the electron donation from the 5σ to empty Pt d AOs, with a clear overlap between these orbitals around -8 eV. In Pt-rich complexes, there is no contribution from Ge in this energy range. At larger dopant concentrations, however, Ge AOs start to overlap with the Pt AOs involved in the donation to CO, therefore, affecting the donation step too. Such an overlap might also lead to a Pauli repulsion weakening the Pt−C bonding, as was previously reported.[399] Although the Blyholder model does not include the 1π MO of CO, in our studies we found that 5σ and 1π MOs of CO are intimately related, being located at similar energies. Both 5σ (*e.g.*, in $Pt_5Ge_5(CO)$) and 1π (*e.g.*, in $Pt_2Ge_2(CO)$) participate in the bonding with Pt, depending on the cluster size. In summary, Ge alloying weakens the Pt−CO interaction, by compromising the availability of Pt AOs to interact with CO, due to the formation of Pt−Ge bonds. In Pt-rich clusters, Ge only affects the back-donation step, but at larger concentrations Ge blocks the donation step too. Nevertheless, the PDOS cannot fully explain why the CO binding energy is minimized in the equimolar clusters, while Ge-rich compositions mildly recover the Pt−CO interaction strength. Thus, several structural and energetic properties of the bare clusters will be analyzed in the following section.

4.3.2 $Pt_{n-m}Ge_m$ ($3 \leq n \leq 10$, $0 \leq m \leq 9$) Clusters

In order to understand what makes the reactivity of equimolar clusters towards CO unique, we have analyzed their thermodynamic stability by means of the intracluster binding energy and the mixing energy (see the Methods section). The data corresponding to the clusters with an even number of atoms are depicted in Figure 4.4 (see Table C.1 for the rest of the structures), where an unexpected trend can be observed for both of these properties.

First, the intracluster binding energy reaches a minimum value in clusters with equal amounts of Pt and Ge, showing the greatest internal stability. Indeed, the strong intracluster bonding is responsible for the spin quenching, as was observed
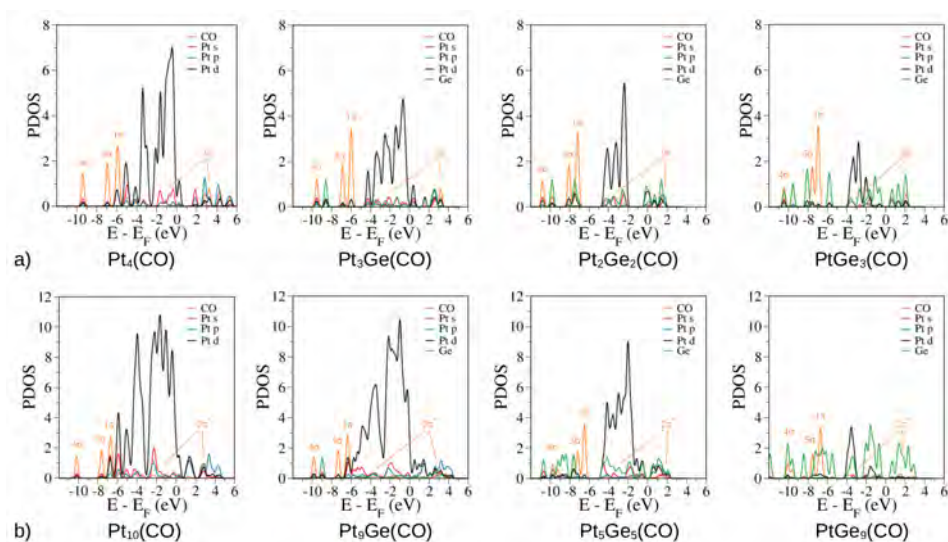
Figure 4.3: Projected density of states (PDOS) of a) $Pt_{4-m}Ge_m(CO)$ ($0 \leq m \leq 3$) and b) $Pt_{10-m}Ge_m(CO)$ ($m = 0, 1, 5, 9$) complexes. The Fermi energy (E_F) is set to zero in all cases. Only α channel is plotted in spin polarized systems.

in $PtSn/SiO_2$.[394] Moreover, the stability of the clusters increases with the size, suggesting that the observed enhanced stability in 1:1 compositions will remain in larger nanoparticles too. Although it is out of the scope of this work, we could hypothesize on the effect that Ge exerts on the sintering propensity of Pt. The intracluster binding energies increase with the size of the cluster regardless of the composition. However, the stabilization gained with size is larger for monometallic clusters. For instance, Pt_{10} is 1.07 eV more stable than Pt_4, while Pt_5Ge_5 is 0.66 eV more stable than Pt_2Ge_2. Therefore, the propensity to sinter or aglomerate should be lessened upon alloying.

Second, the mixing energy is negative for all the studied clusters, indicating a favorable metal mixing instead of a metal separation tendency. The most negative mixing energies are obtained once again for equimolar clusters, exhibiting an outstanding mixing between Pt and Ge. Pt tends to become surrounded by Ge and vice versa, instead of forming islands of Pt and Ge (refer to Figure 4.2 and Figure C.1). In the same line, larger clusters have higher mixing energies. Therefore, clusters with Pt:Ge 1:1 ratio are exceedingly stable, and this conclusion could be

transferred to larger nanoparticles. In clusters with an odd number of atoms a similar trend can be observed for intracluster binding energies and mixing energies. Note that a high degree of atomic mixing can be extremely important for the stability of a catalyst. In $PtSn/Al_2O_3$ catalysts used in dehydrogenation reactions, for instance, Pt and Sn atoms tend to form segregated phases under certain reaction conditions, a fact that leads to a rapid deactivation of the catalyst.[400]
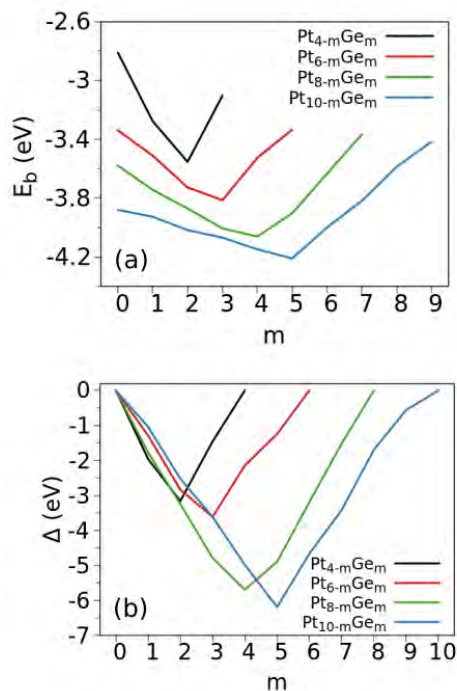
Figure 4.4: a) intracluster binding energies per atom (eV) and b) mixing energies (eV) of $Pt_{n-m}Ge_m$ ($3 \leq n \leq 10$, $0 \leq m \leq 9$) clusters.

To gain insight into the origin of the affinity between Pt and Ge, the AdNDP tool was used to study the chemical bonding in $Pt_{n-m}Ge_m$ ($n = 4, 10$; $m = 2, 5$) clusters, collected in Figure 4.5. AdNDP achieves a seamless description of systems featuring both localized and delocalized bonding, by allowing the interpretation of chemical bonding in terms of n-center two electrons (nc-2e) and n-center one electron (nc-1e) bonds. First, Pt_4 was analyzed in its triplet electronic ground state. AdNDP localizes 16 lone-pairs (4 on each Pt atom) with an occupation number $ON = 1.57$ |e|, while the rest of the electronic density is delocalized over several

atoms. Two 3c-2e bonds (ON = 1.98 |e|) on each triangle that form the tetramer, and one 4c-2e bond (ON = 1.98 |e|) delocalized over the entire molecule. The two unpaired electrons are localized on two additional 3c-1e bonds with ON = 0.99 |e|. Similarly, Pt_{10} exhibits a delocalized bonding too: thirty lone-pairs (ON = 1.83 |e|) and sixteen 3c-2e bonds (ON = 1.97 |e|) on every external triangular face of the cluster. Additionally, the cluster has 8 unpaired electrons and they are localized as follows: four on 3c-1e bonds (ON = 0.99 |e|) on the internal triangular faces and four 4c-1e bonds (ON = 0.93 |e|), similar to what was found in Au_{20}.[401]

In contrast, all the electron pairs in Pt_2Ge_2 and Pt_5Ge_5 can be localized in lone-pairs and 2c-2e covalent bonds. Pt_2Ge_2 possess ten lone-pairs with ON = 1.80 |e| (three on each Pt and two on each Ge atom) and four covalent 2c-2e bonds with ON = 1.98 |e|. And in Pt_5Ge_5 all the electron pairs are localized in fifteen 1c-2e with ON = 1.84 |e| (three on each Pt) and twenty covalent 2c-2e bonds with ON = 1.86 |e| between every Pt−Ge pair. This analysis clearly shows that while delocalized bonding dominates in monometallic clusters, Pt and Ge bond through covalent bonds. A similar chemical bonding picture can be likewise inferred from the PDOS of the complexes (Figure C.4). Indeed while pure Pt clusters have bands that are spread over a larger energy range characteristic of a delocalized bonding, as Ge concentration increases (and specially in equimolar clusters), the total DOS becomes more fragmented and localized, characteristic of a strong covalency. A closer inspection of these PDOS suggests that the Pt−Ge bonding is done through Pt sd hybridized AOs, with a small contribution of Pt p AOs that are populated below E_F. When the amounts of Ge and Pt are similar, the number of heteronuclear bonds is maximized and the number of homonuclear bonds is minimized, conferring these species high thermodynamic stability.

Furthermore, there is an additional electrostatic stabilization in equimolar clusters. As explained above, due to the difference in the electronegativity, the covalent Pt−Ge bonds are polarized resulting in an effective charge transfer from Ge to Pt (see Bader charges in Figure 4.1). In clusters with Pt:Ge 1:1 ratio, there is an alternation of atoms with positive and negative partial charges, leading to an additional electrostatic stabilization of these compounds. A similar effect was found in equimolar PtPd clusters.[190] To summarize, the strong covalency and
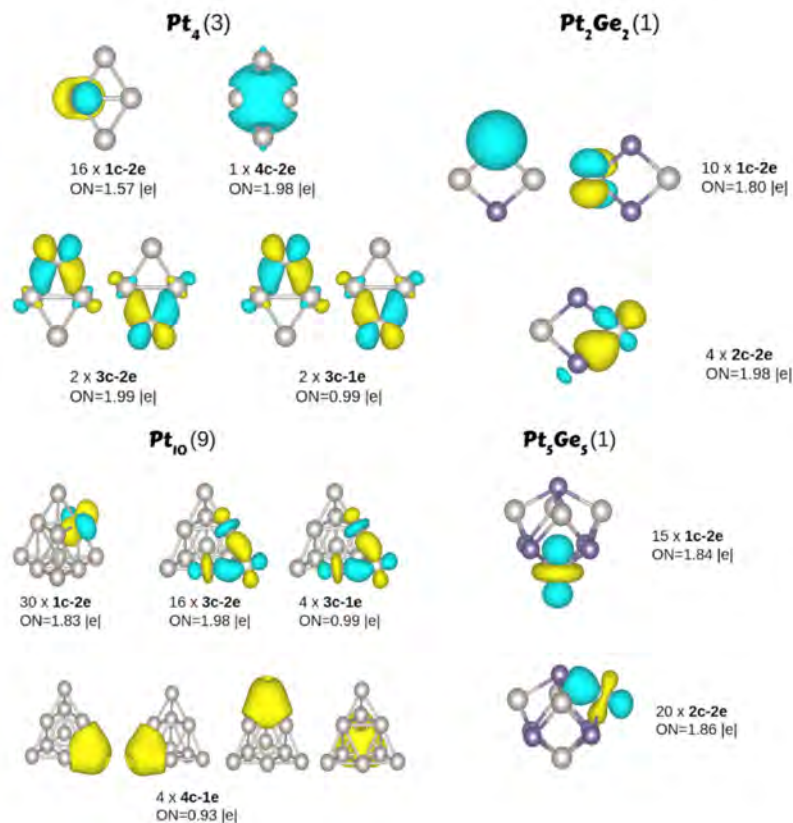
Figure 4.5: AdNDP analysis of Pt_4, Pt_2Ge_2, Pt_{10} and Pt_5Ge_5 clusters. The multiplicity $(2S + 1)$ of the cluster is given in parentheses.

electrostatic stabilization arising from the advantageous $Pt-Ge$ mixing make the equimolar clusters highly resistant towards CO poisoning and therefore, more durable.

4.3.3 H_2 Adsorption on $Pt_{n-m}Ge_m$ $\left(3 \leq 10,\ 0 \leq m \leq 9\right)$ Clusters

Hitherto, we have shown that doping Pt clusters with Ge improves the selectivity towards CO. In order to check whether these clusters are still active towards hydrogen oxidation (HOR), the Tafel step was considered, *i.e.*, the first step in the HOR occurring at the anode of the PEMFC:[381] $H_2 \longrightarrow 2\,H_{ads}$. Due to the vast amount of clusters in this work, we focused on the adsorption of H_2 and 2H on $Pt_{n-m}Ge_m$ $(n = 4, 6, 8, 10;\ 0 \leq m \leq 7)$. The geometries of the $Pt_{n-m}Ge_m$(2H)

($n = 4, 6, 8, 10; 0 \leq m \leq 7$) GM are presented in Figure C.3. As found in Chapter 3, in both monometallic and Ge-alloyed clusters dissociated H_2 is more stable than non-dissociated H_2, where H is always adsorbed on Pt. When H_2 was adsorbed on pure and doped clusters it was found that, on most of the compounds, H_2 dissociation is a barrierless process. In the cases where the reaction is not spontaneous, the barriers were computed and they are small: Pt_2Ge_2 (0.09 eV), Pt_3Ge_3 (0.22 eV), Pt_2Ge_4 (0.01 eV), Pt_3Ge_5 (0.11 eV), Pt_5Ge_5 (0.07 eV). These results suggest that the clusters will still remain active upon alloying. Finally, the computed H binding energies depicted in Figure 4.6 show that hydrogen bonds more weakly as the Ge content increases, facilitating the desorption of the product. Therefore, clusters containing roughly the same amount of Pt and Ge are not only predicted to be exceptionally resistant towards CO poisoning, but also remain catalytically active towards HOR.
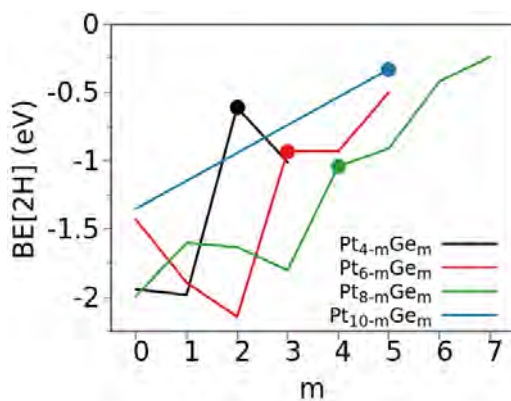
Figure 4.6: 2H binding energies (in eV) of $Pt_{n-m}Ge_m(2H)$ ($n = 4, 6, 8; 0 \leq m \leq 7$) global minima.

4.4 Conclusions

The high activity of Pt is accompanied by a high affinity for CO and thus, it is extremely susceptible to poisoning. CO molecules, part of the reaction or present as a contaminating agent, can hinder the catalytic reactions by blocking the active sites and deactivating the catalyst. This CO poisoning is a major drawback for the commercialization of PEMFCs.

In this chapter, using advanced global minima search techniques and exhaustive electronic structure characterization, the promoter concentration is pinpointed as a crucial factor to improve the CO tolerance of Pt catalysts. By investigating PtGe bimetallic clusters of different sizes and compositions we found that, for those clusters with roughly the same amount of Pt and Ge, the binding to CO is extraordinarily weakened. Such compositions minimize the interaction between Pt and CO, and will improve the durability of the catalyst. Lower and higher Ge concentrations will yield a weaker resistance against CO poisoning. Note that these compositions have the advantage of reducing the Pt loading while offering a large amount of active sites.

The uniqueness of the PtGe equimolar cluster is traced down to electronic effects, *i.e.*, ligand effects. The intermediate compositions provide the maximum number of heteronuclear (Pt−Ge) and the minimum number of homonuclear (Pt−Pt and Ge−Ge) bonds, conferring them high thermodynamic stability. Such a favorable mixing leads to the blocking of both donation and back-donation steps in the Pt−CO interaction. Furthermore, since the Pt−Ge bonds are polarized, clusters with 1:1 Pt:Ge ratio exhibit an alternation of atoms with positive and negative partial charges, leading to an additional electrostatic stabilization of these compounds. Our results demonstrate that Ge could be a promising alloying agent to mitigate the deactivation of Pt and more importantly, the promoter concentration is a critical factor in the design of advanced catalysts.

CO Oxidation Performance of Bimetallic $\mathbf{Pt_4Ge_n}$ Clusters $\mathbf{(n = 0 - 4)}$ Supported on MgO

"Ahead of us lie war and endless strife,
Such that my failing heart despairs of life.
I see what has to be, and choose the way
Of silence since there is no more to say:
But for the Persians I will weep, and for
The House of Sasan ruined by this war:
Alas for their great crown and throne, for all
The royal splendor destined now to fall,
To be fragmented by the Arabs' might;
The stars decree for us defeat and flight.
Four hundred years will pass in which our name
Will be forgotten and devoid of fame."

— Ferdowsi, *Shahnameh*

In this chapter, a computational study of the catalytic activity of small-size PtGe bimetallic clusters for the CO oxidation is carried out. The main objective is to discern the role of Ge concentration on the catalytic properties and find the optimal composition. For this task, a global minima search is carried out to locate the most stable Pt_4Ge_nX ($n = 0 - 4$, X = CO, O_2, 2×O) complexes supported on MgO(100). A very concise mechanistic study is done by a combination of DFT transition state search and microkinetic modeling. Both Langmuir−Hinshelwood and Eley−Rideal pathways are considered. The obtain results hint to a Ge concentration dependence on the catalytic activity, Pt_4Ge_3 being the most active catalyst. The promotional effect is traced down to ligand and bifunctional effects. PtGe clusters show a dual adsorption where CO is adsorbed only on Pt and Ge preferentially to Ge. Through a bifunctional mechanism, part of Ge becomes oxidized to GeO_x, which acts as an independent oxygen reservoir, resistant to CO poisoning. Besides, the portion of Ge remaining on the nanoalloy exerts ligand effects and decreases the CO binding energy to similar values to that of oxygen.

5.1 Introduction

CARBON monoxide (CO) is an odorless gas which is extremely hazardous for health and the environment. It is usually produced as a result of the incomplete combustion of hydrocarbon compounds. Thus the catalytic oxidation of CO has become a crucial step for the control of CO emissions in a wide range of processes, such as vehicle exhaust treatment and purification of hydrogen for fuel cell applications. Moreover, due to its simplicity, CO oxidation is used as a probe reaction to model more complex reactions such as the Fischer−Tropsch synthesis.[402–404]

PGMs including Pt, Pd, Rh, *etc.* are widely known for their excellent catalytic activity for many reactions of critical importance such as CO oxidation.[405] Catalyst NPs are usually stabilized by dispersion over metal-oxide supports in industrial applications.[406] CO oxidation usually displays bistable kinetics over Pt.[407] At low temperature and/or low O_2 pressure, it suffers from CO self–poisoning (chemical deactivation), slowing down the reaction rate. The catalyst surface is then saturated

with a CO layer that prevents the coadsorption of O_2. Therefore, there are not enough free active sites in which the O_2 molecules can impinge and react with the coadsorbed CO, and the catalyst is rendered totally inactive after solely a few number of catalytic cycles, costing billions of dollars annually in the industry.[337, 408] At high temperature and/or high O_2 pressure on the other hand, a first order kinetic phase transition (*i.e.*, alteration of the adsorbates adsorption–desorption equilibrium) occurs leading to a more reactive state. Now, the adsorbed CO reacts immediately increasing the CO_2 formation rate and dissociated O becomes the predominant species. Since high temperature favors catalyst deactivation due to sintering and coking, CO poisoning imposes severe constraints over the maneuverability of the optimal operating reaction conditions. This scenario together with the high cost and limited availability of Pt hampers its use in large–scale production.

Subnanometer clusters have attracted a widespread attention in the last decades since they show unique catalytic properties compared with larger NPs due to finite-size effects.[64, 94, 95, 97] In this regime the catalytic properties become size dependent to the extreme that the addition or subtraction of a single atom can have a drastic impact on them; this is the regime where each atom counts.[409, 410] More importantly, they possess a huge surface to volume ratio which allows a maximal utilization of atoms, *i.e.*, the so–called atomic efficiency. It is important to note that, treating clusters as static structures has been shown to be a simplified picture.[169–171] In reality, clusters display high fluxionality at usual operating temperatures and form an ensemble of statistically relevant isomers, each of which exhibits different catalytic properties and constantly interconverting in response to external stimuli. All in all, clusters present a very strong structure–activity relationship by which the catalytic properties can be tuned by physical and chemical modifications (*e.g.*, size, composition, support, ligand capping, *etc.*); in short, clusters offer a myriad of possibilities for nanocatalyst design.

Alloying the catalyst with an ancillary element is a promising strategy to mitigate CO poisoning.[350] One of the advantages of this strategy is that it allows a reduction in the Pt loading, making them more attractive for commercialization. It is desirable that the bimetallic catalyst should maintain at least the same catalytic activity as Pt, as well as improve the selectivity towards different poisons. Several

Pt–based bimetallic systems have been found in the last years for CO oxidation. For instance, PtNi/γ-Al$_2$O$_3$,[411] PtFe/GA,[412] PtFe/γ-Al$_2$O$_3$,[412] PtSn/AC,[413, 414] PtRu/SiO$_2$[415] and PtRe/SiO$_2$[416] outperform their monometallic counterparts with higher CO conversion rates. The enhancement of the bimetallic catalysts is usually ascribed to ligand (electronic) and/or bifunctional effects. Ligand effects occur when the alloying element modifies the Pt electronic structure (*e.g.*, electron donation and back-donation capacity of Pt) without directly participating in the reaction, while in bifunctional effects the promoter becomes an active component either by forming new bimetallic active ensemble sites or offering new single active sites with different adsorption properties (dual adsorption). This dual adsorption can be achieved by incorporating oxophilic promoters into Pt so that the oxygenated species now adsorb preferentially on them, leaving the Pt sites free for CO adsorption and thus, facilitating CO oxidation.[350, 389]

Building from the previous chapters, herein, we combine first-principles calculations with microkinetic modeling to determine the role of Ge in the CO oxidation by PtGe bimetallic clusters supported on MgO(100). Our aim is to verify whether the reduction of CO poisoning found thereof translates into an improvement of the catalytic activity and what PtGe composition provides the best performance for this reaction. The influence of the Ge concentration on the CO and O$_2$ adsorption properties and the catalytic behavior is thoroughly studied. A concise mechanistic study of CO oxidation is carried out by exploring and unraveling the kinetic details of the two main pathways, *viz.*, Langmuir−Hinshelwood (LH) and Eley−Rideal (ER), along with the electronic reasons behind the observed behavior. In this way, we demonstrate that it is possible to change the bistable kinetics towards a reactive and CO poisoning-free region by adjusting the promoter content on PtGe catalysts.

5.2 Computational Methods

5.2.1 DFT Calculations

DFT calculations were done using the PBE exchange-correlation functional[362, 363] and the PAW pseudopotentials[315] as implemented in the Vienna ab-initio simulation package (VASP).[358–361] The plane wave cutoff energy was set at

450 eV and a convergence criteria of 10^{-6} eV and 10^{-5} eV was employed for the electronic energy and the geometry relaxation, respectively. In addition, we included Grimme's semiempirical DFT-D3 corrections[317] to account for the dispersion interactions. The Brillouin zone was sampled using a $1 \times 1 \times 1$ Monkhorst-Pack mesh centered at the Γ point.

The PtGe clusters were supported on a MgO(100) $4 \times 4 \times 3$ slab composed of 6 layers. The bottom two layers of the support were fixed at the positions of the bulk, while the top four layers were allowed to relax. Periodic images in z direction were separated with *ca.* 15 $\mathring{A}$ of vacuum. The same ensemble of Pt_4Ge_n/MgO(100) ($n = 0 - 4$) isomers as reported in ref. [229] were used in this work. CO and O_2 molecules were adsorbed in all possible orientations on these catalysts with the global optimization toolkit PGOPT.[357] PGOPT uses the bond length distribution algorithm (BLDA) to generate a pool of initial adsorption geometries. Transition states (TSs) were located with the climbing image nudged elastic band (CI-NEB) method.[390, 391] It must be mentioned that in a few cases a preliminary CI-NEB run with low convergence criteria was performed followed by a tighter convergence calculation using the improved dimer method.[417, 418] Due to the high computational cost, we only included the 2 uppermost MgO layers and the criteria for the forces was set to 0.05 eV$\mathring{A}^{-1}$. The nature of the transition states was confirmed with a vibrational analysis, making sure that they only displayed a single imaginary frequency along the reaction coordinate.

The binding energy of CO and O_2 was calculated with the following formula:

$$BE[X] = E(Pt_4Ge_n(X)/MgO) - E(Pt_4Ge_n(X)/MgO) - E(X) \qquad (5.1)$$

where E(Pt_4Ge_n(X)/MgO) is the energy of Pt_4Ge_n cluster ($n = 0 - 4$) supported on MgO with one X molecule adsorbed, E(Pt_4Ge_n/MgO) is the energy of the bare Pt_4Ge_n cluster supported on MgO and E(X) is the energy of the isolated X molecule in gas phase (X = CO, O_2). The same reference E(O_2) is used for O_2 and $2 \times O$ adsorption.

5.2.2 Microkinetic Modeling

Microkinetic modeling is a powerful technique used to analyze complex catalytic networks in terms of elementary reactions.[319, 320] Herein, no assumptions are made, *a priori*, about the rate-determining steps or surface coverage of intermediate species. In this fashion, measured or calculated parameters such as activation and reaction free energies can be incorporated into the rate expressions. Regarding the reactor model, a CSTR was chosen to solve the rate equations. In this way, the time evolution of the coverages and pressures of each species can be obtained. The details of the reaction network are given in the Supporting Information. The simulations were run for at least 10^7 s to ensure convergence to a dynamic steady-state. An important point should be made here mentioning that the achieved dynamic steady-state differs significantly from the thermodynamic equilibrium as there is a continuous gas inlet and outlet which brings the system out of equilibrium in a dynamic way.[419] The total flow rate was set to 8 ml min^{-1} with different O_2:CO compositions. 100 mg of catalyst was used with a Pt loading of 0.35 wt%, based on previous experimental work.[219, 420] Pt and Ge sites were treated equivalently in the spirit of the mean-field approach.

For surface reactions, the rate constants for the forward elementary reactions were determined by the transition state theory (TST)

$$k_{f,i} = \frac{k_B T}{h} e^{-\Delta G_i^{\ddagger}/k_B T} \tag{5.2}$$

where k_B is Boltzmann's constant, h is Planck's constant and T is the temperature. $\Delta G_i^{\ddagger}$ is the Gibbs free activation energy of the ith elementary reaction. The equilibrium constants K_i were calculated as follows:

$$K_i = e^{-\Delta G_i/k_B T} \tag{5.3}$$

where ΔG_i is the Gibbs free energy of the ith elementary reaction. To ensure thermodynamic consistency the reverse rate constants were calculated using the corresponding forward rate constant and equilibrium constant:

$$\frac{k_{f,i}}{k_{r,i}} = K_i \tag{5.4}$$

The ideal gas limit was considered to compute the changes in free energy:

$$\Delta G = \Delta(E_{\text{elec}} + \text{ZPE}) - T\Delta S \qquad (5.5)$$

where E_{elec} is the DFT computed electronic energy, ZPE is the zero-point energy and ΔS is the change in entropy. The ZPE was calculated from the vibrational analysis. For adsorbed species only the harmonic vibrational contribution to entropy was considered, while translational and rotational entropies were also included for gas phase species.

For non-activated unimolecular adsorption, the rate of adsorption is determined by the kinetic theory of gases:[327]

$$k_{\text{ads}} = \frac{PA}{\sqrt{2\pi m k_B T}} S \qquad (5.6)$$

where P is the partial pressure of the adsorbate, m is the mass of the adsorbate and A is the area of the adsorption site. The adsorption site area was set equal to the area of the adjacent triangle. For O_2 chemisorption (bridge site), the area was approximated as the area of a triangle of sides $Pt-Pt-Pt$. For CO chemisorption (top site), the area was set to one-third of the area for O_2. S is the sticking coefficient and was set to 1 for all species, based on their favorable adsorption energies.

5.3 Results and Discussion

5.3.1 CO and O_2 Adsorption on Pt$_4$Ge$_n$/MgO(100) (n $= 0 - 4$)

Before moving to the discussion of the CO reaction mechanisms we first study the adsorption of the reactants, *viz.*, CO and O_2, on Pt$_4$Ge$_n$/MgO with $n = 0-4$. These surface-mounted nanoclusters have been recently characterized and are predicted to be synthetically accessible under Ge-rich conditions.[229] For each composition, various conformers would coexist since they are energetically competitive, except for Pt$_4$Ge in which a single isomer, the GM, dominates the population. Note that, while all the bimetallic clusters have a closed-shell electronic structure, Pt$_4$/MgO possesses unpaired electrons in most cases.[229] Because isomers can exhibit different reactivity, CO and O_2 were adsorbed on the most populated conformers of each Pt$_4$Ge$_n$ composition. The resulting most stable adsorption geometries along with the CO and O_2 binding energies (BEs), Boltzmann populations of each structure at

500K, and Bader effective charges are summarized in Figure 5.1. The first thing to note is that after adsorption the size of the ensemble and the relative stability of the isomers changes, showing the dynamic effect of adsorption.[169] CO adsorption has a profound effect on the cluster population. For instance, in Pt_4Ge_3, isomer IV in ref [229] (population at 500K of 8.3%) becomes predominant upon CO adsorption, while the most stable bare clusters become negligible. In general, CO prefers to adsorb on Pt through the C end in an atop configuration ($\angle$ Pt−C−O 180º), with a few exceptions, where it binds in a bridge fashion. CO adsorption has little impact on the cluster geometry, and CO is never found adsorbed on Ge which indicates the much higher preference towards Pt.

O_2 is found to adsorb either dissociatively ($2 \times O^*$) or non-dissociatively (O_2^*). Contrary to CO, oxygen can bind to both Pt and Ge, the most common active site being a bimetallic PtGe ensemble. In the dissociative adsorption atomic O binds in a M−O−M bridge configuration, while in the non-dissociative adsorption it usually adopts a M−O−O−M two-member bridge site. It should be noted that in many isomers O^* adsorbs at the cluster-support interface bonded to a Mg atom, which is in stark contrast to CO. Moreover, a significant distortion is observed upon adsorption due to the oxophilicity of Ge. In some adducts (*e.g.*, Pt_4Ge2O isomer I) O^* opens the Pt−Ge polar bonds deforming the structure. This effect may become more significant at strong oxidizing conditions.

The Sabatier principle states that the binding strength between reactants and catalysts should not be very strong to avoid overbinding and poisoning effects, nor very weak to give enough time for diffusion and collision. In addition, the products should interact weakly with the surface to guarantee a facile desorption. In Figure 5.1, pure Pt_4CO presents the largest CO binding energy (isomer I, BE[CO] = -3.13 eV), suggestive of a tendency to undergo CO poisoning. Nonetheless, adding a single Ge atom in Pt_4GeCO, the BE[CO] is reduced to -2.63 eV; and as the Ge concentration increases a gradual drop in the BE[CO] is observed. This trend is in line with previous observations in gas-phase (Chapters 3 and 4). According to the Bader analysis (Figure 1) and projected density of states (PDOS, Figure E.1), there is a net charge transfer from the cluster to CO $2\pi^*$. As a result, the C−O bond is weakened and elongated slightly from 1.14 $Å$ in gas–phase to ~ 1.17 $Å$.

As stated above, for O$_2$ both the molecular and dissociative adsorptions are competitive. Comparing the binding energies to oxygen it is evident that the latter is more stable than the former; as explained in the next section, O$_2$ dissociation is an exothermic process. Overall, CO is more strongly adsorbed than molecular oxygen. The same is true for atomic oxygen in monometallic and Pt$_4$Ge clusters. However, as the Ge concentration increases, the adsorption of 2×O* becomes stronger than that of CO* by more than 2 eV in Pt$_4$Ge$_3$ and Pt$_4$Ge$_4$, meaning that O* may become the predominant species on the catalyst surface. Regardless of the adsorption mode, O atoms carry a negative charge owing to an electron transfer from the cluster to the empty 2π* orbitals. As expected, dissociated O* has a significantly larger charge than molecular O$_2$* since a single atom is interacting with two Pt or Ge atoms. Depending on the degree of activation (O$-$O elongation) molecular O$_2$* can change its electronic state. In gas-phase the diatomic distance is 1.21 $\mathring{A}$ (bond order = 2). Upon adsorption, the internal bond weakens (bond order reduction) and elongates. If one electron is transferred to oxygen, the superoxo (O$_2^-$) state is obtained with a O$-$O bond distance of $\sim$ 1.33 $\mathring{A}$ (bond order $\sim$ 1.5). O$_2$* can still accept another electron and achieve the peroxo (O$_2^{2-}$) state with a O$-$O bond distance of $\sim$ 1.47 $\mathring{A}$ (bond order $\sim$ 1.0). Our calculations suggest a large oxygen activation for the PtGe nanoclusters. The internal bond is increased up to $1.47 - 1.50$ $\mathring{A}$ in the bidentate bridge configuration, indicating the presence of a peroxo state; while in the top configuration it is only activated until the superoxo state with a bond length of 1.37 $\mathring{A}$. We believe that such a high activation translates into low oxygen dissociation barriers.
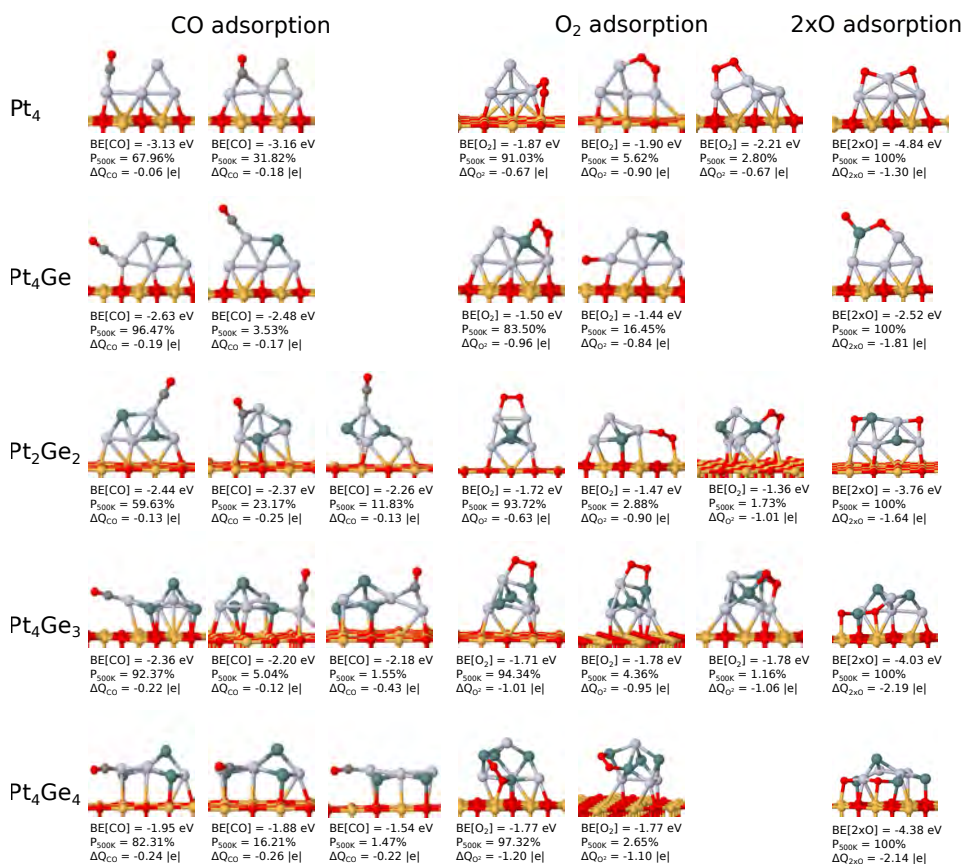
Figure 5.1: Most stable CO, O_2 and $2\times O$ adsorption geometries on Pt_4Ge_n/MgO(100) clusters along with the ligand binding energies (BEs) in units of eV, Boltzmann populations at 500 K (P_{500K}) and charge transfer to ligand (ΔQ) in values of $|e|$. Only isomers with $P_{500K} > 1.00\%$ are shown. Pt, Ge, Mg, O and C are depicted in gray, dark green, orange, red and dark gray, respectively.

5.3.2 O$_2$ Dissociation on Pt$_4$Ge$_n$/MgO(100) (n $= 0 - 4$)

To investigate the O$_2$ molecular and dissociative adsorption mechanisms, we have
computed the O$_2$ dissociation barriers The energy profiles for the different Pt$_4$Ge$_n$
clusters are collected in Figure 5.2. Here, we only show the results for the pathways
with the most stable Pt$_4$Ge$_n$2O final state (FS) adducts for each cluster; the rest of
the isomers are depicted in Figures E.2, E.3, E.4 and E.5 of the Appendix E.

After O$_2$ chemisorption, the cluster activates the O$-$O bond by transferring
electrons to the antibonding 2π* orbitals. For the bridge adsorption mode O$_2$ is
activated in the peroxo state where the IS structure is close to the transition state
(TS). The cluster continues to stretch the bond until finally the O$-$O scission is
achieved. In all cases the O$-$O bond is already cleavaged in the TS, even for the
atop adsorption (see Figure E.2). Our calculations reveal that the O$-$O bond
expands from ~ 1.47 $\AA$ to a value in the range of $1.90 - 2.15$ $\AA$ in the TS. Here the
charges of the O atoms are maximal; each atom carries $0.6 - 0.8$ |e| comparing to
~ 0.4 |e| in the IS. The values of these charges are similar for adsorption on Pt$-$Pt
and Pt$-$Ge of M$-$O$-$O$-$M bridge sites. For the numerical values of the oxygen
Bader charges and O$-$O distances the reader is referred to Table E.1. Afterwards,
the O atoms separate and occupy a bridge site in the vicinity. This process is found
to be exothermic, the greatest energy release occurring when the strong Ge$-$O
bonds distort the cluster structure (*e.g.*, Pt$_4$Ge$_4$ isomer II, Figure E.5). Overall,
the activation barriers are small and most cases lie in the range of $0.4 - 0.6$ eV,
although there are some exceptions where the barrier increases to 0.75 eV, as for the
Pt$_4$Ge$_3$ isomer I (see Figure E.4). Our results indicate that at room temperature
most of the adsorbed oxygen will be in the form of atomic O*.

a) Pt$_4$

O$_2$*   TS (0.39 eV)   2O* (-2.00 eV)

b) Pt$_4$Ge

O$_2$*   TS (0.19 eV)   2O* (-1.54 eV)

c) Pt$_4$Ge$_2$

O$_2$*   TS (0.30 eV)   2O* (-2.45 eV)

d) Pt$_4$Ge$_3$

O$_2$*   TS (0.38 eV)   2O* (-2.43 eV)

e) Pt$_4$Ge$_4$

O$_2$*   TS (0.48 eV)   2O* (-2.70 eV)
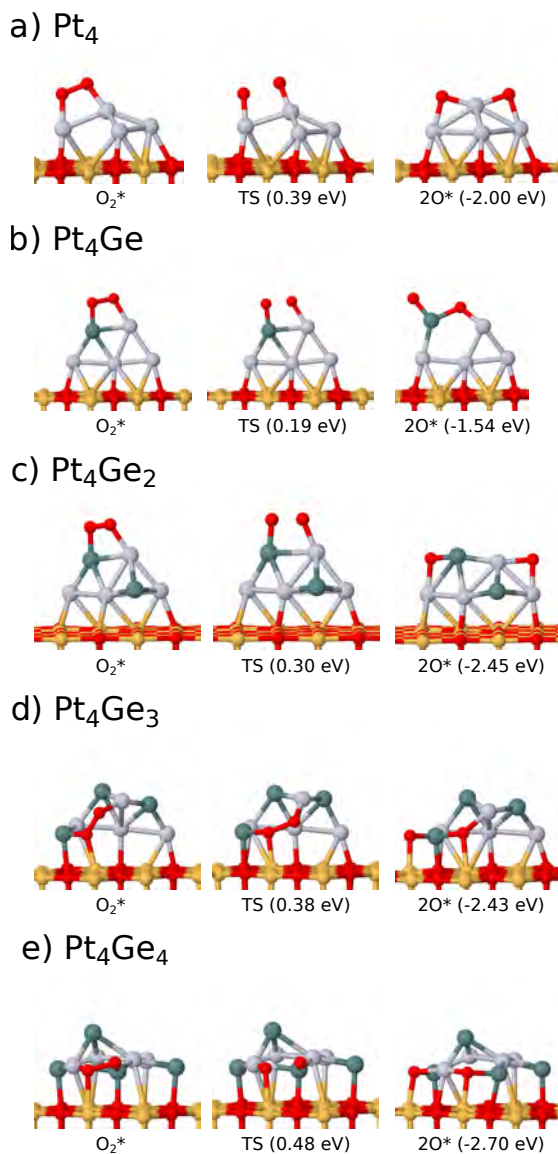
Figure 5.2: Initial state (IS), transition state (TS) and final state (FS) geometries for the O$_2$ dissociation pathway on the Pt$_4$Ge$_n$/MgO(100) isomers with the most stable final state (FS). Activation and reaction energies (in eV) are given relative to the corresponding IS. Pt, Ge, Mg, O and C are depicted in gray, dark green, orange, red and dark gray, respectively.

5.3.3 CO Oxidation on Pt$_4$Ge$_n$/MgO(100) (n = 0 − 4)

Here, we characterize the potential energy surface of CO oxidation on Pt$_4$Ge$_n$ clusters ($n = 0 - 4$) supported on MgO(100). On Pt-based catalysts, CO oxidation usually proceeds via the bimolecular LH or ER mechanisms. In LH prior to the reaction both CO and O$_2$ are adsorbed on the surface, that is, co-adsorption of the reactants is required. Then the reactants diffuse to adjacent sites and react with each other to form CO$_2$, which is released to the environment. Besides, the ER mechanism only involves O$_2$ adsorption followed by a CO attack in the gas-phase. As has been confirmed in the previous section, all clusters present small oxygen dissociation barriers. Hence, CO will be able to react not only with O$_2$* but also with O*; in other words, both O$_2$ and O are available as oxygen sources. We must highlight that all the possible reaction mechanisms were characterized by considering two different structures for each Pt$_4$Ge$_n$/MgO, the isomers with the most stable IS and FS in the O$_2$ dissociation shown in Figures 5.2 and Appendix E. Pt$_4$Ge$_n$O$_2$ was used to study the routes involving CO + O$_2$, while Pt$_4$Ge$_n$2O was employed for the CO + 2×O paths. Since the starting point involves two oxygen atoms in either case, two steps will be needed to complete the catalytic cycle, *i.e.*, the formation of two CO$_2$ molecules.

5.3.3.1 Eley−Rideal Mechanism

The ER mechanism takes place when CO in the gas-phase attacks O$_2$* or predissociated O* on the surface. Given the small size of the nanoclusters explored in this work, the variety of co-adsorption configurations is limited, and hence the ER mechanism may actually be a competitive mechanism within this size regime. Figure 5.3 shows the reaction pathways for both CO(g) + O$_2$* and CO(g) + 2×O* for all Pt$_4$Ge$_n$ considered in this section. For the sake of clarity, we only show the results for the first CO$_2$ formation in both routes; the second CO$_2$ formation is depicted in Figure E.6.

As depicted in Figure 5.3, CO(g) attack to O$_2$* always occurs from the C end. As CO approaches the molecules, the O−O bond starts activating until the TS is reached. It should be remarked that the TS is effectively achieved only under certain angles of attack ($\angle$ O−C−O* between 120º and 125º). In the TS, CO(g) is found at

a distance of ~ 1.70 Å from O_2. The CO internal bond is almost unchanged while $O-O$ is activated to ~ 1.68 Å. After the energy barrier is successfully overcome, CO_2 is directly ejected from the surface without the formation of an intermediate state (IM). The corresponding energy barriers for this route are rather small; Pt_4 has a barrier of 0.25 eV, whereas in the nanoalloys it lies in the range of $0.30-0.60$ eV. In contrast, in the most likely route, the $CO(g) + 2\times O^*$ route (Figure 5.3), the barriers on Pt_4 increase up to 0.80 eV. Pt_4Ge (second step) and Pt_4Ge_4 (first step) also show high barriers of 1.0 eV, whereas in the clusters with medium Ge content they remain below 0.60 eV. All steps are found to be exothermic. These results suggest that Pt_4Ge_2 and Pt_4Ge_3 are the most active compositions. Nonetheless, as long as there is predissociated O*, *i.e.*, CO poisoning is avoided, the reaction will move forward in all cases and thus, the ER channel will proceed similarly regardless of the PtGe composition.

5.3.3.2 Langmuir−Hinshelwood Mechanism

In Figure 5.4 we display the reaction pathways through the first step of the LH channel for CO oxidation by both molecular and atomic oxygen on Pt_4Ge_n clusters; the second step is depicted in Figure E.7.

To search for the most suitable starting point a screening of the most stable co-adsorption complexes was done by adsorbing CO with multiple orientations on adjacent sites to O_2^* or O* in $Pt_4Ge_nO_2$ and Pt_4Ge_n2O. We begin with the CO* + O_2^* reaction (Figure 5.4). As the reactants approach each other the $O-O$ bond is elongated and the reaction proceeds via the first TS to an intermediate (IM). It should be mentioned that in many cases[421] this first step involves the formation of a OCOO* species in the IM. However, our calculations for PtGe reveal that the cleavage of $O-O$ and formation of $C-O$ occurs simultaneously in the first step, so CO_2^* is already formed in the IM. Apart from Pt_4Ge, oxygen is already dissociated in the TS. The charge of the reacting O increases up to ~ 1.0 |e|. In the IM complex CO_2 is usually bonded from the C atom to Pt with a $Pt-C$ distance of ~ 2.05 Å and has an internal angle of $\sim 130^\circ$. When the reaction occurs close to the interface, CO_2 also binds to a substrate Mg atom via one of the oxygens. Subsequently, there is a barrierless release of the formed CO_2 molecule to the environment, leaving an

Figure 5.3: Most stable reaction pathways for the Eley−Rideal (ER) mechanism for both molecular and dissociated oxygen reactions on Pt$_4$Ge$_n$/MgO(100). Initial state (IS), transition state (TS) and final state (FS) geometries are shown together with the relative activation and reaction energies (in eV). Only the first step is given. Pt, Ge, Mg, O and C are depicted in gray, dark green, orange, red and dark gray, respectively.

O* on the surface to further oxidize another CO molecule.

Pure Pt$_4$ presents small barriers for the first (0.19 eV) as well as the second step (0.50 eV). Regarding the bimetallic counterparts, the first step for Pt$_4$Ge and Pt$_4$Ge$_2$ are also rather small (0.29 and 0.52 eV), whereas the second barrier becomes significantly large (> 1.5 eV), while O* has to migrate from one very stable bridge position to the adjacent one. In Pt$_4$Ge$_3$ the first CO$_2$ formation shows a barrier of 0.78 eV, while in Pt$_4$Ge$_4$ both barriers are around 0.55 eV. The first step is always more exothermic than the second as the O−O scission releases extra energy. CO$_2$ desorption is found to be endothermic with a BE of around 0.10 eV and 0.30 eV in the first and second steps, respectively.

The most likely scenario, however, is the one where CO* reacts with predissociated O* (CO* + 2×O*), as shown in Figure 5.4. A detailed inspection reveals that in the TS of this channel CO* and O* are closer than in CO* + O_2*. The reactants are bonded on top of neighbouring atoms and oriented parallel to each other, forming a cyclic Pt−C−O−Pt(Ge) structure. The length of the "to be formed" C−O bond lies between 2.75 and 2.90 Å. Such TS structure has also been observed previously in the CO oxidation by small Pd clusters.[422] Contrary to the previous pathway, Pt_4 has to overcome now larger barriers of ∼ 1.0 eV in both steps. Surprisingly, on Pt_4Ge the first step proceeds almost barrierless, although the second oxidation is highly unfavorable. On the contrary, Pt_4Ge_2 and Pt_4Ge_3 show the best balance between the two steps with low barriers. Moreover, in this route the first IM formation is significantly less exothermic since the reaction starts from a very stable complex. Except for Pt_4Ge_4 (0.85 eV), the first IM formation is still slightly exothermic, while the second step is predicted to be exothermic only on Pt_4Ge_3 and Pt_4Ge_4 (see Figure E.7). Another observation of critical importance is the fact that CO_2 removal becomes highly endothermic in Pt_4, especially in the second step, as opposed to the alloys. This suggests a tendency to get poisoned by CO_2.

It is extremely important to consider the statistical weights of each reaction channel. Indeed, the most likely reaction mechanism for LH will be connected to atomic oxygen. In this case bimetallic clusters present lower energy barriers as compared to pure Pt, as well as the inhibition of the CO and CO_2 poisoning effects.

For the sake of comparison, the complete potential energy diagram of the LH mechanism with predissociated oxygen on all the Pt_4Ge_n nanoclusters is illustrated in Figure 5.5 (the reader is referred to Figure S10 for the results of the other cases). It can be observed that the LH mechanism lies lower in energy than ER since it includes the adsorption of both O_2 and CO, while ER is missing the adsorption of CO. In the ER mechanism for both CO(g) + O_2* and CO(g) + 2×O* (Figure E.8), all steps are exothermic (downhill) for all clusters, the CO_2 release being the most stable state. Consequently, this state will act as a thermodynamic sink shifting the reaction towards CO_2 formation, regardless of the Ge concentration. Notwithstanding, as shown in Figure 5.5, in the LH mechanisms O* + CO* (IS3, O* + CO*) becomes the most stable state for Pt_4, Pt_4Ge and Pt_4Ge_2 due to the
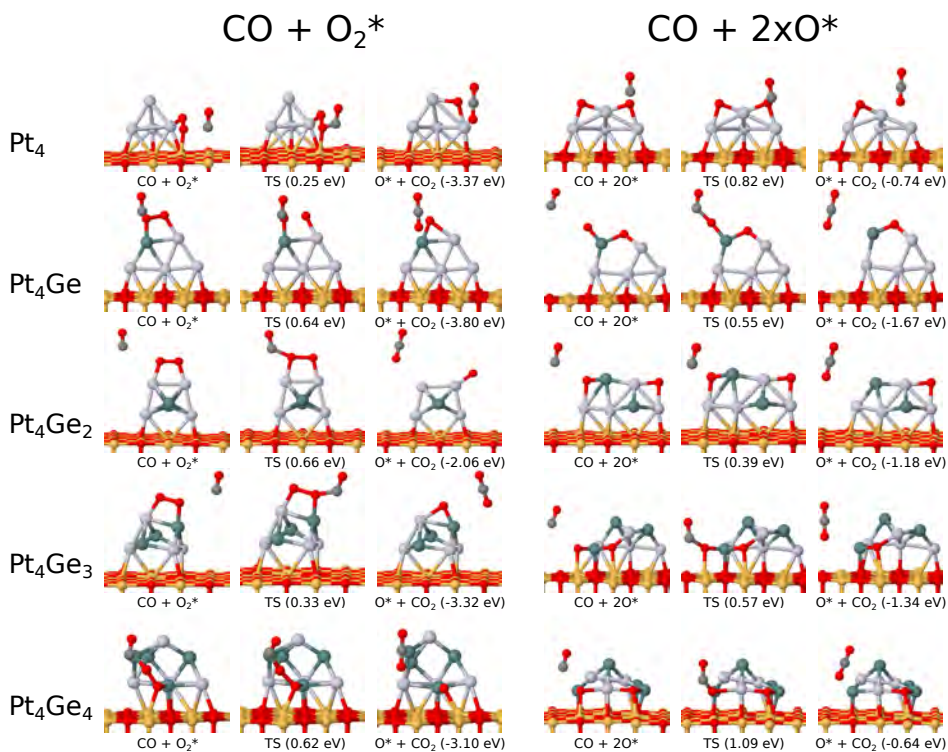
$CO^* + O_2^*$ $CO^* + 2xO^*$
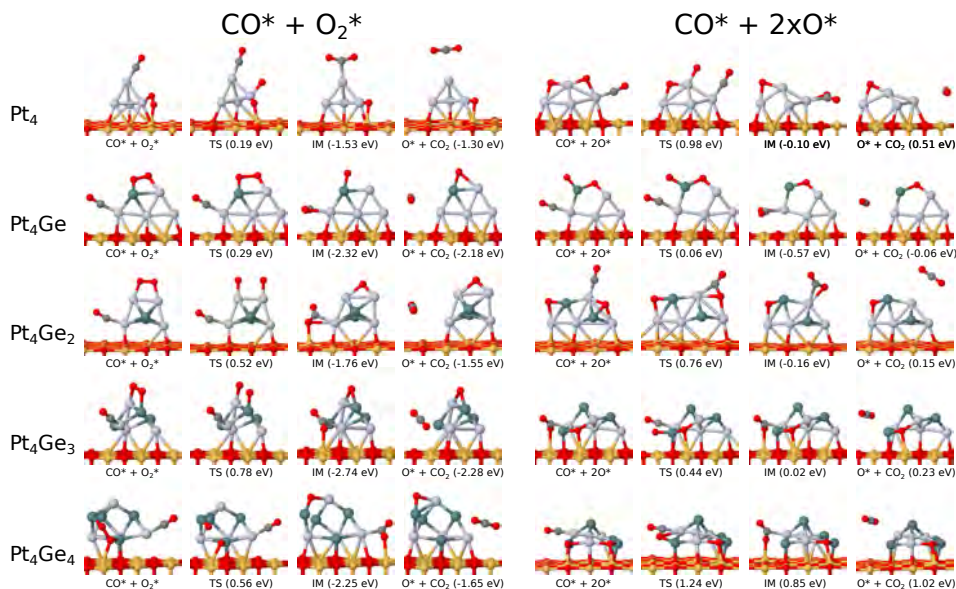
Figure 5.4: Most stable reaction pathways for the Langmuir−Hinshelwood (LH) mechanism for both molecular and dissociated oxygen reactions on Pt_4Ge_n/MgO(100). Initial state (IS), transition state (TS), intermediate state (IM) and final state (FS) geometries are shown together with the relative activation and reaction energies (in eV). Only the first step is given. Pt, Ge, Mg, O and C are depicted in gray, dark green, orange, red and dark gray, respectively.

endothermic nature of the last two steps (second oxidation + desorption). This indicates that IS3 will act as a drain and shift the reaction towards $CO^* + O^*$ formation. In this state O^* could still react with CO in gas-phase via ER mechanism, but part of the surface will be poisoned by CO. The case of Pt_4 is more dramatic since CO_2 desorption is highly endothermic, which means that part of the formed CO_2 will remain on the surface, *i.e.*, Pt_4 will be poisoned by CO_2 as well as CO.

Contrary to pure Pt, the formation of the second CO_2^* (IM3) becomes the lowest stationary point when increasing the Ge content, *i.e.*, in Pt_4Ge_3 and Pt_4Ge_4. Because CO_2 desorption is slightly endothermic in both cases, CO_2 will easily detach from the cluster. On Pt_4Ge_3 the oxidation steps are somewhat reversible, while on Pt_4Ge_4 the first step is very endothermic. From these observations it can be concluded that in either case the surface will be covered by CO^*, O^* and CO_2^*, but in Pt_4Ge_3 once $CO_2(g)$ is formed, the reaction will evolve more easily

towards the final product. Furthermore, these two clusters present a higher BE for O_2 than CO, so O* may become the predominant species together with CO_2*, limiting CO poisoning. The O* in excess should not be considered detrimental since it can still react with CO(g) via the ER channel. In reality, CO is being consumed simultaneously in each one of these routes; in other words, the different pathways are not independent of each other and the reaction should be thought of as a dynamic phenomenon where the coverage of the intermediates obtained through one route may affect the efficiency of the other. Such a relationship cannot be captured with the results obtained so far. In this respect, microkinetic modeling can be a very useful tool to help elucidate the time evolution of complex reaction networks.
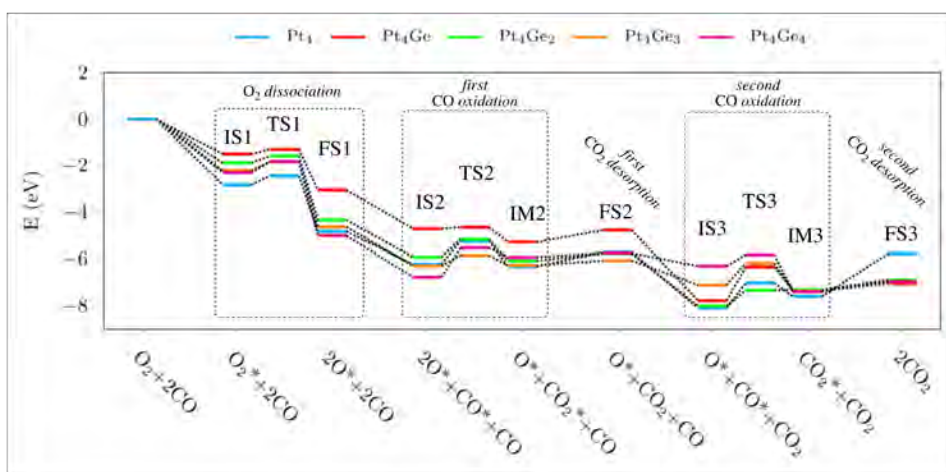
Figure 5.5: Potential energy diagram of the most stable CO* + 2×O* routes (LH mechanism) on Pt_4Ge_n/MgO(100). Energies (in eV) are given relative to the clean Pt_4Ge_n/MgO(100) surface.

5.3.4 Microkinetic Simulations

To shed light on the effect of the alloy concentration over the time evolution of CO_2 production, the DFT calculations were complemented with an 8-step microkinetic model, following the approach of previous work.[423, 424] Microkinetic modeling allows us to make a more direct comparison between DFT calculations and experimental variables such as partial pressures and temperatures. Importantly, the

coverage effects are also considered, offering a thorough assessment of the catalyst poisoning tendency. In the simulations reported herein, the temperature was varied from 100 to 500 K and the O_2:CO ratio of the feed was altered to simulate different environments (*viz.*, $P_{O_2} = 0.5$ bar, $P_{CO} = 0.5$ bar; $P_{O_2} = 0.5$ bar, $P_{CO} = 0.05$ bar; $P_{O_2} = 0.05$ bar, $P_{CO} = 0.5$ bar). It should be stressed that no a priori assumptions were made about the rate-determining step or steady-state surface coverages. The elementary steps and reactor model are described in greater detail in Appendix E.

In Figure 5.6 we compare the steady–state coverages and the CO_2 turnover frequency (TOF_{CO_2}) as a function of temperature and CO and O_2 partial pressures of Pt_4 (pure Pt) with the best alloy candidate, *i.e.*, Pt_4Ge_3; the rest are shown in Figure E.10, along with the discussion. A quick glance reveals that Pt_4 exhibits the well-reported bistable kinetics in agreement with previous studies.[407, 425, 426] Different regimes of slow (severe CO poisoning; Figure 5.6a, right) and fast (CO poisoning-free; Figure 5.6a, left) kinetics can be distinguished based on the surface coverages. High O_2 pressures are the best conditions to avoid CO poisoning and increase the CO_2 formation rate. At equal CO and O_2 pressures (Figure 5.6a, middle), O* ($\theta_O \sim 0.5$ ML) and CO_2* ($\theta_{CO_2} \sim 0.4$ ML) become the main species on the surface in the range of $100 - 200$ K. Interestingly, despite using a feed with a CO:O_2 1:1 composition, the CO coverage only amounts to 0.1 ML. In this temperature regime, Pt_4 is more reactive in the CO* + O_2* route than in the CO* + O* one, making the former the predominant path for CO_2 production. The high endothermicity of CO_2 desorption makes CO_2* block an important portion of the free active sites. In addition, the O* produced via CO* + O_2*, remains mostly unreacted owing to the high energy barrier in the CO* + O* route, which becomes reflected in the low TOF_{CO_2} values. At intermediate temperatures ($200-325$ K) CO_2* becomes the predominant species which may be ascribed to an increment in the CO_2 desorption free energy. The TOF_{CO_2} also increases and remains constant at a fairly moderate level ($TOF_{CO_2} \sim 10^{-1}$ s^{-1}). It should be noted that O* is constantly reacting with CO in gas-phase via ER mechanism. The empty sites left will either become covered with O* again or CO* and CO_2* (the latter being more likely). Then, from 350 K upwards, a change of mechanism occurs and CO* + O* becomes the main route. The barriers for O_2 dissociation and CO* + O* reaction

become lower than the CO* + O_2* ones. Yet, the difference in binding free energies (BGs) between CO and O_2 becomes more important, and therefore CO poisoning also becomes more pronounced, slowing down the reaction rate.

At high O_2 pressures (Figure 5.6a, left) a transition can be observed to the CO poisoning-free regime. Higher O_2 pressures seem to be beneficial, regardless of the temperature, as expected. O_2 adsorption becomes more favorable than CO, which then converts to O* via O_2 dissociation and CO* + O_2*. From 100 K to 275 K the surface composition is 0.4 ML CO_2*, $\sim$ 0.5 ML O* and $\sim$ 0.1 ML O_2*. At higher temperature, O_2 dissociation becomes more favorable and O* coverage increases at the cost of O_2* sites. The presence of CO_2* indicates that the LH channel is not hindered by CO poisoning. However, CO_2* limits the availability of active sites for LH and ER pathways, so the efficiency of CO_2 production is compromised. The TOF_{CO_2} decreases linearly with temperature from 10^{-1} to 10^{-2} s^{-1}. We anticipate that CO_2 poisoning can cause a drop in the TOF_{CO_2} by two orders of magnitude, although the effect is milder than for CO poisoning.

A CO-rich feed (Figure 5.6a, right) has an extremely detrimental effect on the performance of the monometallic cluster at low temperatures; Pt_4 becomes almost completely poisoned by CO ($\theta_{CO} \sim 0.8$ ML). In this regime there is a scarcity of O_2* and O* sites for LH and ER paths and thus the oxidation rate decreases drastically. This behavior can be understood in terms of DFT binding free energies that show the strong adsorption of CO on pure Pt clusters. The TOF_{CO_2} increases with temperature until it is stabilized in the $225 - 325$ K window. CO* nearly disappears but CO_2* coverage becomes more pronounced ($\theta_{CO_2} \sim 0.6$ ML). Nonetheless, there is still a fraction of O* and O_2* which can oxidize CO at rates similar to $P_{O_2} > P_{CO}$. As the temperature increases, CO* coverage starts increasing at the expense of CO_2* and the TOF_{CO_2} is slightly reduced.

We must emphasize that CO and CO_2 poisoning are completely suppressed in Pt_4Ge_3 under the conditions studied in this work (see Figure 5.6b). CO coverage is negligible even at $P_{CO} > P_{O_2}$. Our results indicate that the bistable kinetics of CO oxidation disappears; a single regime of fast CO oxidation rate is obtained by controlling the promoter concentration. The three different pressure conditions show very similar behaviour. O_2* and O* are always the only species found at

steady-state. The O$_2$* coverage changes in a pyramid-like fashion, showing the highest value at intermediate temperatures. At P$_{O_2}$ = P$_{CO}$, O$_2$* remains the main dominant species until 350 K, whereas at P$_{O_2}$ > P$_{CO}$, O* coverage becomes larger in the whole temperature range due to greater availability for O$_2$ dissociation sites. We highlight that the PtGe nanoalloy starts to show very similar BGs for CO and O$_2$ at this precise Ge concentration. Thus, both reactants will adsorb with similar probabilities, and according to the Sabatier principle, the conditions for CO oxidation will be optimal. The importance of the magnitude of the binding energies on the overall performance of the reaction kinetics has been underlined previously.[427] In addition, Pt$_4$Ge$_3$ shows much faster kinetics for the CO* + O* than CO* + O$_2$* step. This means that at initial times the TOF$_{CO_2}$ will be small as there will only be present CO* and O$_2$*. But once O$_2$ starts dissociating, CO* will react immediately with the newly formed O* to give CO$_2$. O$_2$* accumulation is not problematic since it can dissociate to O* or react with CO(g) via ER. It is also important to mention that CO$_2$ desorption becomes spontaneous with increasing temperature, which prevents CO$_2$ poisoning.

Except at P$_{O_2}$ > P$_{CO}$, the TOF$_{CO_2}$ is higher at low temperatures and slightly decreases monotonically with temperature, but always maintains at high value. Interestingly, the highest TOF$_{CO_2}$ is obtained at 100 K for P$_{O_2}$ = P$_{CO}$ and P$_{CO}$ > P$_{O_2}$, which is at least one order of magnitude higher as compared to other compositions. Part of these results may be found somewhat counterintuitive. However, we believe that this behaviour might be the result of the interplay between two effects, *i.e.*, entropic and the dynamic nature of the steady-state. First, the DFT results reflect that the Gibbs free energies of the reactions and barriers have a substantial dependence with temperature (see for instance Figure E.9). This alters the viability of the different reaction channels (*e.g.*, CO* + O* *vs* CO* + O$_2$*) at different temperatures, and thus, yields different steady-state coverages and TOFs. Second, it should be kept in mind that in CSTR conditions the system is not at thermodynamic steady-state (equilibrium) but at a dynamic steady-state, which depends on the gas in/out flow. Namely, the constant flow of gas species also affects the surface composition and can in turn shift the elementary reactions at either direction with different strength. One should be cautious to rely solely

on equilibrium data to rationalize the behaviour of systems out of thermodynamic equilibrium. The changes occur so that O_2^* is formed at the expense of O^*, showing a pyramid-like behaviour. Unfortunately, quantifying this hypothesis is out of the scope of this work. Preliminary steps were done by performing a degree of rate control (DRC) analysis, but unfortunately we faced numerical instabilities with the evaluation of numerical derivatives. Finite difference method has already been reported problematic previously,[428] especially in transient kinetics where the magnitude of the finite-size perturbation can affect the convergence of the dynamic steady-state.[429]

Besides, it is important to point out that Pt_4Ge_3 will also get poisoned eventually at higher CO pressures. The bistable kinetics is a property inherent to CO oxidation. Ge alloying acts by increasing the boundaries of the fast kinetic regime to harsher conditions in the PT phase diagram. The CO-poisoning region does not disappear, although it will occupy a much smaller portion of the phase diagram compared with pure Pt_4.

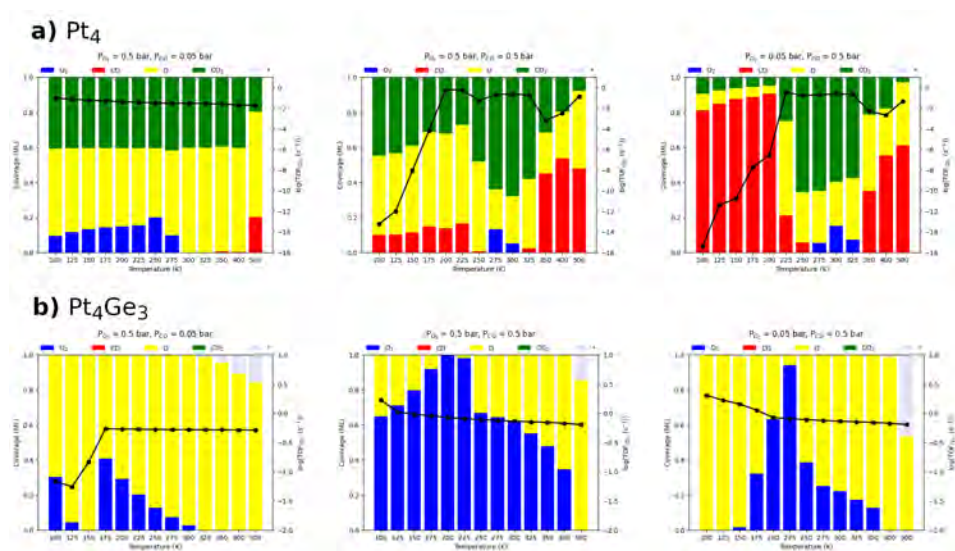Figure 5.6: Microkinetic analysis of CO oxidation for a) Pt_4 and b) Pt_4Ge_3 clusters supported on MgO(100). Steady-state coverages and CO_2 turnover frequencies (TOF_{CO_2}) as a function of temperature with different feed compositions: $P_{O_2} = 0.5$ bar, $P_{CO} = 0.05$ bar (left figure); $P_{O_2} = 0.5$ bar, $P_{CO} = 0.5$ bar (middle figure); $P_{O_2} = 0.05$ bar, $P_{CO} = 0.5$ bar (right figure).

Regarding the role of Ge, DFT results suggest that on the one hand, Ge induces ligand effects (electronic effects) on Pt and reduces the affinity to CO, avoiding the overbinding of CO over O$_2$. Similar ligand effects were also observed by Molina *et al.* for Nb and Mo doping.[430] The advantageous mixing between both elements guarantees that Ge hybridizes with most Pt sites in the nanoalloy. On the other hand, our theoretical findings suggest that PtGe also acts as a bifunctional catalyst. The addition of Ge into the catalyst creates new active sites for a more efficient oxygen adsorption. The nanoalloys show a dual adsorption behavior where CO is preferentially adsorbed on Pt and O$_2$ on Ge avoiding the competition for the active sites. Such behavior is in line with other oxophilic promoters such as Ru, Mo or Sn.[350, 389] Although in many instances PtGe ensembles are needed for O$_2$* and O* bridge adsorption, the ligand effects provide a similar adsorption strength to CO. Again, the high mixing guarantees that CO* and O$_2$* (or O*) sites are in proximity for a facile diffusion and reaction, maximizing the bifunctional effect. Importantly, the ligand and bifunctional effects depend on Ge content, *i.e.*, Ge alloying offers a new degree of freedom to control the catalytic properties of bimetallic catalysts. Apparently, this concentration dependence is very reaction-specific. Our results suggest that Pt$_4$Ge$_3$ composition has the most adequate reactivity for CO oxidation, in contrast to dehydrogenation reactions where Pt$_4$Ge outperforms Pt$_4$Ge$_3$.[229]

The microkinetic simulations further confirm that Ge alloying alters the CO oxidation bistable kinetics. Ge leads to a CO poisoning-free regime and fast CO$_2$ production prevails, at least within the pressure ranges studied in this work. Besides, the microkinetic simulations reveal that in this regime the PtGe clusters may exhibit a high oxidation state (high O* coverage). Although our microkinetic model does not distinguish between Pt and Ge sites, the information about the binding energies is included; and thus, this high oxidation state may be indicative of a bifunctional mechanism. By virtue of these findings and previous work on bigger NPs,[431] we speculate that part of the subnano catalyst may remain reduced to the metallic state with PtGe alloy formation, and part may be oxidized to GeO$_x$. Therefore, now there is available an independent oxygen reservoir resistant to CO poisoning, *i.e.*, GeO$_x$, which can react with CO on Pt metallic sites.

5.4 Conclusions

We have studied the effect of the composition on the CO oxidation reaction catalyzed by Pt_4Ge_n clusters ($n = 0 - 4$) supported on MgO(100) using a combination of DFT and microkinetic simulations. To characterize the most stable CO and O_2 adsorption configurations, a GM search was carried out on the thermally populated isomers of each cluster composition. The DFT results reveal that CO binding energy weakens with the Ge content owing to ligand (electronic) effects induced on Pt upon Ge alloying. Bond-length and PDOS analysis indicate that O_2 is readily activated up to the peroxo state and dissociates to atomic oxygen with low barriers and significant release of energy in all the Pt_4Ge_n clusters.

In continuation, a systematic study of CO oxidation has been performed performed by considering the LH and ER mechanisms initiated by both molecular and atomic oxygen. In the ER mechanism pure and alloyed clusters present similar barriers and the whole process is downhill. Nonetheless, a pronounced dependence on the Ge concentration is found for the LH pathway, which is the most likely reaction channel. For Pt_4, the barriers for the CO* + 2× O* are *ca.* 1 eV. In addition, pure Pt is prone to become poisoned by CO and CO_2. On the contrary, the poisoning effects are overcome on PtGe. Pt_4Ge, Pt_4Ge_2 and Pt_4Ge_4 present acceptable reaction barriers except one of the steps in the CO* + 2 × O* route which is blocked with relatively high activation and reaction energies. For Pt_4Ge_3, all the reaction barriers are attainable (< 1 eV).

The microkinetic simulations hint to a reduced CO and CO_2 poisoning dependence with increased Ge concentration. Pt_4 shows a bistable-like CO oxidation kinetics, in agreement with literature. At low temperatures and/or high CO pressures it suffers from CO poisoning and CO_2 production drops drastically. On top of this, regardless of partial pressures, there is a constant CO_2 poisoning which also diminishes the TOF_{CO_2}. Nevertheless, as the Ge concentration increases CO and CO_2 poisoning subside, until in Pt_4Ge_3 the kinetic regime of severe CO poisoning is removed. A 4:3 Pt to Ge ratio changes the bistable kinetics of pure Pt and instead, a regime of fast CO_2 formation is obtained for all temperatures and pressures considered. CO_2 poisoning does not change in the same way with the Ge content as Pt_4Ge_4 again shows some CO_2 poisoning. Thus, Pt_4Ge_3 appears to be the optimal composition

for the CO oxidation reaction.

Our calculations predict that Ge alloying induces both ligand and bifunctional effects. Charge transfer phenomena and orbital hybridization between Pt and Ge alter the adsorption properties of the catalyst (structure-activity relationship) in a composition dependent fashion. Further, PtGe shows a dual adsorption behavior where CO always binds to Pt sites, while oxygen shows a clear preference towards Ge due to its greater oxophilicity. Precisely, this oxophilicity of Ge makes part of it oxidize to GeO_x, and consequently, a new oxygen source is developed resistant to CO poisoning. The provided results require a more thorough analysis to correctly sample the boundary between the CO poisoning and CO poisoning-free regimes as a function of pressures and temperature. As for now, this remains yet a topic of future study.

On the basis of this work, we believe that Ge alloying can be used for tuning the properties of Pt for catalytic applications. The high CO poisoning resistance conferred by Ge alloying without harming the catalytic activity makes it very appealing for industrial applications such as the water$-$gas shift reaction and PEMFCs.

Screening of 2D Materials as Supports of PtGe Bimetallic Clusters for PEMFC Applications

"She should have died hereafter;
There would have been a time for such a word.
To-morrow, and to-morrow, and to-morrow,
Creeps in this petty pace from day to day
To the last syllable of recorded time,
And all our yesterdays have lighted fools
The way to dusty death. Out, out, brief candle!
Life's but a walking shadow, a poor player
That struts and frets his hour upon the stage
And then is heard no more: it is a tale
Told by an idiot, full of sound and fury,
Signifying nothing."

— William Shakespeare, *The Tragedy of Macbeth*

In this chapter, the performance of pure Pt and bimetallic PtGe clusters supported on a set of 2d materials for PEMFC applications is investigated. The purpose is to understand the precise role of the metal-support interaction on the catalytic properties. For this, a global minima search is carried out on small-size Pt and PtGe clusters supported on 5-8-5-DV, B-doped graphene, silicene, germanene, 2H-MoS$_2$ and SmSI. After a structural and electronic analysis, the resistance to CO poisoning and HOR activity is evaluated. All supports except the graphene-based ones are found to increase significantly the adsorption energy of pure Pt clusters. These clusters adopt a planar geometry and receive a great amount of electrons from the support. After Ge alloying, such effects are partially hindered due to a repulsion between Ge and the support. Likewise, the mayority of the supports have a favourable influence on the interaction with CO and H, being in some cases very close from the Sabatier optimum. Additionally, this work shows that the design parameters such as Ge concentration and support show opposite trends for different catalytic properties, becoming necessary a balance among them.

6.1 Introduction

NERGY conversion is perhaps one of the most critical challenges of current society.[1] The adverse effects of fossil fuels on the environment and their limited reserves, make them an unsustainable energy source in the long term for an ever-growing population. Developing green and efficient energy conversion technologies is crucial to achieve carbon neutrality targets and support a global economic growth.[7–9, 51]

To this end, PEMFCs have attracted considerable attention due to their ability to operate at low-temperature, high energy conversion efficiency, excellent durability, and sustainable regeneration.[14–17, 19] PEMFCs are electrochemical devices that convert the chemical energy of a fuel, H$_2$, directly into electricity without emission of pollutants, *i.e.*, ideally water is the only byproduct. The continuous fuel supply renders PEMFC as the ideal power source for portable electric vehicles and stationary power plants for critical infrastructures.

The redox reaction is divided into two half reactions: the HOR occurring at the

anode and the ORR occurring at the cathode.[25, 29, 432] HOR has zero free energy change while ORR releases ideally 4.92 eV which amounts the total free energy change of the entire electrochemical reaction. ORR has one intrinsic problem, *i.e.*, ORR is inefficient. In acidic media, the kinetics of the ORR is 6 times slower than HOR.[29, 30] Thus, in order to boost the sluggish ORR kinetics an extra potential known as overpotential must be applied. This overpotential causes a significant voltage drop from the ideal open-circuit voltage of 1.23 V, referenced to the standard hydrogen electrode (SHE) . Consequently, very active catalysts become mandatory that minimize this undesired overpotential. To date, commercial Pt supported on carbon black (Pt/C) remains the state-of-the-art catalyst choice.[29, 31] However, even Pt requires large amounts of catalyst loading to reach a reasonable efficiency. Unfortunately, the scarcity and high cost associated with this novel metal represents the main bottleneck for the large-scale application and commercialization of PEMFCs.[433–435] In order to increase the viability of PEMFCs, Pt content has to be reduced. The U.S. DOE has established a target limit of less than 0.125 mg$_{Pt}$ cm^{-2}.[42]

In addition to the catalytic activity, the stability under real electrochemical conditions is also a crucial factor to consider. In commercial Pt/C catalyst, Pt NPs undergo dissolution and aggregation (sintering) during long-term operation.[436, 437] The carbon support also becomes corroded under high oxidizing potentials which in turn promotes further NP sintering. This results in a loss of surface area and hence in a performance degradation. A good support thus should prevent sintering, dissolution, oxidation and corrosion under harsh electrochemical conditions. A strong orbital hybridization between cluster and support is required to stabilize the cluster, as well as excellent electrical conductivity to ensure a fast electron transport. On the above basis, 2D materials have recently emerged as promising novel support materials.[164, 165, 438–445] 2D materials show unique properties compared with their analogous 3D counterparts for the following reasons. First, they have a maximal surface to bulk ratio, providing a vast density of active sites. Second, they have excellent mechanical, carrier mobility, thermal diffusion, optical and phonon properties. And third, all these properties are highly tunable by introducing surface modifications owing to their anisotropy, *i.e.*, they are confined to the 2D plane.

2D materials can be classified as single-element, two-element, and multiele-ment.[165] Examples of the first type are graphene, phosphorene, silicene germanene, stanene, arsenene and bismuthene. Hexagonal boron nitride (h-BN), transition metal dichalcogenides (TMDs) and transition metal carbide and nitride (MXene) belong to the second type, while samarium sulfoiodide (SmSI) belongs to the third type. Despite their promising properties, many of these materials do not possess an adequate band gap for electron transport, which is essential in electrochemistry. However, thanks to their tunability their band gap can be closed by the deposition of metallic clusters. The catalytic activity can also be increased in the same way, as previously reported for the inert basal plane of 2H-MoS$_2$.[446, 447]

In this context, subnanometer clusters have been regarded as functional catalysts to work in tandem with 2D supports.[97, 102, 208, 448–461] First, due to their small size, clusters possess a huge amount of surface area. In contrast to nanoparticles (NPs), all or most of the atoms are part of the surface, namely, potential active sites, with the possibility of reaching the so-called atomic efficiency.[94–97] This, coupled with the high surface area of the 2D support, allows the use of minimal amounts of Pt. Second, clusters offer many degrees of freedom that can be exploited to tailor the catalytic properties. In this size regime, the catalytic properties become size-dependent to the extent that a single atom can make a dramatic difference: every atom counts. The metal-support interaction (MSI) is also maximized due to their large surface area. This, together with the high thermal stability of 2D supports, may confer the clusters an enhanced resistance to sintering.

Currently, the majority of hydrogen is produced by steam reforming of natural gas,[45] thus, it is not entirely "green" hydrogen. H$_2$ produced by this process inevitably contains impurities of carbon monoxide (CO) at concentrations of $\sim$ $10-100$ ppm. The high affinity of Pt towards CO over H$_2$ leads to a severe surface blockage by CO, inhibiting H$_2$ adsorption. An anode potential greater than 0.6 V (*vs* RHE) is required to oxidize CO via a Langmuir$-$Hinshelwood (LH) type reaction between CO* and OH*.[462] This results in an extra voltage loss and HOR deactivation. This process is known as CO poisoning and it is one of the most important drawbacks affecting the manufacturing of PEMFC.[38–40] Purification of the H$_2$ feed is very costly and challenging.[463] Hence, it is essential to develop

HOR catalysts resistant to CO poisoning, as well as alternative greener methods for H_2 production.[21]

One strategy to improve the intrinsic activity and resistance to CO poisoning is to alloy Pt with a second element.[178, 182, 350, 464–470] Changing the composition of the catalyst can be used to modify its electronic structure and thus, optimize the adsorption of the ORR intermediates, enhancing the catalytic properties.[471–473] The improvement of the catalytic properties may be the result of ensemble, strain, ligand and bifunctional effects.[182, 473–475] In particular, bifunctional catalysts are interesting because of their dual adsorption properties.[476] This dual adsorption permits to simultaneously regulate the adsorption strength of H* and OH*, thus obtaining a catalyst active for both HOR and ORR. Bifunctional effects can be achieved by introducing oxophilic promoters. The oxygenated species will now adsorb preferentially to the oxophilic element while H_2 will adsorb to Pt. Note however, that an excessive amount of oxophilic elements may favour an overbinding of oxygenated species and alter the oxidation state of Pt sites, reducing their HOR activity. Therefore, a balance between oxophilicity and hydrophobicity must be reached. Considering these premises, the results obtained on previous chapters suggest that Ge can be an optimum alloying agent to tune the properties of Pt. Furthermore, it could help reduce the price of the catalyst.

Herein, by means of density functional theory (DFT), we characterize the stability, CO poisoning resistance and HOR activity of small-size pure Pt and PtGe alloy clusters supported on a variety of 2D materials, *viz.*, pentagon-octagon-pentagon reconstructed divacancy graphene (5-8-5-DV), boron-doped graphene (gr-B), phosphorene, silicene, germanene, $2H-MoS_2$ and SmSI. In the initial step, we carry out a GM search to find the most stable structures for each cluster-support composition. Afterwards, we investigate their structural and energetic properties and compute the Gibbs free energy diagrams for HOR. Our aim is to simultaneously understand the interplay between promoter and support through a comprehensive systematic study. Alloying and MSI effects work in the two directions. On the one hand, the support increases the stability and changes the electronic structure of the cluster via MSI. On the other hand, the cluster can change the electrical and catalytic properties of the support, which can be modulated with its size and composition.

Hence, the best of both cluster and support can be obtained with an efficient MSI. We hope that the present study may inspire helpful guidance in the pursuit of new Pt-based electrocatalysts resilient to CO poisoning with ultra-low loading of precious Pt.

6.2 Computational Methods

6.2.1 Computational Details

Spin polarized DFT calculations were performed using the Vienna ab initio simulation package (VASP).[358–361] The electron-ion interaction was described by the PAW method[315] and for the exchange-correlation interaction we used PBE version[362, 363] of the GGA. The Grimme's DFT-D3 method[317] was used to account for vdW dispersion interactions. The kinetic energy cutoff was set to 450 eV and a convergence criterion of 10^{-6} eV and 10^{-5} eV was employed for the electronic energy and the geometry relaxation, respectively. The Brillouin zone was integrated using a $1 \times 1 \times 1$ Monkhorst-Pack mesh centered at the Γ point.

6.2.2 Computational Models

The 2D supports were modelled using orthorhombic supercells of appropriate sizes, *viz.*: $17.28\mathring{A} \times 21.38\mathring{A}$ for 5-8-5-DV and B-doped graphene, $16.53\mathring{A} \times 18.21\mathring{A}$ for phosphorene, $23.16\mathring{A} \times 26.79\mathring{A}$ for silicene, $23.93\mathring{A} \times 27.72\mathring{A}$ for germanene, $19.16\mathring{A} \times 22.12\mathring{A}$ for 2H-MoS$_2$ (basal plane) and $23.03\mathring{A} \times 23.93\mathring{A}$ for SmSI. The SmSI supercell was obtained from a rhombohedral R$\bar{3}$m primitive cell with (111) termination. All lattice parameters were converged. A single layer of support was used for all cases, buffered with a vacuum region of 20 $\mathring{A}$ to prevent artificial interactions between periodic images in the z direction. All atoms were allowed to relax during geometry optimization. In the SmSI support, the 4f electrons of Sm were treated as part of the core and hence no efective coulomb (U_{eff}) parameter was required.

GM calculations were performed with the PGOPT toolkit.[357] Within this toolkit, the initial structures are generated using the bond length distribution algorithm (BLDA). The GM search was divided in two stages, *viz.*, cluster/support and a

subsequent cluster(adsorbate)/support generation. In each case, it was ensured that enough structures were generated to sample the PES thoroughly. To determine the most stable surface deposited cluster geometries, the initial pool of structures ranged from 150 for $n = 4$ size clusters to 800 for $n = 10$. This process yields, in addition to the GM, a set of low-lying isomers, which can be populated under electrocatalytic conditions. Nonetheless, owing to the tremendous computational workload, we focused only on the GM structure for each cluster-support composition to further study the adsorption of the molecules. Thus, in the second step, another GM search was done using the same procedure to determine the most stable CO* (CO poisoning) and H* (HOR) adsorption structures on the bare GM cluster structures. In this case an initial pool of 50 structures was generated.

In order to study the effect of the cluster composition and the effect of the support, we studied the properties of Pt_{10} and Pt_5Ge_5 cluster structures for all supports, except phosphorene. The reason behind these particular compositions is that, in Chapter 4, we demonstrated that clusters composed of similar amounts of Pt and Ge are unique since they are significantly more stable than other compositions and they exhibit a remarkable CO poisoning resistance. In the particular case of phosphorene, we additionally wanted to study the effects of size and composition in more detail. For this reason, we included the series Pt_4-Pt_8 and Pt_8-PtGe_7. In other words, clusters made of $4-8$ atoms with a varying composition (from pure Pt to clusters containing a single Pt atom) are considered.

To determine the cluster stability we computed the adsorption energy of the clusters to the supports by Equation (6.1):

$$E_{\text{ads}} = E(\text{PtGe/support}) - E(\text{support}) - E(\text{PtGe}), \qquad (6.1)$$

where $E(\text{PtGe/support})$ is the energy of the PtGe cluster adsorbed on the support, $E(\text{support})$ is the energy of the pristine support and $E(\text{PtGe})$ is the energy of the PtGe cluster in gas-phase. With this definition, the more negative the value, the more stable is the cluster.

The adsorption Gibbs free energies of the intermediates were defined as

$$\Delta G = \Delta(E_{\text{elec}} + \text{ZPE}) - T\Delta S, \qquad (6.2)$$

where ΔE is the adsorption energy (likewise, binding energy) of the intermediate, ΔZPE is the zero-point energy change and ΔS is the entropy change, respectively. ZPEs and Entropies of gas species at standard conditions were taken from the international tables, and the entropy of solid-state species was considered equal to zero. The ZPE and entropy corrections of adsorbed species were computed with a vibrational analysis within the harmonic approximation.

The resistance to undergo CO poisoning was quantified with the CO adsorption free energy using

$$\Delta G_{\text{CO}*} = G_{\text{CO}*} - G_* - G_{\text{CO}}, \tag{6.3}$$

where $G_{\text{CO}*}$ is the free energy of the supported cluster with one CO molecule adsorbed, G_* is the free energy of the bare PtGe/support and G_{CO} is the free energy of the isolated CO in gas-phase. With this definition, an empty site * refers to the bare PtGe/support system. Here the free energy equals the electronic energy.

To compute the Gibbs free energy of electrochemical reactions involving proton-electron transfer, the computational hydrogen electrode (CHE) model was used.[30] In this model, the reference potential is set to be the standard hydrogen electrode (SHE). This makes the free energy of the $(\text{H}^+ + \text{e}^-)$ pair correspond to that of $1/2$ $\text{H}_2(\text{g})$ under standard conditions (1 bar, 298 K and pH = 0).

The HOR performance was tested by computing the adsorption free energy of atomic hydrogen (H*), which in acidic environment at pH = 0 is given by

$$\Delta G_{\text{H}*} = G_{\text{H}*} - G_* - \frac{1}{2} G_{\text{H}_2}, \tag{6.4}$$

where G_{H_2} is the free energy of H_2 in gas-phase.

6.3 Results and Discussion

In this section we present the most relevant findings of this study on the stability and activity of pure Pt and alloyed PtGe clusters supported on a set of 2D materials. It is divided into three parts. We begin by providing details on the stability of the clusters and propensity to sinter, both with respect to the adsorption strength to the substrate underneath. We then move on to the study of CO adsorption and

resistance to CO poisoning. Finally, we discuss the HOR performance. Each of this sections is at the same time divided into two subsections where, on the one hand, we investigate the role of size and composition, using phosphorene as a working example, and on the other hand, we carry out a screening of 2D materials as support candidates, focusing only on Pt_{10} and Pt_5Ge_5 for the sake of comparison of the MSI effect.

6.3.1 Structure and Stability of Monometallic Pt and Bimetallic PtGe Clusters Supported on 2D Materials

6.3.1.1 Effect of Size and Ge Concentration on Phosphorene Deposited Clusters

First, we study the effect of cluster size and Ge content on the structure and stability of phosphorene deposited clusters. Figure 6.1a displays the putative GM structures of the monometallic series (Pt_n, $n = 4 - 8$), as well as the $n = 8$ series ($Pt_{8-m}Ge_m$, $m = 0 - 7$), along with the Bader charges. For all sizes, pure Pt clusters have a very planar geometry, an indicator of a strong MSI. Surprisingly, the most stable cluster structures of Pt_4 and Pt_5 are found to be dissociated in two, forming two dimers and one dimer and a trimer, respectively. This outcome may be related to the armchair structure of phosphorene. A closer inspection reveals that the Pt atoms are arranged in linear clusters anchored in the space between two consecutive planes. These linear clusters are then connected by additional Pt atoms that act as bridging units. In the smallest sizes these bridging atoms are missing and hence the clusters are fragmented. We can hypothesize that a phosphorene support could have a strong beneficial impact in the sintering resistance of Pt, since it might help keep the catalyst dispersed.

Ge alloying also has a big impact on the cluster geometry. Contrary to Pt clusters, a repulsive interaction between Ge and phosphorene is visible which pushes the Ge atoms upwards; no Ge−P bonds are observed. This has two consequences. First, the Ge atoms are available to bridge the linear Pt clusters. Second, high Ge concentrations will result in a poor Pt−Ge mixing (*e.g.*, see Pt_4Ge_4 on Figure 6.1a), which may remove the promoting effects of Ge on Pt. Indeed, as Ge concentration

increases, Pt and Ge clusters tend to form two separate phases, *i.e.*, one made of Pt and the other one of Ge, which is avoiding contact with the surface. This is in stark contrast with their behaviour in gas-phase, as found in Chapter 4. As a consequence, a large amount of Ge could potentially block the active sites.
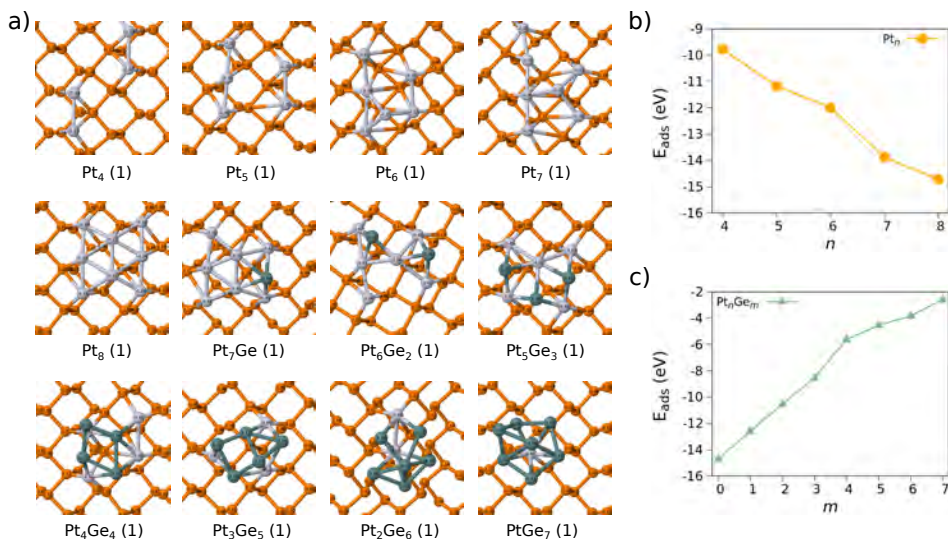

Figure 6.1: a) Putative global minima (GM) structures of the monometallic series Pt_n ($n = 4 - 8$) and $n = 8$ series ($Pt_{8-m}Ge_m$, $m = 0 - 7$) supported on phosphorene. The multiplicity ($2S + 1$) of each structure is given in parenthesis. The Bader charges are printed on top of the atoms in values of $|e|$. Pt, Ge and P are depicted in grey, green and orange, respectively. Adsorption energies (E_{ads}) for the b) monometallic series Pt_n ($n = 4 - 8$) and c) $n = 8$ series ($Pt_{8-m}Ge_m$, $m = 0 - 7$).

Concerning the energetic properties, shown in Figure 6.1b, a monotonous size-dependence can be seen for the adsorption energy, Pt_8 being the most stable structure. Interestingly, the E_{ads} are significantly bigger than the ones reported for common oxide supports, even for the smallest sizes.[229] Another indication of the beneficial effects that this particular support can have in the sintering resistance of Pt. On the contrary, Ge alloying has a detrimental effect on their stability (see Figure 6.1c). Ge-rich clusters may be prompted to undergo sintering. However, we stress that all the catalytic properties must be addressed simultaneously. Even though pure Pt clusters may be more stable than PtGe nanoalloys, the catalytic activity may increase with Ge concentration. So a balance between the two may be

necessary, being intermediate concentrations the best candidates.

Bader charges are indicative of the strong MSI. In Pt_4, 1.33 |e| are transferred from the support to the cluster, while in Pt_8 it increases to 2.19 |e|. In the PtGe clusters this charge transfer is reduced because Ge atoms already donate charge to Pt atoms; the Pt atoms directly bonded to Ge carry larger negative charge than other Pt atoms. All structures are closed-shell, regardless of the size and composition. To shed more light on the electronic structure, we have computed the PDOS of all GM, displayed in Figure F.1. After deposition, the Pt d AOs get very smeared below the E_F and display a strong hybridization with P AOs. But more surprisingly, the interaction between the phosphorene and the cluster leads to new states with Pt d and P character near the E_F. As a result, the band gap is reduced. This effect is found to be size-dependent, becoming stronger with increasing size: the band gap closes for Pt_8. Namely, the addition of Pt increases the carrier concentration and hence the conductivity. On the contrary, the band gap reopens again at high Ge concentration.

6.3.1.2 Effect of the 2D Support

Figure 6.2a displays the GM structures of Pt_{10} and Pt_5Ge_5 deposited on the rest of the 2D supports, *viz.*, 5-8-5-DV, gr-B, silicene, germanene, $2H\text{-}MoS_2$ and SmSI. Overall, the cluster morphology has a strong dependence on the support. In 5-8-5-DV and gr-B the interaction with the support is not very strong and Pt_{10} remains globular. Although the vacancy and B dopant serve as an anchoring site, Pt_{10} still displays quite low E_{ads} (Figure 6.2b) due to the inertness of graphene. Ge alloying reduces even more the stability (Figure 6.2c) due to a repulsion with the support. $Pt_5Ge_5/gr\text{-}B$ is the worst scenario where the E_{ads} drops to -1.81 eV. Both monometallic and bimetallic clusters exhibit a globular shape, maximizing the intracluster bonding to the detriment of the weaker cluster-support interaction. The case of $Pt_{10}/2H\text{-}MoS_2$ is more favourable, where the adsorption energy to the support increases up to E_{ads} = -7.90 eV. The stronger interaction is also reflected on the cluster shape. Pt_{10} no longer adopts a globular geometry, but instead it grows in a layered structure, where the Pt atoms are arranged on two different layers. This is in agreement with previous work which reports that Pt clusters

grow with the (111) orientation on $2H\text{-}MoS_2$.[477] In $Pt_5Ge_5/2H\text{-}MoS_2$ however, Ge avoids interacting with the surface. As a consequence, the cluster adopts a 3D structure again to maximize the intracluster bonding and the adsorption energy is significantly reduced as compared to pure Pt. For this reason, PtGe mixing is not as effective as in gas-phase.

Strikingly, silicene and germanene show quite different behaviour. On Silicene, Pt_{10} becomes completely planar with a triangular shape that allows the cluster to completely wet the surface. The silicene support is slightly deformed. In germanene the interaction is even stronger. The Pt atoms "enter" inside the surface and form a "pocket-like" structure. This resembles the strong metal-support interaction (SMSI) reported for metal-oxides.[85] Unfortunately, a very strong deformation of the support may cause a negative effect since it can compromise its structural integrity, mechanical properties or conductivity. The degree of this deformation may be reduced by growing this 2D support over another stabilizing matrix. The E_{ads} increases up to -22.08 eV for Pt_{10}/silicene and -26.13 eV for Pt_{10}/germanene. Regarding Pt_5Ge_5, Ge shows more affinity with both silicene and germanene and, for the first time, Ge−support bonds are formed. In fact, the bimetallic cluster adopts a quite planar geometry in these supports and the mixing between Pt and Ge is excellent, as found in free-standing clusters. Although the interaction to the surface is weaker than in pure Pt, the E_{ads} values are remarkably large (*ca.* -10 eV), suggesting that silicene and germanene could potentially be used to hold PtGe catalysts.

The SmSI case deserves special attention too. As in the previous two cases, surface wetting is very important. Nonetheless, in Pt_{10}/SmSI some of the Pt atoms detach from the cluster and diffuse to the center of the Sm_3S_3 chair units (see Figure 6.4a for a more clear representation). Until the catalytic activity is tested, this may not necessarily indicate an adverse effect. The molecules in gas-phase have enough space to access these Pt atoms. Even more, this detachment may result in the formation of new active sites with different catalytic properties from the original cluster owing to synergistic effects, acting as single atom catalysts (SACs). Additionally, this effect also occurs in the opposite direction. Some of the I atoms have migrated from the support to the cluster. On Pt_{10} the I atoms occupy bridge

positions with no Sm−I bonds. We hypothesize that this is a consequence of a SMSI effect and under given electrocatalytic conditions the cluster may be encapsulated by an I layer. The E_{ads} is significantly greater than in 5-8-5-DV and 2H-MoS$_2$, although not as large as in phosphorene, silicene and germanene. In general terms, the E_{ads} is decreased to half its value or more in equimolar clusters compared to the pure ones for all supports.
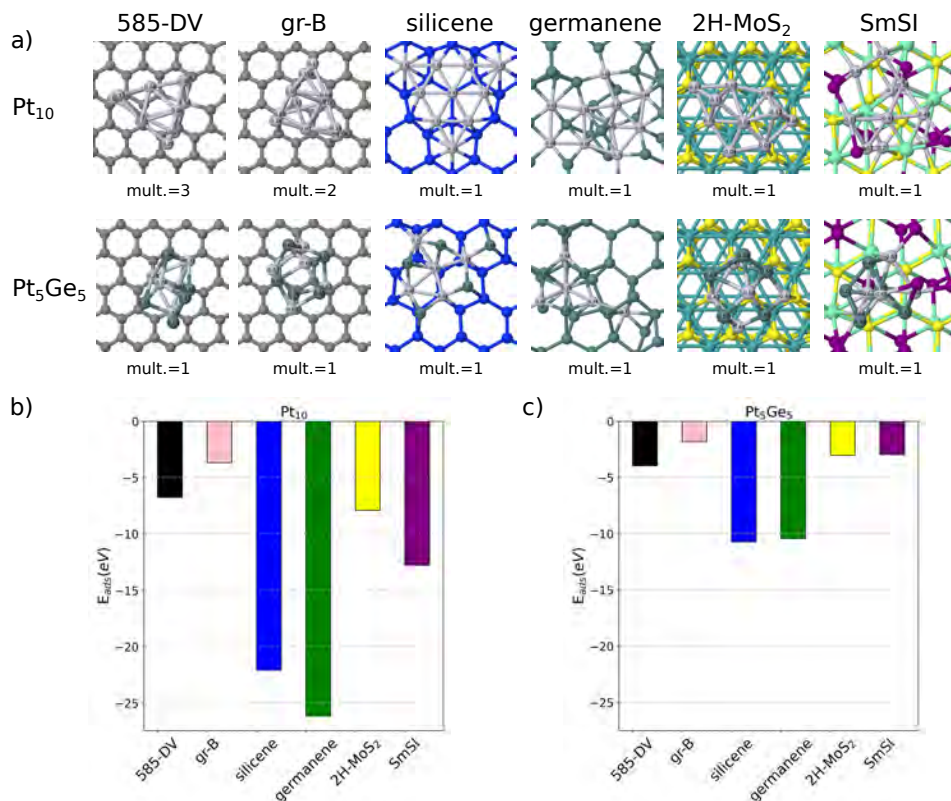
Figure 6.2: a) Putative global minima (GM) structures of Pt$_{10}$ and Pt$_5$Ge$_5$ supported on 5-8-5-DV, gr-B, silicene, germanene, 2H-MoS$_2$ and SmSI. The multiplicity $(2S+1)$ of each structure is given below. The Bader charges are printed on top of the atoms in values of |e|. C, Pt, Ge, B, Si, Mo, S, Sm and I are depicted in dark grey, grey, green, pink, blue, cyan, yellow, lime green and purple, respectively. Adsorption energies (E_{ads}) for b) Pt$_{10}$ and c) Pt$_5$Ge$_5$ as a function of the support.

With the exception of 5-8-5-DV and gr-B, the charge transfer flows from the support to the cluster (see Figure 6.2a). In the former, Pt$_{10}$ and Pt$_5$Ge$_5$ carry ~ 0.2

|e| and 0.4 |e|. Such a small charge transfer is likely to be related to the weak MSI. Among the rest of the 2D materials, the order of charge transfer from the support to Pt_{10} is as follows: 2H-MoS_2 (-0.27 |e|) < SmSI (-3.82 |e|) < germanene (-6.46 |e|) < silicene (-6.78 |e|). As in phosphorene, Pt_5Ge_5 always has a smaller charge because Ge carries a positive charge. Besides, the PDOS analysis in Figure F.2 reveals a strong overlap between Pt d AOs and the support AOs. This is particularly evident for Pt_{10} deposited on silicene and germanene where the overlap happens in the whole width of the Pt d AOs; in fact, every Pt atom is bonded to the surface. In 2H-MoS_2 and SmSI the smearing of the Pt d AOs is also significant, albeit Pt AOs can be observed in the interval from -1.5 eV to E_F not hybridizing with the support, corresponding to the Pt$-$Pt bonds on the uppermost position of the cluster. In Pt_5Ge_5, the Ge AOs extend throughout the whole Pt d AOs, indicating a favourable interaction with Pt sites. Finally, the clusters introduce new states near E_F in all supports, reducing the band gap. Pt_{10}/5-8-5-DV, Pt_{10}/silicene and Pt_{10}/germanene become zero band gap structures. As discussed in subsection 3.1.1, Ge alloying again reopens the band gap since the number of Pt atoms is diminished.

6.3.2 CO poisoning Tolerance of Monometallic Pt and Bimetallic PtGe Clusters Supported on 2D Materials

6.3.2.1 Effect of Size and Ge Concentration on Phosphorene Deposited Clusters

Next, we discuss the role of size and composition on the CO binding strength, which will dictate the propensity of the cluster catalysts to undergo CO poisoning. The most stable adduct structures for the monometallic series Pt_nCO ($n = 4 - 8$) and the $n = 8$ series ($Pt_{8-m}Ge_mCO$, $m = 0 - 4$) are shown in Figure 6.3a. It should be noted that the $Pt_{8-m}Ge_m$ ($m = 5 - 7$) clusters have been discarded as very high Ge content decreases too much the E_{ads}. The most stable adsorption configuration is found to be atop ($\angle$ Pt$-$C$-$O 180º), where CO is always bonded to Pt. The only exception is Pt_7Ge where CO adsorbs in a bridge configuration. In general, single CO adsorption has little impact on the cluster geometry, and the charge transfer from the cluster to the molecule is rather small. Interestingly, the CO affinity is

found to depend non-continuously on size and composition, as indicated in Figure 6.3b and c. Among the pure Pt clusters, Pt_4 shows the weakest affinity to CO. Ge alloying also has a beneficial effect hindering CO poisoning. In a similar fashion to gas-phase, the CO adsorption energy decreases with increasing Ge content. At low Ge concentration the improvement compared with the pure Pt clusters is not very relevant. However, it should be mentioned that the pure Pt clusters already have low ΔG_{CO^*} compared with other typical oxide supports. For example, Pt_4/MgO has a BE[CO] of -3.13 eV (see Figure 5.1). For comparison with previous chapters, the CO binding energies (electronic energy) are also given in Figure F.3.
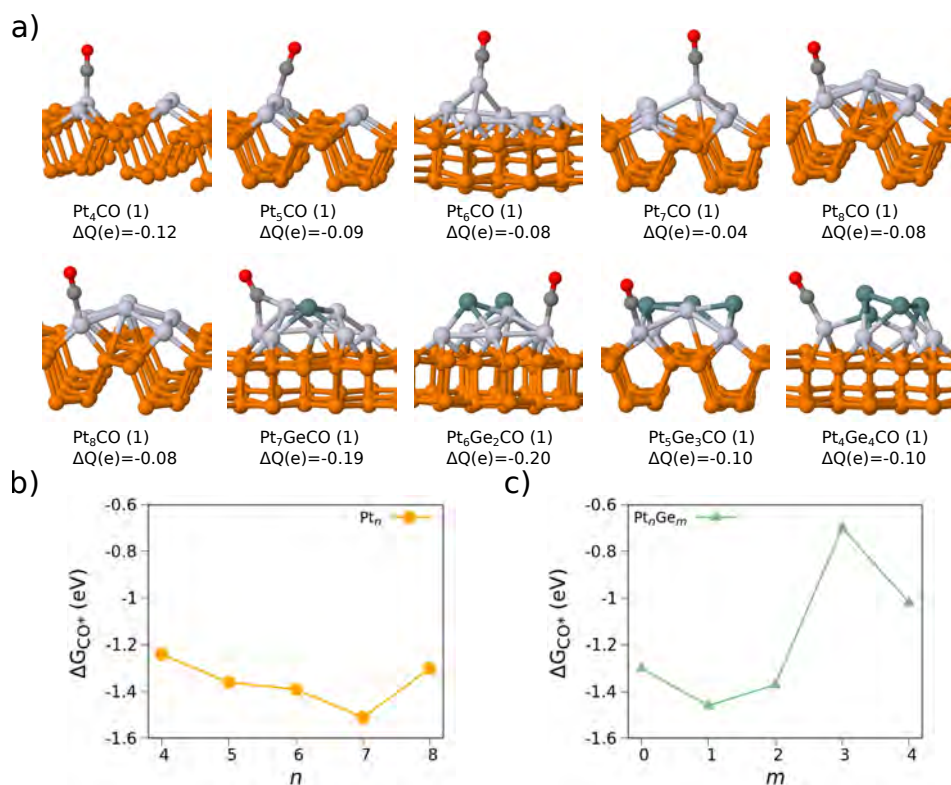
Figure 6.3: a) Putative global minima (GM) complex structures of the monometallic series Pt_nCO ($n = 4 - 8$) and $n = 8$ series ($Pt_{8-m}Ge_mCO$, $m = 0 - 4$) supported on phosphorene. The multiplicity ($2S + 1$) of each structure is given in parenthesis. The total Bader charge of CO* is also given below, in values of $|e|$. Pt, Ge, P, C and O are depicted in grey, green, orange, dark grey and red, respectively. CO adsorption free energies (ΔG_{CO^*}) for the b) monometallic series Pt_n ($n = 4 - 8$) and c) $n = 8$ series ($Pt_{8-m}Ge_m$, $m = 0 - 4$).

6.3.2.2 Effect of the 2D Support

Figure 6.4a presents the most stable adsorption sites of CO on Pt_{10} and Pt_5Ge_5 complexes deposited on the rest of the 2D supports. Our goal is to assess the influence of the support on the CO adsorption properties of the Pt(Ge) clusters. Similar to the case of phosphorene, CO is also found to prefer the atop adsorption configuration, bonded to Pt. Upon adsorption, the charge accumulation on CO is similar in every cluster/2D system. Pt_{10} shows the greatest ΔG_{CO*} when supported on 5-8-5-DV and gr-B (Figure 6.4b), with a ΔG_{CO*} of *ca.* -2.6 eV and -2.0, respectively. This may be explained in terms of the interaction strength of these supports with Pt_{10}. Gr-B shows the weakest interaction with Pt_{10}, and as a result the ΔG_{CO*} comes close to the value in gas-phase complexes reported in Chapter 4 (for comparison we provide the BE[CO] in Figure F.3). Pt_{10}/5-8-5-DV has even a higher CO binding strength than in gas-phase, which may be ascribed to the charge deficiency of the cluster. In the rest of the supports, pure Pt presents a substantial drop in ΔG_{CO*}. Indeed these values are similar to that of Pt_5Ge_5 in gas-phase (Chapter 4). We now demonstrate another strategy to weaken the Pt−CO interaction, without the need of doping or alloying, suggesting that tailoring of the support is as effective as alloying.

In addition, tuning the support and cluster composition simultaneously can enhance further the resistance to CO poisoning, as shown in Figure 6.4c, providing the existence of joint effects between the nanoalloy and support. Every CO−Pt_5Ge_5/2D system weakens the interaction with CO as compared to CO−Pt_{10}/2D. As seen in pure Pt, among the CO−Pt_5Ge_5/2D, the strongest interaction with CO is found when the bimetallic cluster is anchored on graphene-based supports. On Pt_5Ge_5 deposited on silicene and 2H-MoS_2, ΔG_{CO*} are reduced up to *ca.* -0.6 eV and Pt_5Ge_5/SmSI has a ΔG_{CO*} of only -0.20 eV. Even further, no chemisorption is observed in Pt_5Ge_5/germanene; CO is bounded only by physisorption. In this cluster most Pt sites have low exposure and high coordination numbers with neighbouring Ge atoms, causing a repulsive interaction with CO.

Our results taken together suggest that there is a correlation between the cluster-support interaction strength and the cluster−CO interaction strength; the stronger the cluster binds to the 2D surface, the weaker it binds to CO. This is true for

monometallic and bimetallic PtGe nanoclusters. In addition, in line with previous chapters, Ge alloying has the ability to reduce the Pt−CO interaction. Within the 2D materials considered in this work, we show that this effect can be exploited to the point that the interaction with CO is not even favorable, as it is found in the case of Pt_5Ge_5/germanene.
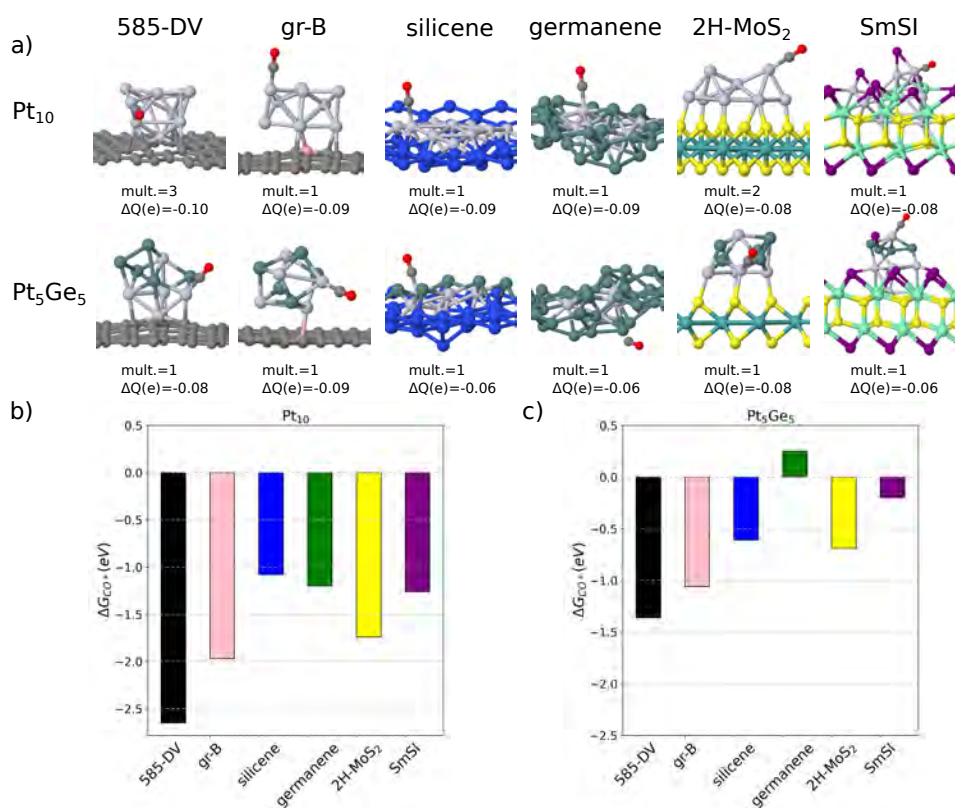
Figure 6.4: a) Putative global minima (GM) complex structures of $Pt_{10}CO$ and Pt_5Ge_5CO supported on 5-8-5-DV, gr-B, silicene, germanene, 2H-MoS$_2$ and SmSI. The multiplicity $(2S + 1)$ of each structure is given below, as well as the total CO* Bader charge, in values of |e|. C, O, Pt, Ge, B, Si, Mo, S, Sm and I are depicted in dark grey, red, grey, green, pink, blue, cyan, yellow, lime green and purple, respectively. CO adsorption free energies (ΔG_{CO^*}) for b) Pt_{10} and c) Pt_5Ge_5 as a function of the support.

6.3.3 HOR Activity of Monometallic Pt and Bimetallic PtGe Clusters Supported on 2D Materials

HOR is a two-electron-transfer reaction in which H_2 loses two electrons and is oxidized to H^+. It is considered the simplest electrochemical reaction as it only involves the formation of a single intermediate, *i.e.*, H*. Three elementary steps can be distinguished in acidic media:[33, 34, 478]

$$H_2(g) + 2* \rightleftharpoons 2H* \qquad\qquad \text{Tafel reaction} \qquad (6.5)$$

$$H_2(g) + * \rightleftharpoons H* + H^+ + e^- \qquad\qquad \text{Heyrovsky reaction} \qquad (6.6)$$

$$H* \rightleftharpoons * + H^+ + e^- \qquad\qquad \text{Volmer reaction} \qquad (6.7)$$

$$H_2(g) \rightleftharpoons 2(H^+ + e^-) \qquad\qquad \text{Overall reaction} \qquad (6.8)$$

These three elementary steps yield two different possible mechanisms on the basis of H_2 dissociation: Tafel−Volmer (TV) and Heyrovsky−Volmer (HV). Both Tafel and Heyrovsky are dissociative adsorption of H_2, albeit the former occurs without proton−electron transfer and the latter with proton−electron transfer. In Tafel step two adjacent sites are required as both H atoms are adsorbed, while in Heyrovsky step only one H is adsorbed and the other H^+ combines with a H_2O molecule to form a solvated proton (*i.e.*, hydronium ion, H_3O^+). Regardless of the mechanism, both Tafel and Heyrovsky provide the key intermediate H* for the following step. The Volmer reaction consists of the electrochemical deprotonation of H* from the surface.

Since all steps involve the H* intermediate, ΔG_{H*} has been suggested as the key descriptor for determining the HOR rate.[30] The barrier of the proton−electron transfer has been demonstrated to scale with ΔG_{H*}. Hence, the usual way to improve the HOR rate comes by regulating ΔG_{H*}. According to the Sabatier principle, the optimal HOR active site should have $\Delta G_{H*} \approx 0$, so that it promotes H* activation on one hand and allows fast H* detachment on the other hand. Too positive ΔG_{H*} means that the Tafel or Heyrovsky step will be hindered, whereas too strong H* adsorption yields a slow Volmer step. Pt is located at the vertex of the volcano plot.

6.3.3.1 Effect of Size and Ge Concentration on Phosphorene Deposited Clusters

In the following we attempt to investigate the effect of the Pt(Ge) cluster size and composition on the HOR activity. The most stable adduct structures for the monometallic series Pt_nH ($n = 4-8$) and the $n = 8$ series ($Pt_{8-m}Ge_mH$, $m = 0-4$) are displayed in Figure 6.5a. Note that in all cases H prefers to bind to a Pt atom, where atop and bridge positions become competitive depending on the cluster size and composition. No thermally relevant isomer was found with H* adsorbed on either Ge or the support. Notwithstanding, it is important to note that both promoter and support may alter the Pt active sites through ligand or geometric effects.

In order to discriminate poor HOR catalyst candidates, we have set the optimal range for ΔG_{H*} between -0.2 eV and 0.2 eV. At first glance, a remarkable size and composition dependence of ΔG_{H*} can be observed in 6.5b and c, characteristic of the subnano regime. ΔG_{H*} becomes more negative as the size increases, being the smallest Ptn clusters the ones with a ΔG_{H*} closer to 0. A closer analysis reveals that Pt_5 is the best candidate with ΔG_{H*} = -0.02 eV, which outperforms commercial Pt/C (ΔG_{H*} = -0.09 eV)[479]. Among the pure clusters, Pt_8 has the strongest H* adsorption and thus, slowest Volmer step. Regarding the nanoalloys, a very small size or a high Ge content is required to yield low ΔG_{H*} values. Indeed, the only clusters with ΔG_{H*} values below the -0.2 eV threshold are Pt_5Ge_3 and Pt_4Ge_4 (ΔG_{H*} = -0.08 and -0.12, respectively). Nevertheless, despite being ~ 0.1 eV higher than in Pt_5, the PtGe nanoalloys may be equal or better than Pt_5 when the HOR activity is weighted together with the CO tolerance. Generally, all clusters except for Pt_4, present a negative ΔG_{H*}, a behaviour that contrasts with the other 2D supports (*vide infra*). Moreover, a slight charge transfer from the cluster to H* is also observed, albeit no correlation with ΔG_{H*} is found.
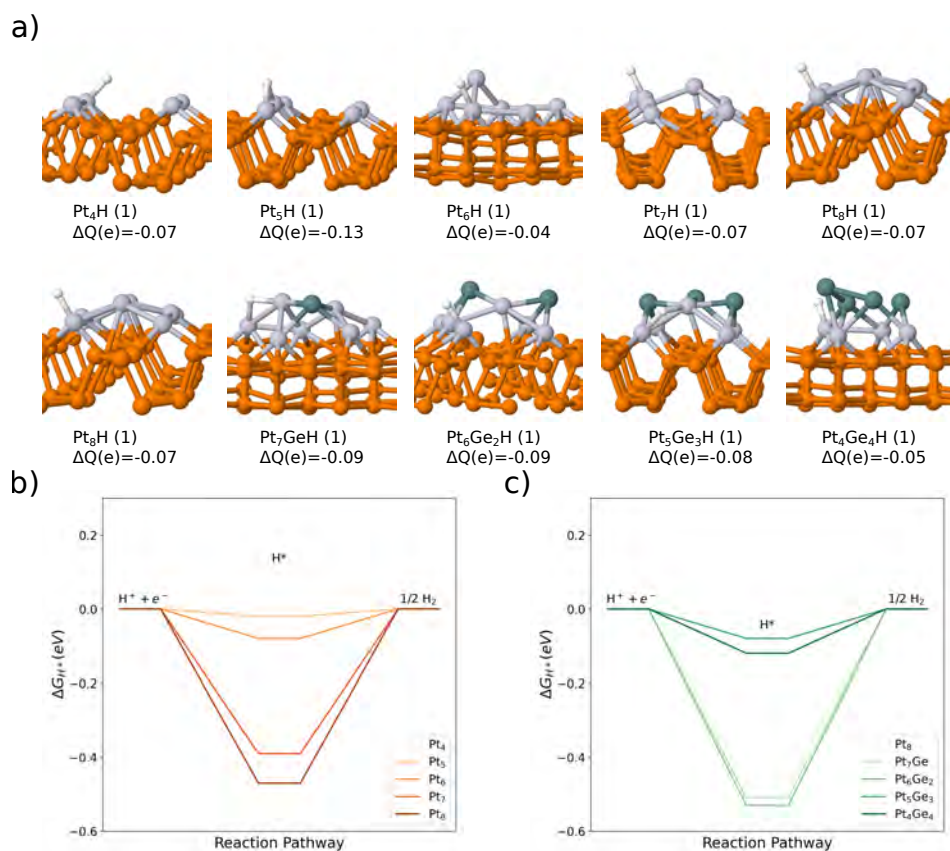
Figure 6.5: a) Putative global minima (GM) complex structures of the monometallic series Pt_nH ($n = 4 - 8$) and $n = 8$ series ($Pt_{8-m}Ge_mH$, $m = 0 - 4$) supported on phosphorene. The multiplicity ($2S + 1$) of each structure is given in parenthesis. The total Bader charge of H* is also given below, in values of |e|. Pt, Ge, P and H are depicted in grey, green, orange and white, respectively. Free energy diagrams for HOR activity at $U = 0$ V (*vs* SHE) on the b) monometallic series Pt_n ($n = 4 - 8$) and c) $n = 8$ series ($Pt_{8-m}Ge_m$, $m = 0 - 4$) supported on phosphorene.

6.3.3.2 Effect of the 2D Support

The most stable binding sites for H on Pt_{10} and Pt_5Ge_5 deposited on the rest of the 2D supports are shown in Figure 6.6a. Strikingly, in some of these supports the surface atoms become competing active sites for H*. Specifically, in Pt_{10}/5-8-5-DV, Pt_5Ge_5/5-8-5-DV and Pt_5Ge_5/silicene H* prefers to bind to the surface instead of Pt. This may be indicative of hydrogen spillover phenomena. In the rest of the Pt(Ge)/2D systems, the most stable H* adsorption sites are found to be the Pt sites on the cluster-support interface. Our results reveal that in Pt_{10} all supports except SmSI present a negative ΔG_{H*}, whereas in Pt_5Ge_5 all supports except gr-B and silicene present a positive ΔG_{H*} (see Figure 6.6b and c). It is thus clear that Ge introduces a repulsive interaction with H*. Based on previous chapters, we believe this effect to be concentration dependent, so Ge alloying could be used to adjust ΔG_{H*} to the optimal value. The clusters that fall inside the optimal ΔG_{H*} energy range are, in order of decreasing absolute $|\Delta G_{H*}|$ value: Pt_{10}/silicene, Pt_5Ge_5/germanene, Pt_{10}/SmSI, Pt_5Ge_5/2H-MoS$_2$ and Pt_5Ge_5/silicene. Surprisingly, on most of the 2D surfaces, alloyed clusters exhibit smaller ΔG_{H*} values, indicating higher catalytic activity. This scenario is unexpected because usually doping or alloying Pt with a second element improves sintering or poisoning resistance, selectivity, *etc.* but at the expense of the catalytic activity.[89, 185, 187, 228, 229, 394] In this case, equimolar Pt_5Ge_5 clusters are predicted to be more active for the HOR.
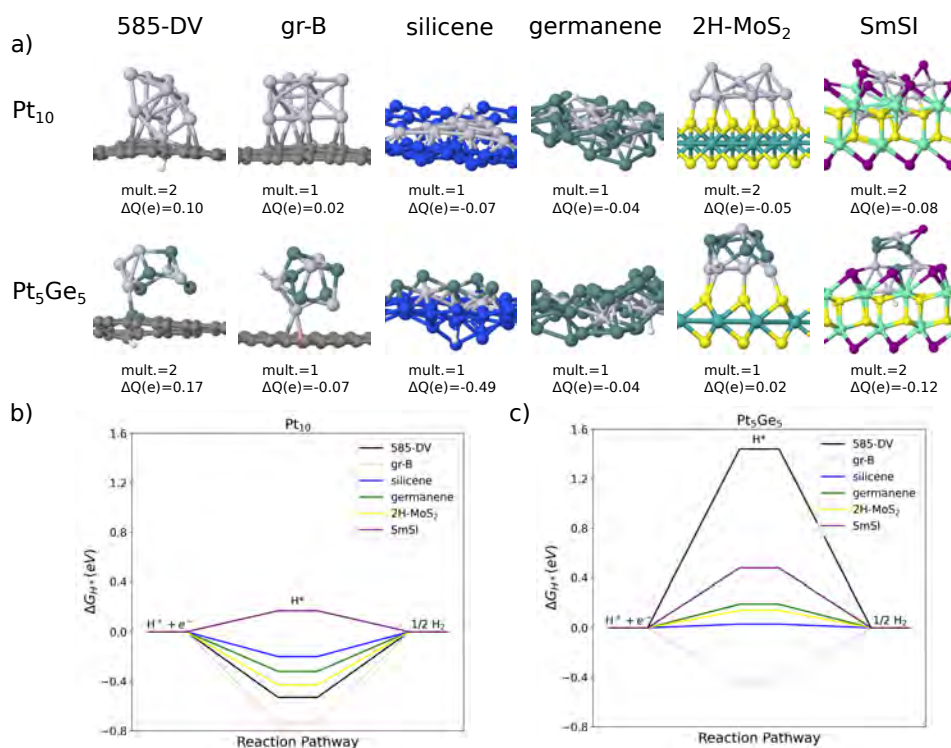
Figure 6.6: a) Putative global minima (GM) complex structures of $Pt_{10}H$ and Pt_5Ge_5H supported on 5-8-5-DV, gr-B, silicene, germanene, 2H-MoS$_2$ and SmSI. The multiplicity $(2S + 1)$ of each structure is given in parenthesis. The total Bader charge of H* is also given below, in values of $|e|$. Pt, Ge, B, Si, Mo, S, Sm, I and H are depicted in dark grey, red, grey, green, pink, blue, cyan, yellow, lime green, purple and white, respectively. Free energy diagrams for HOR activity at $U = 0$ V (*vs* SHE) on b) Pt_{10} and c) Pt_5Ge_5 as a function of the support.

6.4 Conclusions

In the present chapter we have studied the stability, CO poisoning tendency and HOR activity of small-size pure Pt and bimetallic PtGe clusters deposited on a series of 2D supports. More specifically, a screening of size, composition and support material has been carried out to obtain the combinations that yield the best results. Except for the graphene-based supports, the rest of the 2D materials are very effective in anchoring the clusters. Indeed, a very important MSI is observed which translates into the complete wetting of the cluster to the surface and a huge support-to-cluster charge transfer. Pt clusters on germanene and SmSI get encapsulated by Ge and I atoms, hinting that these supports are able to induce SMSI effects. On phosphorene E_{ads} increases with the size of Pt_n, and decreases with Ge concentration. Moreover, Ge avoids contact with the surface, locating on top of the clusters. Consequently, high Ge contents might lead to the blocking of active sites. On the rest of the surfaces, the interaction to the surface in PtGe is weaker compared to Pt. However, when PtGe is supported on silicene and germanene the E_{ads} values are remarkably large suggesting that these monolayers could potentially be used to hold PtGe catalysts. Furthermore, cluster deposition is observed to be an effective method to reduce the band gap of the support and facilitate electron transport.

Additionally, the support assists pure Pt clusters in reducing the CO binding strength to values comparable to equimolar PtGe clusters in gas-phase, which can be reduced further by Ge alloying. Within the 2D materials considered in this work, we show that this effect can be exploited to the point that the interaction with CO is not even favorable, as it is found in the case of Pt_5Ge_5/germanene.

On phosphorene, only the smallest Pt_n and Ge-rich PtGe clusters provide ΔG_{H*} values close to 0. Nevertheless, on most of the 2D surfaces, alloyed clusters exhibit smaller ΔG_{H*} values, indicating higher catalytic activity. This scenario is unexpected because usually doping or alloying Pt with a second element improves sintering or poisoning resistance, but at the expense of the catalytic activity. In this case, equimolar Pt_5Ge_5 clusters are predicted to be more active for HOR.

In light of these results, the combination of PtGe bimetallic clusters and 2D supports seems very promising for the design of resistant and active electrocatalysts.

The simultaneous tailoring of alloy composition and support is demonstrated to be an effective strategy to successfully adjust the catalytic properties. For future work we intend to explore the ORR mechanism and extend our pool of 2D materials to include h-BN and MXenes.

Chapter 7

Summary and Concluding Remarks

"I had a dream. That on nights with a full moon, I become an infant, and feel the embrace of a familiar warmth. But, as I wake from that dream, only a faint of loneliness remains... and that, too, takes but a moment to disappear. With a single tear-drop. Like the morning dew."

— Kentaro Miura, *Berserk*

IN a context of great socio-economical transformations, subnano clusters have emerged as promising catalytic devices for next-generation PEM-FCs. Their huge surface-to-volume ratio, a result of their small size, has two important consequencies. First, the catalytic efficiency is maximized as almost all atoms are part of the surface, and hence, the amount of precious Pt is optimized. Second, the properties are governed by the surface atoms, meaning that alterations on the surface can induce changes on the catalytic properties. Surface modifications are indeed accesible and realizable experimentally by a control of size, morphology (isomers), composition (doping/alloying), metal-semiconductor junction (support) and environment (ligand coverage). Precisely, it is this flexibility to control the catalytic properties that turns clusters into superb candidates for catalysis. In this thesis, the potential catalytic properties of small-size PtGe bimetallic clusters have been studied, since Ge has been suggested in few key investigations to be an effective alloying agent. This thesis aims to provide new insight into the promotional role of

Ge as a CO resistant alloying agent by putting special emphasis on the connection between electronic structure and catalytic performance (*i.e.*, structure-property relationship), two concepts tightly interwoven and difficult to separate, as remarked throughout this manuscript; understanding of the catalytic properties requires an understanding of the electronic structure.

Specifically, herein, we intend to design a highly-engineered catalyst where all its components play an active rather than passive role, using a bottom-up approach. Each chapter is built upon the results of previous chapters. In this sense, first, the ability of Ge-single-atom doping to reduce CO poisoning is assessed on charged Pt clusters in gas-phase. Then, we move beyond single-atom doping and study the effect of Ge concentration on the interaction of Pt with CO. Often, high promoter concentrations can dilute the catalytic activity of Pt. For this reason, next we investigate the catalytic activity of PtGe clusters for the CO oxidation. A composition dependence is found where Ge induces ligand and bifunctional effects to alleviate CO poisoning. Having identified the composition as a key parameter, afterwards, we try to understand how this parameter interacts with others, *i.e.*, the support, and try to optimize simultaneously both parameters for a superior catalytic activity.

With such a complex task in our hands, in this thesis we employ state-of-the-art computational techniques to investigate the PtGe clusters. First, a GM search is done to sample thoroughly the PES and identify all low-lying isomers. Then, the electronic structure and chemical bond is characterized by a variety of tools. Once the structural and electronic properties are understood, a subsequent GM search is done to locate the most stable active sites and binding modes of the different adsorbates. Finally, the different reaction mechanisms are evaluated on the basis of a TS search and microkinetic modeling.

In the following, the most relevant findings of each chapter are revisited and summarized.

7.1 Effect of Ge-Single-Atom Doping

First, in Chapter 3 we have considered doping free-standing charged Pt_n^+ ($n = 5 - 9$) clusters with Ge so as to make a direct comparison with experimental mass spectrometric experiments. A robust framework has been employed to perform the GM search. Namely, it has been benchmarked with two different methods (*viz.*, BLDA and GA), as well as three different functionals (*viz.*, PBE, TPSSh, and LC-ωPBEh) and several spin states (*viz.*, doublet to octuplet). This protocol has ensured us that the located GM are in fact very close to the true GM. A size dependence is found for the Pt_n^+ cluster geometries. It is interesting to note that even single-atom-doping can alter significantly the geometry. The most radical case is for $n = 5$ where a 3D to 2D transition is observed.

The propensity to undergo CO poisoning is usually quantified in terms of binding energies. Nonetheless, these binding energies depend on the choice of a reference system for the bare cluster, which may not always be trivial. For this reason, besides the binding energies, other descriptors have been used that solely depend on the cluster$-$CO, such as the CO stretching frequency, charge density of the Pt$-$C bond critical point and NBO population of the $2\pi^*$ MO. All descriptors point to a reduction in the affinity to CO after Ge doping, where they evolve in a non-continuous way with the cluster size. Except for the biggest clusters, a correlation is found for all descriptors connected with the Pt$-$C bond. Namely, a reduction in the BE[CO] upon doping is reflected in a reduction of the Pt$-$C bond distance and Pt$-$C stretching frequency.

The PDOS analysis reveals that Pt and Ge forms polarized covalent bonds, with charge accumulation on Pt due to a charge transfer from Ge. These polarized bonds have two consequences: first, the number of unpaired electrons is quenched; and second, the availability of Pt d AOs to interact with CO $2\pi^*$ MOs in the the back-donation step becomes compromised. This observation is in agreement with a redshift in the C$-$O stretching frequency (weakening of the C$-$O bond) and a diminution of the NBO population of $2\pi^*$.

So as to verify that doping does not harm the catalytic activity we have computed the H_2 binding energies. It is found that dissociative adsorption is more stable than non-dissociative adsorption. Moreover, $GePt_n^+$ clusters show very similar or lower

BE[2H] to pure Pt, suggesting an easier desorption.

7.2 Effect of Ge Concentration

Moving beyond single-atom doping, in Chapter 4 we have studied PtGe clusters in gas-phase with a larger Ge concentration. The goal is to first observe whether Ge-rich clusters perform better than single-atom doped ones, and if so, find then the Pt:Ge composition with the highest resistance to CO poisoning. To reach this goal, all possible compositions have been studied for sizes $n \leq 10$, starting from pure Pt to pure Ge clusters.

A strong effect of Ge concentration has been observed on BE[CO]. BE[CO] changes in a volcano-fashion with Ge concentration, showing the minimum (weakest Pt−CO interaction and thus least tendency to be deactivated by CO poisoning) at equimolar concentrations. The ulterior reason lies in the good mixing between Pt and Ge, which has an electronic origin. The effective mixing is reflected in the maximization of the number of polarized Pt−Ge covalent bonds, conferring the equimolar clusters extra thermodynamic and electrostatic stability. As a result, equimolar compositions display the greatest intracluster energy and quenching of unpaired electrons. Furthermore, the formation of Pt−Ge bonds increases the covalent character of the cluster, which adds further stability. This is confirmed with the AdNDP and PDOS analysis. In the former, the delocalized nc-2e ($n \geq 3$) bonds of pure Pt_n are contrasted to the covalent 2c-2e bonds on Pt_nGe_n. In the latter, a strong hybridization between Pt s and d AOs with Ge s and p AOs is visible, which reduces the delocalization of the Pt d band below E_F. Due to the polarization, the Pt−Ge bonds act as individual dipoles which increases the electrostatic stability.

Regarding the interaction with CO, the large stability of equimolar clusters is translated as a blockage of the back-donation as well as donation steps with CO. Ge participates in both steps by diminishing the interaction strength. On the one hand, the formation of Pt−Ge bonds decreases the number of Pt AOs to interact with CO in the back-donation step. On the other hand, the charge accumulation in Pt due to the bond polarization, increases the Pauli repulsion and hinders the charge tranfer from CO 5σ to Pt AOs, *i.e.*, the donation step.

Besides, the catalytic activity of the PtGe nanoalloys has been tested for the H_2 dissociation reaction. The computed reaction barriers confirm that the clusters are able to dissociate spontaneously (or with very low barriers) H_2, regardless of Ge concentration.

7.3 Test of Catalytic Activity

In the third part of this thesis (Chapter 5), we have carried out a concise mechanistic study of the CO oxidation catalized by Pt_4Ge_n ($n = 0 - 4$) clusters supported on MgO(100). The objective is to understand the impact of Ge content on the viability of the different reaction pathways. For this, a robust combination of DFT and microkinetic simulations has been employed to correctly capture the dynamic behaviour of the reaction kinetics.

Regarding the adsorption of the reactants, CO is found to adsorb only on Pt sites while O_2 (or atomic O) adsorbs preferentially on Ge sites. Both pure Pt and alloyed PtGe clusters are able to activate the O_2 bond and dissociate it with fairly low barriers in an exothermic process, suggesting that the mayority of adsorbed O_2 will be present as O*.

The DFT mechanistic study puts in evidence that Ge does not play an important role on the ER mechanism. The corresponding reaction energy diagram is downhill for all compositions, indicating that the equilibrium will shift towards CO_2 production. Notwithstanding, a completely opposite behaviour is found for the LH channel. Here, a composition dependent behaviour is found where the relative stability of the intermediates and reaction barriers vary with Ge content. In Pt_4, Pt_4Ge and Pt_4Ge_2, the O* + CO* intermediate becomes the most stable state in the whole reaction profile. Consequently, this state acts as a thermodynamic sink, shifting the equilibrium towards O* + CO* instead of CO_2 formation. Additionally, the CO_2 desorption step is highly endothermic in Pt_4, hinting to a likely CO_2 poisoning. On the contrary, in Pt_4Ge_3 and Pt_4Ge_4, CO_2* becomes the most stable state owing to a increase in the exothermicity of the second CO oxidation step. Therefore, the reaction will evolve easier towards CO_2 formation.

With the purpose of discerning the dynamic interplay between the different

reaction pathways, we have performed microkinetic simulations. Pt_4Ge_3 is found to be the best candidate. In this case, the CO poisoning regime of the CO oxidation bistable kinetics disappears at the reaction conditions considered in this work, and instead, moderate TOF_{CO_2} are obtained. O* becomes the mayority species on the surface with hardly any amount of CO* and CO_2*, which can be explained with the high oxophilicity of Ge.

Overall, our results reveal that Ge induces ligand and bifunctional effects on Pt. On the one hand, in agreement with previous chapters, the formation of the Pt−Ge polarized bonds brings a series of electronic effects that reduce the affinity to CO. In this way, the BE[CO] equiparates with that of oxygen, resulting in a higher reactivity according to the Sabatier principle. The high mixing guarantees that all Pt sites undergo ligand effects. On the other hand, the greater oxophilicity of Ge creates new and more stable active sites for oxygen through a bifunctional effect. As a result, part of Ge gets oxidized to GeO_x, which remains in contact with the PtGe alloy. This oxide acts as an oxygen reserviour resistant to CO poisoning. Now there is not a competition between CO and O_2 for adsorption since they each prefer different adsorption sites (dual adsorption), resulting in high reaction rates.

7.4 Effect of 2D Support

The last part of this thesis (Chapter 6) has focused on the MSI effect. For this, we have deposited pure Pt and PtGe bimetallic clusters on a set of 2D materials to investigate the role of the MSI on the cluster stability, resistance to CO poisoning and catalytic activity. Precisely, 2D materials show very strong surface effects owing to their single layer structure, and thus, they are expected to be excellent supports to modify the properties of adsorbed catalysts.

With the exception of the graphene-based supports, the rest show a remarkable interaction with the Pt clusters, as can be judged by their planar geometry. This also becomes evident with the high adsorption energies and surface-to-cluster charge transfer. The greatest values are observed in germanene and silicene, followed by phosphorene. The case of SmSI deserves special attention. Despite not showing a so large adsorption energies, the area of the cluster/support interface is still

very high, since almost all atoms are bonded to the surface. Indeed, some Pt atoms are observed to diffuse inside the surface and stabilize in the Sm_3I_3 chair structures. Additionally, SmSI is predicted together with germanene to trigger cluster encapsulation, a proccess commonly known as SMSI. As can be expected increasing Ge content has an adverse effect on the cluster stability. Bimetallic clusters decrease the contact area with the support and adopt more globular shapes due to the repulsion between the surface and Ge atoms. This also affects the high mixing observed in gas-phase. The reason lies in the fact that alloying introduces an extra interaction, *i.e.*, intracluster interaction, which is in competition with the cluster-support interaction. Alloying favours the cluster internal stability at the expense of weakening the adsorption strength to the support, while the support has the opposite effect.

In addition, it has been proved that the deposition of metallic cluster can reduce or close the band gap, enhancing electron movility.

Interestingly, our results reveal that pure Pt clusters supported in 2D materials (except in 585-DV and gr-B) display a weaker affinity to CO than in gas-phase or supported on other metal-oxides, hinting that the 2D material contributes favourably to decreasing CO poisoning. Surprisingly, encapsulation by Ge atoms can protect the cluster from CO chemisorption. In agreement with previous chapters, alloying Pt with Ge reduces further the CO binding energies.

To conclude with Chapter 6, we have studied the HOR activity of these systems within the CHE approximation. The support, cluster size and Ge content are observed to be excellent degrees of freedom to control the binding strength of H. For instance, in phosphorene, ΔG_{H*} appears to increase with the cluster size, while no clear trend is apparent for the composition. In contrast, for the rest of the supports increasing Ge concentration reduces ΔG_{H*}. In particular, Pt_5 and Pt_5Ge_3 on phosphorene, and Pt_5Ge_5 on silicene, $2H-MoS_2$ and germanene yield the weakest interaction with H* and therefore the best HOR performance.

The results obtained in Chapter 6 stress the fact that the behaviour observed for PtGe free-standing clusters may not hold after surface deposition. Equimolar composition is no longer the ideal composition since it will not be sufficiently stabilized by the support to avoid sintering. Nonetheless, Ge is still a versatile

promoter judging by the good CO poisoning resistance and HOR performance of PtGe nanoalloys, the difference with gas-phase being that on 2D materials a lower Ge concentration might be more favorable to boost the catalytic performance of Pt.

7.5 Future Work and Perspectives

This thesis has provided extensive work on the promotional effects of Ge to Pt clusters. Throughout this thesis, relationships have been stablished between the catalytic properties, either binding energies of ligands or reaction mechanisms, and electronic structure. However, at the same time, it has been evidenced that much work is still required to gain a thorough comprehension of cluster catalysts. Herein, we provide brief indications on how the work developed in each chapter could be continued.

The following guidelines are given to continue Chapter 3:

- Benchmark the CO binding energy against further DFT functionals.

- Analyze how the relative stability of the isomers changes with the functional.

- Study in greater detail the electron correlation with multiconfigurational methods.

The following suggestions are given as a follow up of Chapter 4:

- Increase the range of the cluster size to observe structural transitions in PtGe bimetallic clusters in gas-phase. Moving to bigger clusters may raise many interesting questions: are globular geometries favoured for bigger sizes as well? Does the good mixing between Pt and Ge hold for bigger sizes? Are equimolar clusters still effective to reduce CO poisoning for bigger sizes?

- Analyze in greater detail the delocalization of Pt−Pt bonds *vs* the covalency of Pt−Ge bonds.

The following suggestions are given as a follow up of Chapter 5:

- Study the adsorption of CO, O_2 and CO_2 at higher coverages to better understand the bifunctional mechanism. Increasing the cluster size could also help in this direction.

- Incorporate the coverage effects into the microkinetic model with lateral interactions.

- Build a phase diagram as a function of pressure and temperature to i) obtain the most stable coverages at different working conditions, ii) determine the most favourable working conditions, and iii) correctly sample the boundary between the slow-kinetic regime (CO poisoning) and fast kinetic regime of the bistable kinetics of CO oxidation.

- Understand better how the fluxionality of PtGe clusters evolves with ligand coverage.

- Convey similar studies using other oxide supports such as CeO_2, TiO_2 and Al_2O_3.

The following guidelines are given as a continuation of Chapter 6:

- Carry out a mechanistic study of the ORR reaction.

- Study the adsorption of CO, H as well as the ORR intermediates at higher coverages.

- Include also the intermediate compositions between pure Pt_{10} and Pt_5Ge_5 for 5-8-5-DV, gr-B, silicene, germanene, 2H-MoS$_2$ and SmSI surfaces.

- Perform more realistic electrochemical calculations beyond the CHE approximation by including explicitely the electrode potential.

- Perform *ab initio* molecular dynamics (AIMD) to better understand the SMSI on germanene and SmSI supports.

- Include further 2D supports such as h-BN and MXenes.

Another interesting direction could be to study materials containing Pt and Ge but not in the form of clusters. One possible example are Pt nanowires (NWs) supported on Ge(001) surface. Recently, it has been reported that Pt deposition onto a Ge(001) surface leads to the formation of Pt NWs.[480–482] These NWs are made of isolated Pt atoms, not bonded to each other, which may act as single atom

catalysts (SACs) . The interesting part here is to compare the catalytic porperties of Pt and Ge in this system with the PtGe clusters and observe if there are any susbtantial differences.

Regarding the future perspectives, we believe that subnano clusters may become crucial in reshaping and directing the field of catalysis towards new challenges. Cluster catalysis is still in its infancy and there are many possible routes in catalyst design to be discovered. For instance, one could envision adhering molecular sensors sensitive to external conditions to the cluster surface. These sensors can then be used to trigger structural transformations to the cluster by taking advantage of their fluxionality and increase the population of the most active isomers. Similarly, the MSI could still be further exploited by taking advantage of not only the charge transfer, but also the spin degree of freedom. For example, a material displaying spin Hall effect (SHE) could be used as a support. In this way, it would be possible to pump a pure spin polarized current into the cluster. Such an approach would be advantageous for example for spin forbidden reactions. In short, the support may be thought of as being a kind of electronic circuit with which one can control and direct the electron charge and spin to change the electronic structure of the cluster, and thus the catalytic performance.

The study of high entropy alloys (HEAs) at the subnano regime also holds great promise. HEAs are alloys containing five or more components in near-equimolar percentage in one crystalline solid-solution phase.[483–485] Comparing with traditional alloys, HEAs have a more flexible composition range owing to their combinatorial number of permutation. This "cocktail" effect offers the possibility to modulate the electronic structure and create unique active sites of multiple dissimilar elements located next to each other, which results in a complex multielement synergy. This approach allows a considerable reduction of precious Pt loading. Or even more, precisely because of this "cocktail" effect, it may be possible to design Pt-free catalysts with equal catalytic activity, making them very appealing for large-scale manufacturing.

As has been discussed throughout this thesis, unfortunately, there does not exist a unique formula to design the ideal catalyst for all reactions. The different strategies to control the catalytic properties are often rection specific, so a good catalyst for one

reaction may yield a poor performance for anther. Likewise, the catalytic properties may display opposite trends with the different design parameters such as size, composition and support. As the complexity of the catalyst increases, it becomes intractable to explore all the parameter space manually. Here comes the importance of autonomous material screening techniques.[486–490] High-throughput computing is able to explore autonomously combinations of thousands of materials, saving a huge amount of computational time. This technique will accelerate substantially the material screening process and is expected to play an important role in the following years.

Last but not least, the hope of this thesis is to try to inspire future guidance or at least raise fruitful discussion into the emerging field of cluster catalysis. Catalysis stands as an essential player in the pursuit of a green energy production network. However, such a task can only be accomplished through a continuous, innovative and interconnected scientific endeavour.

Appendix A

Calculation of Thermodynamic Quantities

In this appendix we review the most important equations in thermochemistry.[87] Gibbs free energies are estimated in the ideal gas limit with

$$G = (E_{\text{elec}} + \text{ZPE}) - TS \tag{A.1}$$

where E_{elec} is the KS electronic energy at $0K$, ZPE is the zero point energy and S is the total entropy of a given state. The ZPE is calculated as half the sum of the energies of all vibrational modes

$$\text{ZPE} = \frac{1}{2} \sum_i h\nu_i \tag{A.2}$$

where h is the Planck constant and ν_i is the vibrational frequency for the mode i.

The evaluation of activation free energy requires the identification of the transition state (TS). It is calculated as

$$\Delta G^{\ddagger} = G_{\text{TS}} - G_{\text{IS}} \tag{A.3}$$

where G_{IS} and G_{TS} are the free energy of the initial state (IS) and TS. The higher the value of $\Delta G^{\ddagger}$, the more kinetically hindered the reaction will be.

The reaction free energy is computed as

$$\Delta G_r = G_{\text{FS}} - G_{\text{IS}} \tag{A.4}$$

where G_{FS} is the free energy of the final state (FS). $\Delta G_r < 0$ indicates an exergonic reaction while $\Delta G_r > 0$ is endergonic.

The total entropy of a species is given by the contributions from translational (S_{trans}), rotational (S_{rot}) and vibrational (S_{vib}) entropies:

$$S = S_{\text{trans}} + S_{\text{rot}} + S_{\text{vib}} \tag{A.5}$$

For adsorbed species only vibrational entropy is considered, while for the gaseous species translational and rotational entropy contributions are also included. The translational entropy of the gaseous molecules is estimated using the Sackur-Tetrode equation

$$S_{\text{trans}} = R \left[\ln \left[\left(\frac{2\pi M k_B T}{h^2} \right)^{\frac{3}{2}} \frac{k_B T}{P} \right] + \frac{5}{2} \right] \tag{A.6}$$

where R is the gas constant and P and M are the pressure and molar mass of the gaseous molecule. The rotational entropy is approximated with the rigid rotor model for linear molecules

$$S_{\text{rot}} = R \left[\ln \left(\frac{8\pi^2 I k_B T}{\sigma h^2} \right) + 1 \right] \tag{A.7}$$

where σ is the symmetry number corresponding to the molecule (*e.g.*, 1 for CO, 2 for O_2 and 2 for CO_2) and I is the principal moment of inertia

$$I = \mu R_e^2 \tag{A.8}$$

where μ is the reduced mass and R_e is the equilibrium bond distance of the molecule.

Vibrational entropy is calculated using the harmonic oscillator approximation

$$S_{\text{vib}} = R \sum_i \left[\frac{h\omega_i}{k_B T \left(e^{h\omega_i / k_B T} - 1 \right)} - \ln \left(1 - e^{-h\omega_i / k_B T} \right) \right] \tag{A.9}$$

where ω_i is the frequency of each vibrational mode of the molecule, which are obtained with a vibrational analysis at the DFT level.

Appendix B

Supplementary Material of Chapter 3

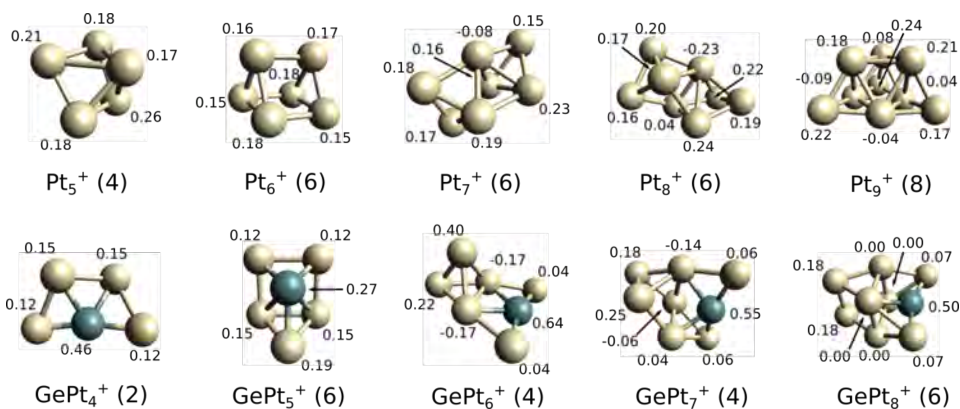## B.1 Global Minima Structures of Pt_n^+ and $GePt_{n-1}^+$ Clusters

Figure B.1: Global minima (GM) geometries of Pt_n^+ and $GePt_{n-1}^+$ ($n = 5 - 9$) clusters calculated at LC-ωPBEh/def2-TZVP level. The multiplicity of each structure is given in parentheses. The natural charges are shown on the atoms. Pt and Ge are depicted in white and dark green respectively.
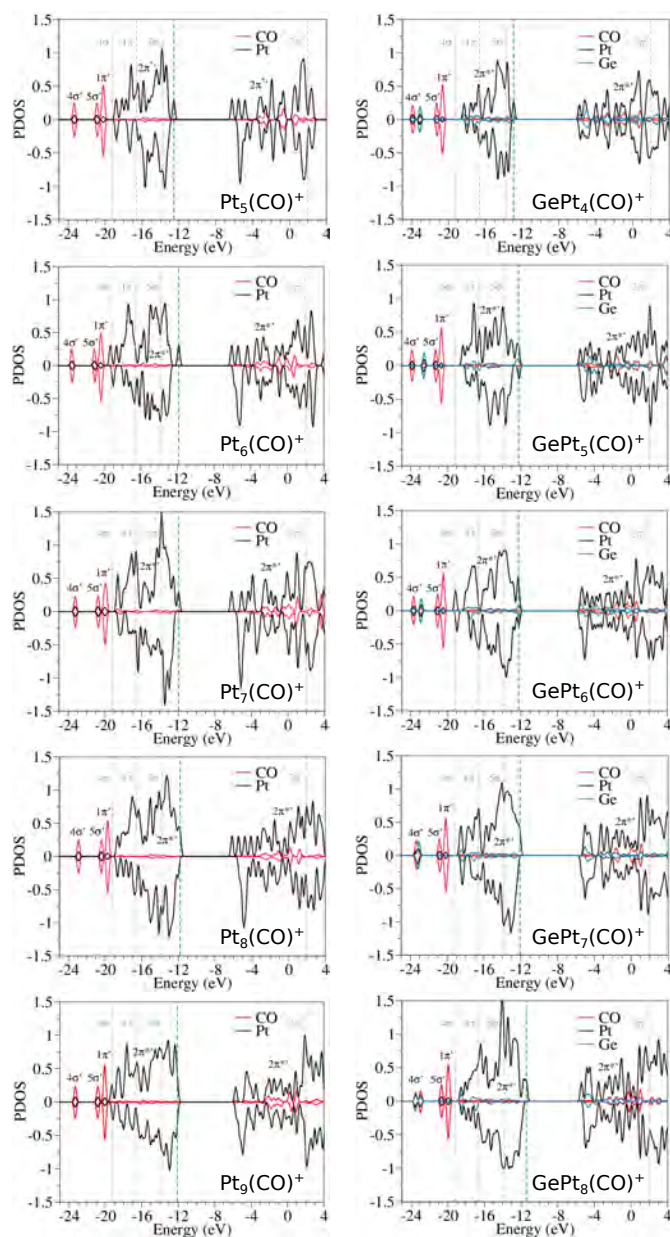
B.2 Electronic Structure Analysis

Figure B.2: Projected density of states (PDOS) of the monometallic $Pt_n(CO)^+$ and doped $GePt_{n-1}(CO)^+$ ($n = 5 - 9$) complex global minima. Gaussian full width at half-maximum (FWHM): 0.3 eV. Positive and negative values correspond to α and β electrons, respectively. The green dashed vertical lines indicate the position of the α HOMO orbital. The grey dashed lines in the CO complexes indicate the orbital energies of the free CO molecule.
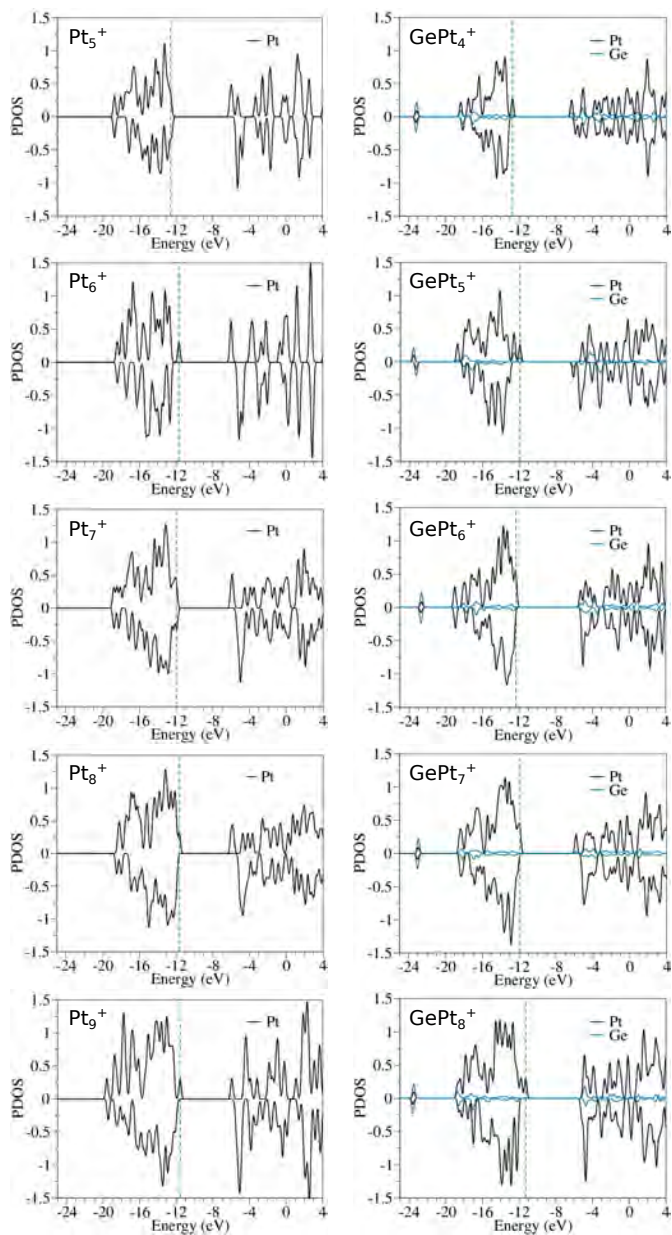
Figure B.3: Projected density of states (PDOS) of the monometallic Pt_n^+ and doped $GePt_{n-1}^+$ ($n = 5 - 9$) cluster global minima. Gaussian full width at half-maximum (FWHM): 0.3 eV. Positive and negative values correspond to α and β electrons, respectively. The green dashed vertical lines indicate the position of the α HOMO orbital. The grey dashed lines in the CO complexes indicate the orbital energies of the free CO molecule.

B.3 H$_2$ Adsorption on Pt$_n^+$ and GePt$_{n-1}^+$ Clusters

Pt$_5$(2H)$^+$ (4)   Pt$_6$(2H)$^+$ (4)   Pt$_7$(2H)$^+$ (4)   Pt$_8$(2H)$^+$ (4)   Pt$_9$(2H)$^+$ (6)

GePt$_4$(2H)$^+$ (2)   GePt$_5$(2H)$^+$ (4)   GePt$_6$(2H)$^+$ (4)   GePt$_7$(2H)$^+$ (4)   GePt$_8$(2H)$^+$ (4)
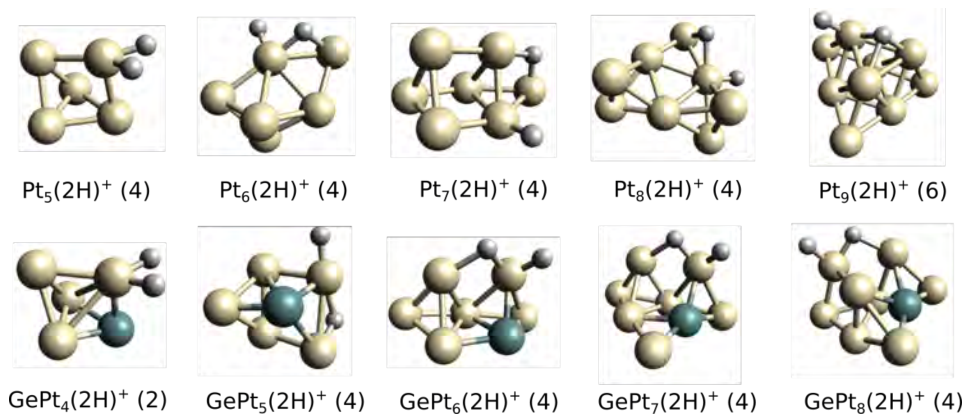
Figure B.4: Global minima geometries of Pt$_n$(2H)$^+$ and GePt$_{n-1}$(2H)$^+$ ($n = 5-9$) complexes calculated at LC-ωPBEh/def2-TZVP level. The multiplicity of each structure is given in round parentheses. Pt, Ge and H are depicted in white, dark green and silver, respectively.

Appendix C

Supplementary Material of Chapter 4

C.1 Structural and Energetic Analysis of Bare Clusters and CO- and 2H- Complexes

Table C.1: Structural and energetic properties of $Pt_{n-m}Ge_m$ ($3 \leq n \leq 10$, $0 \leq m \leq 9$): Pt−C and C−O bond distances, binding energies per atom, mixing energies, CO binding energies and 2H binding energies.

|	Cluster	$d_{Pt-C}(\text{Å})$	$d_{C-O}(\text{Å})$	E_b (eV)	Δ (eV)	BE[CO] (eV)	BE[2H] (eV)
$n = 3$	Pt_3	1.83	1.17	-2.50	0.0	-2.84	
	Pt_2Ge	1.84	1.16	-3.14	-2.17	-2.95	
	$PtGe_2$	1.92	1.16	-2.91	-1.75	-1.36	
$n = 4$	Pt_4	1.83	1.16	-2.81	0.0	-2.94	-1.94
	Pt_3Ge	1.83	1.17	-3.28	-1.96	-3.04	-1.98
	Pt_2Ge_2	1.86	1.16	-3.55	-3.16	-1.27	-0.61
	$PtGe_3$	1.90	1.16	-3.10	-1.46	-1.99	-1.01
$n = 5$	Pt_5	1.83	1.17	-3.07	0.0	-2.92	
	Pt_4Ge	1.82	1.17	-3.42	-1.88	-2.87	
	Pt_3Ge_2	1.84	1.16	-3.64	-3.13	-2.84	
	Pt_2Ge_3	1.86	1.16	-3.43	-2.24	-2.07	
	$PtGe_4$	1.90	1.16	-3.16	-1.06	-1.68	
$n = 6$	Pt_6	1.82	1.16	-3.34	0.0	-2.68	-1.43
	Pt_5Ge	1.82	1.17	-3.51	-1.29	-3.14	-1.89
	Pt_4Ge_2	1.82	1.17	-3.73	-2.84	-3.01	-2.14
	Pt_3Ge_3	1.89	1.17	-3.81	-3.61	-1.57	-0.93
	Pt_2Ge_4	1.89	1.16	-3.53	-2.14	-1.78	-0.93
	$PtGe_5$	1.88	1.16	-3.33	-1.24	-1.62	-0.50
$n = 7$	Pt_7	1.83	1.17	-3.39	0.0	-3.08	
	Pt_6Ge	1.82	1.17	-3.64	-1.90	-2.96	
	Pt_5Ge_2	1.84	1.17	-3.84	-3.52	-2.54	
	Pt_4Ge_3	1.84	1.17	-3.91	-4.18	-2.57	
	Pt_3Ge_4	1.85	1.16	-3.81	-3.72	-1.71	
	Pt_2Ge_5	1.90	1.16	-3.64	-2.71	-1.60	
	$PtGe_6$	1.89	1.16	-3.35	-0.82	-1.82	
$n = 8$	Pt_8	1.82	1.17	-3.58	0.0	-2.86	-1.99
	Pt_7Ge	1.83	1.17	-3.74	-1.77	-2.86	-1.60
	Pt_6Ge_2	1.83	1.17	-3.87	-3.24	-3.01	-1.63
	Pt_5Ge_3	1.85	1.17	-4.00	-4.78	-2.46	-1.80
	Pt_4Ge_4	1.86	1.16	-4.06	-5.68	-1.64	-1.04
	Pt_3Ge_5	1.90	1.16	-3.90	-4.89	-1.42	-0.91
	Pt_2Ge_6	1.86	1.17	-3.63	-3.19	-1.66	-0.42
	$PtGe_7$	1.86	1.17	-3.37	-1.52	-2.08	-0.24
$n = 9$	Pt_9	1.82	1.17	-3.69	0.0	-2.98	
	Pt_8Ge	1.82	1.17	-3.83	-1.72	-2.84	
	Pt_7Ge_2	2.01	1.19	-3.94	-3.23	-2.92	
	Pt_6Ge_3	1.83	1.17	-4.02	-4.40	-3.01	
	Pt_5Ge_4	1.83	1.17	-4.10	-5.62	-2.49	
	Pt_4Ge_5	1.90	1.16	-4.04	-5.62	-2.95	
	Pt_3Ge_6	1.91	1.16	-3.87	-4.51	-1.35	
	Pt_2Ge_7	1.88	1.16	-3.58	-2.41	-2.10	
	$PtGe_8$	1.87	1.17	-3.40	-1.20	-1.56	
$n = 10$	Pt_{10}	1.82	1.17	-3.88	0.0	-2.37	-1.35
	Pt_9Ge	1.83	1.17	-3.92	-1.04	-2.69	
	Pt_8Ge_2	1.83	1.17	-4.02	-2.52	-2.72	
	Pt_7Ge_3	2.00	1.19	-4.07	-3.61	-3.13	
	Pt_6Ge_4	1.83	1.17	-4.15	-4.98	-2.69	
	Pt_5Ge_5	1.88	1.17	-4.21	-6.18	-1.64	-0.33
	Pt_4Ge_6	1.90	1.16	-4.00	-4.66	-1.72	
	Pt_3Ge_7	1.89	1.16	-3.82	-3.42	-1.88	
	Pt_2Ge_8	1.87	1.16	-3.59	-1.69	-2.36	
	$PtGe_9$	1.89	1.16	-3.42	-0.56	-1.73	
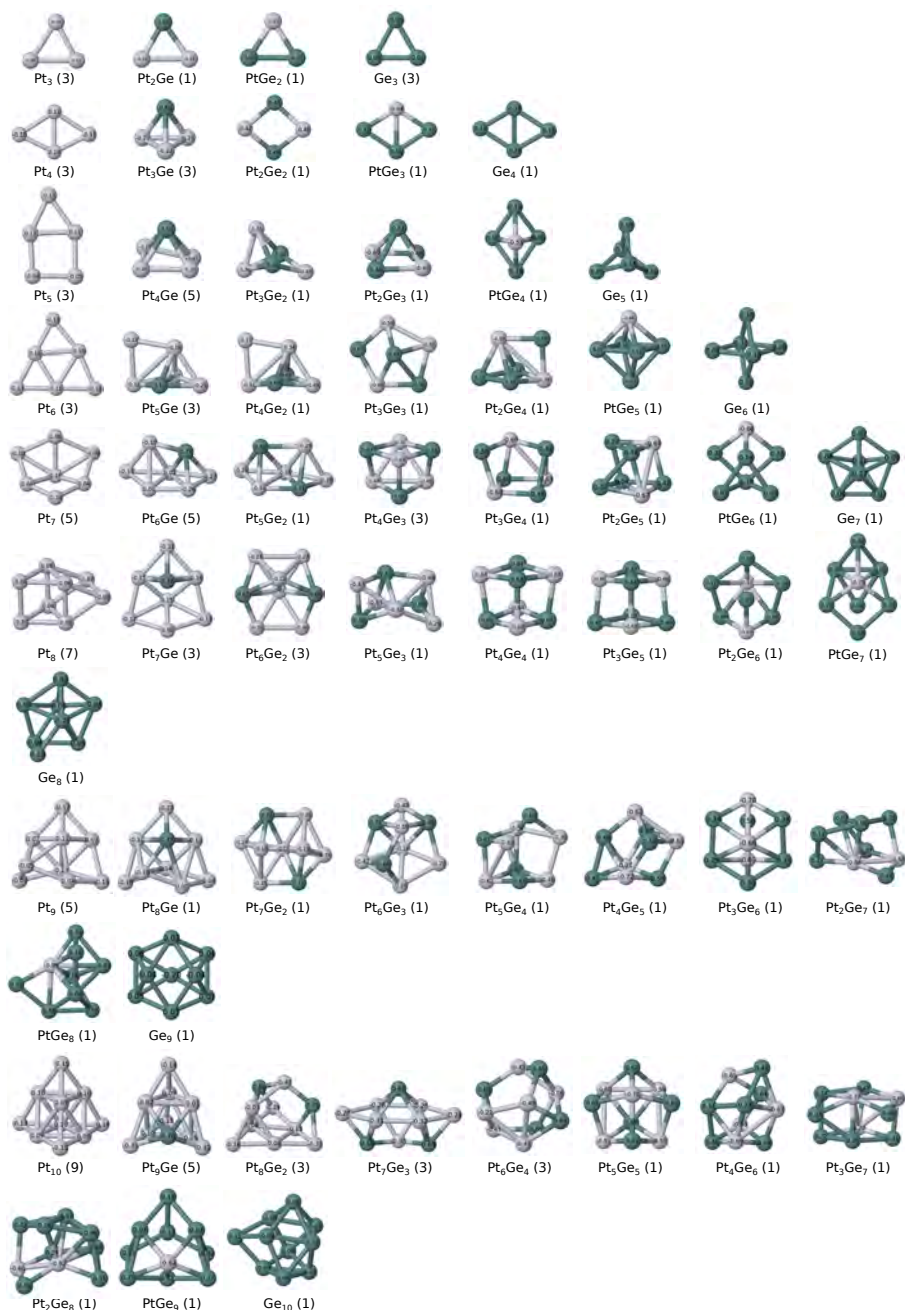
Figure C.1: Optimized geometries of $\mathrm{Pt}_{n-m}\mathrm{Ge}_m$ ($3 \leq n \leq 10$, $0 \leq m \leq 10$) clusters. The multiplicity $(2S + 1)$ of each structure is given in parentheses. Bader charges are printed on the atoms in values of $|e|$. Pt and Ge are depicted in grey, and green, respectively.
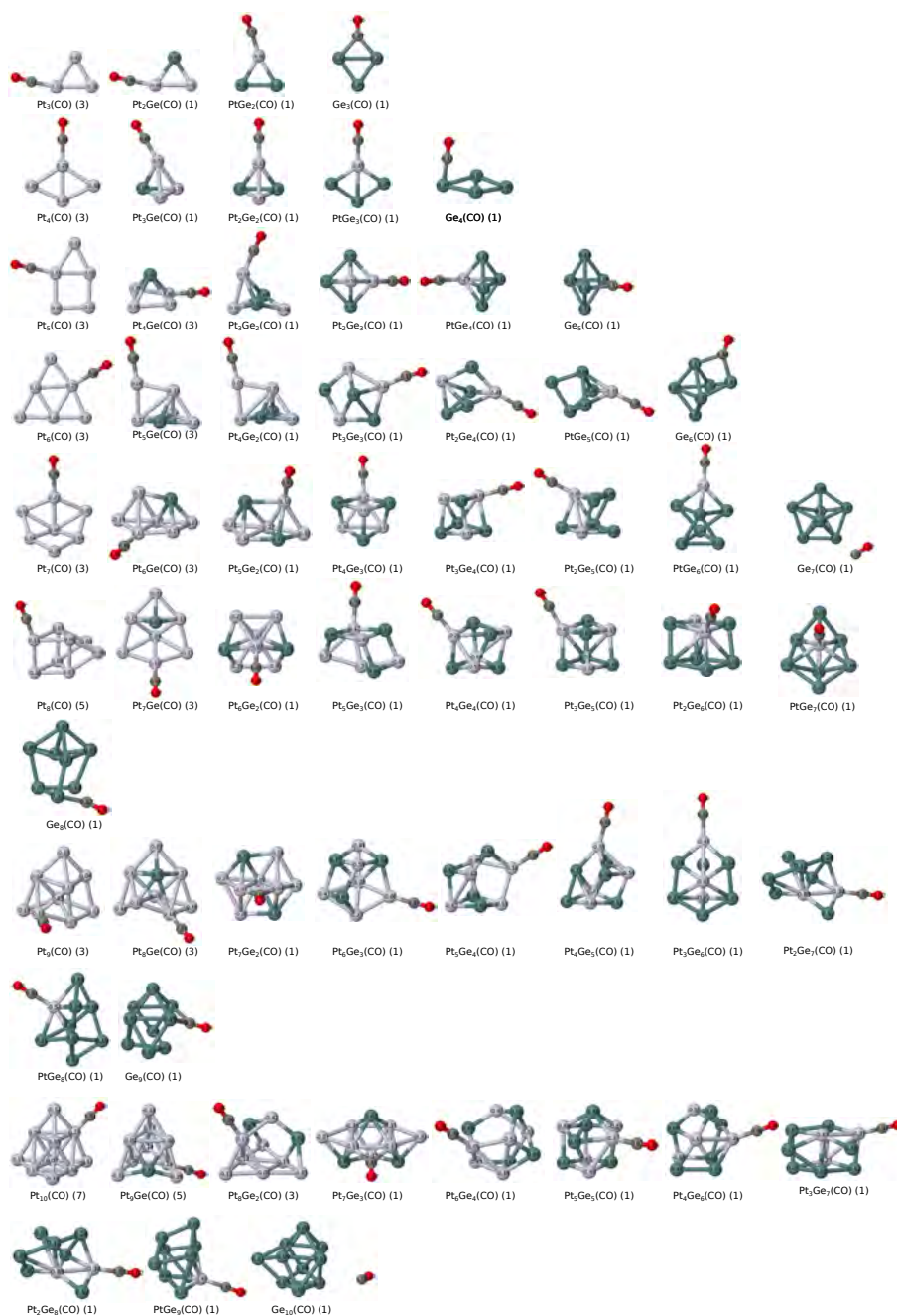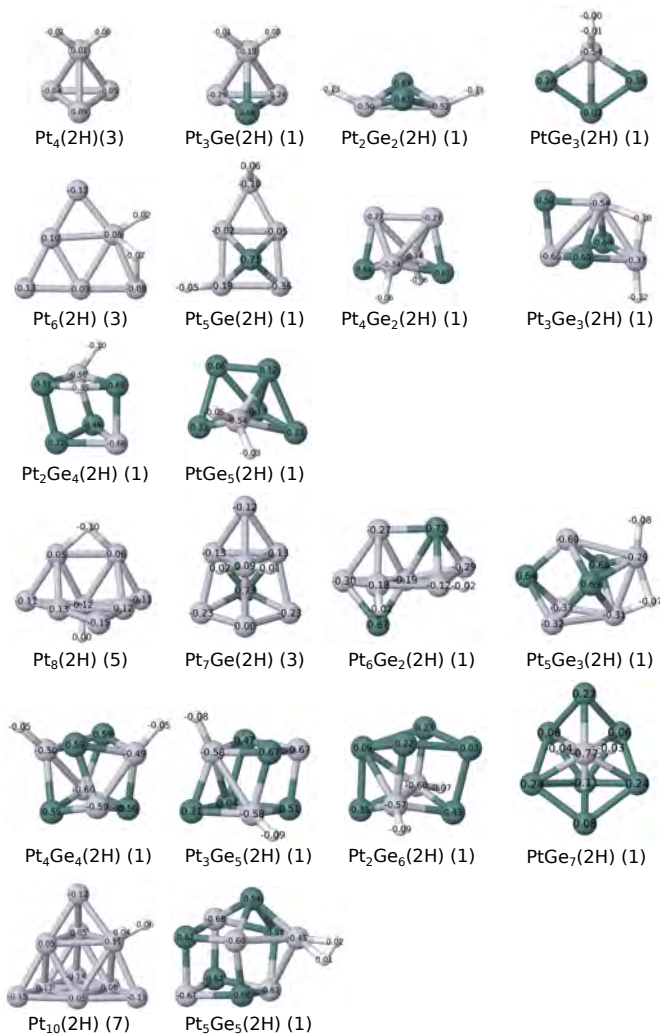
Figure C.2: Global minima geometries of $Pt_{n-m}Ge_m(CO)$ ($3 \leq n \leq 10$, $0 \leq m \leq 10$) complexes. The multiplicity ($2S + 1$) of each structure is given in parentheses. Bader charges are printed on the atoms in values of $|e|$. Pt, Ge, C and O are depicted in grey, green, dark grey and red, respectively.

Figure C.3: Global minima geometries of $Pt_{n-m}Ge_m(2H)$ ($n = 4, 6, 8, 10$; $0 \leq m \leq 7$) complexes. The multiplicity $(2S + 1)$ of each structure is given in parentheses. Bader charges are printed on the atoms in values of |e|. Pt, Ge and H are depicted in grey, green and white, respectively.

C.2 Electronic Structure Analysis of CO- and 2H-Complexes
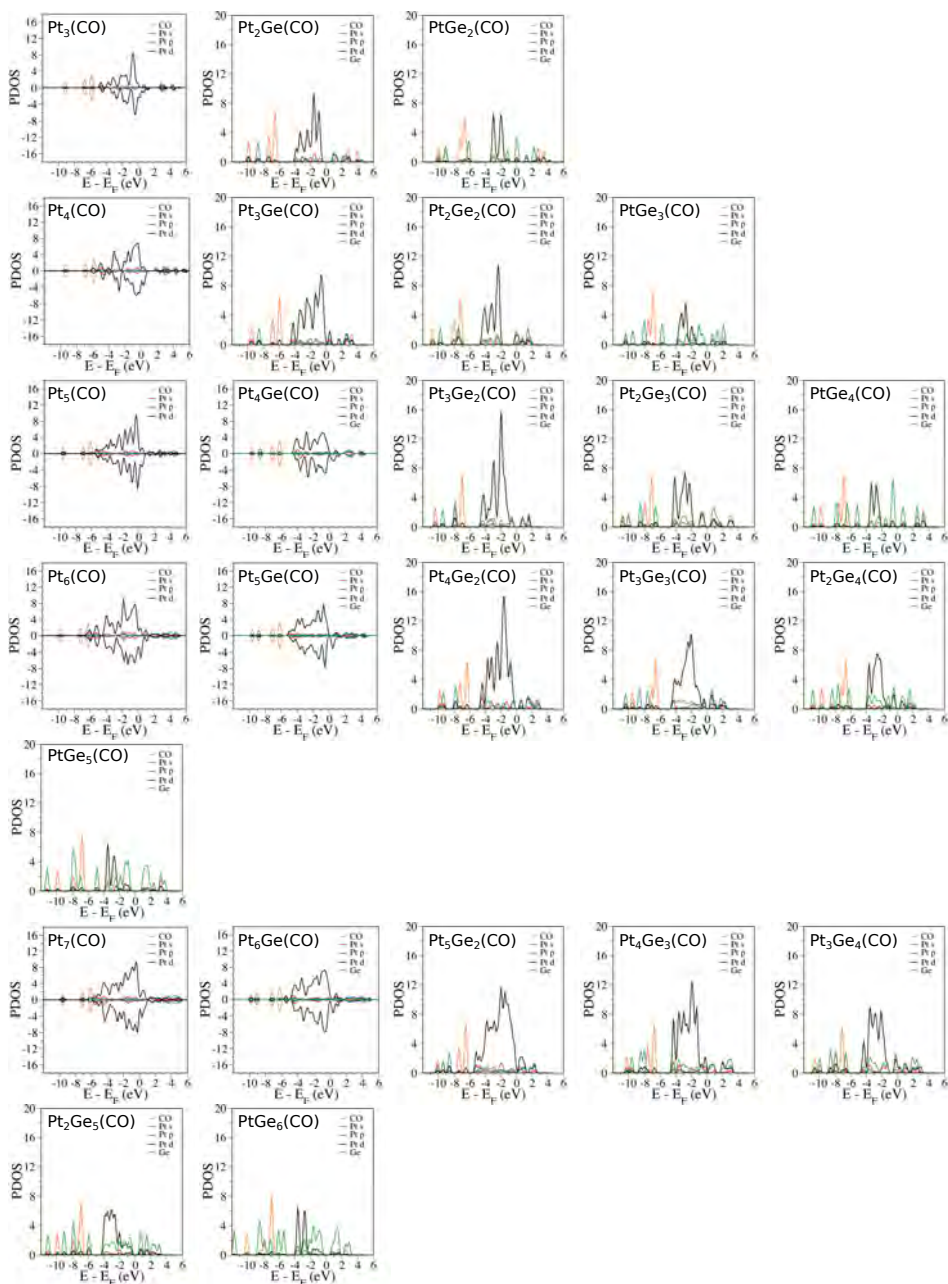
Figure C.4: Projected density of states (PDOS) of $Pt_{n-m}Ge_m(CO)$ ($3 \leq n \leq 10$, $0 \leq m \leq 9$) complexes. The Fermi energy (E_F) is set to zero in all cases. In spin polarized systems α and β channels are plotted separately, whereas in non-polarized systems the sum of α and β is plotted.
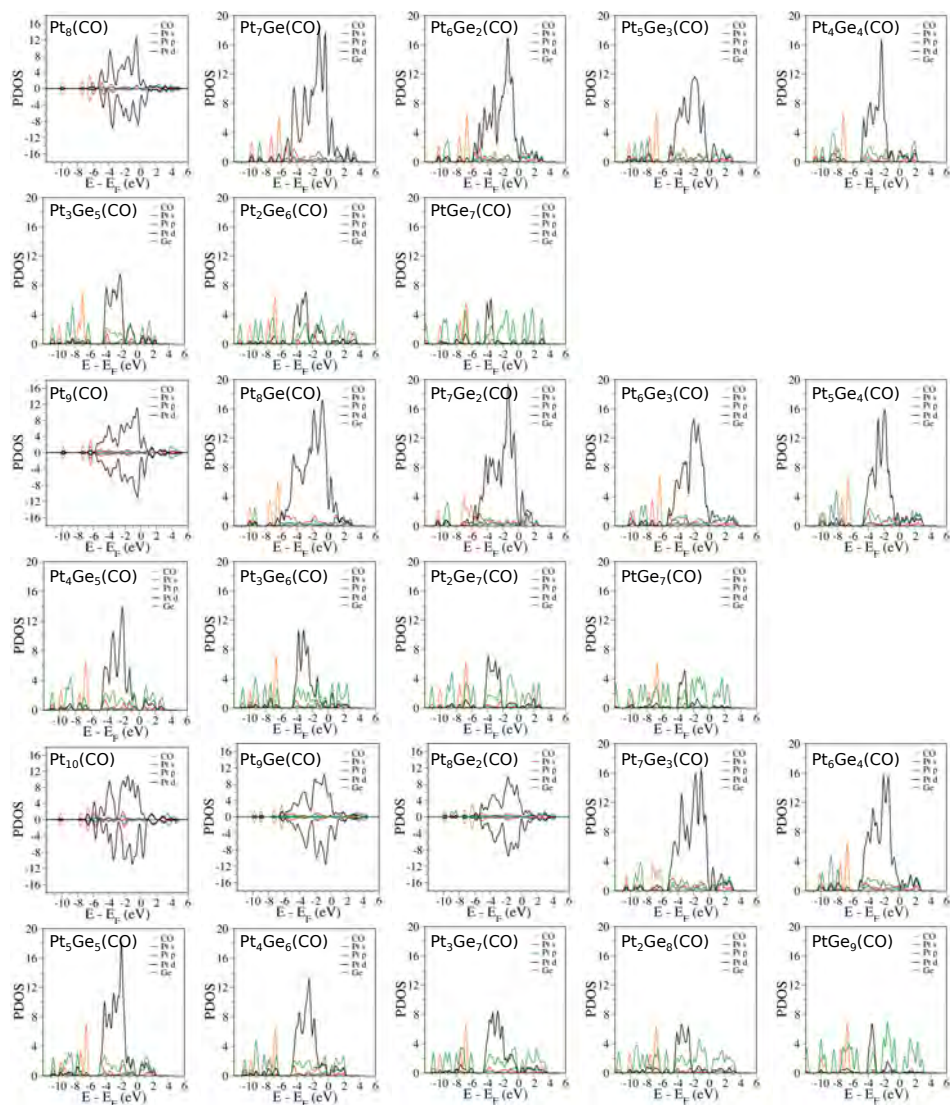
Figure C.4: Continued.
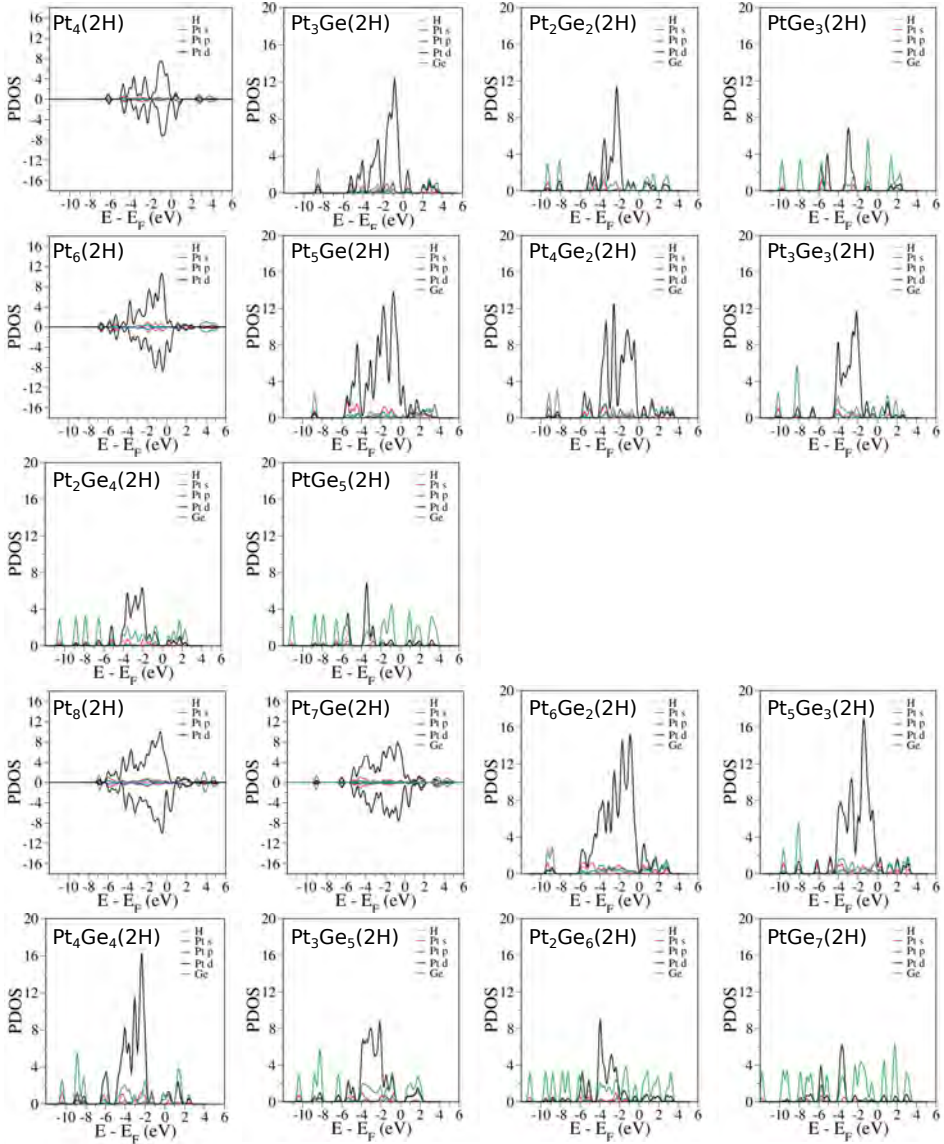
Figure C.5: Projected density of states (PDOS) of $Pt_{n-m}Ge_m(2H)$ ($n = 4, 6, 8$; $0 \leq m \leq 7$) complexes. The Fermi energy (E_F) is set to zero in all cases. In spin polarized systems α and β channels are plotted separately, whereas in non-polarized systems the sum of α and β is plotted.

Appendix D

Study of CO Adsorption on Small-Size Pt$_2$X Clusters Supported on MgO(100) (X = Al, B, Ge and Si)

In this appendix we assess the tendency to CO poisoning of several doped small Pt$_2$X clusters supported on MgO(100). Our pool of comparison includes Al, B, Ge and Si dopants. The GM structures of the bare deposited clusters were taken from Ref [187]. The results for the electronic structure calculations are shown in Figure D.1. As can be observed, after doping, CO still adsorbs preferentially to Pt. The adsorption geometry corresponds to atop configuration from the C end and a $\angle$ Pt$-$C$-$O angle of 180º. All dopants reduce significantly the binding strength to CO. Interestingly, Ge shows the greatest reduction in binding energy (BE[CO] $= -1.44$ eV). As revealed by Bader charges, there is a net charge transfer from the cluster to CO (back-donation) in all cases. In agreement, the charge density difference (CDD) analysis also displays charge accumulation on the Pt$-$C bond and a charge depletion on the C$-$O internal bond. Nonetheless, the Pt atoms in

the cluster retain considerable negative charge due to the dopant charge transfer.

The projected density of states (PDOS) of the Pt_2XCO complexes are collected on Figure D.1c. After surface deposition, the d band gets smeared in the region -6 to -1.5 eV, corresponding to the formation of covalent bonds with the surface. Similarly, the molecular orbitals (MOs) of CO are stabilized to lower energies: 4σ to ~ -11 eV, 5σ to ~ -8 eV and 1π to ~ -7 eV. In addition, a strong hybridization can be observed between Pt and the dopant below E_F. A closer inspection suggests that the dopants also participate in the bonding between Pt and CO.
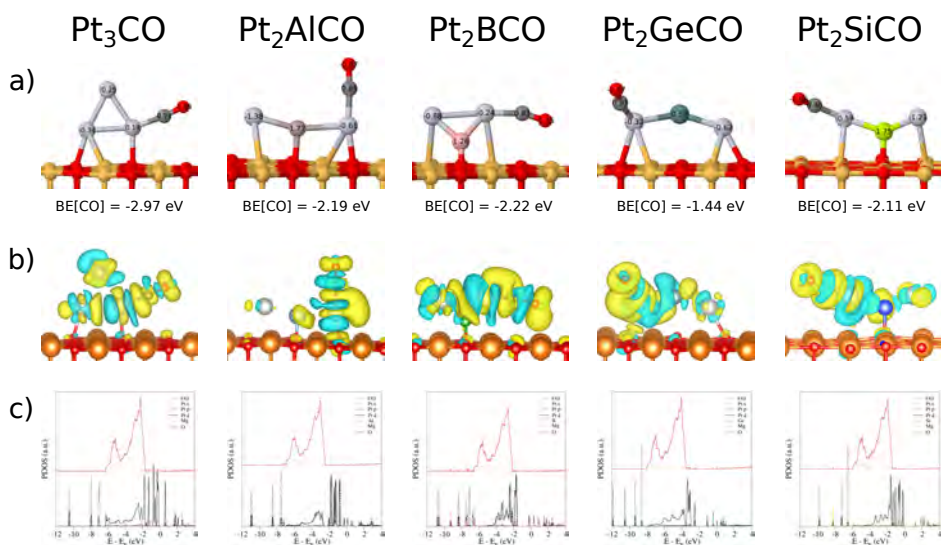
Figure D.1: Structural and electronic analysis of $Pt_2X(CO)$ complexes supported on MgO(100) with X = Pt, Al, B, Ge and Si. a) Putative global minima (GM) geometries, together with CO binding energies. Bader charges are printed on top of the atoms. Pt, Al, B, Ge, Si, Mg, O and C are depicted in gray, brown, pink, dark green, yellow, orange, red and dark gray, respectively. b) Charge density difference (CDD) between CO and the cluster. Yellow and cyan colors represent positive (charge accumulation) and negative (charge depletion) regions, respectively. c) Projected density of states (PDOS). For each case the total DOS is projected onto the total Pt s, Pt p, Pt d bands and dopant, Mg and O atoms. The Fermi energy (E_F) is set to zero in all cases. Both α (solid lines) and β (dotted lines) channels are shown in spin polarized systems.

Appendix

Supplementary Material

of Chapter 5

E

E.1 ELectronic Structure of the Pt_4Ge_nX Adducts ($n = 0 - 4$; X = CO, O_2, 2×O) Supported on MgO(100)

In order to understand the electronic structure in greater detail we computed the projected density of states (PDOS). Figure E.1a displays the PDOS analysis for each Pt_4Ge_nCO GM projected onto CO, Pt d orbitals and Ge. After adsorption the 5σ and 1π are shifted to lower energies due to the interaction with Pt, while the $2\pi^*$ gets partially populated below the Fermi energy (E_F). The promoter in PtGe/MgO behaves in a similar way to than gas-phase PtGe, as shown in Chapters 3 and 4. Basically, Ge overlaps with Pt in the 5σ and d_π regions, which might suggest a direct participation of Ge in both donation and back-donation steps.

As shown in Figure E.1b, the O_2 $2\pi^*$ orbitals are virtually occupied below E_F due to a considerable charge transfer from the cluster to O_2. This suggests a high degree of activation for O_2, which reaches the peroxo state, as confirmed with the bond-length analysis. In addition, in comparison with molecular O_2, the occupied orbitals become even more smeared in atomic O (Figure E.1c) as a result of a stronger interaction (hybridization) with the cluster (Pt d and Ge s and p orbitals).
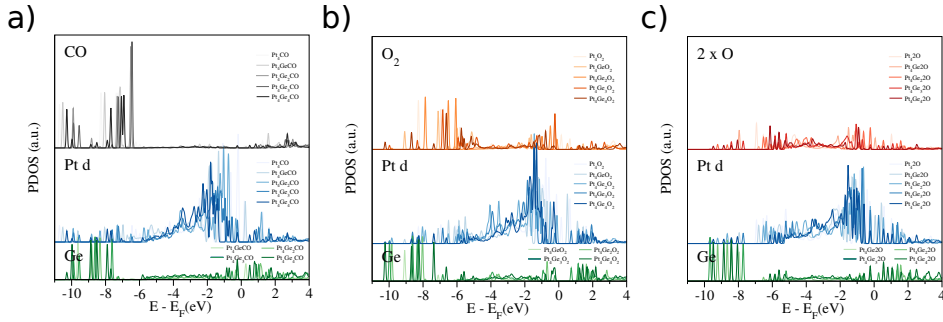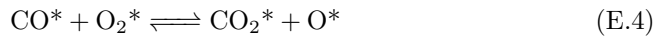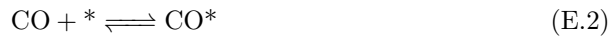
Figure E.1: Projected density of states (PDOS) of the most stable a) Pt_4Ge_nCO, b) $Pt_4Ge_nO_2$ and c) Pt_4Ge_n2O adducts supported on MgO(100). For each case the total DOS is projected onto the ligand, Pt d band and Ge. The Fermi energy (E_F) is set to zero in all cases. Only the α channel is shown in spin polarized systems.

E.2 Details of the Microkinetic Model

The microkinetic model for CO oxidation on Pt_4Ge_n/MgO ($n = 0 - 4$) is built upon the following 8-step reaction network:

$$O_2 + * \rightleftharpoons O_2* \tag{E.1}$$

$$CO + * \rightleftharpoons CO* \tag{E.2}$$

$$O_2* + * \rightleftharpoons 2\,O* \tag{E.3}$$

$$CO* + O_2* \rightleftharpoons CO_2* + O* \tag{E.4}$$

$$CO* + O* \rightleftharpoons CO_2* + * \tag{E.5}$$

$$CO + O_2* \rightleftharpoons CO_2 + O* \tag{E.6}$$

$$CO + O* \rightleftharpoons CO_2 + * \tag{E.7}$$

$$CO_2* \rightleftharpoons CO_2 + * \tag{E.8}$$

An asterisk (*) represents a free site on the cluster surface.

The reaction rates (r_i) were calculated using surface coverages (θ_i), forward $k_{f,i}$ and backward $k_{r,i}$ rate constants:

$$r_1 = k_{f,1}P_{O_2}\theta_* - k_{r,1}\theta_{O_2} \tag{E.9}$$

$$r_2 = k_{f,2}P_{CO}\theta_* - k_{r,2}\theta_{CO} \tag{E.10}$$

$$r_3 = k_{f,3}\theta_{O_2}\theta_* - k_{r,3}\theta_O^2 \tag{E.11}$$

$$r_4 = k_{f,4}\theta_{CO}\theta_{O_2} - k_{r,4}\theta_{CO_2}\theta_O \tag{E.12}$$

$$r_5 = k_{f,5}\theta_{CO}\theta_O - k_{r,5}\theta_{CO_2}\theta_* \tag{E.13}$$

$$r_6 = k_{f,6}P_{CO}\theta_{O_2} - k_{r,6}P_{CO_2}\theta_O \tag{E.14}$$

$$r_7 = k_{f,7}P_{CO}\theta_O - k_{r,7}P_{CO_2}\theta_* \tag{E.15}$$

$$r_8 = k_{f,8}P_{CO_2} - k_{r,8}P_{CO_2}\theta_* \tag{E.16}$$

The time evolution of surface coverages is governed by the reaction rates defined above.

$$\frac{d}{dt}\theta_{O_2} = r_1 - r_3 - r_4 - r_6 \tag{E.17}$$

$$\frac{d}{dt}\theta_{CO} = r_2 - r_4 - r_5 \tag{E.18}$$

$$\frac{d}{dt}\theta_O = 2r_3 + r_4 - r_5 + r_6 - r_7 \tag{E.19}$$

$$\frac{d}{dt}\theta_{CO_2} = r_4 + r_5 - r_8 \tag{E.20}$$

The surface coverages was constrained to fulfill Equation (2.65).

The microkinetic equations were solved using a continuous stirred–tank reactor (CSTR). The mass balance of the reactants (CO, O_2) and product (CO_2) is as follows:

$$\frac{d}{dt}N_{O_2} = F_{O_2}^{\text{inlet}} - F_{O_2}^{\text{outlet}}(t) - n_{\text{sites}}r_1 \tag{E.21}$$

$$\frac{d}{dt}N_{CO} = F_{CO}^{\text{inlet}} - F_{CO}^{\text{outlet}}(t) - n_{\text{sites}}(r_2 + r_6 + r_7) \tag{E.22}$$

$$\frac{d}{dt}N_{CO_2} = -F_{CO_2}^{\text{outlet}}(t) + n_{\text{sites}}(r_6 + r_7 + r_8) \tag{E.23}$$

Equations (E.20) and (E.23) form a system of stiff ODEs which are solved simultaneously by integrating over time. The resolution of the ODEs is done with the variable coefficient ODE solver (VODE) and the backward-differentiation formulas (BDF) method, as implemented in the Scipy package.[491]

## E.3 O_2 Dissociation on Pt_4Ge_n/MgO(100) (n $= 0 - 4$)

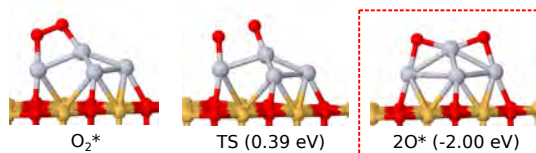Table E.1: O−O bond distance (d_{O-O}) and total Bader charge (ΔQ) of oxygen in the initial state (IS), transition state (TS) and final state (FS) geometries for the O_2 dissociation pathway on the Pt_4Ge_n/MgO(100) isomers with the most stable final state (FS).

	O_2*		TS		FS	
	d_{O-O} ($\AA$)	ΔQ ($|e|$)	d_{O-O} ($\AA$)	ΔQ ($|e|$)	d_{O-O} ($\AA$)	ΔQ ($|e|$)
Pt_4	1.47	-0.67	2.06	-0.94	3.61	-1.30
Pt_4Ge	1.53	-1.02	1.85	-1.20	2.86	-1.81
Pt_4Ge_2	1.53	-0.99	1.95	-1.20	5.76	-1.64
Pt_4Ge_3	1.46	-1.08	1.61	-1.22	2.94	-2.19
Pt_4Ge_4	1.52	-1.22	1.92	-1.47	4.05	-2.14

a) Pt_4 I isom
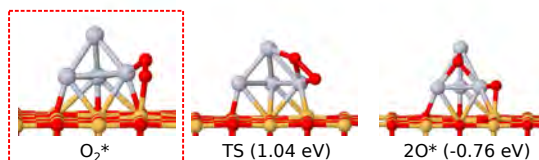
b) Pt_4 II isom
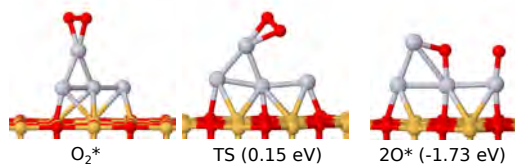
c) Pt_4 III isom

Figure E.2: Initial state (IS), transition state (TS), and final state (FS) geometries for the O_2 dissociation pathway on all the Pt_4/MgO(100) isomers. Activation and reaction energies (in eV) are given relative to the corresponding IS. The most stable complexes for the IS and FS are highlighted in red boxes. Pt, Ge, Mg, O and C are depicted in gray, dark green, orange, red and dark gray, respectively.
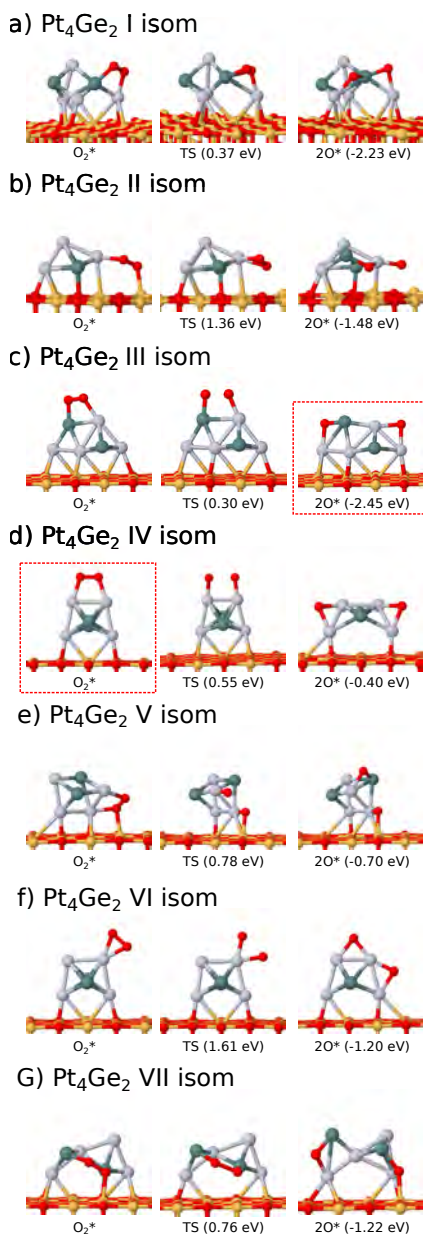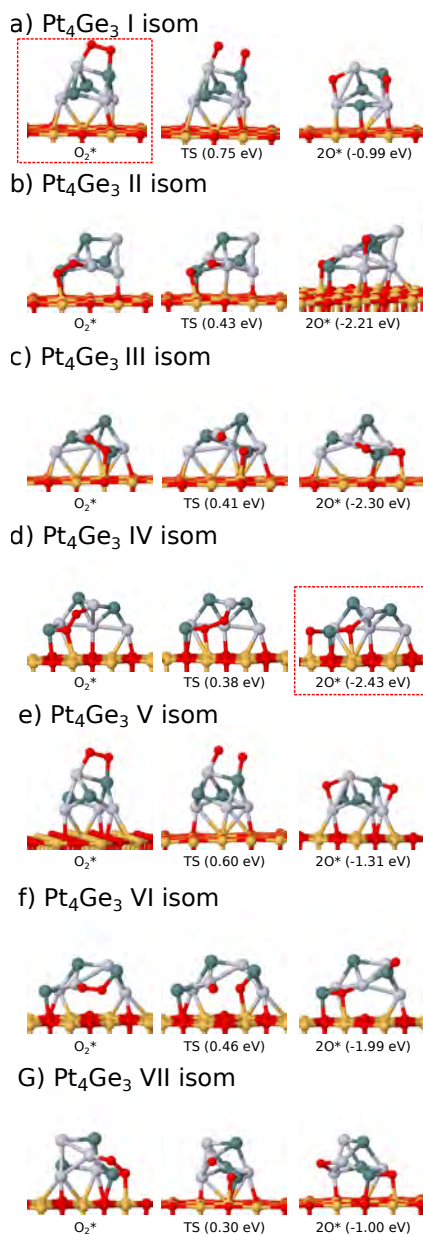
Figure E.3: Initial state (IS), transition state (TS), and final state (FS) geometries for the O_2 dissociation pathway on all the $Pt_4Ge_2/MgO(100)$ isomers. Activation and reaction energies (in eV) are given relative to the corresponding IS. The most stable complexes for the IS and FS are highlighted in red boxes. Pt, Ge, Mg, O and C are depicted in gray, dark green, orange, red and dark gray, respectively.
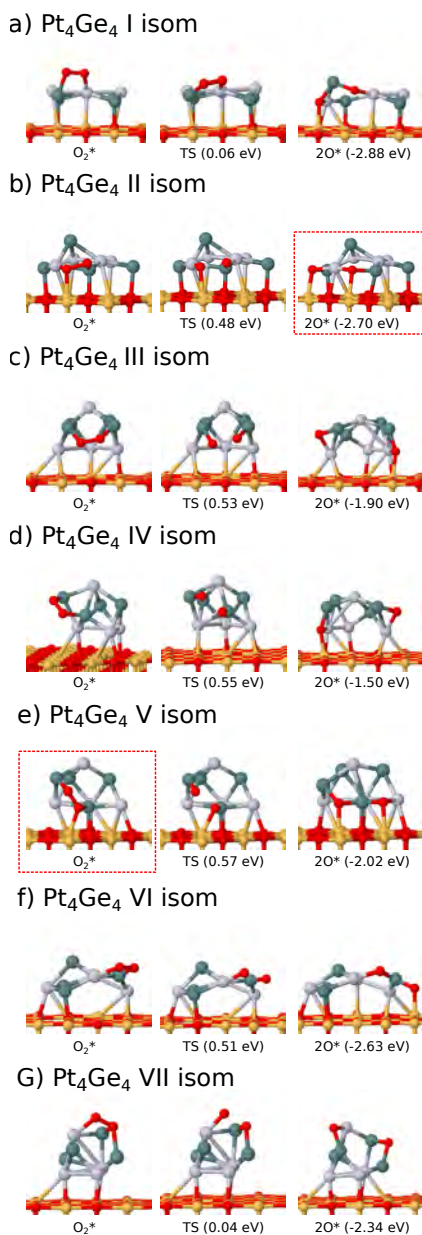
a) Pt$_4$Ge$_3$ I isom

O$_2$*   TS (0.75 eV)   2O* (-0.99 eV)

b) Pt$_4$Ge$_3$ II isom

O$_2$*   TS (0.43 eV)   2O* (-2.21 eV)

c) Pt$_4$Ge$_3$ III isom

O$_2$*   TS (0.41 eV)   2O* (-2.30 eV)

d) Pt$_4$Ge$_3$ IV isom

O$_2$*   TS (0.38 eV)   2O* (-2.43 eV)

e) Pt$_4$Ge$_3$ V isom

O$_2$*   TS (0.60 eV)   2O* (-1.31 eV)

f) Pt$_4$Ge$_3$ VI isom

O$_2$*   TS (0.46 eV)   2O* (-1.99 eV)

G) Pt$_4$Ge$_3$ VII isom

O$_2$*   TS (0.30 eV)   2O* (-1.00 eV)

Figure E.4: Initial state (IS), transition state (TS), and final state (FS) geometries for the O$_2$ dissociation pathway on all the Pt$_4$Ge$_3$/MgO(100) isomers. Activation and reaction energies (in eV) are given relative to the corresponding IS. The most stable complexes for the IS and FS are highlighted in red boxes. Pt, Ge, Mg, O and C are depicted in gray, dark green, orange, red and dark gray, respectively.

a) Pt$_4$Ge$_4$ I isom

b) Pt$_4$Ge$_4$ II isom

c) Pt$_4$Ge$_4$ III isom

d) Pt$_4$Ge$_4$ IV isom

e) Pt$_4$Ge$_4$ V isom

f) Pt$_4$Ge$_4$ VI isom

G) Pt$_4$Ge$_4$ VII isom

Figure E.5: Initial state (IS), transition state (TS), and final state (FS) geometries for the O$_2$ dissociation pathway on all the Pt$_4$Ge$_4$/MgO(100) isomers. Activation and reaction energies (in eV) are given relative to the corresponding IS. The most stable complexes for the IS and FS are highlighted in red boxes. Pt, Ge, Mg, O and C are depicted in gray, dark green, orange, red and dark gray, respectively.

E.4 CO Oxidation on Pt_4Ge_n/MgO(100) (n $= 0 - 4$)

CO + O_2* CO + 2xO*

|		
Pt$_4$	CO + O*	TS (0.33 eV)	CO$_2$ (-1.33 eV)
	CO + O*	TS (0.78 eV)	CO$_2$ (-0.53 eV)
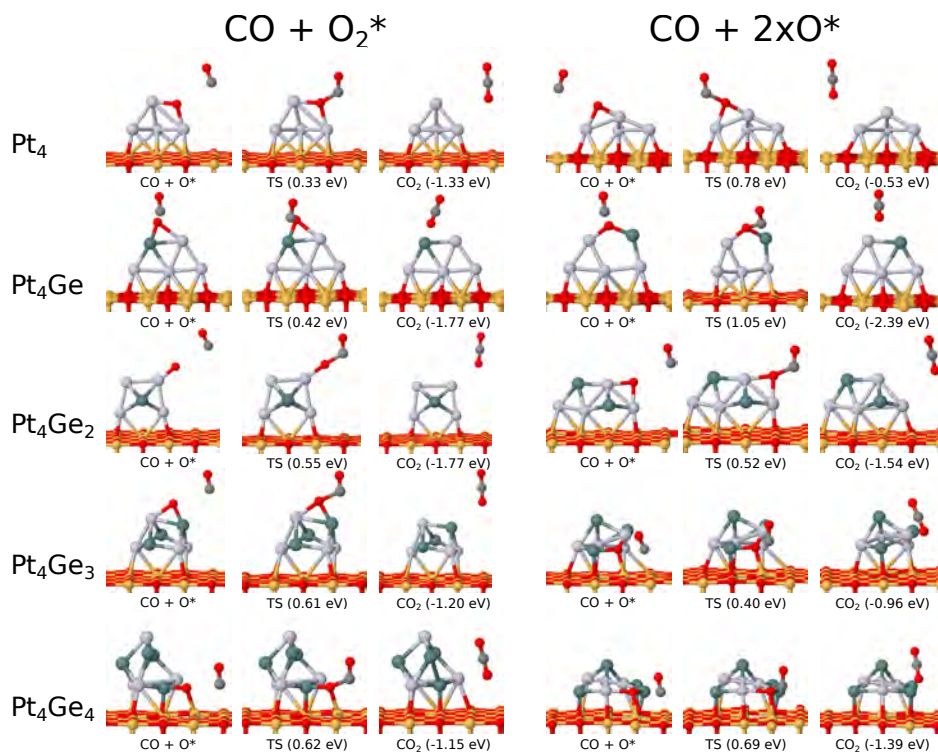
Figure E.6: Most stable reaction pathways for the Eley−Rideal (ER) mechanism for both molecular and dissociated oxygen reactions on Pt_4Ge_n/MgO(100). Initial state (IS), transition state (TS) and final state (FS) geometries are shown together with the relative activation and reaction energies (in eV). Only the second step is given. Pt, Ge, Mg, O and C are depicted in gray, dark green, orange, red and dark gray, respectively.
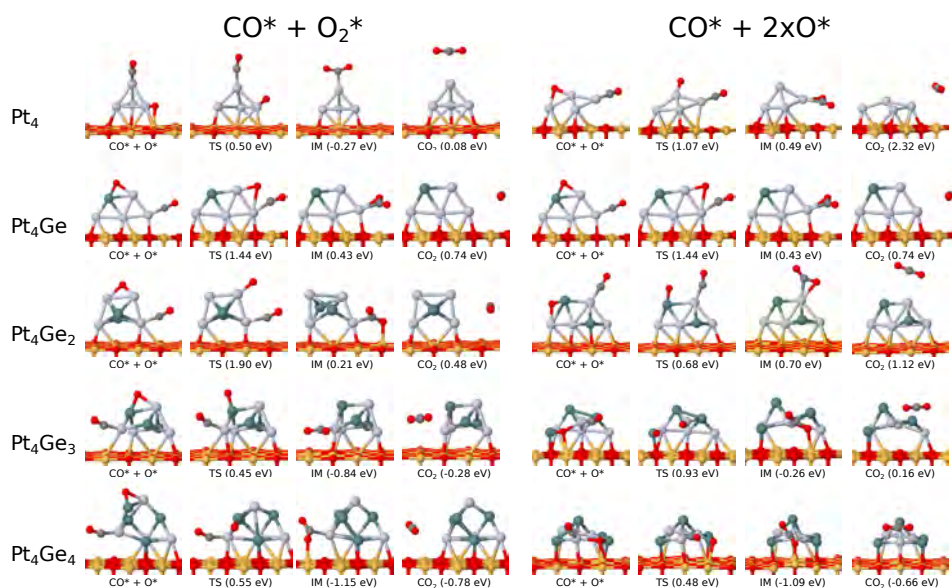
Figure E.7: Most stable reaction pathways for the Langmuir−Hinshelwood (LH) mechanism for both molecular and dissociated oxygen reactions on $Pt_4Ge_n/MgO(100)$. Initial state (IS), transition state (TS), intermediate state (IM) and final state (FS) geometries are shown together with the relative activation and reaction energies (in eV). Only the second step is given. Pt, Ge, Mg, O and C are depicted in gray, dark green, orange, red and dark gray, respectively.
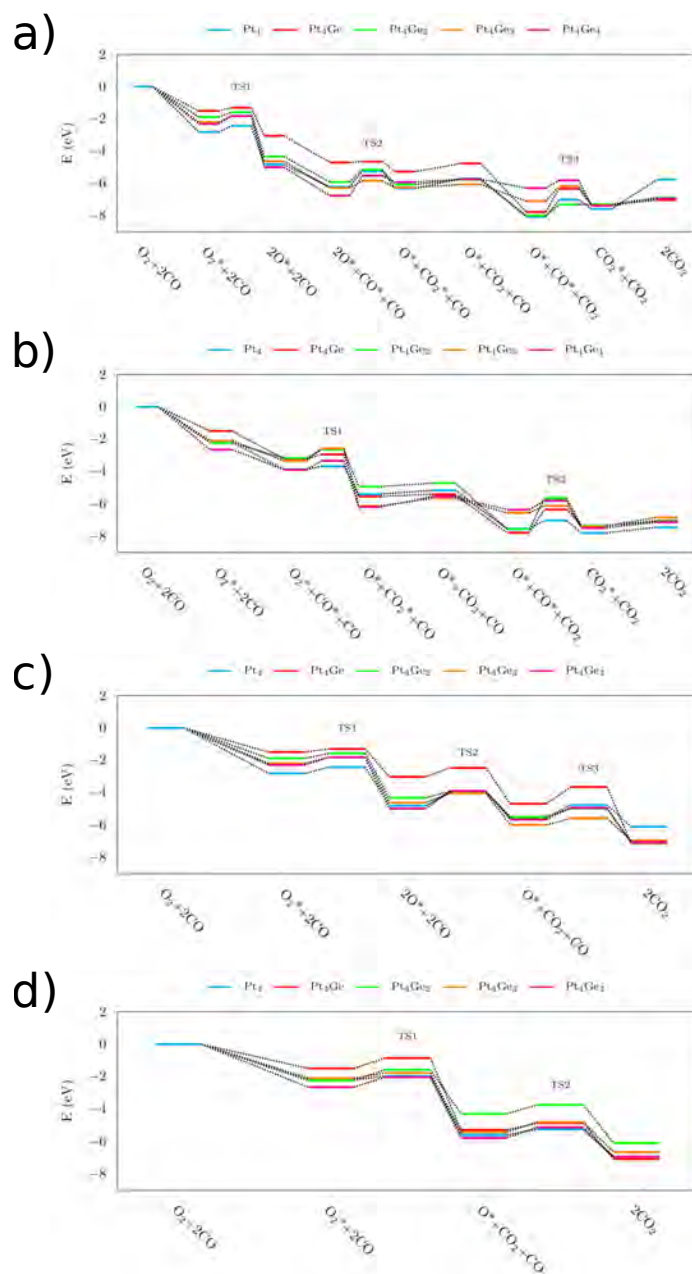
Figure E.8: Potential energy diagram of the most stable a) $CO^* + 2\times O^*$ (LH), b) $CO^* + O_2^*$ (LH), c) $CO(g) + 2\times O^*$ (ER) and d) $CO(g) + O_2^*$ (ER) routes on $Pt_4Ge_n/MgO(100)$. Energies (in eV) are given relative to the clean $Pt_4Ge_n/MgO(100)$ surface.
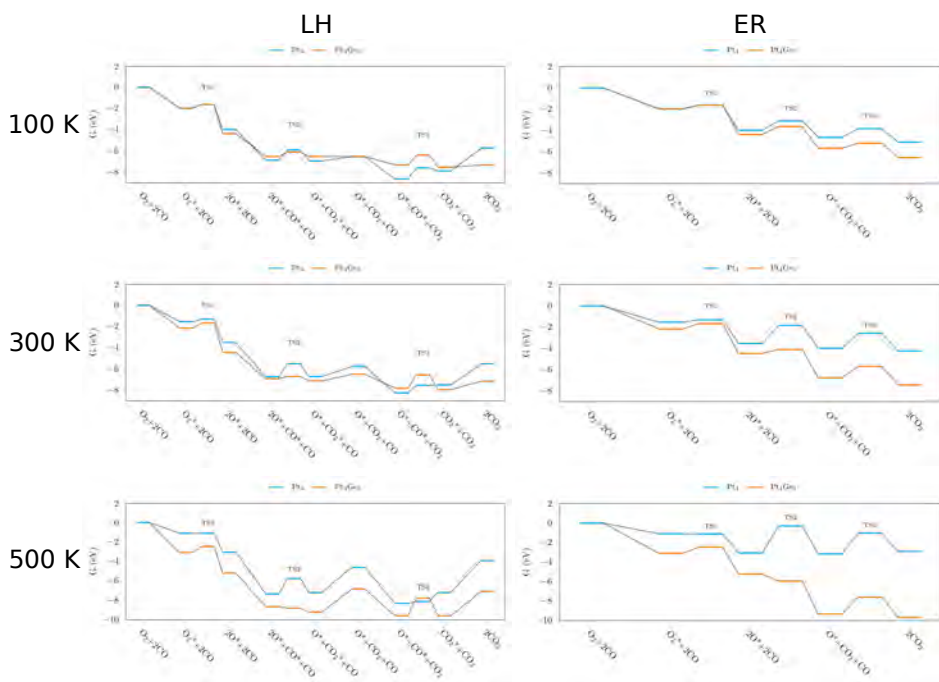
Figure E.9: Potential free energy diagram of the most stable CO* + 2×O* (LH) and CO(g) + 2×O* (ER) routes on Pt_4 and Pt_4Ge_3 supported on MgO(100) at 100, 300 and 500 K. Free energies (in eV) are given relative to the clean Pt_4Ge_n/MgO(100) surface.

E.5 Microkinetic Simulations

Adding one Ge atom alters significantly the reaction kinetics, as evidenced by Figure E.10. In this case, no CO poisoning can be observed at equimolar feed composition which is attributed to the fast $CO^* + O^*$ kinetics on Pt_4Ge. CO will oxidize as soon as it is adsorbed on this catalyst, provided there is enough surface area precovered with O^*. At low temperatures, Pt_4Ge is almost completely covered (0.7 ML) with O_2^*, but as the reactor is heated, O_2 dissociation rate increases and O^* becomes the dominant species. The TOF_{CO_2} also increases, since $CO^* + O^*$ is more reactive than $CO^* + O_2^*$ in this regime, and it keeps constant at a considerable rate. At 325 K CO_2 poisoning becomes more acute and the TOF_{CO_2} descends to some degree. A similar behavior of the coverages can be observed for $P_{O_2} > P_{CO}$, but the CO oxidation rate is about one order of magnitude bigger. At $P_{CO} > P_{O_2}$ CO poisoning becomes critical in the range $100-300$ K as in Pt_4, and the TOF_{CO_2} falls around ten orders of magnitude. Incrementing the temperature appears to alleviate CO poisoning (although CO_2 poisoning is still an issue) and fairly moderate rates are obtained even in a CO-rich environment.

O_2^* and O^* are the main species on Pt_4Ge_2 in the $100-225$ K interval at $P_{O_2} = P_{CO}$ and $P_{O_2} > P_{CO}$ (see Figure E.10). Their corresponding coverages oscillate with temperature in a pyramid-like fashion and the TOF_{CO_2} remains at quite high values. Higher O^* coverages are obtained in an atmosphere richer in O_2. Beginning at 225 K, CO_2^* coverage raises and an apparent drop becomes visible in the CO_2 production rate. Notice, however, that when $P_{CO} > P_{O_2}$ the CO poisoning is less intense in comparison with Pt_4Ge (θ_{CO} reaches at most ~ 0.5 ML). At low temperature similar reaction rates to the other two feed compositions are obtained. Apparently, increasing Ge concentration further enhances the CO poisoning resistance. Nonetheless, as temperature increases the TOF_{CO_2} starts to decline due to a combination of CO and CO_2 poisoning.

Finally, in Pt_4Ge_4 no CO poisoning is observed either (see E.10). It seems that after a certain threshold in the Ge concentration CO poisoning is inhibited. In the range of $100-275$ K, Pt_4Ge_4 shows a similar behavior to Pt_4Ge_3 for all the feed compositions. O_2^* coverage changes in a pyramid-like fashion and O^* is produced at the expense of O_2^*, which may come from O_2 dissociation, $CO^* + O_2^*$ or $CO(g)$

+ O_2*. The TOF_{CO_2} remains high but slightly lower than in Pt_4Ge_3. Then at $300-350$, O_2* saturates completely the surface for $P_{O_2} = P_{CO}$ and $P_{O_2} > P_{CO}$, and causes a drop in the TOF_{CO_2}. In contrast to Pt_4Ge_3, at higher temperatures, the surface is poisoned with CO_2 and further diminishes the TOF_{CO_2}.
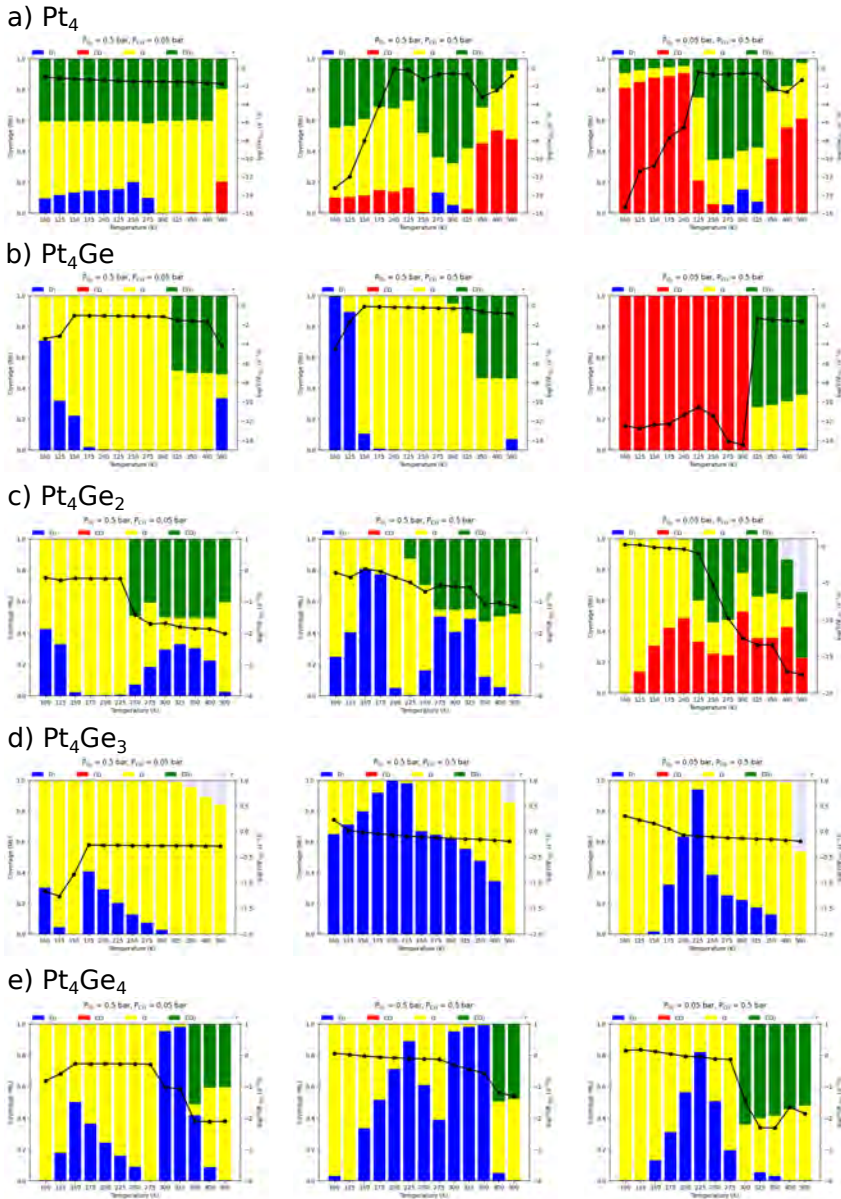
a) Pt$_4$

b) Pt$_4$Ge

c) Pt$_4$Ge$_2$

d) Pt$_4$Ge$_3$

e) Pt$_4$Ge$_4$

Figure E.10: Microkinetic analysis of CO oxidation for a) Pt$_4$ and b) Pt$_4$Ge, c) Pt$_4$Ge$_2$, d) Pt$_4$Ge$_3$ and e) Pt$_4$Ge$_4$ clusters supported on MgO(100). Steady-state coverages and CO$_2$ turnover frequencies (TOF$_{CO_2}$) as a function of temperature with different feed compositions: $P_{O_2} = 0.5$ bar, $P_{CO} = 0.05$ bar (left figure); $P_{O_2} = 0.5$ bar, $P_{CO} = 0.5$ bar (middle figure); $P_{O_2} = 0.05$ bar, $P_{CO} = 0.5$ bar (right figure).

Appendix F

Supplementary Material of Chapter 6
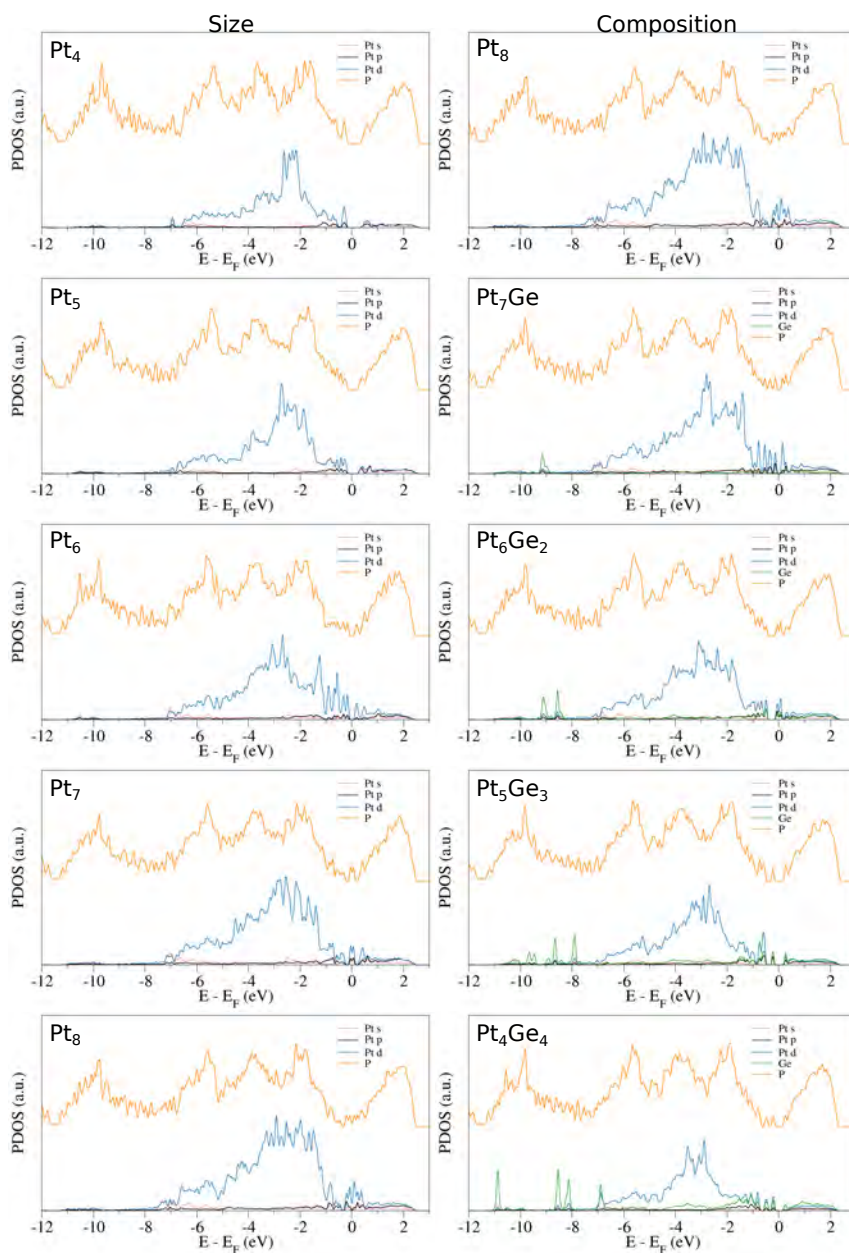
Figure F.1: Projected density of states (PDOS) of the most stable structures for the Pt_n ($n = 4 - 8$) (left) and $Pt_{n-m}Ge_m$ ($n = 8$, $m = 0 - 4$) (right) series supported on phosphorene. For each case the total DOS is projected onto the Pt s, Pt p Pt d, Ge and total surface atoms. The Fermi energy (E_F) is set to zero in all cases. Only the α channel is shown in non-spin polarized systems, while both α (solid lines) and β (dotted lines) channels are shown in spin polarized systems.
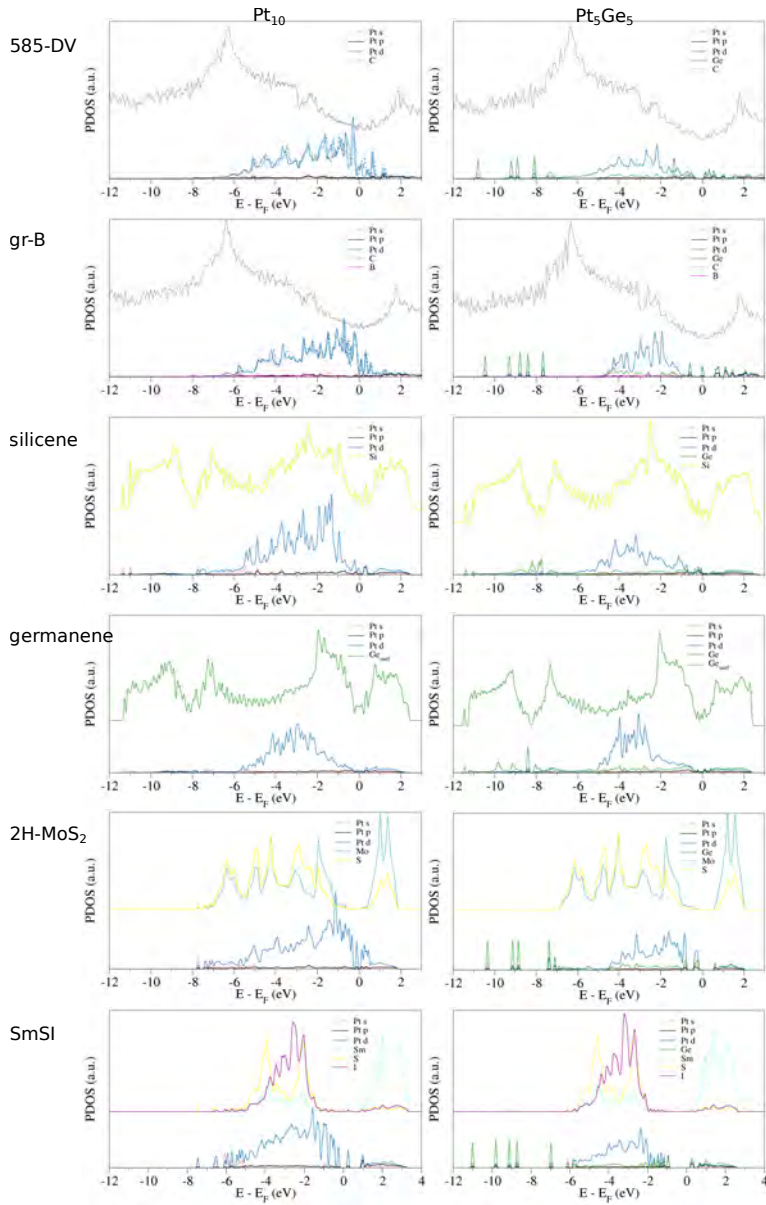
Figure F.2: Projected density of states (PDOS) of the most stable Pt_{10} (left) and Pt_5Ge_5 (right) structures supported on 5-8-5-DV, B-doped graphene, silicene, germanene, 2H-MoS$_2$ and SmSI. For each case the total DOS is projected onto the Pt s, Pt p Pt d, Ge and total surface atoms. The Fermi energy (E_F) is set to zero in all cases. Only the α channel is shown in non-spin polarized systems, while both α (solid lines) and β (dotted lines) channels are shown in spin polarized systems.
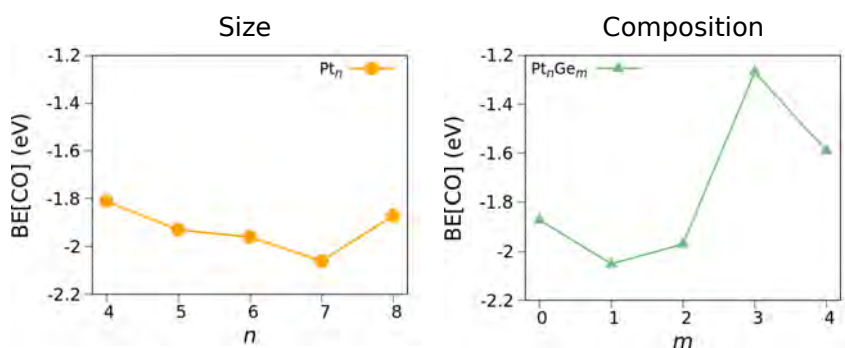
Figure F.3: CO binding energies (BE[CO]) of the monometallic series Pt_n ($n = 4-8$) (left) and $n = 8$ series ($Pt_{8-m}Ge_m$, $m = 0-4$) (right) supported on phosphorene.
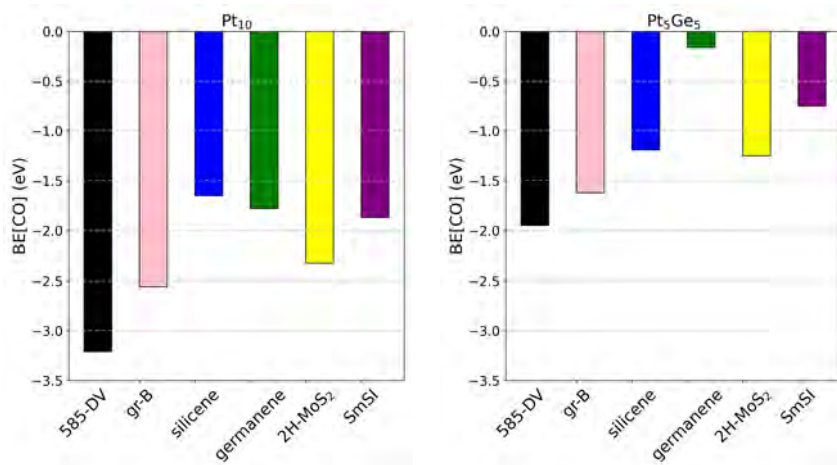

Figure F.4: CO binding energies (BE[CO]) of Pt_{10} (left) and Pt_5Ge_5 (right) supported on 5-8-5-DV, gr-B, silicene, germanene, 2H-MoS_2 and SmSI.

Bibliography

[1] B.P., *"BP statistical review of world energy 2022"*, Technical Report (BP p.l.c., London, June 2022).

[2] R. Lee, "The outlook for population growth", Science **333**, 569–573 (2011).

[3] J. Butler and S. Montzka, *"The NOAA annual greenhouse gas index"*, National Oceanic & Atmospheric Administration (2016); http://go.nature.com/2fWAEjv.

[4] IPCC Working Group III, *Climate change 2022: mitigation of climate change. contribution of working group III to the sixth assessment report of the intergovernmental panel on climate change*, edited by P. R. Shukla, J. Skea, R. Slade, A. Al Khourdajie, R. van Diemen, D. McCollum, M. Pathak, S. Some, P. Vyas, R. Fradera, M. Belkacemi, A. Hasija, G. Lisboa, S. Luz and J. Malley (Cambridge University Press, Cambridge, UK and New York, NY, USA, 2022).

[5] S. Solomon, G.-K. Plattner, R. Knutti and P. Friedlingstein, "Irreversible climate change due to carbon dioxide emissions", PNAS **106**, 1704–1709 (2009).

[6] D. Roemmich, J. Church, J. Gilson, D. Monselesan, P. Sutton and S. Wijffels, "Unabated planetary warming and its ocean structure since 2006", Nat. Clim. Change **5**, 240–245 (2015).

[7] S. Chu and A. Majumdar, "Opportunities and challenges for a sustainable energy future", Nature **488**, 294–303 (2012).

[8] S. Chu, Y. Cui and N. Liu, "The path towards sustainable energy", Nat. Mater. **16**, 16–22 (2017).

[9] D. Gielen, F. Boshell, D. Saygin, M. Bazilian, N. Wagner and R. Gorini, "The role of renewable energy in the global energy transformation", Energy Strategy Rev. **24**, 38–50 (2019).

[10] M. Bilgili, A. Özbek, B. Sahin and A. Kahraman, "An overview of renewable electric power capacity and progress in new technologies in the world", Renew. Sustain. Energy Rev. **49**, 323–334 (2015).

[11] X. Chen, C. Li, M. Grätzel, R. Kostecki and S. Mao, "Nanomaterials for renewable energy production and storage", Chem. Soc. Rev. **41**, 7909–7937 (2012).

[12] J. Masa, C. Andronescu and W. Schuhmann, "Electrocatalysis as the nexus for sustainable renewable energy: the gordian knot of activity, stability, and selectivity", Angew. Chem. Int. Ed. **59**, 15298–15312 (2020).

[13] J. Andújar and F. Segura, "Fuel cells: history and updating. a walk along two centuries", Renew. Sustain. Energy Rev. **13**, 2309–2322 (2009).

[14] E.G. *& G Technical Services, Inc., *Fuel cell handbook*, 7th ed. (US DOE, Morgantown, WV, 2004).

[15] A. Kirubakaran, S. Jain and R. Nema, "A review on fuel cell technologies and power electronic interface", Renew. Sustain. Energy Rev. **13**, 2430–2440 (2009).

[16] N. Sazali, W. Salleh, A. Jamaludin and M. Razali, "New perspectives on fuel cell technology: A brief review", Membranes **10**, 99–116 (2020).

[17] B. Steele and A. Heinzel, "Materials for fuel-cell technologies", Nature **414**, 345–352 (2001).

[18] S. Wang and S. Jiang, "Prospects of fuel cell technologies", Natl. Sci. Rev. **4**, 163–166 (2017).

[19] K. Jiao, J. Xuan, Q. Du, Z. Bao and B. Xie, "Designing the next generation of proton-exchange membrane fuel cells", Nature **595**, 361–369 (2021).

[20] S. Peighambardoust, S. Rowshanzamir and M. Amjadi, "Review of the proton exchange membranes for fuel cell applications", Int. J. Hydrog. Energy **35**, 9349–9384 (2010).

[21] J. Spendelow and D. Papageorgopoulos, "Progress in PEMFC MEA component R *& D at the DOE fuel cell technologies program", Fuel Cells **11**, 775–786 (2011).

[22] M. Tellez-Cruz, J. Escorihuela, O. Solorza-Feria and V. Compañ, "Proton Exchange Membrane Fuel Cells (PEMFCs): Advances and Challenges", Polymers **13**, 3064–3117 (2021).

[23] X. Ren, Y. Wang, A. Liu, Z. Zhang, Q. Lv and B. Liu, "Current progress and performance improvement of pt/c catalysts for fuel cells", J. Mater. Chem. A **8**, 24284–24306 (2020).

[24] S. Zhu, J. Ge, C. Liu and W. Xing, "Atomic-level dispersed catalysts for PEMFCs: Progress and future prospects", EnergyChem **1**, 100018–100040 (2019).

[25] N. Markovic and P. Ross Jr, "Surface science studies of model fuel cell electrocatalysts", Surf. Sci. Rep. **45**, 117–229 (2002).

[26] R. Ma, G. Lin, Y. Zhou, Q. Liu and T. Zhang, "A review of oxygen reduction mechanisms for metal-free carbon-based electrocatalysts", Npj Comput. Mater **5**, 78–92 (2019).

[27] M. Zhou, H.-L. Wang and S. Guo, "Towards high-efficiency nanoelectrocatalysts for oxygen reduction through engineering advanced carbon nanomaterials", Chem. Soc. Rev. **45**, 1273–1307 (2016).

[28] J. Greeley, I. Stephens, A. Bondarenko, T. Johansson and H. Hansen, "Alloys of platinum and early transition metals as oxygen reduction electrocatalysts", Nat. Chem. **1**, 552–556 (2009).

[29] M. Debe, "Electrocatalyst approaches and challenges for automotive fuel cells", Nature **486**, 43–51 (2012).

[30] J. Nørskov, J. Rossmeisl, A. Logadottir, L. Lindqvist, J. Kitchin, T. Bligaard and H. Jónsson, "Origin of the Overpotential for Oxygen Reduction at a Fuel-Cell Cathode", J. Phys. Chem. B **108**, 17886–17892 (2004).

[31] H. Gasteiger, S. Kocha, B. Sompalli and F. Wagner, "Activity benchmarks and requirements for Pt, Pt-alloy, and non-Pt oxygen reduction catalysts for PEMFCs", Appl. Catal. B: Environ. **56**, 9–35 (2005).

[32] C. Campos-Roldán and N. Alonso-Vante, "The Hydrogen Oxidation Reaction in Alkaline Medium: An Overview", Electrochem. Energy Rev. **2**, 312–331 (2019).

[33] W. Sheng, H. Gasteiger and Y. Shao-Horn, "Hydrogen Oxidation and Evolution Reaction Kinetics on Platinum: Acid vs Alkaline Electrolytes", J. Electrochem. Soc. **157**, 1529–1536 (2010).

[34] J. Hu, K. Kuttiyiel, K. Sasaki, C. Zhang and R. Adzic, "Determination of Hydrogen Oxidation Reaction Mechanism Based on Pt−H$_{ad}$ Energetics in Alkaline Electrolyte", J. Electrochem. Soc. **165**, J3355–J3362 (2018).

[35] C. Campos-Roldán, R. González-Huerta and N. Alonso-Vante, "Experimental Protocol for HOR and ORR in Alkaline Electrochemical Measurements", J. Electrochem. Soc. **165**, 3001–3007 (2018).

[36] J. Durst, A. Siebel, C. Simon, F. Hasché, J. Herranza and H. Gasteige, "New insights into the electrochemical hydrogen oxidation and evolution reaction mechanism", Energy Environ. Sci. **7**, 2255–2260 (2014).

[37] W. Liu, K. Lyu, L. Xiao, J. Lu and L. Zhuan, "Hydrogen oxidation reaction on modified platinum model electrodes in alkaline media", Electrochim. Acta **327**, 1350162–135022 (2019).

[38] X. Cheng, Z. Shi, N. Glass, L. Zhang and J. Zhang, "A review of PEM hydrogen fuel cell contamination: Impacts, mechanisms, and mitigation", J. Power Sources **165**, 739–756 (2007).

[39] E. Christoffersen, P. Liu, A. Ruban, H. Skriver and J. Nørskov, "Anode materials for low-temperature fuel cells: A density functional theory study", J. Catal. **199**, 123–131 (2001).

[40] J. Baschuk and X. Li, "Carbon monoxide poisoning of proton exchange membrane fuel cells", Int. J. Energy Res. **25**, 695–713 (2001).

[41] X. Yang, Y. Wang, X. Wang, B. Mei and E. Luo, "CO-tolerant PEMFC anodes enabled by synergistic catalysis between iridium single-atom sites and nanoparticles", Angew. Chem. Int. Ed. **60**, 6177–6183 (2021).

[42] S. Satyapal, *U.S. Department of Energy Hydrogen Program: 2021 Annual Merit Review and Peer Evaluation Report; June 7-11, 2021*, Technical Report (National Renewable Energy Lab. (NREL), Golden, CO (United States), 2022).

[43] R. Moradi and K. Groth, "Hydrogen storage and delivery: Review of the state of the art technologies and risk and reliability analysis", Int. J. Hydrog. Energy **44**, 12254–12269 (2019).

[44] M. Usman, "Hydrogen storage methods: Review and current status", Renew. Sust. Energ. Rev. **167**, 112743–112753 (2022).

[45] H. Ishaq, I. Dincer and C. Crawford, "A review on hydrogen production and utilization: Challenges and opportunities", Int. J. Hydrog. Energy **47**, 26238–26264 (2022).

[46] I. Dincer and C. Acar, "Review and evaluation of hydrogen production methods for better sustainability", Int. J. Hydrog. Energy **40**, 11094–11111 (2015).

[47] S. Shiva and K. Himabindu, "Hydrogen production by PEM water electrolysis-A review", Materials Science for Energy Technologies **2**, 442–454 (2019).

[48] M. Chatenet, B. Pollet, D. Dekel, F. Dionigi and J. Deseure, "Water electrolysis: from textbook knowledge to the latest scientific strategies and industrial developments", Chem. Soc. Rev. **51**, 4583–4762 (2022).

[49] M. Carmo, D. Fritz, J. Mergel and D. Stolten, "A comprehensive review on PEM water electrolysis", Int. J. Hydrog. Energy **38**, 4901–4934 (2013).

[50] M. Yu, E. Budiyanto and H. Tüysüz, "Principles of Water Electrolysis and Recent Progress in Cobalt-, Nickel-, and Iron-Based Oxides for the Oxygen Evolution Reaction", Angew. Chem. Int. Ed. **61**, 202103824–202103847 (2022).

[51] Z. Seh, J. Kibsgaard, C. Dickens, I. Chorkendorff, J. Nørskov and T. Jaramillo, "Combining theory and experiment in electrocatalysis: Insights into materials design", Science **355**, 146–157 (2017).

[52] B. Pivovar, N. Rustagi and S. Satyapal, "Hydrogen at Scale (H2@Scale): Key to a Clean, Economic, and Sustainable Energy System", Electrochem. Soc. Interface **27**, 47–52 (2018).

[53] J. Abe, A. Popoola, E. Ajenifuja and O. Popool, "Hydrogen energy, economy and storage: Review and recommendation", Int. J. Hydrog. Energy **44**, 15072–15086 (2019).

[54] Z. Abdin, A. Zafaranloo, A. Rafiee, W. Mérid, W. Lipiński and K. Khalilpour, "Hydrogen as an energy vector", Renew. Sust. Energ. Rev. **120**, 109620–109651 (2020).

[55] I. Chorkendorff and J. Niemantsverdriet, *Concepts of modern catalysis and kinetics*, 2nd (Wiley-VCH Verlag Gmbh & Co. KGaA, Weinheim, 2007).

[56] A. Bell, "The Impact of Nanoscience on Heterogeneous Catalysis", Science **299**, 1688–1691 (2003).

[57] J. Nørskov, F. Abild-Pedersen, F. Studt and T. Bligaard, "Density functional theory in surface chemistry and catalysis", PNAS **108**, 937–943 (2011).

[58] L. Pettersson and A. Nilsson, "A Molecular Perspective on the d-Band Model: Synergy Between Experiment and Theory", Top. Catal. **57**, 2–13 (2014).

[59] B. Hammer and J. Nørskov, "Why gold is the noblest of all metals", Nature **376**, 2238–2240 (1995).

[60] M. Che, "Nobel prize in chemistry 1912 to sabatier: organic chemistry or catalysis?", Catal. Today **218**, 162–171 (2013).

[61] H. Ooka, J. Huang and K. Exner, "The Sabatier Principle in Electrocatalysis: Basics, Limitations, and Extensions", Front. Energy Res. **9**, 654460–654480 (2021).

[62] H. Taylor, "A theory of the catalytic surface", Proc. R. Soc. Lond. A **108**, 105–111 (1925).

[63] C. Vogt and B. Weckhuysen, "The concept of active site in heterogeneous catalysis", Nat. Rev. Chem. **6**, 89–111 (2022).

[64] L. Liu and A. Corma, "Metal Catalysts for Heterogeneous Catalysis: From Single Atoms to Nanoclusters and Nanoparticles", Chem. Rev. **118**, 4981–5079 (2018).

[65] M.-C. Daniel and D. Astruc, "Gold Nanoparticles: Assembly, Supramolecular Chemistry, Quantum-Size-Related Properties, and Applications toward Biology, Catalysis, and Nanotechnology", Chem. Rev. **104**, 293–346 (2004).

[66] I. Chakraborty and T. Pradeep, "Atomically Precise Clusters of Noble Metals: Emerging Link between Atoms and Nanoparticles", Chem. Rev. **117**, 8208–8271 (2017).

[67] R. Jin, C. Zeng, M. Zhou and Y. Chen, "Atomically Precise Colloidal Metal Nanoclusters and Nanoparticles: Fundamentals and Opportunities", Chem. Rev. **116**, 10346–10413 (2016).

[68] Y. Luab and W. Chen, "Sub-nanometre sized metal clusters: from synthetic challenges to the unique property discoveries", Chem. Soc. Rev. **41**, 3594–3623 (2012).

[69] M. El-Sayed, "Small Is Different: Shape-, Size-, and Composition-Dependent Properties of Some Colloidal Semiconductor Nanocrystals", Acc. Chem. Res. **37**, 326–333 (2004).

[70] S. Maity, D. Bain and A. Patra, "An overview on the current understanding of the photophysical properties of metal nanoclusters and their potential applications", Nanoscale **11**, 22685–22723 (2019).

[71] T. Schaaff, M. Shafigullin, J. Khoury, I. Vezmar and R. Whetten, "Isolation of Smaller Nanocrystal Au Molecules: Robust Quantum Effects in Optical Spectra", J. Phys. Chem. B **101**, 7885–7891 (1997).

[72] E. Roduner, "Size matters: why nanomaterials are different", Chem. Soc. Rev. **35**, 583–592 (2006).

[73] X. Kang and M. Zhu, "Tailoring the photoluminescence of atomically precise nanoclusters", Chem. Soc. Rev. **48**, 2422–2457 (2019).

[74] R. Jin, "Quantum sized, thiolate-protected gold nanoclusters", Nanoscale **2**, 343–362 (2010).

[75] Y. Negishi, K. Nobusada and T. Tsukuda, "Glutathione-Protected Gold Clusters Revisited: Bridging the Gap between Gold(I)-Thiolate Complexes and Thiolate-Protected Gold Nanocrystals", J. Am. Chem. Soc. **127**, 5261–5270 (2005).

[76] P. Ferrari, G.-L. Hou, O. Lushchikova, F. Calvo, J. Bakker and E. Janssens, "The structures of cationic gold clusters probed by far-infrared spectroscopy", Phys. Chem. Chem. Phys. **22**, 11572–11577 (2022).

[77] P. Gruene, D. Rayner, B. Redlich, A. Meer, J. Lyon and G. Meijer, "Structures of Neutral Au_7, Au_{19}, and Au_{20} Clusters in the Gas Phase", Science **321**, 674–676 (2008).

[78] J. Wang, G. Wang and J. Zhao, "Density-functional study of Au_n ($n = 2 - 20$) clusters: Lowest-energy structures and electronic properties", Phys. Rev. B **66**, 035418–035423 (2002).

[79] B. Assadollahzadeha and P. Schwerdtfeger, "A systematic search for minimum structures of small gold clusters Au_n ($n = 2 - 20$) and their electronic properties", J. Chem. Phys. **131**, 064306–064316 (2009).

[80] V. Kumar and Y. Kawazoe, "Evolution of atomic and electronic structure of Pt clusters: Planar, layered, pyramidal, cage, cubic, and octahedral growth", Phys. Rev. B **77**, 205418–205427 (2008).

[81] P. Nava, M. Sierkaa and R. Ahlrichs, "Density functional study of palladium clusters", Phys. Chem. Chem. Phys. **5**, 3372–3381 (2003).

[82] W.-C. Lu, C. Wang, L.-Z. Zhao, W. Zhang, W. Qin and K. Ho, "Appearance of bulk-like motifs in Si, Ge, and Al clusters", Phys. Chem. Chem. Phys. **12**, 8551–8556 (2010).

[83] H.-L. Xu, N. Tkachenko, D. Szczepanik, I. Popov, A. Muñoz-Castro and A. Boldyrev, "Symmetry collapse due to the presence of multiple local aromaticity in Ge_{24}^{4-}", Nat. Commun. **13**, 2149–2149 (2022).

[84] D. Wu, R. Shi, Q. Du, X. Wu, X. Liang and X. Huang, "Atomic Structures and Electronic Properties of Large-Sized Ge_N Clusters ($N = 45, 50, 55, 60, 65, 70$) by First-Principles Global Search", J. Clust. Sci. **30**, 371–377 (2019).

[85] J. Liu, "Advanced Electron Microscopy of Metal-Support Interactions in Supported Metal Catalysts", ChemCatChem **3**, 934–948 (2011).

[86] T. Deelen, C. Mejía and K. Jong, "Control of metal-support interactions in heterogeneous catalysts to enhance activity and selectivity", Nat. Catal. **2**, 955–970 (2019).

[87] M. Ahmadi, H. Mistry and B. Roldan Cuenya, "Tailoring the Catalytic Properties of Metal Nanoparticles via Support Interactions", J. Phys. Chem. Lett. **7**, 3519–3533 (2016).

[88] C. Dong, Y. Li, D. Cheng, M. Zhang, J. Liu and Y.-G. Wang, "Supported Metal Clusters: Fabrication and Application in Heterogeneous Catalysis", ACS Catal. **10**, 11011–11045 (2020).

[89] J. Dadras, L. Shen and A. Alexandrova, "Pt-Zn Clusters on Stoichiometric MgO(100) and TiO_2(110): Dramatically Different Sintering Behavior", J. Phys. Chem. C **119**, 6047–6055 (2015).

[90] F. Buendía, J. Vargas, M. Beltrán, J. Davis and R. Johnston, "A comparative study of $Au_m Rh_n$ ($4 \leq m+n \leq 6$) clusters in the gas phase versus those deposited on (100) MgO", Phys. Chem. Chem. Phys. **18**, 22122–22128 (2016).

[91] Z. Luo, G. Zhao, H. Pan and W. Sun, "Strong Metal-Support Interaction in Heterogeneous Catalysts", Adv. Energy Mater. **12**, 2201395–2201409 (2022).

[92] Y. Guo and Y.-W. Zhang, "Metal Clusters Dispersed on Oxide Supports: Preparation Methods and Metal-Support Interactions", Top. Catal. **61**, 855–874 (2018).

[93] X. Liu, A. Wang, T. Zhang and C.-Y. Mou, "Catalysis by gold: new insights into the support effect", Nano Today **8**, 403–416 (2013).

[94] E. Jimenez-Izal and A. Alexandrova, "Computational design of clusters for catalysis", Annu. Rev. Phys. Chem. **69**, 377–400 (2018).

[95] E. Jimenez-Izal, B. Gates and A. Alexandrova, "Designing clusters for heterogeneous catalysis", Phys. Today **72**, 38–43 (2019).

[96] X. Chen, M. Peng, D. Xiao, H. Liu and D. Ma, "Fully Exposed Metal Clusters: Fabrication and Application in Alkane Dehydrogenation", ACS Catal. **12**, 12720–12743 (2022).

[97] A. Halder, L. Curtiss, A. Fortunelli and S. Vajda, "Perspective: Size selected clusters for catalysis and electrochemistry", J. Chem. Phys. **148**, 110901–110915 (2018).

[98] E. Tyo and S. Vajda, "Catalysis by clusters with precise numbers of atoms", Nat. Nanotechnol. **10**, 577–588 (2015).

[99] S. Vajda, M. Pellin, J. Greeley, C. Marshall, L. Curtiss and G. Ballentine, "Subnanometre platinum clusters as highly active and selective catalysts for the oxidative dehydrogenation of propane", Nat. Mater. **8**, 213–216 (2009).

[100] M. Haruta, "Chance and Necessity: My Encounter with Gold Catalysts", Angew. Chem. Int. Ed. **53**, 52–56 (2014).

[101] S. Tian, Q. Fu, W. Chen, Q. Feng, Z. Chen and J. Zhang, "Carbon nitride supported Fe_2 cluster catalysts with superior performance for alkene epoxidation", Nat. Commun. **9**, 2353–2359 (2018).

[102] X. Chen, M. Peng, X. Cai, Y. Chen, Z. Jia and Y. Deng, "Regulating coordination number in atomically dispersed Pt species on defect-rich graphene for n-butane dehydrogenation reaction", Nat. Commun. **12**, 2664–2672 (2021).

[103] R. Jin, G. Li, S. Sharma, Y. Li and X. Du, "Toward Active-Site Tailoring in Heterogeneous Catalysis by Atomically Precise Metal Nanoclusters with Crystallographic Structures", Chem. Rev. **121**, 567–648 (2021).

[104] Y. Du, H. Sheng, D. Astruc and M. Zhu, "Atomically Precise Noble Metal Nanoclusters as Efficient Catalysts: A Bridge between Structure and Properties", Chem. Rev. **120**, 526–622 (2020).

[105] A. Kulkarni, R. Lobo-Lapidus and B. Gates, "Metal clusters on supports: synthesis, structure, reactivity, and catalytic properties", Chem. Commun. **46**, 5997–6015 (2010).

[106] D. Tomalia, "Dendrons/dendrimers: quantized, nano-element like building blocks for soft-soft and soft-hard nano-compound synthesis", Soft Matter **6**, 456–474 (2010).

[107] L. Liu, M. Lopez-Haro, D. Meira, P. Concepcion, J. Calvino and A. Corma, "Regioselective Generation of Single-Site Iridium Atoms and Their Evolution into Stabilized Subnanometric Iridium Clusters in MWW Zeolite", Angew. Chem. Int. Ed. **59**, 15695–15702 (2020).

[108] M. Argyle and C. Bartholomew, "Heterogeneous Catalyst Deactivation and Regeneration: A Review", Catalysts **5**, 145–269 (2015).

[109] J. Moulijn, A. Diepen and F. Kapteijn, "Catalyst deactivation: is it predictable?: What to do?", Appl. Catal. A: Gen **212**, 3–16 (2001).

[110] P. Forzatti and L. Lietti, "Catalyst deactivation", Catal. Today **52**, 165–181 (1999).

[111] Y. Dai, P. Lu, Z. Cao, C. Campbell and Y. Xia, "The physical chemistry and materials science behind sinter-resistant catalysts", Chem. Soc. Rev. **47**, 4314–4331 (2018).

[112] E. Goodman, J. Schwalbe and M. Cargnello, "Mechanistic Understanding and the Rational Design of Sinter-Resistant Heterogeneous Catalysts", ACS Catal. **7**, 7156–7173 (2017).

[113] J. Nørskov, T. Bligaard, J. Rossmeisl and C. Christensen, "Towards the computational design of solid catalysts", Nat. Chem. **1**, 37–46 (2009).

[114] B. Roldan Cuenya, "Synthesis and catalytic properties of metal nanoparticles: Size, shape, support, composition, and oxidation state effects", Thin Solid Films **518**, 3127–3150 (2010).

[115] B. Roldan Cuenya and F. Behafarid, "Nanocatalysis: size- and shape-dependent chemisorption and catalytic reactivity", Surf. Sci. Rep. **70**, 135–187 (2015).

[116] E. Vorobyeva, E. Fako, Z. Chen, S. Collins, D. Johnstone and P. Midgley, "Atom-by-Atom Resolution of Structure-Function Relations over Low-Nuclearity Metal Catalyst", Angew. Chem. Int. Ed. **58**, 8724–8729 (2019).

[117] A. Fernando, K. Weerawardene, N. Karimova and C. Aikens, "Quantum Mechanical Studies of Large Metal, Metal Oxide, and Metal Chalcogenide Nanoparticles and Clusters", Chem. Rev. **115**, 6112–6216 (2015).

[118] S. Chee, T. Lunkenbein, R. Schlögl and B. Roldan Cuenya, "In situ and operando electron microscopy in heterogeneous catalysis-insights into multi-scale chemical dynamics", J. Phys.: Condens. Matter **33**, 153001–153029 (2021).

[119] K. Kalz, R. Kraehnert, M. Dvoyashkin, R. Dittmeyer, R. Gläser and U. Krewer, "Future Challenges in Heterogeneous Catalysis: Understanding Catalysts under Dynamic Reaction Conditions", ChemCatChem **9**, 17–29 (2017).

[120] D. Sharapa, D. Doronkin, F. Studt, J.-D. Grunwaldt and S. Behrens, "Moving Frontiers in Transition Metal Catalysis: Synthesis, Characterization and Modeling", Adv. Mater. **31**, 1807381–1807391 (2019).

[121] C. Brieger, J. Melke, N. Bosch, U. Reinholz, H. Riesemeier and A. Buzanich, "A combined in-situ XAS-DRIFTS study unraveling adsorbate induced changes on the Pt nanoparticle structure", J. Catal. **339**, 57–67 (2016).

[122] H. Wang and J. Lu, "A Review on Particle Size Effect in Metal-Catalyzed Heterogeneous Reactions", Chin. J. Chem. **38**, 1422–1444 (2020).

[123] L. Li, A. Larsen, N. Romero, V. Morozov, C. Glinsvad and F. Abild-Pedersen, "Investigation of Catalytic Finite-Size-Effects of Platinum Metal Clusters", J. Phys. Chem. Lett. **4**, 222–226 (2013).

[124] A. Green, J. Justen, W. Schöllkopf, A. Gentleman, A. Fielicke and S. Mackenzie, "IR Signature of Size-Selective CO_2 Activation on Small Platinum Cluster Anions, Pt_n^- $(n = 4 - 7)$", Angew. Chem. Int. Ed. **57**, 14822–14826 (2018).

[125] R. Santen, "Complementary Structure Sensitive and Insensitive Catalytic Relationships", Acc. Chem. Res. **42**, 57–66 (2009).

[126] W. Zhang, H. Wang, J. Jiang, Z. Sui, Y. Zhu and D. Chen, "Size Dependence of Pt Catalysts for Propane Dehydrogenation: from Atomically Dispersed to Nanoparticles", ACS Catal. **10**, 12932–12942 (2020).

[127] C. Dong, Z. Gao, Y. Li, M. Peng, M. Wang and Y. Xu, "Fully exposed palladium cluster catalysts enable hydrogen production from nitrogen heterocycles", Nat. Catal. **5**, 485–493 (2022).

[128] S. Abbet, A. Sanchez, U. Heiz, W.-D. Schneider, A. Ferrari and G. Pacchioni, "Acetylene Cyclotrimerization on Supported Size-Selected Pd_n Clusters $(1 \leq n \leq 30)$: One Atom Is Enough!", J. Am. Chem. Soc. **122**, 3453–3457 (2000).

[129] L. Molina, S. Lee, K. Sell, G. Barcaro, A. Fortunelli and B. Lee, "Size-dependent selectivity and activity of silver nanoclusters in the partial oxidation of propylene to propylene oxide and acrolein: A joint experimental and theoretical study", Catal. Today **160**, 116–130 (2011).

[130] A. Genest, J. Silvestre-Albero, W.-Q. Li, N. Rösch and G. Rupprechter, "The origin of the particle-size-dependent selectivity in 1-butene isomerization and hydrogenation on Pd/Al_2O_3 catalysts", Nat. Commun. **12**, 6098–6105 (2021).

[131] F. Schweinberger, M. Berr, M. Döblinger, C. Wolff, K. Sanwald and A. Crampton, "Cluster Size Effects in the Photocatalytic Hydrogen Evolution Reaction", J. Am. Chem. Soc. **135**, 13262–13265 (2013).

[132] A. Beniya, S. Higashi, N. Ohba, R. Jinnouchi, H. Hirata and Y. Watanabe, "CO oxidation activity of non-reducible oxide-supported mass-selected few-atom Pt single-clusters", Nat. Commun. **11**, 1888– 1897 (2020).

[133] A. Corma, P. Concepción, M. Boronat, M. Sabater, J. Navas and M. Yacaman, "Exceptional oxidation activity with size-controlled supported gold clusters of low atomicity", Nat. Chem. **5**, 775–781 (2013).

[134] W. Kaden, T. Wu, W. Kunkel and S. Anderson, "Electronic Structure Controls Reactivity of Size-Selected Pd Clusters Adsorbed on TiO_2 Surfaces", Science **326**, 826–829 (2009).

[135] R. Isaifan, S. Ntais and E. Baranova, "Particle size effect on catalytic activity of carbon-supported Pt nanoparticles for complete ethylene oxidation", Appl. Catal. A: Gen **464-465**, 87–94 (2013).

[136] W. Chen and S. Chen, "Oxygen Electroreduction Catalyzed by Gold Nanoclusters: Strong Core Size Effects", Angew. Chem. Int. Ed. **48**, 4386–4389 (2009).

[137] F. Haase, A. Bergmann, T. Jones, J. Timoshenko, A. Herzog and H. Jeon, "Size effects and active state formation of cobalt oxide nanoparticles during the oxygen evolution reaction", Nat. Energy **7**, 765–773 (2022).

[138] A. Weber, E. Baxter, S. Proch, M. Kane, M. Rosenfelder and H. White, "Size-dependent electronic structure controls activity for ethanol electro-oxidation at Pt_n/indium tin oxide ($n = 1 \text{to} 14$)", Phys. Chem. Chem. Phys. **17**, 17601–17610 (2015).

[139] M. Shao, A. Peles and K. Shoemaker, "Electrocatalysis on Platinum Nanoparticles: Particle Size Effect on Oxygen Reduction Reaction Activity", Nano Lett. **11**, 3714–3719 (2011).

[140] A. Weber, E. Baxter, H. White and S. Anderson, "Cluster Size Controls Branching between Water and Hydrogen Peroxide Production in Electrochemical Oxygen Reduction at Pt_n/ITO", J. Phys. Chem. C **119**, 11160–11170 (2015).

[141] H. Mistry, R. Reske, Z. Zeng, Z.-J. Zhao, J. Greeley and P. Strasser, "Exceptional Size-Dependent Activity Enhancement in the Electroreduction of CO_2 over Au Nanoparticles", J. Am. Chem. Soc. **136**, 16473–16476 (2014).

[142] B. Yang, C. Liu, A. Halder, E. Tyo, A. Martinson and S. Seifert, "Copper Cluster Size Effect in Methanol Synthesis from CO_2", J. Phys. Chem. **C 121**, 10406–10412 (2017).

[143] T. Imaoka, H. Kitazawa, W.-J. Chun, S. Omura, K. Albrecht and K. Yamamoto, "Magic Number Pt_{13} and Misshapen Pt_{12} Clusters: Which One is the Better Catalyst?", J. Am. Chem. Soc. **135**, 13089–13095 (2013).

[144] G. Kwon, G. Ferguson, C. Heard, E. Tyo, C. Yin and J. DeBartolo, "Size-Dependent Subnanometer Pd Cluster (Pd_4, Pd_6, and Pd_{17}) Water Oxidation Electrocatalysis", ACS Nano **7**, 5808–5817 (2013).

[145] P. Poths, Z. Hong, G. Li, S. Anderson and A. Alexandrova, ""Magic" sinter-resistant cluster sizes of Pt_n supported on Alumina", J. Phys. Chem. Lett. **13**, 11044–11050 (2022).

[146] R. Narayanan and M. El-Sayed, "Shape-Dependent Catalytic Activity of Platinum Nanoparticles in Colloidal Solution", Nano Letters **4**, 1343–1348 (2004).

[147] H. Liu, J. Timoshenko, L. Bai, Q. Li, M. Rüscher and C. Sun, "Low-Coordination Rhodium Catalysts for an Efficient Electrochemical Nitrate Reduction to Ammonia", ACS Catal. **13**, 1513–1521 (2023).

[148] I. Lee, F. Delbecq, R. Morales, M. Albiter and F. Zaera, "Tuning selectivity in catalysis by controlling particle shape", Nat. Mater. **8**, 132–138 (2009).

[149] K. An and G. Somorjai, "Size and Shape Control of Metal Nanoparticles for Reaction Selectivity in Catalysis", ChemCatChem **4**, 1512–1524 (2012).

[150] L. Lin, J. Liu, X. Liu, Z. Gao, N. Rui and S. Yao, "Reversing sintering effect of Ni particles on γ-Mo_2N via strong metal support interaction", Nat. Commun. **12**, 6978–6988 (2021).

[151] S. Lee, M. Kishore, D. Kim, H. Kang, J. Chun and L. Oh, "Direct O−O Coupling Promoted the Oxygen Evolution Reaction by Dual Active Sites from Ag/LaNiO$_3$ Interfaces", ACS Appl. Energy Mater. **5**, 14658–14668 (2022).

[152] H. Fang, C. Liao, Y. Ying, J. Cheng, Q. Wang and H. Huang, "Creating metal-carbide interactions to boost ammonia oxidation activity for low-temperature direct ammonia fuel cells", J. Catal. **417**, 129–139 (2023).

[153] A. Puigdollers, P. Schlexer, S. Tosoni and G. Pacchioni, "Increasing Oxide Reducibility: The Role of Metal/Oxide Interfaces in the Formation of Oxygen Vacancies", ACS Catal. **7**, 6493–6513 (2017).

[154] S. Kattel, B. Yan, Y. Yang, J. Chen and P. Liu, "Optimizing Binding Energies of Key Intermediates for CO$_2$ Hydrogenation to Methanol over Oxide-Supported Copper", J. Am. Chem. Soc. **138**, 12440–12450 (2016).

[155] S. Kattel, P. Liu and J. Chen, "Tuning selectivity of co$_2$ hydrogenation reactions at the metal/oxide interface", J. Am. Chem. Soc. **139**, 9739–9754 (2017).

[156] X. Zhang, L. Liu, J. Wang, X. Ju, R. Si and J. Feng, "The role of lanthanum hydride species in La$_2$O$_3$ supported Ru cluster catalyst for ammonia synthesis", J. Catal. **417**, 382–395 (2023).

[157] E. Lee, J. Lee, S. Hwang and D. Kim, "Role of CeO$_2$ in promoting the spillover in CO oxidation reaction over platinum nanoparticle-supported CeO$_2$ catalyst", J. Catal. **417**, 421–431 (2023).

[158] Y. Gao, W. Wang, S. Chang and W. Huang, "Morphology Effect of CeO$_2$ Support in the Preparation, Metal-Support Interaction, and Catalytic Performance of Pt/CeO$_2$ Catalysts", ChemCatChem **5**, 3610–3620 (2013).

[159] B. Yoon, H. Häkkinen, U. Landman, A. Wörz, J.-M. Antonietti and S. Abbet, "Charging Effects on Bonding and Catalyzed Oxidation of CO on Au$_8$ Clusters on MgO", Science **307**, 403–407 (2005).

[160] X. Liu, S. Jia, M. Yang, Y. Tang, Y. Wen and S. Chu, "Activation of subnanometric Pt on Cu-modified CeO$_2$ via redox-coupled atomic layer deposition for CO oxidation", Nat. Commun. **11**, 4240–4247 (2020).

[161] L. Liu and A. Corma, "Evolution of Isolated Atoms and Clusters in Catalysis", Trends Chem. **2**, 383–400 (2020).

[162] S. Wang, Y. Gao, F. Yi, M. Yan, D. Zhu and D. Xu, "Regulation of sub-nanometric platinum on BaKL zeolite for boosting n-heptane aromatization", Fuel **328**, 125281–125290 (2022).

[163] J. Lee, I. Song and D. Kim, "Suppressed Strong Metal-Support Interactions in Platinum on Sulfated Titania and Their Influence on the Oxidation of Carbon Monoxide", ChemCatChem **10**, 1258–1262 (2018).

[164] S. Lalwani, M. AlNahyan, A. Zaabi, F. AlMarzooqi and A. Qurashi, "Advances in Interfacial Engineering and Their Role in Heterostructure Formation for HER Applications in Wider pH", ACS Appl. Energy Mater. **5**, 14571–14592 (2022).

[165] L. Zhao, B. Wang and R. Wang, "A Critical Review on New and Efficient 2D Materials for Catalysis", Adv. Mater. Interfaces **9**, 2200771–2200802 (2022).

[166] B. Peters, "Simple Model and Spectral Analysis for a Fluxional Catalyst: Intermediate Abundances, Pathway Fluxes, Rates, and Transients", ACS Catal. **12**, 8038–8047 (2022).

[167] H. Zhai and A. Alexandrova, "Fluxionality of Catalytic Clusters: When It Matters and How to Address It", ACS Catal. **7**, 1905–1911 (2017).

[168] H. Zhai and A. Alexandrova, "Local Fluxionality of Surface-Deposited Cluster Catalysts: The Case of Pt_7 on Al_2O_3", J. Phys. Chem. Lett. **9**, 1696–1702 (2018).

[169] R. Lavroff, H. Morgan, Z. Zhang, P. Poths and A. Alexandrova, "Ensemble representation of catalytic interfaces: soloists, orchestras, and everything in-between", Chem. Sci. **13**, 8003–8016 (2022).

[170] Z. Zhang, B. Zandkarimi and A. Alexandrova, "Ensembles of Metastable States Govern Heterogeneous Catalysis on Dynamic Interfaces", Acc. Chem. Res. **53**, 447–458 (2020).

[171] B. Zandkarimi and A. Alexandrova, "Surface-supported cluster catalysis: Ensembles of metastable states run the show", WIREs Comput. Mol. Sci. **9**, 1420–1436 (2019).

[172] Z. Zhang, B. Zandkarimi, J. Munarriz, C. Dickerson and A. Alexandrova, "Fluxionality of Subnano Clusters Reshapes the Activity Volcano of Electrocatalysis", ChemCatChem **14**, 202200345–202200350 (2022).

[173] B. Zandkarimi, P. Poths and A. Alexandrova, "When Fluxionality Beats Size Selection: Acceleration of Ostwald Ripening of Sub-Nano Clusters", Angew. Chem. Int. Ed. **60**, 11973–11982 (2021).

[174] J. Jasík, A. Fortunelli and S. Vajda, "Exploring the materials space in the smallest particle size range: from heterogeneous catalysis to electrocatalysis and photocatalysis", Phys. Chem. Chem. Phys. **24**, 12083–12115 (2022).

[175] P. Poths and A. Alexandrova, "Theoretical Perspective on Operando Spectroscopy of Fluxional Nanocatalysts", J. Phys. Chem. Lett. **13**, 4321–4334 (2022).

[176] E. Baxter, M.-A. Ha, A. Cass, A. Alexandrova and S. L. Anderson, "Ethylene Dehydrogenation on $Pt_{4,7,8}$ Clusters on Al_2O_3: Strong Cluster Size Dependence Linked to Preferred Catalyst Morphologies", ACS Catal. **7**, 3322–3335 (2017).

[177] A. Halder, M.-A. Ha, H. Zhai, B. Yang and M. Pellin, "Oxidative Dehydrogenation of Cyclohexane by Cu vs Pd Clusters: Selectivity Control by Specific Cluster Dynamics", ChemCatChem **12**, 1307–1315 (2020).

[178] R. Ferrando, J. Jellinek and R. Johnston, "Nanoalloys: From Theory to Applications of Alloy Clusters and Nanoparticles", Chem. Rev. **108**, 845–910 (2008).

[179] X. Kang, Y. Li, M. Zhu and R. Jin, "Atomically precise alloy nanoclusters: syntheses, structures, and properties", Chem. Soc. Rev. **49**, 6443–6514 (2020).

[180] M. Sankar, N. Dimitratos, P. Miedziak, P. Wells, C. Kielye and G. Hutchings, "Designing bimetallic catalysts for a green and sustainable future", Chem. Soc. Rev. **41**, 8099–8139 (2012).

[181] A. Ghosh, O. Mohammed and O. Bakr, "Atomic-Level Doping of Metal Clusters", Acc. Chem. Res. **51**, 3094–3103 (2018).

[182] Y. Nakaya and S. Furukawa, "Catalysis of Alloys: Classification, Principles, and Design for a Variety of Materials and Reactions", Chem. Rev, **123**, 5859–5947 (2023).

[183] Y.-J. Deng, V. Tripkovic, J. Rossmeisl and M. Arenz, "Oxygen Reduction Reaction on Pt Overlayers Deposited onto a Gold Film: Ligand, Strain, and Ensemble Effect", ACS Catal. **6**, 671–676 (2016).

[184] H. Abdulhussein, P. Ferrari, J. Vanbuel, C. Heard, A. Fielicke and P. Lievens, "Altering CO binding on gold cluster cations by Pd-doping", Nanoscale **11**, 16130–16141 (2019).

[185] J. Dadras, E. Jimenez-Izal and A. Alexandrova, "Alloying Pt Sub-nano-clusters with Boron: Sintering Preventative and Coke Antagonist?", ACS Catal. **5**, 5719–5727 (2015).

[186] S. Xie, H. Tsunoyama, W. Kurashige, Y. Negishi and T. Tsukuda, "Enhancement in Aerobic Alcohol Oxidation Catalysis of Au_{25} Clusters by Single Pd Atom Doping", ACS Catal. **2**, 1519–1523 (2012).

[187] E. Jimenez-Izal, H. Zhai, J.-Y. Liu and A. Alexandrova, "Nanoalloying MgO-Deposited Pt Clusters with Si To Control the Selectivity of Alkane Dehydrogenation", ACS Catal. **8**, 8346–8356 (2018).

[188] O. Ayodele, R. Cai, J. Wang, Y. Ziouani, Z. Liang and M. Spadaro, "Synergistic Computational-Experimental Discovery of Highly Selective PtCu Nanocluster Catalysts for Acetylene Semihydrogenation", ACS Catal. **10**, 451–457 (2020).

[189] Y. Zhang, F. Zhang, L. Li, H. Qi, Z. Yu and X. Liu, "Decoration of Ru nanoparticles with mononuclear MoO_x boosts the hydrodeoxygenation of amides to amines", J. Catal. **417**, 301–313 (2023).

[190] M.-A. Ha, J. Dadras and A. Alexandrova, "Rutile-Deposited Pt−Pd clusters: A Hypothesis Regarding the Stability at 50/50 Ratio", ACS Catal. **4**, 3570–3580 (2014).

[191] M. Escudero-Escribano, K. Jensen and A. Jensen, "Recent advances in bimetallic electrocatalysts for oxygen reduction: design principles, structure-function relations and active phase elucidation", Curr. Opin. Electrochem. **8**, 135–146 (2018).

[192] Y.-J. Wang, N. Zhao, B. Fang, H. Li, X. Bi and H. Wang, "Carbon-Supported Pt-Based Alloy Electrocatalysts for the Oxygen Reduction Reaction in Polymer Electrolyte Membrane Fuel Cells: Particle Size, Shape, and Composition Manipulation and Their Impact to Activity", Chem. Rev. **115**, 3433–3467 (2015).

[193] E. Antolini, "Platinum-based ternary catalysts for low temperature fuel cells: Part I. Preparation methods and structural characteristics", Appl. Catal. B: Environ. **74**, 324–336 (2007).

[194] E. Antolini, "Platinum-based ternary catalysts for low temperature fuel cells: Part II. Electrochemical properties", Appl. Catal. B: Environ. **74**, 337–350 (2007).

[195] E. Antolini, "Formation of carbon-supported PtM alloys for low temperature fuel cells: a review", Mater. Chem. Phys. **78**, 563–573 (2003).

[196] J. Wu and H. Yang, "Platinum-Based Oxygen Reduction Electrocatalysts", Acc. Chem. Res. **46**, 1848–1857 (2013).

[197] M. Liu, R. Zhang and W. Chen, "Graphene-Supported Nanoelectrocatalysts for Fuel Cells: Synthesis, Properties, and Applications", Chem. Rev. **114**, 5117–5160 (2014).

[198] W. Yan, S. Cao, H. Liu, Q. Xing, J. Ren and Z. Li, "Facile Solid-Phase Method for Preparing a Highly Active and Stable PtZn-Based Oxygen Reduction/Hydrogen Evolution Bifunctional Electrocatalyst: Effect of Bi-Facet Lattice Strain on Catalytic Activity", ACS Appl. Energy Mater. **5**, 13791–13801 (2022).

[199] T. Liu, F. Sun, M. Huang and L. Guan, "Ternary PtZnCu Intermetallic Nanoparticles as an Efficient Oxygen Reduction Electrocatalyst for Fuel Cells with Ultralow Pt Loading", ACS Appl. Energy Mater. **5**, 12219–12226 (2022).

[200] S. Gong, M. Sun, Y. Lee, N. Becknell, J. Zhang and Z. Wang, "Bulk-like Pt(100)-oriented Ultrathin Surface: Combining the Merits of Single Crystals and Nanoparticles to Boost Oxygen Reduction Reaction", Angew. Chem. Int. Ed. **62**, 202214516–202214522 (2022).

[201] X. Xie, V. Briega-Martos, R. Farris, M. Dopita, M. Vorokhta and T. Skála, "Optimal Pt-Au Alloying for Efficient and Stable Oxygen Reduction Reaction Catalysts", ACS Appl. Mater. Interfaces **15**, 1192–1200 (2023).

[202] Y. Wu, S. Wang, M. Zhang, Y. Hong, X. Zhang and C. Wang, "Enhanced Activity of Oxygen Reduction Reaction on Pr_6O_{11}-Assisted PtPr Alloy Electrocatalysts", ACS Appl. Mater. Interfaces **14**, 41861–41869 (2022).

[203] S. Wang, C. Zhou, Y. Cao, L. Song, L. Zhen and K. Ma, "Pt-O-Cu anchored on Fe_2O_3 boosting electrochemical water-gas shift reaction for highly efficient H_2 generation", J. Catal. **417**, 98–108 (2023).

[204] L. Lu, S. Zou and B. Fang, "The Critical Impacts of Ligands on Heterogeneous Nanocatalysis: A Review", ACS Catal. **11**, 6020–6058 (2021).

[205] V. Truttmann, H. Drexler, M. Stöger-Pollach, T. Kawawaki, Y. Negishi, N. Barrabés and G. Rupprechter, "CeO_2 Supported Gold Nanocluster Catalysts for CO Oxidation: Surface Evolution Influenced by the Ligand Shell", ChemCatChem **14**, e202200322–e202200334 (2022).

[206] G. Sun, A. Alexandrova and P. Sautet, "Pt_8 cluster on alumina under a pressure of hydrogen: Support-dependent reconstruction from first-principles global optimization", J. Chem. Phys. **151**, 194703–194717 (2019).

[207] K. Weerawardene, H. Häkkinen and C. Aikens, "Connections Between Theory and Experiment for Gold and Silver Nanoclusters", Annu. Rev. Phys. Chem. **69**, 205–229 (2018).

[208] X. Wang, L. Zhao, X. Li, Y. Liu, Y. Wang and Q. Yao, "Atomic-precision Pt_6 nanoclusters for enhanced hydrogen electro-oxidation", Nat. Commun. **13**, 1596–1605 (2022).

[209] D. Strmcnik, M. Escudero-Escribano, K. Kodama, V. Stamenkovic, A. Cuesta and N. Marković, "Enhanced electrocatalysis of the oxygen reduction reaction based on patterning of platinum surfaces with cyanide", Nat. Chem. **2**, 880–885 (2010).

[210] X. Chen, L. Granda-Marulanda, I. McCrum and M. Koper, "How palladium inhibits CO poisoning during electrocatalytic formic acid oxidation and carbon dioxide reduction", Nat. Commun. **13**, 38–48 (2022).

[211] A. Petersen, K. Jensen, H. Wan, A. Bagger, I. Chorkendorff and I. Stephens, "Modeling Anion Poisoning during Oxygen Reduction on Pt Near-Surface Alloys", ACS Catal. **13**, 2735–2743 (2023).

[212] D. Gao, I. Zegkinoglou, N. Divins, F. Scholten, I. Sinev and P. Grosse, "Plasma-Activated Copper Nanocube Catalysts for Efficient Carbon Dioxide Electroreduction to Hydrocarbons and Alcohols", ACS Nano **11**, 4825–4831 (2017).

[213] H. Mistry, A. Varela, C. Bonifacio, I. Zegkinoglou, I. Sinev and Y.-W. Choi, "Highly selective plasma-activated copper catalysts for carbon dioxide reduction to ethylene", Nat. Commun. **7**, 12123–12130 (2016).

[214] H. Guo, P. Sautet and A. Alexandrova, "Reagent-Triggered Isomerization of Fluxional Cluster Catalyst via Dynamic Coupling", J. Phys. Chem. Lett. **11**, 3089–3094 (2020).

[215] Z. Zhang, T. Masubuchi, P. Sautet, S. Anderson and A. Alexandrova, "Hydrogen Evolution on Electrode-Supported Pt_n Clusters: Ensemble of Hydride States Governs the Size Dependent Reactivity", Angew. Chem. Int. Ed. **62**, 2022182–2022190 (2023).

[216] P. Poths, G. Li, T. Masubuchi, H. Morgan, Z. Zhang and A. Alexandrova, "Got Coke? Self-Limiting Poisoning Makes an Ultra Stable and Selective Sub-Nano Cluster Catalyst", ACS Catal. **13**, 1533–1544 (2023).

[217] P. Poths, H. Morgan, G. Li, A. Fuchs, S. Anderson and A. Alexandrova, "Promoter-Poison Partnership Protects Platinum Performance in Coked Cluster Catalysts", J. Phys. Chem. C **127**, 5376–5384 (2023).

[218] R. Mariscal, J. Fierro, J. Yori, J. Parera and J. Grau, "Evolution of the properties of $PtGe/Al_2O_3$ reforming catalysts with Ge content", Appl. Cat. A: Gen. **327**, 123–131 (2007).

[219] V. Mazzieri, C. Pieck, C. Vera, J. Yori and J. Grau, "Effect of Ge content on the metal and acid properties of $Pt-Re-Ge/Al_2O_3-Cl$ catalysts for naphtha", Appl. Cat. A: Gen. **353**, 93–100 (2009).

[220] A. Borgna, T. Garetto and C. Apesteguía, "Simultaneous deactivation by coke and sulfur of bimetallic Pt-Re(Ge, Sn)/Al$_2$O$_3$ catalysts for n-hexane reforming", Appl. Cat. A: Gen. **197**, 11–21 (2000).

[221] T. Garetto, A. Borgna and C. Apesteguía, "High-thiotolerant Pt-Ge/Al$_2$O$_3$ naphtha reforming catalysts by in situ alloying", Stud. Surf. Sci. Catal. **101**, 1155–1164 (1996).

[222] E. Crabb and M. Ravikumar, "Synthesis and characterisation of carbon-supported PtGe electrocatalysts for CO oxidation", Electrochim. Acta **46**, 1033–1041 (2001).

[223] N. Veizaga, V. Paganin, T. Rocha, O. Scelza, S. Miguel and E. Gonzalez, "Development of PtGe and PtIn anodic catalysts supported on carbonaceous materials for DMFC", Int. J. Hydrog. Energy **39**, 8728–8737 (2014).

[224] K. Fukutani, T. Magkoev, Y. Murata, M. Matsumoto, T. Kawauchi and T. Magome, "Electronic structure of a Pt(111)-Ge surface alloy and adsorbed CO", J. Electron Spectrosc. Relat. Phenom. **88-91**, 597–601 (1998).

[225] S.-C. Lim, M.-C. Hsiao, M.-D. Lu, Y.-L. Tung and H.-Y. Tuan, "Synthesis of germanium-platinum nanoparticles as high-performance catalysts for spray-deposited large-area dye-sensitized solar cells (DSSC) and the hydrogen evolution reaction (HER)", Nanoscale **10**, 16657–16666 (2018).

[226] N. Veizaga, V. Rodriguez, M. Bruno and S. Miguel, "The role of surface functionalities in PtGe and PtIn catalysts for direct methanol fuel cells", Electrocatalysis **10**, 125–133 (2019).

[227] Y. Ma, S. Song, C. Liu, L. Liu, L. Zhang and Y. Zhao, "Germanium-enriched double-four-membered-ring units inducing zeolite-confined subnanometric Pt clusters for efficient propane dehydrogenation", Nat. Catal. **6**, 506–518 (2023).

[228] E. Jimenez-Izal, J.-Y. Liu and A. Alexandrova, "Germanium as key dopant to boost the catalytic performance of small platinum clusters for alkane dehydrogenation", J. Catal. **374**, 93–100 (2019).

[229] P. Poths, B. Zandkarimi, A. Alexandrova and E. Jimenez-Izal, "Pt:Ge Ratio as a Lever of Activity and Selectivity Control of Supported PtGe Clusters in Thermal Dehydrogenation", ChemCatChem **15**, 202201533–202201542 (2023).

[230] S. Rimaz, L. Chen, S. Kawi and A. Borgna, "Promoting effect of Ge on Pt-based catalysts for dehydrogenation of propane to propylene", Appl. Cat. A: Gen. **588**, 117266–117275 (2019).

[231] S. Rimaz, L. Chen, A. Monzón, S. Kawi and A. Borgna, "Enhanced selectivity and stability of $Pt-Ge/Al_2O_3$ catalysts by Ca promotion in propane dehydrogenation", J. Chem. Eng. **405**, 126656–126655 (2021).

[232] S. Rimaz, M. Kosari, L. Chen, S. Xi, A. Monzón and S. Kawi, "Insights into catalyst structure, kinetics and reaction mechanism during propane dehydrogenation on $Pt-Ge$ bimetallic catalysts", Appl. Cat. A: Gen. **643**, 118751–118761 (2022).

[233] M. Planck, "Ueber das Gesetz der Energieverteilung im Normalspectrum", Ann. Phys. **309**, 553–563 (1901).

[234] A. Einstein, "Über einen die Erzeugung und Verwandlung des Lichtes betreffenden heuristischen Gesichtspunkt", Ann. Phys. **322**, 132–148 (1905).

[235] E. Rutherford, "The scattering of α and β particles by matter and the structure of the atom", Lond. Edinb. Dublin Philos. Mag. J. Sci. **21**, 669–688 (1911).

[236] N. Bohr, "On the constitution of atoms and molecules, Part I", Lond. Edinb. Dublin Philos. Mag. J. Sci. **26**, 1–25 (1913).

[237] N. Bohr, "On the constitution of atoms and molecules, Part II, Systems Containing Only a Single Nucleus", Lond. Edinb. Dublin Philos. Mag. J. Sci. **26**, 476–502 (1913).

[238] N. Bohr, "On the constitution of atoms and molecules, Part III, Systems containing several nuclei", Lond. Edinb. Dublin Philos. Mag. J. Sci. **26**, 857–875 (1913).

[239] L. D. Broglie, "Recherches sur la théorie des Quanta", Ann. Phys. **10**, 22–128 (1925).

[240] W. Heisenberg, "Über quantentheoretische Umdeutung kinematischer und mechanischer Beziehungen", Z. Für Phys. **33**, 879–893 (1925).

[241] M. Born and P. Jordan, "Zur Quantenmechanik", Z. Für Phys. **34**, 858–888 (1925).

[242]M. Born, W. Heisenberg and P. Jordan, "Zur Quantenmechanik. II.", Z. Für Phys. **35**, 557–615 (1926).

[243]W. Heisenberg, "Über den anschaulichen Inhalt der quantentheoretischen Kinematik und Mechanik", Z. Für Phys. **43**, 172–198 (1927).

[244]E. Schrödinger, "Quantisierung als Eigenwertproblem", Ann. Phys. **384**, 361–376 (1926).

[245]E. Schrödinger, "Quantisierung als Eigenwertproblem", Ann. Phys. **384**, 489–527 (1926).

[246]E. Schrödinger, "Quantisierung als Eigenwertproblem", Ann. Phys. **385**, 437–490 (1926).

[247]M. Born, "Zur Quantenmechanik der Stoßvorgänge", Z. Für Phys. **37**, 863–867 (1926).

[248]P. A. M. Dirac, *The Principles of Quantum Mechanics* (Clarendon Press, Oxford, 1930).

[249]J. von Neumann, *Mathematische Grundlagen der Quantenmechanik* (Springer, Berlin, Heidelberg, 1932).

[250]M. J. Nye, *From Chemical Philosophy to Theoretical Chemistry: Dynamics of Matter and Dynamics of Disciplines, 1800-1950* (University of California Press, 1993).

[251]E. P. Wigner, "The unreasonable effectiveness of mathematics in the natural sciences", Commun. Pure Appl. Math. **13**, 1–14 (1960).

[252]W. Heitler and F. London, "Wechselwirkung neutraler Atome und homöopolare Bindung nach der Quantenmechanik", Z. Für Phys. **44**, 455–472 (1927).

[253]J. C. Slater, "Cohesion in Monovalent Metals", Phys. Rev. **35**, 509–529 (1930).

[254]J. C. Slater, "Molecular Energy Levels and Valence Bonds", Phys. Rev. **38**, 1109–1144 (1931).

[255]J. C. Slater, "Note on Molecular Structure", Phys. Rev. **41**, 255–257 (1932).

[256]L. Pauling, "The Shared-Electron Chemical Bond", Proc. Natl. Acad. Sci. **14**, 359–362 (1928).

[257] L. Pauling, "The Nature of the Chemical Bond. Application of Results Obtained from the Quantum Mechanics and from a Theory of Paramagnetic Susceptibility to the Structure of Molecules", J. Am. Chem. Soc. **53**, 1367–1400 (1931).

[258] L. Pauling, "The Nature of the Chemical Bond. II. The One-Electron Bond and the Three-Electron Bond", J. Am. Chem. Soc. **53**, 3225–3237 (1931).

[259] G. N. Lewis, "The Atom and the Molecule", J. Am. Chem. Soc. **38**, 762–785 (1916).

[260] E. A. Hylleraas, "Über den Grundzustand des Heliumatoms", Z. Für Phys. **48**, 469–494 (1928).

[261] F. Hund, "Zur Deutung der Molekelspektren. I", Z. Für Phys. **40**, 742–764 (1927).

[262] F. Hund, "Zur Deutung der Molekelspektren. II", Z. Für Phys. **42**, 93–120 (1927).

[263] F. Hund, "Zur Deutung der Molekelspektren. III.", Z. Für Phys. **43**, 805–826 (1927).

[264] R. S. Mulliken, "The Assignment of Quantum Numbers for Electrons in Molecules. I", Phys. Rev. **32**, 186–222 (1928).

[265] R. S. Mulliken, "The Assignment of Quantum Numbers for Electrons in Molecules. II. Correlation of Molecular and Atomic Electron States", Phys. Rev. **32**, 761–772 (1928).

[266] R. S. Mulliken, "The Assignment of Quantum Numbers for Electrons in Molecules. III. Diatomic Hydrides", Phys. Rev. **33**, 730–747 (1929).

[267] R. S. Mulliken, "Electronic Structures of Polyatomic Molecules and Valence", Phys. Rev. **40**, 55–62 (1932).

[268] D. R. Hartree, "The Wave Mechanics of an Atom with a Non-Coulomb Central Field. Part I. Theory and Methods", Math. Proc. Camb. Philos. Soc. **24**, 89–110 (1928).

[269] D. R. Hartree, "The Wave Mechanics of an Atom with a Non-Coulomb Central Field. Part II. Some Results and Discussion", Math. Proc. Camb. Philos. Soc. **24**, 111–132 (1928).

[270]V. Fock, "Näherungsmethode zur Lösung des quantenmechanischen Mehrkörperproblems", Z. Für Phys. **61**, 126–148 (1930).

[271]V. Fock, ""Selfconsistent field" mit Austausch für Natrium", Z. Für Phys. **62**, 795–805 (1930).

[272]C. C. J. Roothaan, "New Developments in Molecular Orbital Theory", Rev. Mod. Phys. **23**, 69–89 (1951).

[273]G. G. Hall, "The molecular orbital theory of chemical valency VIII. A method of calculating ionization potentials", Proc. R. Soc. Lond. Ser. Math. Phys. Sci. **205**, 541–552 (1951).

[274]P. Löwdin, "On the Non-Orthogonality Problem Connected with the Use of Atomic Wave Functions in the Theory of Molecules and Crystals", J. Chem. Phys. **18**, 365–375 (1950).

[275]L. Pauling, *The Nature of the Chemical Bond and the Structure of Molecules and Crystals: An Introduction to Modern Structural Chemistry* (Cornell University Press, 1939).

[276]A. Szabo and N. S. Ostlund, *Modern quantum chemistry* (Dover Publications, New York, 1996).

[277]M. Born and R. Oppenheimer, "Zur Quantentheorie der Molekeln", Ann. Phys. **389**, 457–484 (1927).

[278]C. Møller and M. S. Plesset, "Note on an Approximation Treatment for Many-Electron Systems", Phys. Rev. **46**, 618–622 (1934).

[279]B. Roos, "A new method for large-scale CI calculations", Chem. Phys. Lett. **15**, 153–159 (1972).

[280]I. Shavitt, "The history and evolution of configuration interaction", Mol. Phys. **94**, 3–17 (1998).

[281]C. David Sherrill and H. F. Schaefer, "The Configuration Interaction Method: Advances in Highly Correlated Approaches", in *Advances in Quantum Chemistry*, Vol. 34 (Academic Press, 1st Jan. 1999), pp. 143–269.

[282]F. Coester, "Bound states of a many-particle system", Nucl. Phys. **7**, 421–424 (1958).

[283] F. Coester and H. Kümmel, "Short-range correlations in nuclear wave functions", Nucl. Phys. **17**, 477–485 (1960).

[284] O. Sinanoğlu, "Many-Electron Theory of Atoms and Molecules. I. Shells, Electron Pairs vs Many-Electron Correlations", J. Chem. Phys. **36**, 706–717 (1962).

[285] J. Čížek, "On the Correlation Problem in Atomic and Molecular Systems. Calculation of Wavefunction Components in Ursell-Type Expansion Using Quantum-Field Theoretical Methods", J. Chem. Phys. **45**, 4256–4266 (1966).

[286] J. Čižek and J. Paldus, "Correlation problems in atomic and molecular systems III. Rederivation of the coupled-pair many-electron theory using the traditional quantum chemical methodst", Int. J. Quantum Chem. **5**, 359–379 (1971).

[287] P. Siegbahn, A. Heiberg, B. Roos and B. Levy, "A Comparison of the Super-CI and the Newton-Raphson Scheme in the Complete Active Space SCF Method", Phys. Scr. **21**, 323 (1980).

[288] B. O. Roos, P. R. Taylor and P. E. M. Sigbahn, "A complete active space SCF method (CASSCF) using a density matrix formulated super-CI approach", Chem. Phys. **48**, 157–173 (1980).

[289] P. E. M. Siegbahn, J. Almlöf, A. Heiberg and B. O. Roos, "The complete active space SCF (CASSCF) method in a Newton–Raphson formulation with application to the HNO molecule", J. Chem. Phys. **74**, 2384–2396 (1981).

[290] J. Olsen, B. O. Roos, P. Jørgensen and H. J. A. Jensen, "Determinant based configuration interaction algorithms for complete and restricted configuration interaction spaces", J. Chem. Phys. **89**, 2185–2192 (1988).

[291] P.-A. Malmqvist, A. Rendell and B. O. Roos, "The restricted active space self-consistent-field method, implemented with a split graph unitary group approach", J. Phys. Chem. **94**, 5477–5482 (1990).

[292] K. Andersson, P.-A. Malmqvist, B. O. Roos, A. J. Sadlej and K. Wolinski, "Second-order perturbation theory with a CASSCF reference function", J. Phys. Chem. **94**, 5483–5488 (1990).

[293] K. Andersson, P.-A. Malmqvist and B. O. Roos, "Second-order perturbation theory with a complete active space self-consistent field reference function", J. Chem. Phys. **96**, 1218–1226 (1992).

[294] S. R. White, "Density matrix formulation for quantum renormalization groups", Phys. Rev. Lett. **69**, 2863–2866 (1992).

[295] P. Hohenberg and W. Kohn, "Inhomogeneous electron gas", Phys. Rev. **136**, B864–B871 (1964).

[296] R. M. Martin, *Electronic Structure: Basic Theory and Practical Methods* (Cambridge University Press, Cambridge, 2004).

[297] J. K. Percus, "The role of model systems in the few-body reduction of the N-fermion problem", Int. J. Quantum Chem. **13**, 89–124 (1978).

[298] M. Levy, "Universal variational functionals of electron densities, first-order density matrices, and natural spin-orbitals and solution of the v-representability problem", Proc. Natl. Acad. Sci. **76**, 6062–6065 (1979).

[299] E. H. Lieb, "Density functionals for coulomb systems", Int. J. Quantum Chem. **24**, 243–277 (1983).

[300] W. Kohn and L. J. Sham, "Self-Consistent Equations Including Exchange and Correlation Effects", Phys. Rev. **140**, A1133–A1138 (1965).

[301] C. A. Ullrich, *Time-Dependent Density-Functional Theory: Concepts and Applications* (Oxford University Press, Oxford, 2011).

[302] S. H. Vosko, L. Wilk and M. Nusair, "Accurate spin-dependent electron liquid correlation energies for local spin density calculations: a critical analysis", Can. J. Phys. **58**, 1200–1211 (1980).

[303] J. P. Perdew and Y. Wang, "Accurate and simple analytic representation of the electron-gas correlation energy", Phys. Rev. B **45**, 13244–13249 (1992).

[304] A. D. Becke, "A new mixing of Hartree–Fock and local density-functional theories", J. Chem. Phys. **98**, 1372–1377 (1993).

[305] J. Harris, "Adiabatic-connection approach to Kohn-Sham theory", Phys. Rev. A **29**, 1648–1659 (1984).

[306] A. D. Becke, "Density-functional thermochemistry. III. The role of exact exchange", J. Chem. Phys. **98**, 5648–5652 (1993).

[307] C. Lee, W. Yang and R. G. Parr, "Development of the Colle-Salvetti correlation-energy formula into a functional of the electron density", Phys. Rev. B **37**, 785–789 (1988).

[308] P. J. Stephens, F. J. Devlin, C. F. Chabalowski and M. J. Frisch, "Ab Initio Calculation of Vibrational Absorption and Circular Dichroism Spectra Using Density Functional Force Fields", J. Phys. Chem. **98**, 11623–11627 (1994).

[309] N. Ashcroft and N. D. Mermin, *Solid State Physics* (Saunders College Publishing, New York, 1976).

[310] F. Bloch, "Über die Quantenmechanik der Elektronen in Kristallgittern", Z. Für Phys. **52**, 555–600 (1929).

[311] R. Hoffmann, "How Chemistry and Physics Meet in the Solid State", Angew. Chem. Int. Ed. **26**, 846–878 (1987).

[312] D. R. Hamann, M. Schlüter and C. Chiang, "Norm-Conserving Pseudopotentials", Phys. Rev. Lett. **43**, 1494–1497 (1979).

[313] D. Vanderbilt, "Soft self-consistent pseudopotentials in a generalized eigenvalue formalism", Phys. Rev. B **41**, 7892–7895 (1990).

[314] P. E. Blöchl, "Projector augmented-wave method", Phys. Rev. B **50**, 17953–17979 (1994).

[315] G. Kresse and D. Joubert, "From ultrasoft pseudopotentials to the projector augmented-wave method", Phys. Rev. B **59**, 1758–1775 (1999).

[316] A. J. Stone, *The Theory of Intermolecular Forces*, 2nd ed. (Oxford University Press, Oxford, 2013).

[317] S. Grimme, J. Antony, S. Ehrlich and H. Krieg, "A consistent and accurate ab initio parametrization of density functional dispersion correction (DFT-D) for the 94 elements H-Pu", J. Chem. Phys. **132**, 154104–154122 (2010).

[318] O. T. Hofmann, E. Zojer, L. Hörmann, A. Jeindl and R. J. Maurer, "First-principles calculations of hybrid inorganic–organic interfaces: from state-of-the-art to best practice", Phys. Chem. Chem. Phys. **23**, 8132–8180 (2021).

[319] A. H. Motagamwala and J. A. Dumesic, "Microkinetic Modeling: A Tool for Rational Catalyst Design", Chem. Rev. **121**, 1049–1076 (2021).

[320] B. W. J. Chen, L. Xu and M. Mavrikakis, "Computational Methods in Heterogeneous Catalysis", Chem. Rev. **121**, 1007–1048 (2021).

[321] I. A. W. Filot, *Introduction to microkinetic modeling* (Technische Universiteit Eindhoven, Eindhoven, 2018).

[322] J. A. Dumesic, D. F. Rudd, L. M. Aparicio, J. E. Rekoske and T. A. A., *The Microkinetics of Heterogeneous Catalysis* (American Chemical Society, Washington DC, 1993).

[323] P. Stoltze and J. K. Nørskov, "The surface science based ammonia kinetics revisited", Top. Catal. **1**, 253–263 (1994).

[324] C. V. Ovesen, B. S. Clausen, B. S. Hammershøi, G. Steffensen, T. Askgaard, I. Chorkendorff, J. K. Nørskov, P. B. Rasmussen, P. Stoltze and P. Taylor, "A Microkinetic Analysis of the Water–Gas Shift Reaction under Industrial Conditions", J. Catal. **158**, 170–180 (1996).

[325] J. Z. H. Zhang and W. H. Miller, "Quantum reactive scattering via the S-matrix version of the Kohn variational principle: Differential and integral cross sections for $D + H_2 \longrightarrow HD + H$", J. Chem. Phys. **91**, 1528–1547 (1989).

[326] J. I. Steinfeld, J. S. Francisco and W. L. Hase, *Chemical Kinetics and Dynamics* (Prentice Hall, New Jersey, 1989).

[327] R. D. Cortright and J. A. Dumesic, "Kinetics of heterogeneous catalytic reactions: Analysis of reaction schemes", in *Adv. catal.* Vol. 46 (Academic Press, 1st Jan. 2001), pp. 161–264.

[328] H. Eyring, "The Activated Complex in Chemical Reactions", J. Chem. Phys. **3**, 107–115 (1935).

[329] M. G. Evans and M. Polanyi, "Some applications of the transition state method to the calculation of reaction velocities, especially in solution", Trans. Faraday Soc. **31**, 875–894 (1935).

[330] Z.-J. Zhao, C.-C. Chiu and J. Gong, "Molecular understandings on the activation of light hydrocarbons over heterogeneous catalysts", Chem. Sci. **6**, 4403–4425 (2015).

[331] J. Sattler, J. Ruiz-Martinez, E. Santillan-Jimenez and B. Weckhuysen, "Catalytic Dehydrogenation of Light Alkanes on Metals and Metal Oxides", Chem. Rev. **114**, 10613–10653 (2014).

[332] E. Auer, A. Freund, J. Pietsch and T. Tacke, "Carbons as supports for industrial precious metal catalysts", Appl. Catal. A: Gen. **173**, 259–271 (1998).

[333] C. Zhang, L. Xu, N. Shan, T. Sun, J. Chen and Y. Yan, "Surface Composition and Lattice Ordering-Controlled Activity and Durability of CuPt Electrocatalysts for Oxygen Reduction Reaction", ACS Catal. **4**, 1926–1930 (2014).

[334] J. Yu, S. Kang, S. Yoon and G. Chai, "Fabrication of Ordered Uniform Porous Carbon Networks and Their Application to a Catalyst Supporter", J. Am. Chem. Soc. **124**, 9382–9383 (2002).

[335] B. Steele, "Running on natural gas", Nature **400**, 619–621 (1999).

[336] S. Litster and G. McLean, "PEM fuel cell electrodes", J. Power Sources **130**, 61–76 (2004).

[337] C. H Bartholomew, "Mechanisms of catalyst deactivation", Appl. Catal. A: Gen. **212**, 17–60 (2001).

[338] J. Delgado, V. Águeda, M. Uguina, J. Sotelo, P. Brea and C. Grande, "Adsorption and Diffusion of H_2, CO, CH_4, and CO_2 in BPL Activated Carbon and 13X Zeolite: Evaluation of Performance in Pressure Swing Adsorption Hydrogen Purification by Simulation", Ind. Eng. Chem. Res. **53**, 15414–15426 (2014).

[339] P. Panagiotopoulou, D. Kondarides and X. Verykios, "Mechanistic Study of the Selective Methanation of CO over Ru/TiO_2 Catalyst: Identification of Active Surface Species and Reaction Pathways", J. Phys. Chem. C **115**, 1220–1230 (2011).

[340] S. Kenarsari, D. Yang, G. Jiang, S. Zhang, J. Wang, A. Russell, Q. Wei and M. Fan, "Review of recent advances in carbon dioxide separation and capture", RSC Adv. **3**, 22739–22773 (2013).

[341] A. Yousaf, M. Imran, A. Zeb, T. Wen, X. Xie, Y.-F. Jiang, C.-Z. Yuan and A.-W. Xu, "Single Phase PtAg Bimetallic Alloy Nanoparticles Highly Dispersed on Reduced Graphene Oxide for Electrocatalytic Application of Methanol Oxidation Reaction", Electrochim. Acta **197**, 117–125 (2016).

[342] M. Yin, Y. Huang, L. Liang, J. Liao, C. Liu and W. Xing, "Inhibiting CO formation by adjusting surface composition in PtAu alloys for methanol electrooxidation", Chem. Comm. **47**, 8172–8174 (2011).

[343] S. Stolbov, M. Ortigoza, R. Adzic and T. Rahman, "High CO tolerance of Pt/Ru nanocatalyst: Insight from first principles calculations", J. Chem. Phys. **130**, 124714–124718 (2009).

[344] S. Lee, S. Mukerjee, E. Ticianelli and J. McBreen, "Electrocatalysis of CO tolerance in hydrogen oxidation reaction in PEM fuel cells", Electrochim. Acta **44**, 3283–3293 (1999).

[345] B. Hayden, M. Rendall and O. South, "Electro-oxidation of Carbon Monoxide on Well-Ordered Pt(111)/Sn Surface Alloys", J. Am. Chem. Soc. **125**, 7738–7742 (2003).

[346] G. Samjeské, H. Wang, T. Löffler and H. Baltruschat, "CO and methanol oxidation at Pt-electrodes modified by Mo", Electrochim. Acta **47**, 3681–36902 (2002).

[347] P. Ferrari, L. Molina, V. Kaydashev, J. Alonso, P. Lievens and E. Janssens, "Controlling the Adsorption of Carbon Monoxide on Platinum Clusters by Dopant-Induced Electronic Structure Modification", Angew. Chem. Int. Ed. **55**, 11059–11063 (2016).

[348] P. Ferrari, J. Vanbuel, N. Tam, M. Nguyen, S. Gewinner, W. Schöllkopf, A. Fielicke and E. Janssens, "Effects of Charge Transfer on the Adsorption of CO on Small Molybdenum-Doped Platinum Clusters", Chem. Eur. J. **23**, 4120–4127 (2017).

[349] M. Obradović, A. Tripković and S. Gojković, "Oxidation of carbon monoxide and formic acid on bulk and nanosized Pt−Co alloys", J. Solid State Electrochem. **16**, 587–595 (2012).

[350] S. M. M. Ehteshami and S. H. Chan, "A review of electrocatalysts with enhanced CO tolerance and stability for polymer electrolyte membarane fuel cells", Electrochim. Acta **93**, 334–345 (2013).

[351] Z. Chen, D. Rao, J. Zhang, Y. Liu, Y. Wang, C. Liu, W. Hu and Y. Deng, "Highly Active and CO-Tolerant Trimetallic NiPtPd Hollow Nanocrystals as Electrocatalysts for Methanol Electro-oxidation Reaction", ACS Appl. Energy Mater. **2**, 4763–4773 (2019).

[352] J. Ribeiro, E. Neto, G. Salazar-Banda and K. Eguiluz, "Carbon-Supported Pt and Pt−Ir Nanowires for Methanol Electro-Oxidation in Acidic Media", Cat. Lett. **149**, 2614–2626 (2019).

[353] P. Ferrari, G. Libeert, N. Tam and E. Janssens, "Interaction of carbon monoxide with doped metal clusters", CrystEngComm **22**, 4807–4815 (2020).

[354] H. Schwarz, "Doping Effects in Cluster-Mediated Bond Activation", Angew. Chem. Int. Ed. **54**, 10090–10100 (2015).

[355] S. Zhou, J. Li, M. Schlangen and H. Schwarz, "Bond Activation by Metal−Carbene Complexes in the Gas Phase ", Acc. Chem. Res. **49**, 494–502 (2016).

[356] J. Vanbuel, P. Ferrari and E. Janssens, "Few-atom cluster model systems for a hydrogen economy", Adv. Phys. X **5**, 1754132–1754160 (2020).

[357] H. Zhai and A. N. Alexandrova, "Ensemble-Average Representation of Pt Clusters in Conditions of Catalysis Accessed through GPU Accelerated Deep Neural Network Fitting Global Optimization", J. Chem. Theory Comput. **12**, 6213–6226 (2016).

[358] G. Kresse and J. Hafner, "Ab initio molecular dynamics for liquid metals", Phys. Rev. B **47**, 558–561 (1993).

[359] G. Kresse and J. Hafner, "Ab initio molecular-dynamics simulation of the liquid-metal–amorphous-semiconductor transition in germanium", Phys. Rev. B **49**, 14251–14269 (1994).

[360] G. Kresse and J. Furthmüller, "Efficiency of ab-initio total energy calculations for metals and semiconductors using a plane-wave basis set", Comput. Mater. Sci. **6**, 15–50 (1996).

[361] G. Kresse and J. Furthmüller, "Efficient iterative schemes for ab initio total-energy calculations using a plane-wave basis set", Phys. Rev. B **54**, 11169–11186 (1996).

[362] J. P. Perdew, K. Burke and M. Ernzerhof, "Generalized Gradient Approximation Made Simple", Phys. Rev. Lett. **77**, 3865–3868 (1996).

[363] J. P. Perdew, K. Burke and M. Ernzerhof, "Generalized Gradient Approximation Made Simple [Phys. Rev. Lett. 77, 3865 (1996)]", Phys. Rev. Lett. **78**, 1396–1396 (1997).

[364] M. Sierka, "Synergy between theory and experiment in structure resolution of low-dimensional oxides", Prog. Surf. Sci. **85**, 398–434 (2010).

[365] R. Ahlrichs, M. Bär, M. Häser, M. Horn and C. Kölmel, "Electronic structure calculations on workstation computers: The program system turbomole", Chem. Phys. Lett. **162**, 165–169 (1989).

[366] S. Balasubramani, G. Chen, S. Coriani, M. Diedenhofen, M. Frank, Y. Franzke, F. Furche, R. Grotjahn, M. Harding, C. Hättig, A. Hellweg, B. Helmich-Paris, C. Holzer, U. Huniar, M. Kaupp, A. Khah, S. Khani, T. Müller, F. Mack, B. Nguyen, S. Parker, E. Perlt, D. Rappoport, K. Reiter, S. Roy, M. Rückert, G. Schmitz, M. Sierka, E. Tapavicza, D. Tew, C. Wüllen, V. Voora, F. Weigend, A. Wodynski and J. Yu, "TURBOMOLE: Modular program suite for ab initio quantum-chemical and condensed-matter simulations", J. Chem. Phys. **152**, 184107–184142 (2020).

[367] V. Staroverov, G. Scuseria, J. Tao and J. Perdew, "Comparative assessment of a new nonempirical density functional: Molecules and hydrogen-bonded complexes", J. Chem. Phys. **119**, 12129–12137 (2003).

[368] V. Staroverov, G. Scuseria, J. Tao and J. Perdew, "Erratum: "Comparative assessment of a new nonempirical density functional: Molecules and hydrogen-bonded complexes" [J. Chem. Phys. 119, 12129 (2003)]", J. Chem. Phys. **121**, 11507 (2004).

[369] F. Weigend, M. Haser and H. Patzelt, "RI-MP2: optimized auxiliary basis sets and demonstration of efficiency", Chem. Phys. Lett. **294**, 143–152 (1998).

370 F. Weigend and R. Ahlrichs, "Balanced basis sets of split valence, triple zeta valence and quadruple zeta valence quality for H to Rn: Design and assessment of accuracy", Phys. Chem. Chem. Phys. **7**, 3297–3305 (2005).

371 O. Vydrov and G. Scuseria, "Assessment of a long-range corrected hybrid functional", J. Chem. Phys. **125**, 234109–234117 (2006).

372 M. Rohrdanz, K. Martins and J. Herbert, "A long-range-corrected density functional that performs well for both ground-state properties and time-dependent density functional theory excitation energies, including charge-transfer excited states", J. Chem. Phys. **130**, 054112–054119 (2009).

373 M. J. Frisch, G. W. Trucks, H. B. Schlegel, G. E. Scuseria, M. A. Robb, J. R. Cheeseman, G. Scalmani, V. Barone, G. A. Petersson, H. Nakatsuji, X. Li, M. Caricato, A. V. Marenich, J. Bloino, B. G. Janesko, R. Gomperts, B. Mennucci, H. P. Hratchian, J. V. Ortiz, A. F. Izmaylov, J. L. Sonnenberg, D. Williams-Young, F. Ding, F. Lipparini, F. Egidi, J. Goings, B. Peng, A. Petrone, T. Henderson, D. Ranasinghe, V. G. Zakrzewski, J. Gao, N. Rega, G. Zheng, W. Liang, M. Hada, M. Ehara, K. Toyota, R. Fukuda, J. Hasegawa, M. Ishida, T. Nakajima, Y. Honda, O. Kitao, H. Nakai, T. Vreven, K. Throssell, J. A. Montgomery Jr., J. E. Peralta, F. Ogliaro, M. J. Bearpark, J. J. Heyd, E. N. Brothers, K. N. Kudin, V. N. Staroverov, T. A. Keith, R. Kobayashi, J. Normand, K. Raghavachari, A. P. Rendell, J. C. Burant, S. S. Iyengar, J. Tomasi, M. Cossi, J. M. Millam, M. Klene, C. Adamo, R. Cammi, J. W. Ochterski, R. L. Martin, K. Morokuma, O. Farkas, J. B. Foresman and D. J. Fox, *Gaussian 16 Revision C.01*, Gaussian Inc. Wallingford CT, 2016.

374 A. Shayeghi, R. Schäfer, D. Rayner, R. Johnston and A. Fielicke, "Charge-induced dipole vs. relativistically enhanced covalent interactions in Ar-tagged Au−Ag tetramers and pentamers", J. Chem. Phys. **143**, 024310–024318 (2015).

375 A. Shayeghi, R. Johnston, D. Rayner, R. Schäfer and A. Fielicke, "The Nature of Bonding between Argon and Mixed Gold−Silver Trimers", Angew. Chem. Int. Ed. **54**, 10675–10680 (2015).

376 T. Lu and F. Chen, "Multiwfn: A multifunctional wavefunction analyzer", J. Comput. Chem. **33**, 580–592 (2012).

[377]E. Glendening, A. Reed, J. Carpenter and W. F., *NBO version 3.1, TCI* (University of Wisconsin, Madison, 1998).

[378]G. Blyholder, "Molecular Orbital View of Chemisorbed Carbon Monoxide", J. Phys. Chem. **68**, 2772–2777 (1964).

[379]H. Aizawa and S. Tsuneyuki, "First-principles study of CO bonding to Pt(111): validity of the Blyholder model", Surf. Sci. **399**, 364–370 (1989).

[380]S. Lubbe, P. Vermeeren, C. Guerra and M. Bickelhaupt, "The Nature of Nonclassical Carbonyl Ligands Explained by Kohn–Sham Molecular Orbital Theory", Chem. Eur. J **26**, 15690–15699 (2020).

[381]E. Skúlason, V. Tripkovic, M. Björketun, S. Gudmundsdóttir, G. Karlberg, J. Rossmeisl, T. Bligaard, H. Jónsson and J. Nørskov, "Modeling the Electrochemical Hydrogen Oxidation and Evolution Reactions on the Basis of Density Functional Theory Calculations", J. Phys. Chem. C **114**, 18182–18197 (2010).

[382]W. Sheng, M. Myint, J. Chen and Y. Yan, "Correlating the hydrogen evolution reaction activity in alkaline electrolytes with the hydrogen binding energy on monometallic surfaces", Energy Environ. Sci. **6**, 1509–1512 (2013).

[383]W. Sheng, Z. Zhuang, M. Gao, J. Zheng, J. Chen and Y. Yan, "Correlating hydrogen oxidation and evolution activity on platinum at different pH with measured hydrogen binding energy", Nat. Commun. **6**, 5848–5853 (2015).

[384]L. Ellingsen, C. Hung, G. Majeau-Bettez, B. Singh, Z. Chen, M. Whittingham and A. Strømman, "Nanotechnology for environmentally sustainable electromobility", Nat. Nanotechnol. **11**, 1039–1051 (2016).

[385]P. Owusu and S. Asumadu-Sarkodie, "A review of renewable energy sources, sustainability issues and climate change mitigation", Cogent. Eng. **3**, 1167990–1168003 (2016).

[386]J. Gong and R. Luque, "Catalysis for production of renewable energy", Chem. Soc. Rev. **43**, 7466–7468 (2014).

[387] M. Wakisaka, S. Mitsui, Y. Hirose, K. Kawashima, H. Uchida and M. Watanabe, "Electronic Structures of Pt−Co and Pt−Ru Alloys for CO-Tolerant Anode Catalysts in Polymer Electrolyte Fuel Cells Studied by EC-XPS", J. Phys. Chem. B **110**, 23489–23496 (2006).

[388] C. Zhan, Y. Xu, L. Bu, H. Zhu, Y. Feng, T. Yang, Y. Zhang, Z. Yang, B. Huang, Q. Shao and X. Huang, "Subnanometer high-entropy alloy nanowires enable remarkable hydrogen oxidation catalysis", Nature Comm. **12**, 6261–6268 (2021).

[389] M. J. Lee, J. S. Kang, Y. S. Kang, D. Y. Chung, H. Shin, C.-Y. Ahn, S. Park, M.-J. Kim, S. Kim, K.-S. Lee and Y.-E. Sung, "Understanding the Bifunctional Effect for Removal of CO Poisoning: Blend of a Platinum Nanocatalyst and Hydrous Ruthenium Oxide as a Model System", ACS Catal. **6**, 2398–2407 (2016).

[390] G. Henkelman, B. P. Uberuaga and H. Jónsson, "A climbing image nudged elastic band method for finding saddle points and minimum energy paths", J. Chem. Phys. **113**, 9901–9904 (2000).

[391] G. Henkelman and H. Jónsson, "Improved tangent estimate in the nudged elastic band method for finding minimum energy paths and saddle points", J. Chem. Phys. **113**, 9978–9985 (2000).

[392] D. Y. Zubarev and A. I. Boldyrev, "Developing paradigms of chemical bonding: adaptive natural density partitioning", Phys. Chem. Chem. Phys. **10**, 5207–5217 (2008).

[393] L. Li, R. Huang, Y. Wen and R. L. Johnston, "Structural and magnetic properties of Co−Pt clusters: A spin-polarized density functional study", J. Magn. Magn. Mater. **503**, 166651–166660 (2020).

[394] T. Gorey, B. Zandkarimi, G. Li, E. Baxter, A. Alexandrova and S. Anderson, "Coking-Resistant Sub-Nano Dehydrogenation Catalyst: Pt_nSn_x/SiO_2 ($n = 4, 7$)", ACS Catal. **10**, 4543–4558 (2020).

[395] G. Li, B. Zandkarimi, A. Cass, T. Gorey, B. Allen, A. Alexandrova and S. Anderson, "Sn-modification of Pt_7/alumina model catalysts: Suppression of carbon deposition and enhanced thermal stability", J. Chem. Phys. **152**, 024702–024714 (2020).

[396] I. Demiroglu, K. Yao, H. Hussein and R. Johnston, "DFT Global Optimization of Gas-Phase Subnanometer Ru−Pt Clusters", J. Phys. Chem. C **121**, 10773–10780 (2017).

[397] X. Lian, W. Tian, W. Guo, F. Liu, P. Xiao and Y. Zhang, "DFT study of $Pt_{7-x}Ru_x$ ($x = 0, 1, 2, 3$) clusters and their interactions with CO", Eur. Phys. J. D **68**, 72–79 (2014).

[398] L. Gálvez-González, A. Posada-Amarillas and L. Paz-Borbón, "Structure, Energetics, and Thermal Behavior of Bimetallic Re−Pt Clusters", J. Phys. Chem. A **125**, 4294–4305 (2021).

[399] G. Gunasooriya and M. Saeys, "CO Adsorption Site Preference on Platinum: Charge Is the Essence", ACS Catal. **8**, 3770–3774 (2018).

[400] A. Motagamwala, R. Almallahi, J. Wortman, V. Igenegbai and S. Linic, "Stable and selective catalysts for propane dehydrogenation operating at thermodynamic limit", Science **373**, 217–222 (2021).

[401] D. Zubarev and A. Boldyrev, "Deciphering Chemical Bonding in Golden Cages", J. Phys. Chem. A **113**, 866–868 (2009).

[402] H.-J. Freund, G. Meijer, M. Scheffler, R. Schlögl and M. Wolf, "CO oxidation as a prototypical reaction for heterogeneous processes", Angew. Chem. Int. Ed. **50**, 10064–10094 (2011).

[403] N. K. Soliman, "Factors affecting CO oxidation reaction over nanosized materials: A review", J. Mater. Res. Technol. **8**, 2395–2407 (2019).

[404] T. Engel and G. Ertl, "Elementary Steps in the Catalytic Oxidation of Carbon Monoxide on Platinum Metals", in *Adv. catal.* Vol. 28, edited by D. D. Eley, H. Pines and P. B. Weez (Academic Press, 1st Jan. 1979), pp. 1–78.

[405] A. K Santra and D. W Goodman, "Catalytic oxidation of CO by platinum group metals: from ultrahigh vacuum to elevated pressures", Electrochim. Acta **47**, 3595–3609 (2002).

[406] S. Royer and D. Duprez, "Catalytic Oxidation of Carbon Monoxide over Transition Metal Oxides", ChemCatChem **3**, 24–65 (2011).

[407]P.-A. Carlsson, M. Skoglundh, P. Thormählen and B. Andersson, "Low-temperature CO oxidation over a Pt/Al_2O_3 monolith catalyst investigated by step-response experiments and simulations", Top. Catal. **30**, 375–381 (2004).

[408]A. D. Allian, K. Takanabe, K. L. Fujdala, X. Hao, T. J. Truex, J. Cai, C. Buda, M. Neurock and E. Iglesia, "Chemisorption of CO and Mechanism of CO Oxidation on Supported Platinum Nanoclusters", J. Am. Chem. Soc. **133**, 4498–4517 (2011).

[409]A. Beniya, S. Higashi, N. Ohba, R. Jinnouchi, H. Hirata and Y. Watanabe, "CO oxidation activity of non-reducible oxide-supported mass-selected few-atom Pt single-clusters", Nat. Commun. **11**, 1888–1897 (2020).

[410]F. Wang, Z. Li, H. Wang, M. Chen, C. Zhang, P. Ning and H. He, "Nano-sized Ag rather than single-atom Ag determines CO oxidation activity and stability", Nano Res. **15**, 452–456 (2022).

[411]E.-Y. Ko, E. D. Park, K. W. Seo, H. C. Lee, D. Lee and S. Kim, "Pt−Ni/γ-Al_2O_3 catalyst for the preferential CO oxidation in the hydrogen stream", Catal. Lett. **110**, 275–279 (2006).

[412]R. Mandapaka, S. Bachu, C. Srivastava and G. Madras, "Microkinetic Modeling of CO Oxidation over FePt-Decorated Graphene Oxide", Ind. Eng. Chem. Res. **56**, 8465–8473 (2017).

[413]A. E. Aksoylu, M. M. A Freitas and J. L. Figueiredo, "Bimetallic Pt−Sn catalysts supported on activated carbon. II. CO oxidation", Catal. Today **62**, 337–346 (2000).

[414]B. S. Caglayan, I. I. Soykal and A. E. Aksoylu, "Preferential oxidation of CO over Pt−Sn/AC catalyst: Adsorption, performance and DRIFTS studies", Appl. Catal. B: Environ. **106**, 540–549 (2011).

[415]S. Y. Chin, O. S. Alexeev and M. D. Amiridis, "Structure and reactivity of Pt−Ru/SiO_2 catalysts for the preferential oxidation of CO under excess H_2", J. Catal. **243**, 329–339 (2006).

[416]T. Ebashi, Y. Ishida, Y. Nakagawa, S. Ito, T. Kubota and K. Tomishige, "Preferential CO Oxidation in a H_2-Rich Stream on $Pt-ReO_x/SiO_2$: Catalyst Structure and Reaction Mechanism", J. Phys. Chem. C **114**, 6518–6526 (2010).

[417]G. Henkelman and H. Jónsson, "A dimer method for finding saddle points on high dimensional potential surfaces using only first derivatives", J. Chem. Phys. **111**, 7010–7022 (1999).

[418]A. Heyden, A. T. Bell and F. J. Keil, "Efficient methods for finding transition states in chemical reactions: Comparison of improved dimer method and partitioned rational function optimization method", J. Chem. Phys. **123**, 224101–224115 (2005).

[419]M. M. Kauppinen, M. M. Melander, A. S. Bazhenov and K. Honkala, "Unraveling the Role of the $Rh-ZrO_2$ Interface in the Water$-$Gas-Shift Reaction via a First-Principles Microkinetic Study", ACS Catal. **8**, 11633–11647 (2018).

[420]N. M. Alghamdi, R. Gautam, J. Gascon, D. G. Vlachos and S. M. Sarathy, "Low-temperature CO oxidation over Rh/Al_2O_3 in a stagnation-flow reactor", React. Chem. Eng. **7**, 2497–2507 (2022).

[421]J.-X. Liu, I. A. W. Filot, Y. Su, B. Zijlstra and E. J. M. Hensen, "Optimum Particle Size for Gold-Catalyzed CO Oxidation", J. Phys. Chem. C **122**, 8327–8340 (2018).

[422]J. C. González-Torres, V. Bertin, E. Poulain and O. Olvera-Neria, "The CO oxidation mechanism on small Pd clusters. A theoretical study", J. Mol. Model. **21**, 279–288 (2015).

[423]L. Ma, M. Melander, T. Weckman, K. Laasonen and J. Akola, "CO Oxidation on the $Au_{15}Cu_{15}$ Cluster and the Role of Vacancies in the MgO(100) Support", J. Phys. Chem. C **120**, 26747–26758 (2016).

[424]L. Ma, K. Laasonen and J. Akola, "Catalytic Activity of AuCu Clusters on MgO(100): Effect of Alloy Composition for CO Oxidation", J. Phys. Chem. C **121**, 10876–10886 (2017).

[425] M. Di, K. Simmance, A. Schaefer, Y. Feng, F. Hemmingsson, M. Skoglundh, T. Bell, D. Thompsett, L. I. Ajakaiye Jensen, S. Blomberg and P.-A. Carlsson, "Chasing PtO_x species in ceria supported platinum during CO oxidation extinction with correlative operando spectroscopic techniques", J. Catal. **409**, 1–11 (2022).

[426] S. Johansson, L. Österlund and B. Kasemo, "CO Oxidation Bistability Diagrams for Pt/CeO_x and Pt/SiO_2 Model Catalysts Prepared by Electron-Beam Lithography", J. Catal. **201**, 275–285 (2001).

[427] L. Skubic, D. Kopač, B. Likozar and M. Huš, "Microkinetic modelling of heterogeneous catalysis revisited: Adsorption energies can triumph over activation barriers", Appl. Surf. Sci. **601**, 154135–154149 (2022).

[428] Y. Yang, S. K. Achar and J. R. Kitchin, "Evaluation of the degree of rate control via automatic differentiation", AIChE J. **68**, e17653 (2022).

[429] C. T. Campbell, "The Degree of Rate Control: A Powerful Tool for Catalysis Research", ACS Catal. **7**, 2770–2779 (2017).

[430] L. M. Molina, C. Arranz-Simón and J. A. Alonso, "Mechanistic insight into the CO oxidation reaction at pure, Nb-doped and Mo-doped medium size Pt clusters", Mol. Catal. **533**, 112749–112758 (2022).

[431] H. P. Bideberripe, J. M. Ramallo-López, S. J. A. Figueroa, M. A. Jaworski, M. L. Casella and G. J. Siri, "Ge-modified Pt/SiO_2 catalysts used in preferential CO oxidation (CO-PROX)", Catal. Commun. **12**, 1280–1285 (2011).

[432] K. Gong, F. Du, Z. Xia, M. Durstock and L. Dai, "Nitrogen-Doped Carbon Nanotube Arrays with High Electrocatalytic Activity for Oxygen Reduction", Science **323**, 760–764 (2009).

[433] R. Bellabarba, P. Johnston, S. Moss, C. Sievers, B. Subramaniam, C. Tway, Z. Wang and H. Zhu, "Net Zero Transition: Possible Implications for Catalysis", ACS Catal. **13**, 7917–7928 (2023).

[434] X. X. Wang, M. T. Swihart and G. Wu, "Achievements, challenges and perspectives on cathode catalysts in proton exchange membrane fuel cells for transportation", Nat. Catal. **2**, 578–589 (2019).

[435] I. E. L. Stephens, A. S. Bondarenko, U. Grønbjerg, J. Rossmeisl and I. Chorkendorff, "Understanding the electrocatalysis of oxygen reduction on platinum and its alloys", Energy Environ. Sci. **5**, 6744–6762 (2012).

[436] H. R. Colón-Mercado and B. N. Popov, "Stability of platinum based alloy cathode catalysts in PEM fuel cells", J. Power Sources **155**, 253–263 (2006).

[437] Y. Shao, G. Yin and Y. Gao, "Understanding and approaches for the durability issues of Pt-based catalysts for PEM fuel cell", J. Power Sources **171**, 558–566 (2007).

[438] J. Greeley, T. F. Jaramillo, J. Bonde, I. Chorkendorff and J. K. Nørskov, "Computational high-throughput screening of electrocatalytic materials for hydrogen evolution", Nat. Mater. **5**, 909–913 (2006).

[439] H. Zhang, "Ultrathin Two-Dimensional Nanomaterials", ACS Nano **9**, 9451–9469 (2015).

[440] X. Chia and M. Pumera, "Characteristics and performance of two-dimensional materials for electrocatalysis", Nat. Catal. **1**, 909–921 (2018).

[441] D. Deng, K. S. Novoselov, Q. Fu, N. Zheng, Z. Tian and X. Bao, "Catalysis with two-dimensional materials and their heterostructures", Nat. Nanotechnol. **11**, 218–230 (2016).

[442] L. X. Chen, Z. W. Chen, M. Jiang, Z. Lu, C. Gao, G. Cai and C. V. Singh, "Insights on the dual role of two-dimensional materials as catalysts and supports for energy and environmental catalysis", J. Mater. Chem. A **9**, 2018–2042 (2021).

[443] T. Li, T. Jing, D. Rao, S. Mourdikoudis, Y. Zuo and M. Wang, "Two-dimensional materials for electrocatalysis and energy storage applications", Inorg. Chem. Front. **9**, 6008–6046 (2022).

[444] H. Jin, T. Song, U. Paik and S.-Z. Qiao, "Metastable Two-Dimensional Materials for Electrocatalytic Energy Conversions", Acc. Mater. Res. **2**, 559–573 (2021).

[445] Q. Zhu, Y. Qu, D. Liu, K. Ng and H. Pan, "Two-Dimensional Layered Materials: High-Efficient Electrocatalysts for Hydrogen Evolution Reaction", ACS Appl. Nano Mater. **3**, 6270–6296 (2020).

[446] P. Bothra, M. Pandey and S. Pati, "Size-selective electrocatalytic activity of Pt_n/MoS_2 for oxygen reduction reaction", Catal. Sci. Technol. **6**, 6389–6395 (2016).

[447] G. Wang, X.-L. Jiang, Y.-F. Jiang, Y.-G. Wang and J. Li, "Screened Fe_3 and Ru_3 Single-Cluster Catalysts Anchored on MoS_2 Supports for Selective Hydrogenation of CO_2", ACS Catal. **13**, 8413–8422 (2023).

[448] R. Yoo, E. Pranada, D. Johnson, Z. Qiao and A. Djire, "Review–The Oxygen Reduction Reaction on MXene-Based Catalysts: Progress and Prospects", J. Electrochem. Soc. **169**, 063513 (2022).

[449] H. Fu, Z. Chen, X. Chen, F. Jing, H. Yu, D. Chen, B. Yu, Y. H. Hu and Y. Jin, "Modification Strategies for Development of 2D Material-Based Electrocatalysts for Alcohol Oxidation Reaction", Adv. Sci. **n/a**, 2306132.

[450] J. H. Kim, D. Y. Lee, N. Ling, Y. Lee, H. Yang and S. Cho, "Engineering Active Sites of 2D Materials for Active Hydrogen Evolution Reaction", Adv. Phys. Res. **2**, 2200060 (2023).

[451] B. He, X. Tao, L. Li, X. Liu and L. Chen, "Environmental TEM Study of the Dispersion of Au/α-MoC: From Nanoparticles to Two-Dimensional Clusters", Nano Lett. **23**, 10367–10373 (2023).

[452] J. Zhu, L. Xia, R. Yu, R. Lu, J. Li, R. He, Y. Wu, W. Zhang, X. Hong, W. Chen, Y. Zhao, L. Zhou, L. Mai and Z. Wang, "Ultrahigh Stable Methanol Oxidation Enabled by a High Hydroxyl Concentration on Pt Clusters/MXene Interfaces", J. Am. Chem. Soc. **144**, 15529–15538 (2022).

[453] G. Kim, S.-M. Jung, A. Giri, J.-S. Kim, Y.-W. Kim, K.-S. Kim, D. Kim, Y. Choi, B.-J. Lee, Y.-T. Kim and U. Jeong, "Enhanced hydrogen desorption via charge transfer in Pt Nanoclusters/ReS_2 hybrid electrocatalyst for efficient hydrogen evolution reaction", J. Power Sources **579**, 233287 (2023).

[454] L. Duan, C.-T. Hung, J. Wang, C. Wang, B. Ma, W. Zhang, Y. Ma, Z. Zhao, C. Yang, T. Zhao, L. Peng, D. Liu, D. Zhao and W. Li, "Synthesis of Fully Exposed Single-Atom-Layer Metal Clusters on 2D Ordered Mesoporous TiO_2 Nanosheets", Angew. Chem. Int. Ed. **61**, e202211307 (2022).

[455] G. Boschetto, S. Carapezzi and A. Todri-Sanial, "Supported Pt Nanoclusters on Single-Layer MoS_2 for the Detection of Cortisol: From Atomistic Scale to Device Modeling", ACS Appl. Electron. Mater. **5**, 2977–2987 (2023).

[456] X. Deng, D. Alfonso, T.-D. Nguyen-Phan and D. Kauffman, "Breaking the Limit of Size-Dependent CO_2RR Selectivity in Silver Nanoparticle Electrocatalysts through Electronic Metal−Carbon Interactions", ACS Catal. **13**, 15301–15309 (2023).

[457] C. Yao, N. Guo, S. Xi, C.-Q. Xu, W. Liu, X. Zhao, J. Li, H. Fang, J. Su, Z. Chen, H. Yan, Z. Qiu, P. Lyu, C. Chen, H. Xu, X. Peng, X. Li, B. Liu, C. Su, S. Pennycook, C.-J. Sun, J. Li, C. Zhang, Y. Du and J. Lu, "Atomically-precise dopant-controlled single cluster catalysis for electrochemical nitrogen reduction", Nat. Commun. **11**, 4389–4398 (2020).

[458] J.-T. Ren, L. Chen, H.-Y. Wang, W.-W. Tian, X. Zhang, T.-Y. Ma, Z. Zhou and Z.-Y. Yuan, "Inducing electronic asymmetricity on Ru clusters to boost key reaction steps in basic hydrogen evolution", Appl. Catal. B: Environ. **327**, 122466 (2023).

[459] F. Guo, Z. Zou, Z. Zhang, T. Zeng, Y. Tan, R. Chen, W. Wu, N. Cheng and X. Sun, "Confined sub-nanometer PtCo clusters as a highly efficient and robust electrocatalyst for the hydrogen evolution reaction", J. Mater. Chem. A **9**, 5468–5474 (2021).

[460] F. He, H. Li, Y. Ding, K. Li, Y. Wang and Z. Wu, "The oxygen reduction reaction on graphitic carbon nitride supported single Ce atom and Ce_xPt_{6-x} cluster catalysts from first-principles", Carbon **130**, 636–644 (2018).

[461] A. Ohnuma, K. Takahashi, H. Tsunoyama, T. Inoue, P. Zhao, A. Velloth, M. Ehara, N. Ichikuni, M. Tabuchi and A. Nakajima, "Enhanced oxygen reduction activity of size-selected platinum subnanocluster catalysts: Pt_n $(n = 3 − 9)$", Catal. Sci. Technol. **12**, 1400–1407 (2022).

[462] H. Gasteiger, N. Markovic, P. J. Ross and E. Cairns, "Methanol electrooxidation on well-characterized platinum-ruthenium bulk alloys", J. Phys. Chem. **97**, 12020–12029 (1993).

[463] Y. Zhou, Z. Xie, J. Jiang, J. Wang, X. Song, Q. He, W Ding and Z. Wei, "Lattice-confined Ru clusters with high CO tolerance and activity for the hydrogen oxidation reaction", Nat. Catal. **3**, 454–462 (2020).

[464] C. Yang, Y. Gao, T. Ma, M. Bai, C. He, X. Ren, X. Luo, C. Wu, S. Li and C. Cheng, "Metal Alloys-Structured Electrocatalysts: Metal−Metal Interactions, Coordination Microenvironments, and Structural Property−Reactivity Relationships", Adv. Mater. **35**, 2301836–2301881.

[465] L. Huang, S. Zaman, X. Tian, Z. Wang, W. Fang and B. Xia, "Advanced Platinum-Based Oxygen Reduction Electrocatalysts for Fuel Cells", Acc. Chem. Res. **54**, 311–322 (2021).

[466] Z. Xia, R. Zhu, R. Yu, S. Zhang, J.-Y. Jung and J. Zhang, "Review−Recent Progress in Highly Efficient Oxygen Reduction Electrocatalysts: From Structural Engineering to Performance Optimization", J. Electrochem. Soc. **169**, 034512 (2022).

[467] X. Huang, Z. Zhao, L. Cao, Y. Chen, E. Zhu, Z. Lin, M. Li, A. Yan, A. Zettl, Y. M. Wang, X. Duan, T. Mueller and Y. Huang, "High-performance transition metal−doped Pt_3Ni octahedra for oxygen reduction reaction", Science **348**, 1230–1234 (2015).

[468] J. Liu, F. Lucci, M. Yang, S. Lee, M. Marcinkowski, A. Therrien, C. Williams, E. Sykes and M. Flytzani-Stephanopoulos, "Tackling CO Poisoning with Single-Atom Alloy Catalysts", J. Am. Chem. Soc. **138**, 6396–6399 (2016).

[469] M. Escudero-Escribano, P. Malacrida, M. Hansen, U. Vej-Hansen, A. Velázquez-Palenzuela, V. Tripkovic, J. Schiøtz, J. Rossmeisl, I. Stephens and I. Chorkendorff, "Tuning the activity of Pt alloy electrocatalysts by means of the lanthanide contraction", Science **352**, 73–76 (2016).

[470] T. Lozano and R. Rankin, "Computational predictive design for metal-decorated-graphene size-specific subnanometer to nanometer ORR catalysts", Catal. Today **312**, 105–117 (2018).

[471] B. Wang and F. Zhang, "Main Descriptors To Correlate Structures with the Performances of Electrocatalysts", Angew. Chem. Int. Ed. **61**, e202111026 (2022).

[472] W. Zheng, R. Zhu, H. Wu, T. Ma, H. Zhou, M. Zhou, C. He, X. Liu, S. Li and C. Cheng, "Tailoring Bond Microenvironments and Reaction Pathways of Single-Atom Catalysts for Efficient Water Electrolysis", Angew. Chem. Int. Ed. **61**, e202208667 (2022).

[473] V. Giulimondi, S. Mitchell and J. Pérez-Ramírez, "Challenges and Opportunities in Engineering the Electronic Structure of Single-Atom Catalysts", ACS Catal. **13**, 2981–2997 (2023).

[474] H.-C. Tsai, Y.-C. Hsieh, T. Yu, Y.-J. Lee, Y.-H. Wu, B. Merinov, P.-W. Wu, S.-Y. Chen, R. Adzic and W. Goddard, "DFT Study of Oxygen Reduction Reaction on Os/Pt Core−Shell Catalysts Validated by Electrochemical Experiment", ACS Catal. **5**, 1568–1580 (2015).

[475] C. Roth, N. Benker, T. Buhrmester, M. Mazurek, M. Loster, H. Fuess, D. Koningsberger and D. Ramaker, "Determination of O[H] and CO Coverage and Adsorption Sites on PtRu Electrodes in an Operating PEM Fuel Cell", J. Am. Chem. Soc. **127**, 14607–14615 (2005).

[476] X. Zhang, Y. Xie and L. Wang, "Progress and prospect of Pt-based catalysts for electrocatalytic hydrogen oxidation reactions", Nano Res. (2023).

[477] Y. Shi, B. Song, R. Shahbazian-Yassar, J. Zhao and W. Saidi, "Experimentally Validated Structures of Supported Metal Nanoclusters on MoS_2", J. Phys. Chem. Lett. **9**, 2972–2978 (2018).

[478] X. Tian, P. Zhao and W. Sheng, "Hydrogen Evolution and Oxidation: Mechanistic Studies and Material Advances", Adv. Mater. **31**, 1808066 (2019).

[479] P. Wang, X. Zhang, J. Zhang, S. Wan, S. Guo, G. Lu, J. Yao and X. Huang, "Precise tuning in platinum−nickel/nickel sulfide interface nanowires for synergistic hydrogen evolution catalysis", Nat. Commun. **8**, 14580–14588 (2017).

[480] I. Mochizuki, Y. Fukaya, A. Kawasuso, K. Yaji, A. Harasawa, I. Matsuda, K. Wada and T. Hyodo, "Atomic configuration and phase transition of Pt-induced nanowires on a Ge(001) surface studied using scanning tunneling microscopy, reflection high-energy positron diffraction, and angle-resolved photoemission spectroscopy", Phys. Rev. B **85**, 245438–245443 (2012).

[481] D. E. P. Vanpoucke and G. Brocks, "Formation of Pt-induced Ge atomic nanowires on Pt/Ge(001): A density functional theory study", Phys. Rev. B **77**, 241308–241311 (2008).

[482] D. E. P. Vanpoucke and G. Brocks, "CO adsorption on Pt-induced Ge nanowires", Phys. Rev. B **81**, 235434–235446 (2010).

[483] E. P. George, D. Raabe and R. O. Ritchie, "High-entropy alloys", Nat. Rev. Mater. **4**, 515–534 (2019).

[484] H. Liu, L. Syama, L. Zhang, C. Lee, C. Liu, Z. Dai and Q. Yan, "High-entropy alloys and compounds for electrocatalytic energy conversion applications", SM & T **1**, 482–505 (2021).

[485] T. Löffler, A. Savan, A. Garzón-Manjón, M. Meischein, C. Scheu, A. Ludwig and W. Schuhmann, "Toward a Paradigm Shift in Electrocatalysis Using Complex Solid Solution Nanoparticles", ACS Energy Lett. **4**, 1206–1214 (2019).

[486] C. L. Allen, D. C. Leitch, M. S. Anson and M. A. Zajac, "The power and accessibility of high-throughput methods for catalysis research", Nat. Catal. **2**, 2–4 (2019).

[487] B. C. Yeo, H. Nam, H. Nam, M.-C. Kim, H. W. Lee, S.-C. Kim, S. O. Won, D. Kim, K.-Y. Lee, S. Y. Lee and S. S. Han, "High-throughput computational-experimental screening protocol for the discovery of bimetallic catalysts", npj Comput. Mater. **7**, 1–10 (2021).

[488] D. Roy, S. C. Mandal and B. Pathak, "Machine Learning-Driven High-Throughput Screening of Alloy-Based Catalysts for Selective CO_2 Hydrogenation to Methanol", ACS Appl. Mater. Interfaces **13**, 56151–56163 (2021).

[489] T. Mou, H. S. Pillai, S. Wang, M. Wan, X. Han, N. M. Schweitzer, F. Che and H. Xin, "Bridging the complexity gap in computational heterogeneous catalysis with machine learning", Nat. Catal. **6**, 122–136 (2023).

[490] T. Williams, K. McCullough and J. A. Lauterbach, "Enabling Catalyst Discovery through Machine Learning and High-Throughput Experimentation", Chem. Mater. **32**, 157–165 (2020).

[491] E. Jones, T. Oliphant and P. Peterson, *"SciPy: Open Source Scientific Tools for Python"*, (2001) https://scipy.org/ (visited on 29/05/2023).

Alphabetical Index